STRUCTURAL AND AEROELASTIC ANALYSES OF A COMPOSITE TACTICAL
UNMANNED AIR VEHICLE

A THESIS SUBMITTED TO
THE GRADUATE SCHOOL OF NATURAL AND APPLIED SCIENCES
OF
MIDDLE EAST TECHNICAL UNIVERSITY

BY

SEDAT ÖZÖZTÜRK

IN PARTIAL FULFILLMENT OF THE REQUIREMENTS
FOR
THE DEGREE OF MASTER OF SCIENCE
IN
AEROSPACE ENGINEERING

SEPTEMBER 2011

Approval of the thesis:

STRUCTURAL AND AEROELASTIC ANALYSES OF A COMPOSITE TACTICAL UNMANNED AIR VEHICLE

Submitted by **SEDAT ÖZÖZTÜRK** in partial fulfillment of the requirements for the degree of **Master of Science in Aerospace Engineering Department, Middle East Technical University** by,

Prof. Dr. Canan Özgen   _____
Dean, Graduate School of **Natural and Applied Sciences**

Prof. Dr. Ozan TEKİNALP   _____
Head of Department, **Aerospace Engineering**

Prof. Dr. Altan Kayran   _____
Supervisor, **Aerospace Engineering Dept., METU**

Prof. Dr. Nafiz Alemdaroğlu   _____
Co-Supervisor, **Aerospace Engineering Dept., METU**

Examining Committee Members:

Prof. Dr. Altan Kayran   _____
Aerospace Engineering Dept., METU

Prof. Dr. Nafiz Alemdaroğlu   _____
Aerospace Engineering Dept., METU

Prof. Dr. Yavuz YAMAN   _____
Aerospace Engineering Dept., METU

Asst. Prof. Dr. Demirkan Çöker   _____
Aerospace Engineering Dept., METU

Prof. Dr. Levend Parnas,   _____
Mechanical Engineering Dept., METU

Date: _____

I hereby declare that all information in this document has been obtained and presented in accordance with academic rules and ethical conduct. I also declare that, as required by these rules and conduct, I have fully cited and referenced all material and results that are not original to this work.

Name, Last Name   : **Sedat ÖZÖZTÜRK**

Signature   :

ABSTRACT

STRUCTURAL AND AEROELASTIC ANALYSES OF A COMPOSITE TACTICAL UNMANNED AIR VEHICLE

Özöztürk, Sedat

M.Sc., Department of Aerospace Engineering

Supervisor   : Prof. Dr. Altan KAYRAN

Co-Supervisor: Prof. Dr. Nafiz ALEMDAROĞLU

September 2011, 172 pages

In this thesis, computational aerodynamics, structural and aeroelastic analyses of the composite tactical unmanned air vehicle which is designed and manufactured in the Department of Aerospace Engineering are performed. Verification of the structural integrity of the air vehicle is shown at the minimum maneuvering and the dive speeds at the static limit loads which are calculated by the computational aerodynamics analysis of the full aircraft model. In the current work, aerodynamic loads are re-calculated for more accurately determined dive speed angle of attack in an effort to match the overall vertical pressure load more closely to the half of the aircraft weight at the positive load factor.

Finite element models of the fuselage, wing and the vertical-horizontal tail plane are prepared including the filament wound boom connecting the wing and the tail plane. Structural analyses of the composite wing, vertical and horizontal tail plane are performed under the limit aerodynamic loads calculated at the corner points of the V-N diagram using the structural finite element model of the wing-tail plane combination only. Global finite element analysis of the wing-tail plane combination showed that composite and isotropic materials of the wing-tail plane combination have positive margins of safety. Woven carbon and E-glass fabric that was procured

to be used for the serial production version of the airplane are characterized for the tensile properties by the tests.

Comprehensive aeroelastic stability analyses of the airplane are conducted by adding one sub-structure at a time to the aeroelastic model. Specifically, aeroelastic models which are used are the wing only, wing-tail plane combination, complete air vehicle with and without wing control surfaces. With such a study it is intended to address the effect each sub-structure adds to the aeroelastic model on the critical aeroelastic stability modes and speeds, and to see how sensitive the aeroelastic stability modes and speeds are to model fidelity.

Detailed structural and aeroelastic analyses showed that the airplane has sufficient structural integrity under the action of static limit loads, and no aeroelastic instability is expected to occur within the flight envelope of the airplane.

Keywords: UAV, compputional aerodynamics, structural finite element analysis, aeroelastic analysis, composite materials

ÖZ

KOMPOZİT BİR TAKTİK HAVA ARACININ YAPISAL VE AEROELASTİK KARARLILIK ANALİZLERİ

Özöztürk, Sedat

Yüksek Lisans, Havacılık ve Uzay Mühendisliği Bölümü

Tez Yöneticisi : Prof. Dr. Altan KAYRAN

Ortak Tez Yöneticisi: Prof. Dr. Nafiz ALEMDAROĞLU

Eylül 2011, 172 sayfa

Bu tezde Havacılık ve Uzay Mühendisliği bölümünde tasarlanan ve üretilen kompozit bir taktik insansız hava aracının hesaplamalı aerodinamik, yapısal ve aeroelastik analizleri gerçekleştirilmiştir. Hava aracı yapısal bütünlüğünün doğrulanması, minimum manevra ve pike hızlarında, tüm hava aracı için hesaplamalı akışkanlar dinamiği (HAD) yöntemiyle hesaplanan statik limit yük koşullarında gerçekleştirilmiştir. Bu çalışmada Hesaplamalı akışkanlar dinamiği (HAD) yükleri daha doğru hesaplanmış bir pike hızı hücum açısında dikey yönlü toplam basınç yükünün pozitif yük faktöründeki uçak ağırlığının yarısına daha yakın bulunması amacı ile tekrar hesaplanmıştır.

Kanat ve yatay-dikey kuyruk düzlemi sonlu elemanlar modeli kanat kuyruk birleşimini sağlayan elyaf sargılı boru modeli de dahil edilerek birlikte oluşturulmuştur. Kompozit kanat yapısal analizleri, birleşik kanat-kuyruk yapısal sonlu elemanlar modeli kullanılarak V-N diagramının köşe noktalarında hesaplanan limit aerodinamik yükleri altında gerçekleştirilmiştir. Kanat kuyruk düzleminin global sonlu eleman analizleri, kompozit ve izotropik malzemelerinde pozitif güvenlik marjı bulunduğunu göstermiştir. Hava aracının seri üretiminde kullanılacak örgü karbon ve cam-elyaf kumaşların çekme özellikleri testler ile belirlenmiştir.

Hava aracı kapsamlı aeroelastik kararlılık analizleri modele alt yapılar tek tek eklenerek gerçekleştirilmiştir. Kullanılan aeroelastik modeller kanat, kanat kuyruk düzlemi birleşimi, kontrol yüzeyleri dahil edilmemiş tüm hava aracı ve kontrol yüzeyleri dahil edilmiş tüm hava aracı modelleridir. Böyle bir çalışma ile aeroelastik modele eklenen alt-yapıların kritik aeroelastik kararlılık modlarına ve hızlarına etkisinin belirlenmesi ve aeroelastik kararlılık modları ve hızlarının model doğruluğuna ne kadar duyarlı olduğunun belirlenmesi amaçlanmıştır.

Detaylı yapısal ve aeroelastik analizler sonucunda hava aracının limit statik yükler altında yeterli yapısal bütünlüğe sahip olduğu ve uçuş zarfı içerisinde herhangi bir aeroelastik kararsızlık durumu oluşmadığı görülmüştür.

Anahtar Kelimeler: İHA, hesaplamalı akışkanlar, yapısal analiz, aeroelastik analiz, kompozit malzemeler

to my family…

ACKNOWLEDGEMENTS

TABLE OF CONTENTS

LIST OF TABLES

LIST OF FIGURES

xvi

LIST OF SYMBOLS

C_L	lift coefficient
C_D	drag coefficient
$C_{L\alpha}$	lift curve slope
C_{L0}	lift coefficient at zero angle of attack
FEM	Finite Element Model
MOS	margin of safety
MPC	Multi point contraint
UAV	unmanned air vehicle
$UCAV$	unmanned combat air vehicle
FI	failure index
F_i	strength tensor of the 2nd rank
F_{ij}	strength tensor of the 4th rank
σ_i	stress components
TX	tensile strength along the $x-$axis
TY	tensile strength along the $y-$axis
CX	compresive strength along the $x-$axis
CY	compresive strength along the $y-$axis
SXY	shear strength in the xy plane
IXY	interaction term of Tsai $-$ Wu equation
M_{hh}	modal mass matrix
B_{hh}	modal damping matrix
K_{hh}	modal stiffness matrix
Q_{hh}^I	modal aerodynamic damping matrix
Q_{hh}^R	modal aerodynamic stiffness matrix
u_{hh}	modal amplitude vector
G_{as}	spline matrix
x	fuselage axis
y	wing axis
z	axis perpendicular to x and y axes
ρ	density
α	angle of attack

CHAPTER 1

INTRODUCTION

In the last two decades, there has been a widespread interest in the use of UAVs in civil and military aviation sectors. Because of different operational requirements, unmanned air vehicles are generally classified into various categories such as mini, tactical, medium altitude long endurance, high altitude long endurance, combat (UCAV) etc. One of the most desired operational requirements of unmanned air vehicles is the reconnaissance activity for long time periods. Long reconnaissance durations require structurally optimized vehicles such that maximum endurance can be achieved with the air vehicle. The demand to carry highly sophisticated avionics and payloads with unmanned air vehicles is also increasing at a high pace. The increased payload carrying capacity demand from unmanned air vehicles also puts pressure on the structural designers to reduce the structural weight even further. There is also a strong interest in modifying the intended purpose of the UAVs such that UAVs designed as pure reconnaissance platforms are adapted to carry weapons, while UCAV designs are adapted to reconnaissance missions.

Because of their specific strength and stiffness advantages along with others, composite materials are widely used in the design of unmanned air vehicles. To confront the challenge of optimum structural weight, composite materials are usually used in sandwich configuration in building the sub-structures of unmanned air vehicles. From manufacturing point of view, composite materials also present various advantages. Integration of different parts is simpler in composite structures and molded composite construction allows for simple strong structures that can be built without requiring expensive equipment and highly skilled assemblers. [1]

There exist new regulations that are adopted in the design and analysis of unmanned vehicles similar to the regulations used for manned air vehicles. For instance, USAR 3.0 [2] is a first European (French) regulation for unmanned air systems applicable to military UAV systems. This document, which is applicable to military UAV Systems to be certificated by DGA Technical Authority, is an airworthiness code mostly based upon EASA2 CS-233 (ex JAR 23) requirements as

reference code duly tailored to fixed-wing UAV Systems. USAR 3.0 airworthiness code is applicable to fixed wing single or multiengine unmanned aerial vehicles that have a maximum certificated take-off weight more than 150 kg. FEM analysis became a necessity in order to optimize the weight of UAV's in the last decades. The finite element (FE) method has proven to be computationally efficient to solve aerospace structures problems [3].

Frulla and Cestino observed consistency between test results and FEM analysis results of HALE-UAV wing in their study [4]. In their study, theoretical load distribution is applied to wing structure. The static tests of a scaled-prototype of the HELIPLAT UAV performed at points A and D of the flight envelope and test results showed a good agreement with the FEM analysis.

Structural analysis and testing of a composite wing for an ultralight UAV was presented by Sullivan et.al. [5] The FE analysis predictions were fairly well with the experimental observations and the measured data. In their study, lift distribution on the wing was estimated using the vortex-lattice method.

Instead of using theoretical aerodynamics load, a computational aerodynamics analysis can be performed in order to increase accuracy of loading. An automated Fluid-Structure Interaction analysis is implemented by Isaac and Iverson [6]. Pressure distribution of CFD results are interpolated and applied to FE model as boundary condition; then, solution is iterated until it converges in their study.

The increased demand to optimize the structural weight of unmanned air vehicles necessiates the use of aeroelastic analysis tools early in the design of such vehicles. The demand for increased payload carrying capacity or the demand for very flexible UAV platforms is a significant challenge for designers to make sure that aeroelastic stability problems do not exist within the flight envelope of the unmanned air vehicle. Various studies have been conducted on the evaluation of aeroelastic stability of unmanned air vehicles. An aeroelastic stability investigation was performed on the General Atomics Aeronautical Systems (GA-ASI) Predator composite aircraft by Kosmatka and Panza.[7] The critical aeroelastic stability speeds were obtained using the "wing only" model and the entire aircraft model to

see how sensitive the aeroelastic stability speeds were to model fidelity. In a follow up study Kosmatka and Panza conducted an aeroelastic analysis on the combined Predator/FINDER vehicle to address potential changes in the Predator's aeroelastic characteristics due to the addition of the FINDER mini UAV under the wing via pylons and attachment points.[8] Pitcher[9] examined the static aeroelastic behavior of the Nighthawk mini unmanned aerial vehicle using a combined experimental and computational approach. A flexible wing, a stiff wing, and a fictitious rigid wing with zero deflection were examined in terms of their static aeroelastic performance. Di Palma et.al.[10] developed an integrated methodology that combines the aeroelastic and structural analysis to support the structural design of an UAV demonstrator having a joined-wing configuration and high structural flexibility.

Influence of structural and aerodynamic modeling on aeroelastic stability is also a very critical issue in aeroelastic analysis. Designers require reliable data on the important aero-structural instabilities such as flutter and divergence to optimize the structural design. Therefore, reliable aeroelastic models which couple aerodynamic and structural models are required. Computational approaches which couple aerodynamic and structural models are sensitive to other parameters such as splining of the aerodynamic grid to the structural grid, selection of different points off the structural model for splining, number of selected modes etc. The work of Striz and Venkayya [11] is one example study on the influence of structural and aerodynamic modeling on flutter analysis. Their work includes the effect of various modeling factors such as structural and aerodynamic grid refinement, number of selected modes, splining methods etc. on the flutter analysis of various built-up wings with different aspect ratios.

It should also be noted that UAV designs often have unusual shapes with features whose integration provides performance trade-offs that do not occur in conventional aircraft.[12] Designs affected include oblique wing vehicles, forward swept wing aircraft, X-wings, flying wings, joined wings etc.. Twin wing-tail boom configuration UAV, that is subject of the present article, is a configuration that is rarely seen in manned aircraft. Aeroelastic analysis of unconventional configuration UAVs require special care in order not to overlook a modeling detail which may cause significant impact on the critical aeroelastic stability mode and speed.

Design Features of the current UAV

The present study aims at presenting the main design features, detailed structural analysis and detailed aeroelastic stability analysis of a twin wing-tail boom configuration tactical UAV that is designed and manufactured.

Twin wing-tail boom configuration unmanned air vehicle is an experimental pusher type aircraft that is designed and manufactured. Figure 1 shows the manufactured twin wing-tail boom UAV and Table 1 summarizes the main technical specifications of the unmanned air vehicle. Air vehicle is designed to have a maximum take-off weight of 105 kg, maximum payload of 20 kg, and maximum endurance of 3-4 hours.

Integral horizontal and vertical tail
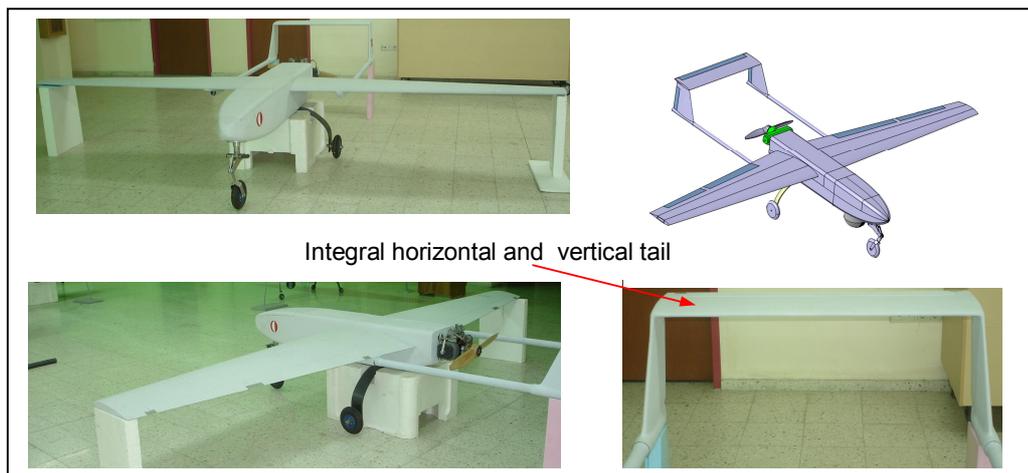
Figure 1: Twin wing-tail boom composite UAV and integral horizontal/vertical tail

Table 1: Main technical specifications of the UAV

Maximum take off weight	105 kg
Maximum payload weight	20 kg
Aspect ratio of the wing	8.4
Wing span	4.3 m
Taper ratio of the wing	0.45
Aspect ratio of the horizontal tail	4

Aspect ratio of the vertical tail	1.2
Overall length	3 m
Cruise altitude	3000 m
Maximum velocity at sea level	80 m/s
Engine	21 HP two cylinder gasoline engine
Maximum endurance	3- 4 hours

Air vehicle has two separate wings which are connected to the main bulkheads in the fuselage. The wing has two spars. The front spar is perpendicular to the fuselage and it has a root extension which enters into a box which is connected to the main bulkhead inside the fuselage. The rear spar does not have a root extension entering into the fuselage. Rear spar terminates at the side wall of the fuselage and it is connected to a circumferential frame inside the fuselage by means of two bolts. Wing has an outboard aileron and inboard hinged flap. Horizontal and vertical tails are permanently connected to each other by composite material after the adjustment of the set angle of the horizontal stabilizer has been made. Such a design feature is used to prevent any probable free play of the connection elements between the horizontal and vertical tails in case a removable connection was designed. Tail booms are manufactured by the filament winding process. Tail booms enter into their counterpart tubes which are permanently bonded underneath the wing and the vertical stabilizers by composite material. Tail booms are then secured to the wing and to the vertical stabilizers by bolts. Fuselage has four main frames and a rear engine firewall. Two of the frames are used to connect the wing and the main landing gear to the fuselage. Main landing gear is manufactured in house by several layers carbon-epoxy composite by compression molding. In the proceeding sections each sub-structure of the air vehicle will be introduced in more detail to generate a reliable MSC/Nastran finite element model which is used in the detailed structural analysis.

In the initial structural design phase of the composite air vehicle, certain paragraphs of USAR 3.02 UAV systems airworthiness requirements are used to calculate the critical design speeds such as dive speed and to construct the V-N diagram. Although USAR 3.02 UAV systems airworthiness requirements is applicable to unmanned air vehicles that have a take-off weight more than 150 kg, certain

paragraphes of USAR 3.0 are still referenced since the maximum take-off weight of the UAV designed is close to the lower limit of the maximum take-off weight specified in USAR 3.0. The positive and negative load factors used in the structural design are determined as 3.8 and 1.52 based on the paragraphes 337a and 337b of USAR 3.0. According to paragraph 335b, the dive speed should not be less than 1.25 times the maximum cruise speed. In the article aeroelastic analyses are conducted at the sea level at which the maximum speed is calculated as 80 m/s. Therefore, the dive speed at the sea level is taken as 100 m/s.

CHAPTER 2

DETERMINATION OF AERODYNAMIC LOADS BY COMPUTATIONAL AERODYNAMICS

2.1. Introduction

This section introduces the computational aerodynamic (CA) study performed in this thesis. The computational study has been performed in a built-up approach to identify the effect of different sub-structures of the airplane on the pressure distribution in general. More specifically, computational aerodynamic studies of the wing only and the wing-body-tail plane have been conducted to ascertain the effect of interactions of different sub-structures of the airplane on the pressure distribution, thus loading induced. However, it should be stressed that the main objective of the study is to perform the structural analysis of the wing, fuselage and the tail plane in order to verify the structural integrity of the airplane. Therefore, in the thesis computational aerodynamic study has been conducted only to get reliable load data to carry out structural analysis. A comprehensive CA study can be performed in a separate study to better identify the aerodynamic characteristic of the airplane.

Three different boundary condition cases are examined and results are compared for wing geometry. CA analyses of both cases have been performed using Euler solver. Flow is incompressible for Case 1 and Case 2; however, it is compressible for Case 3 and air is assumed to be ideal gas. CA solution domain is prepared by Gambit [13], which is a mesh generator and Fluent r6.2.16 [13] is used as CA solver.

2.2. Generation of the Mesh and CA Solutions for the Wing Geometry

Determining boundary conditions and meshing computational domain are quite important subjects in CA calculations. Boundary conditions may easily affect solutions at all nodes of the domain, therefore they should be chosen carefully. While meshing surfaces of the wing, finer mesh should be used at curved regions in order to ensure that mesh matches the geometry and preferably course mesh could be used at smooth regions in order not to increase the number of nodes

unnecessarily. Firstly, proper wing surface meshes have been created. Edges of the wing at the tip and at the root are meshed using double sided grading option of Gambit [13]; so that, finer mesh is obtained at leading edge and trailing edge. The most curved region is leading edge of the wing. Because of that, uniform fine mesh is used at leading edge of the wing. In order to create fine mesh around wing tip and wing root, where flow is not uniform, trailing edge of the wing is meshed using double sided grading. Creating fine mesh around wing root and wing tip, error is decreased for these high gradient regions. Then tetrahedral elements created for solution domain. Figure 2 and Figure 3 show the meshed domain which is created by Gambit. As it is seen, finer mesh is used at trailing edge, wing root and wing tip.
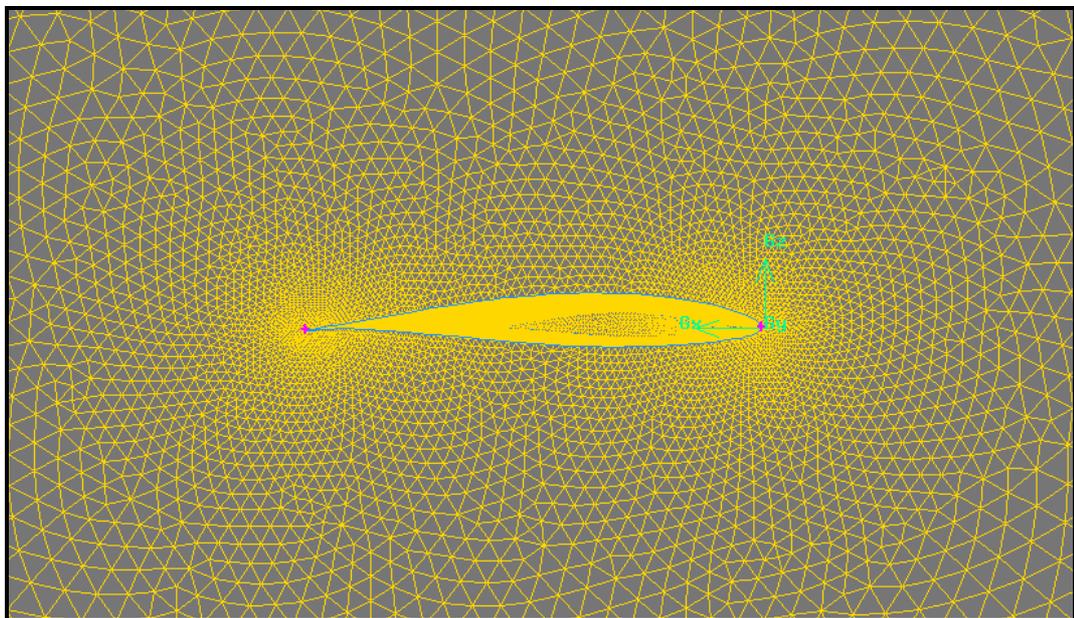
Figure 2: Domain mesh around root of the wing
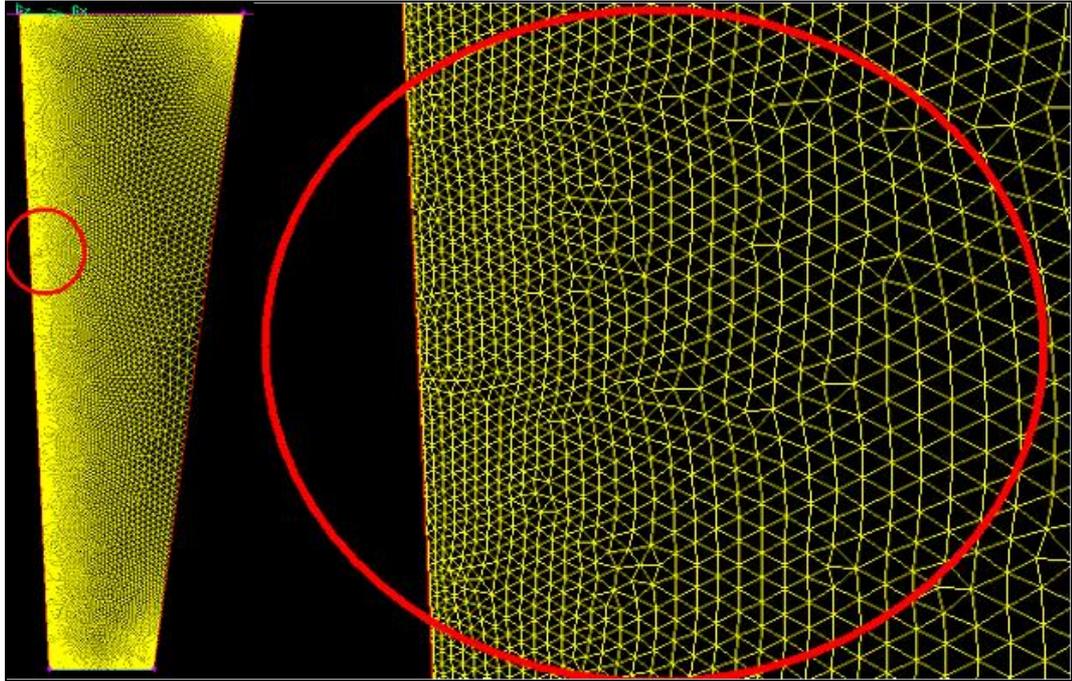
Figure 3: Surface mesh of the wing

Proper boundary conditions should be selected to get an accurate CA result. To study the effect of the boundary conditions on the converged steady state solutions, three different boundary condition cases for the wing geometry at 5 degree angle of attack and at 100m/s speed are examined and results are compared.

Different boundary condition choices like 'Velocity inlet', 'Pressure outlet', 'Symmetry' etc. can be defined in Fluent. Gage pressure is defined for the pressure outlet boundary condition. Outward flow flux may exist at pressure outlet boundaries. Pressure outlet boundary condition may be applied at the domain boundaries where gage pressure is zero, because domain boundaries are far away from the wing structure. Velocity inlet boundary condition is applied to boundaries where inward flow flux exists. Domain position and free stream direction should be examined carefully and proper boundaries should set as velocity inlet boundary. Velocity direction and magnitude should be defined for this boundary condition. Symmetry boundary condition is applied to boundaries where flow flux through boundary does not exist.

Case 1

In the first mesh generation method, the wing geometry is rotated and the domain mesh is generated by referencing the rotated wing. In the sample analysis the wing geometry is rotated by 5 degrees and solution domain is meshed. As it is seen in the Figure 4, velocity inlet boundary condition is used at upstream, pressure outlet boundary condition is used at downstream and symmetry boundary condition is used at other faces of the domain. Symmetry boundary condition is used at one of the side faces of domain due to half structure analysis is performed. For other three faces, flow is assumed to be not disturbed at these boundaries, because of that, they are far away from wing structure. Thus, all faces are tangent to flow and flow flux does not exist through these faces. So symmetry boundary condition is applicable for these faces.

Disadvantage of this computational domain is that, changing the angle of attack is difficult. That is; all computational domain should be re-created and re-meshed to get a solution at a different angle of attack. This increases the work load substantially, since for each attitude of the wing a new mesh must be generated. Figure 5 shows the position of wing and solution domain with respect to flow direction. As it is seen, flow direction is x-direction and 5 degrees angle of attack is obtained by rotating wing.
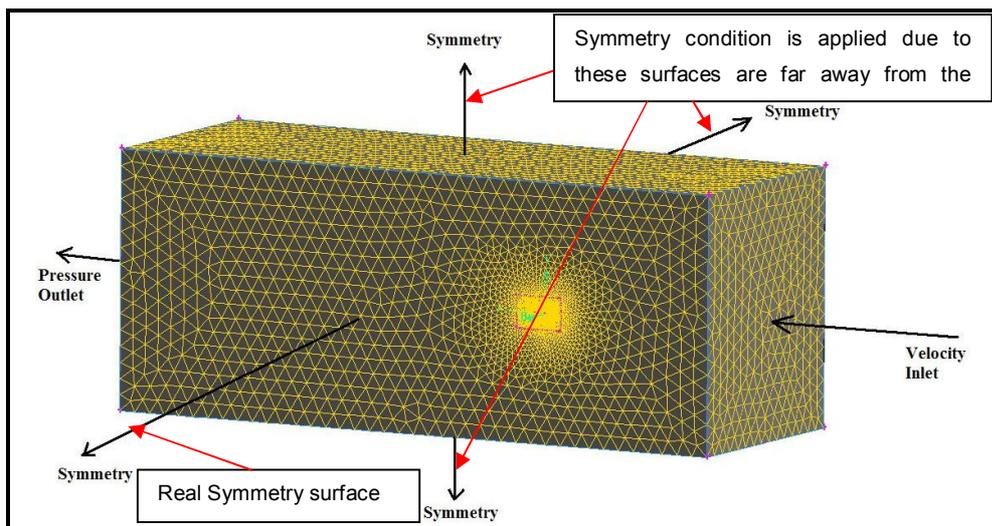
Figure 4: Boundary conditions for Case 1

Figure 5: Wing and domain positions with respect to free-stream for Case 1

Case 2

In the second approach the wing geometry is not rotated. But this time the input velocity is defined accordingly so as to create the same angle of attack effect as the rotated wing. As it is seen in the Figure 6, in this case velocity inlet boundary condition is used at the upstream and at the lower surface of the domain.

Figure 6: Boundary conditions for Case 2

11

Figure 7: Wing and domain positions with respect to free-stream for Case 2

In this case, the x-component of velocity and the z-component of velocity values are set such that, the wing is at 5 degree angle of attack. In this case symmetry is destroyed at the upper surface of the domain due to the velocity inlet condition on the lower surface of the domain. Therefore, pressure outlet boundary condition is used at downstream and upper surface of the domain. Symmetry boundary condition is used at the right and at the left surfaces of computational domain. It should be noted that upper surface should be set as velocity inlet boundary condition and lower surface should be set as pressure outlet boundary condition when angle of attack is a negative value.

Changing the angle of attack is much easier for this case. Redefining velocity components will result in solution at a different angle of attack and there is no need to mesh the domain which is very time consuming. However, it should be noted that in cases when computational aerodynamic study is required for a lifting surface with the control surface in deflected position, the domain has to be re-meshed.

Case 3
Finally, a semi-cylindrical domain is used instead of the rectangular domain. The symmetry boundary condition is used at the symmetry plane and other surfaces are

set as "Pressure Far Field" boundary condition. The mach number and flow direction components are defined at "Pressure Far Field surfaces" with respect to the global axis. The freestream velocity and freestream flow direction can be defined on these surfaces because of that, all surfaces are far away from the wing. For this case, the angle of attack can be easily changed by re-defining flow direction components. Unlike the previous cases, this solution is compressible.
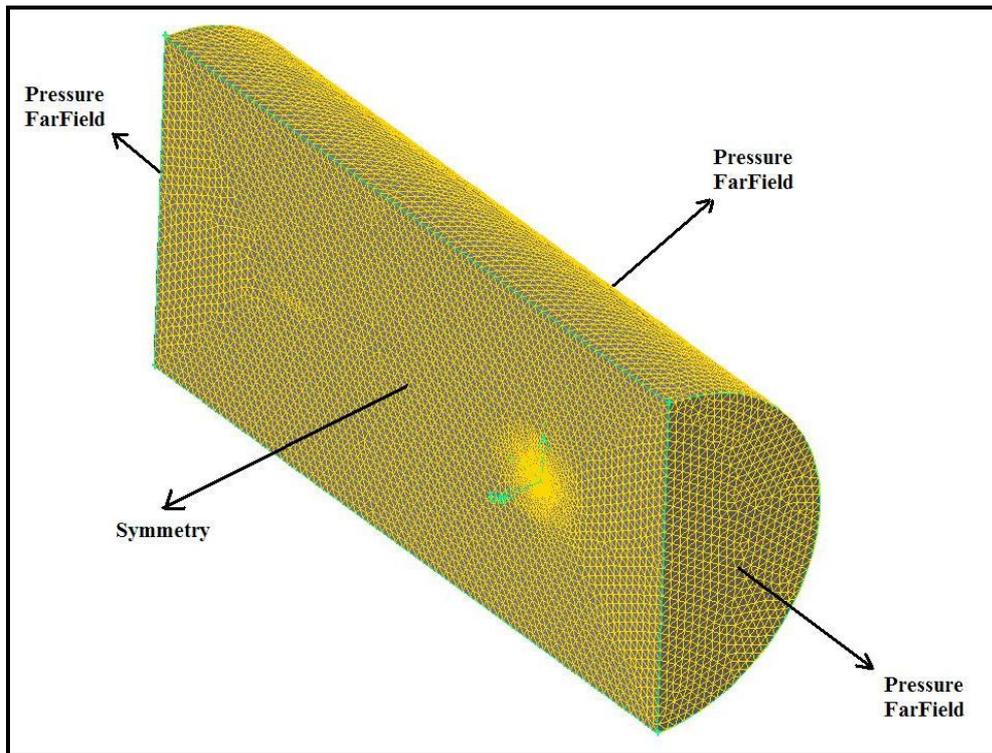
Figure 8: Boundary conditions for Case 3

CA analyses of the three cases are performed by Fluent r6.2.16 [13]. Figure 9 and Figure 10 show gage pressure distributions on the lower surface and upper surface of the wing for the three cases. As it is seen, similar pressure distributions are obtained although different boundary conditions are applied. Although third case was compressible solution, pressure contours did not change much.
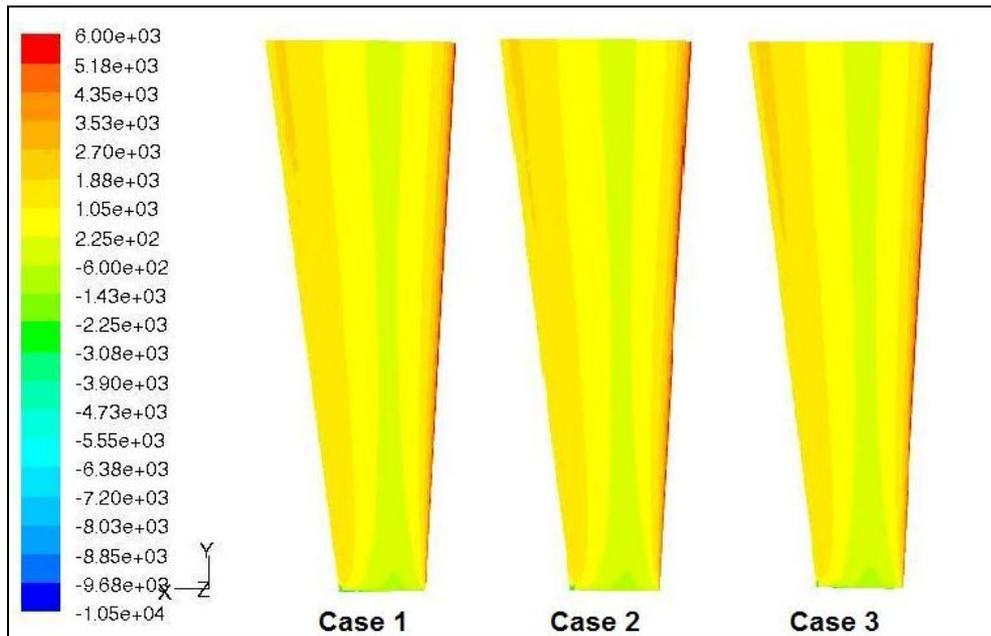
Figure 9: Pressure distribution on lower surface
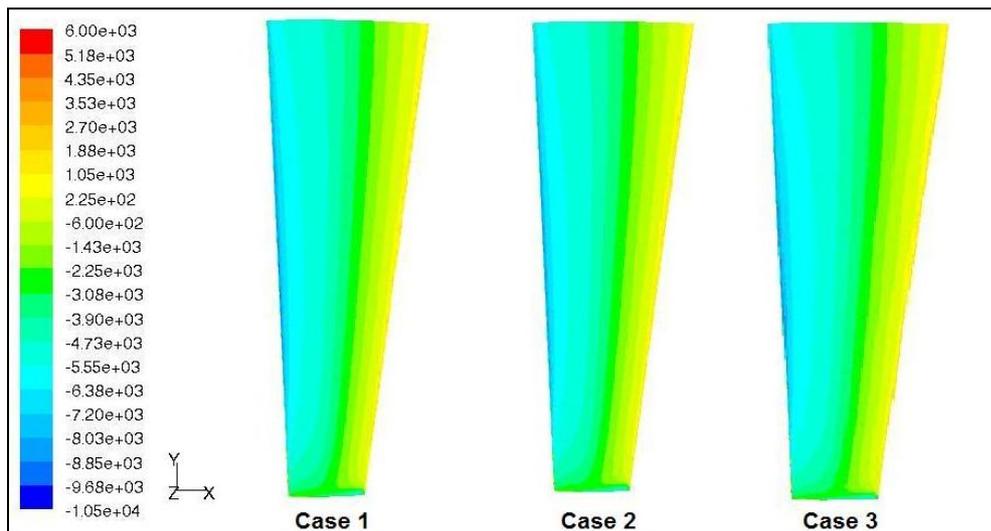
Figure 10: Pressure distribution on upper surface

Results of the three cases are tabulated in Table 2 for comparison purposes. First two cases are nearly equal to each other and the third case differs slightly. Taking the first case as a reference, error in C_L is 0.30% for case 2, 1.61% for case 3 and error in C_D is 2.37% for case 2, 6.57% for case 3.

Table 2: Results for different boundary condition cases

	Case1	Case 2	Case 3
Number of Cells	2609365	2520853	1604799
Number of Faces	5252568	5075428	3246929
Number of Nodes	450711	435942	285636
Lift (N)	4432,308	4419,181	4503,718
Drag (N)	150,453	154,02	160,336
C_L	0,72163	0,71949	0,733255
C_D	0,0245	0,02508	0,026104

Figure 11 shows lift forces obtained for the three cases with different element sizes. It is observed that the lift force converges when number of elements used in the CA analysis is increased. Convergenge of lift forces confirms the CA results.
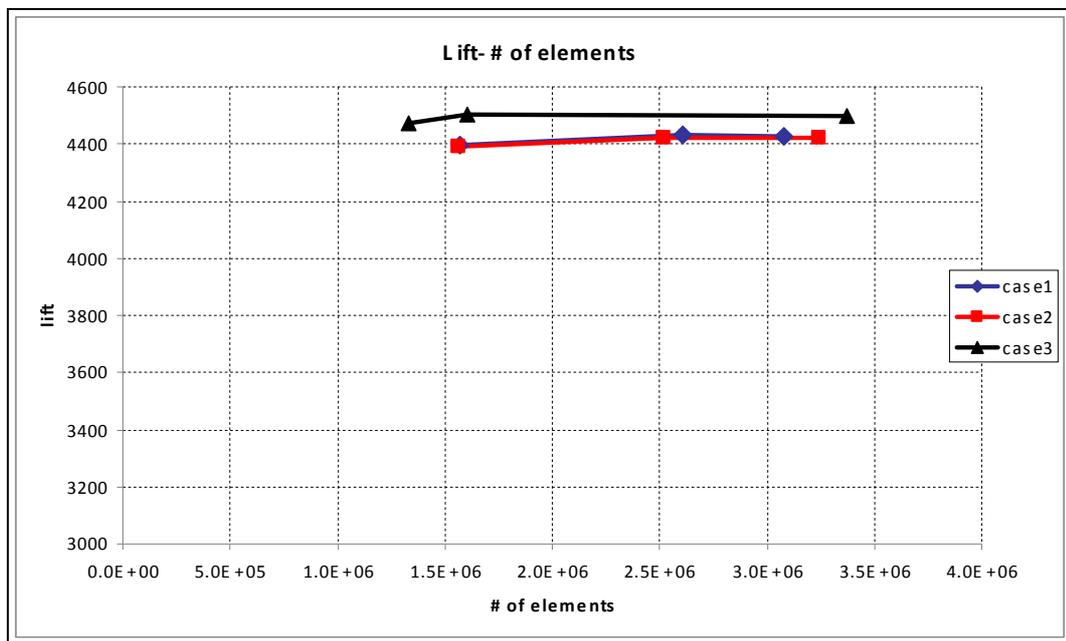
Figure 11: Lift vs. Number of elements

Lift coefficient vs. angle of attack plot of the wing is obtained by analyzing the wing at different angle of attacks. Boundary condition of case 2 is used in order to obtain the lift curve. The reason of this is that, it is advantageous to set a new angle of attack without rotating the wing, but by only adjusting the velocity components. Thus, it is not necessary to re-mesh the domain for the new angle of attack. Lift coefficient vs. angle of attack plot obtained is given in Figure 12.
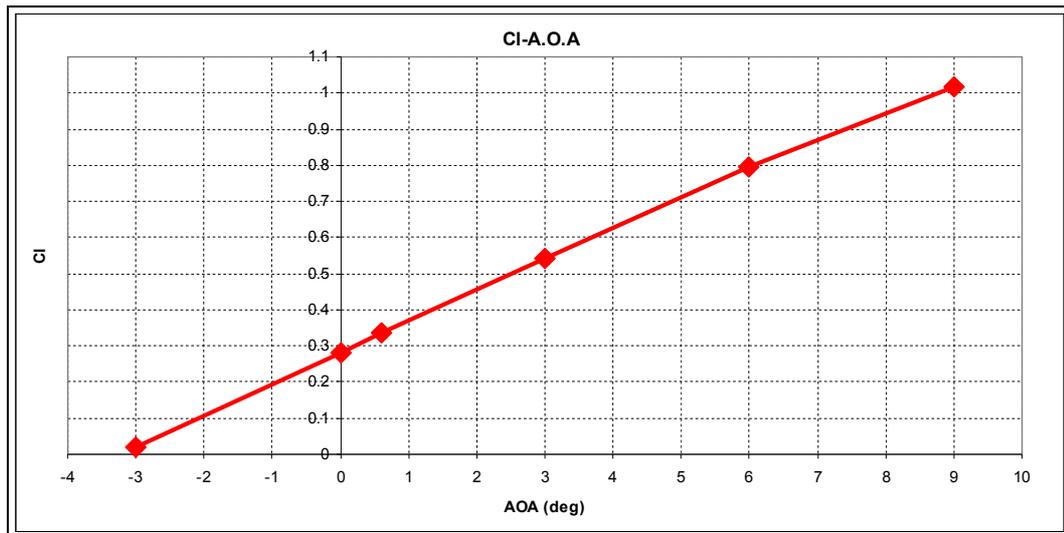
Figure 12: Lift coefficient vs. angle of attack plot

2.3. Determination of the lift-curve slope by the ESDU data base

In the present work, ESDU data base is also utilized to get the lift curve slope by a different method. This way the lift curve slope determined by the Fluent can be compared with the lift curve slope obtained by a more approximate but independent approach. ESDU95010 code [14] is used in order to get lift coefficient curve and both curves are plotted in a single graph and they are compared. It should be noted that ESDU95010 provides a computer program for the estimation of span-wise loading of wings with camber and twist in subsonic attached flow. ESDU 95010 introduces two Fortran computer programs, ESDUpacs A9510 and B9510, that use lifting-surface theory based on the Multhopp-Richardson solution. All loadings, force and moment output by the programs have been factored by the ratio of the lift-curve slope from the Multhopp-Garner lifting-surface solution to that from the Multhopp-Richardson solution to take advantage of the slightly more accurate solutions provided by the former [14].

Figure 13 shows lift coefficient curves obtained by ESDU 95010 by using different number of camber points in approximating the mean camber of the wing and Fluent r6.2.16. As it is seen, as the number of camber points is increased the lift curve slope determined by the ESDU code approaches the lift-curve slope determined by the computational aerodynamic analysis. Although this behavior does not prove the

16

absolute accuracy of the CA solution, it is an indication of the reliability of the CA solution. Therefore, in this study, lift coefficient curve obtained by Fluent is used to calculate dive angle of attack.
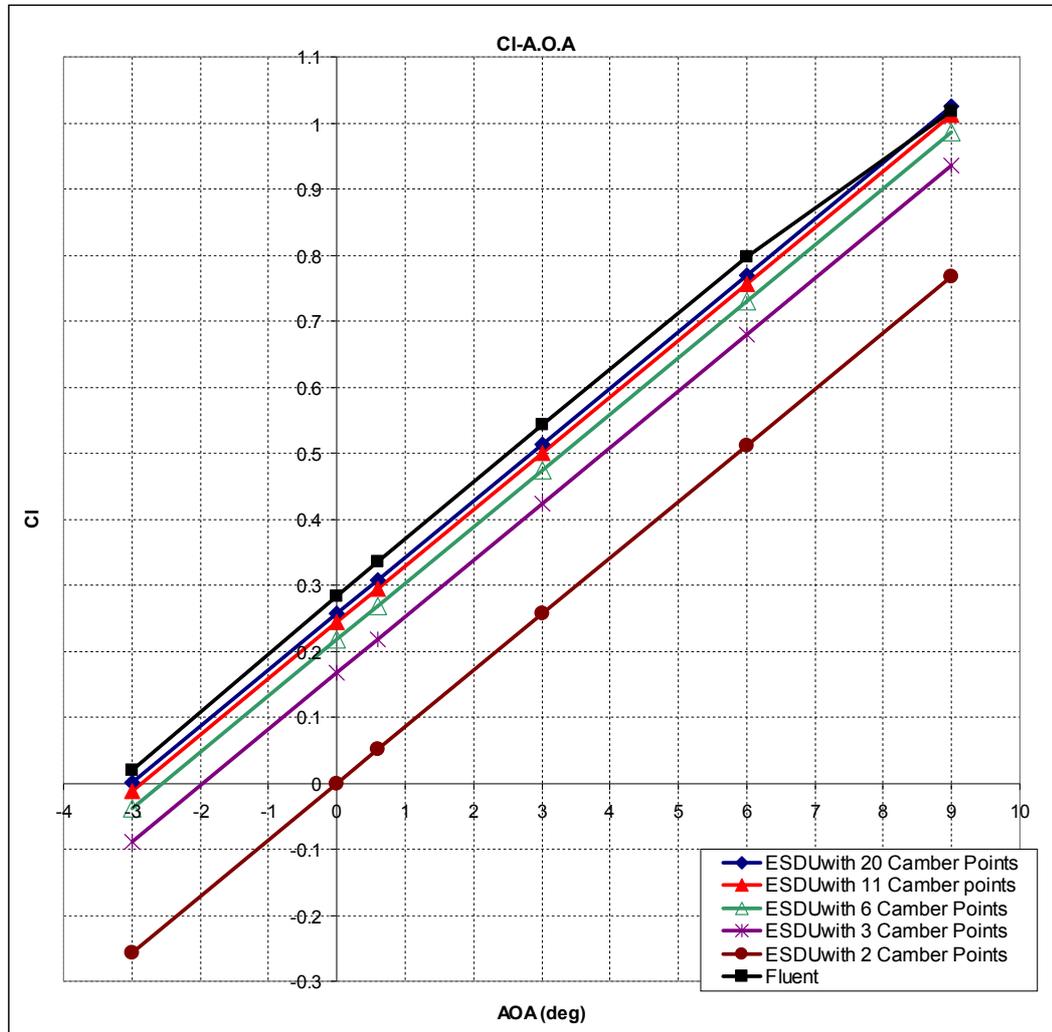
Figure 13: Lift coefficient curves obtained by ESDU and Fluent

2.4. Calculation of dive angle of attack and wing loading by CA Solution

In this section the dive angle of attack is calculated based on the CA solution performed by Fluent. The main aim is to determine the dive angle of attack accurately. The accuracy of the dive angle of attack will be checked by comparing the lift force determined by the CA solution at the determined dive angle of attack and half of the weight of the aircraft at the positive load factor. In the structural

17

analysis of the wing, to be more conservative the whole lift is assumed to be created by the wing.

In order to calculate the dive angle of attack, firstly the best line for the lift curve is found. Best line for the lift curve is found using the data points obtained by Fluent r6.2.16 for case 2. Data at 9 degrees angle of attack is not used, because 9 degrees is a high angle of attack and trend of lift curve changes at this angle according to Fluent results. At high angle of attacks separation may exists and reliability of Euler solution naturally decreases.

Equation of the best line is;

$$y = mx + b \qquad (1)$$

Where;

$$m = \frac{n\sum(xy) - \sum x \cdot \sum y}{n\sum(x^2) - (\sum x)^2}$$

$$b = \frac{\sum y - m\sum x}{n}$$

And n is the number of data points.

Using 5 data obtained by Fluent, best line is found as;

$$y = 0.086386x + 0.28111 \qquad (2)$$

This leads to;

$$C_L(\alpha) = C_{LO} + \alpha \cdot C_{L\alpha}$$
$$C_L(\alpha) = 0.28111 + 0.086386 \cdot \alpha \qquad (3)$$

where lift curve slope is given in terms of per degrees.

At the dive speed condition, the required C_L can be found from following calculations:

$$n \cdot W = \frac{1}{2} \cdot \rho_\infty \cdot V_\infty^2 \cdot C_L \cdot S$$

$$C_L = \frac{n \cdot W}{\frac{1}{2} \rho_\infty \cdot V_\infty^2 \cdot S}$$

$$C_L = 0.31864$$

(4)

where the positive load factor at dive speed is 3.8g

In these calculations, dive speed is taken as 100 m/s [15] and the reference area is taken as 2.2 m^2 and sea level air density is used.

Substituting the required C_L value into Equation 3, the dive angle of attack is found as;

$$\alpha_{DIVE} = 0.43°.$$

To check the net lift produced at the dive speed flight condition, computational aerodynamic analysis of the wing has been performed at 0.43 degree angle of attack. Figure 14 shows pressure distribution on the wing at dive. The CA solution gave the following lift and drag force at the dive angle of attack:

Lift = 1954.66 N
Drag = 48.16 N
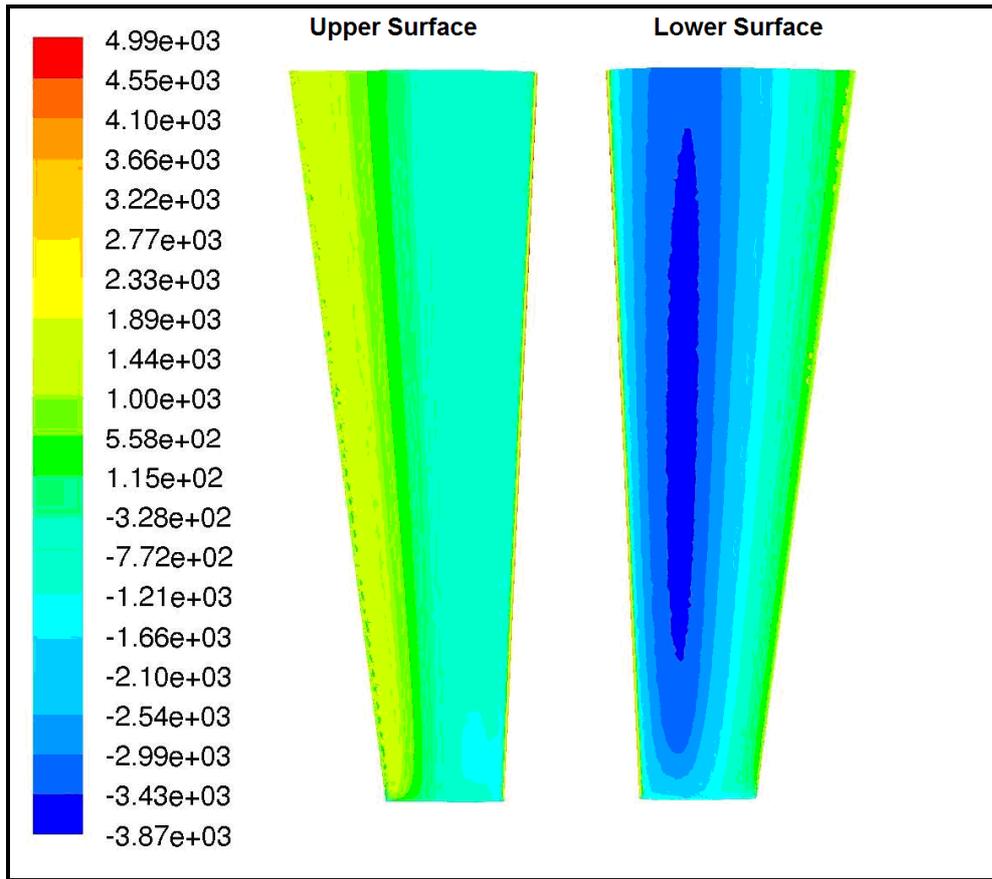
Figure 14: Pressure distribution on wing at dive speed and 3.8g pull-up maneuver

The total weight per wing at the positive low angle of attack condition is given by n*W/2, and it is 1957 N at 3.8g. As it is seen, the CA solution gives a very close lift value at 0.43° angle of attack. Thus, it can be said that an accurate angle of attack for the dive speed is found.

CA results for the three boundary conditions are tabulated in Table 3 below. As it is seen, lift value differs at maximum 0.36% between these 3 cases. It should not be missed that the dive angle of attack is calculated using the results of Case 2. Analysing Case 1 and 3 for different angle of attacks and calculating dive angle of attacks for these 2 cases would be more accurate. However, as it is seen in Table 3 lift forces, which are critical for structural analysis, are quite close to each other for the three cases. Besides, results show that the highest lift value which is closest to 1957N, which is the half weight of the airplane, belongs to case 2. This is because, the dive angle of attack is calculated from the $C_L - \alpha$ curve obtained for Case 2.

Table 3: Comparison of results for different boundary conditions

	Case1	Case 2	Case 3
Number of Cells	2627631	2037184	1604799
Number of Faces	5288855	4105134	3246929
Number of Nodes	453685	354147	285636
Lift	1953,82	1954,66	1947,55
Drag	38,15	48,16	40,48
CL	0,3181	0,3182	0,3171
CD	0,0062	0,0078	0,0066

2.5. Computational aerodynamic analysis of the whole airplane at the dive angle of attack

Computational aerodynamics analyses at this section are aimed at the determination of aerodynamic pressure distribution over the aircraft at critical points of the V-N diagram. The main goal is to get more accurate distribution of the external aerodynamic loading to be used in the structural analysis. In the computational aerodynamic analyses Euler solver is used.

As it was mentioned before, in the structural finite element analysis, it is assumed that the lift force is generated for wings only and the dive angle of attack found for the wing is used in CA anaysis of fuselage-wing-tail combination. The pressure distribution over wing-tail-fuselage combination is obtained by the half model symmetric CA analysis. Figure 14 shows pressure distribution over the whole aircraft at the dive speed condition.
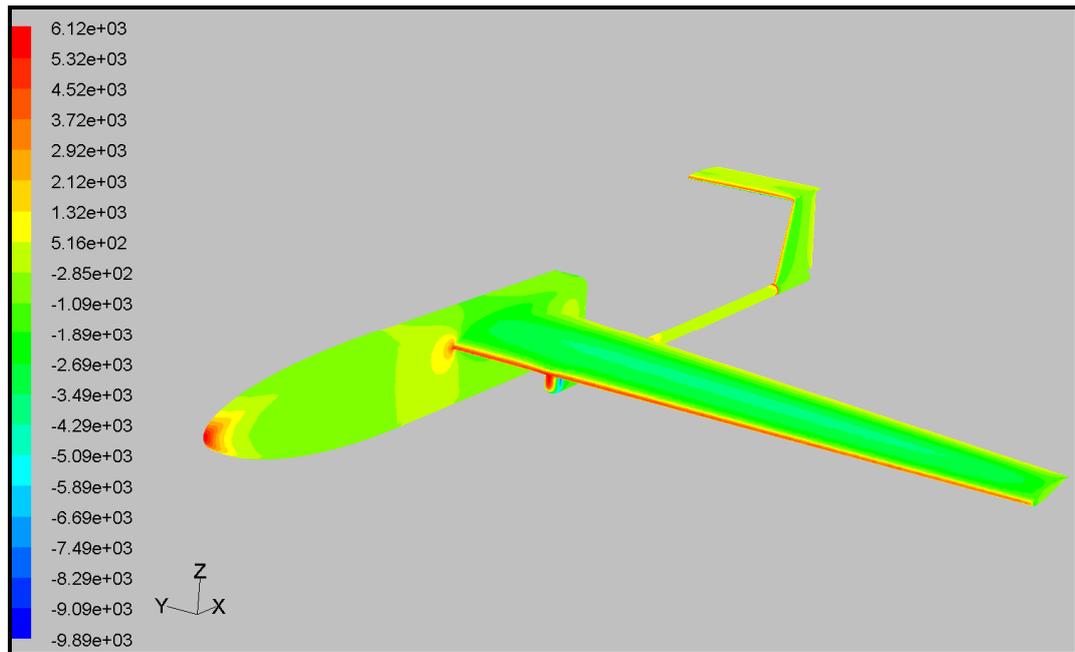
Figure 15: Pressure distribution over whole aircraft at the dive speed condition (Pa)

Table 4 shows the number of elements used for this analysis, total lift and drag forces obtained by this analysis. Besides, this table shows lift and drag forces produced by wing, fuselage, boom and tail separately.

Table 4: CA results for whole airplane at dive speed

	Number of Cells		2410184	
	Number of Faces		4920288	
	Number of Nodes		453395	
	Lift (N)		1409,78	
	Drag (N)		139,36	
	Wing	Fuselage	Boom	Tail
Lift (N)	1762,39	21,73	-25,97	-344,95
Drag (N)	51,93	59,67	10,06	17,71

It should be noted that, the lift force generated by the wing-only model at the dive angle of attack calculated for the wing only was very close to 1957 N. However, it is seen that the lift force generated by the wing decreases to 1762.79 N when fuselage, tail and tail boom are included in the analysis. However, in the current study it is decided that the CA analysis results for whole airvehicle will be used in the structural analysis but all forces will be scaled so that the lift created by wing will be 1957 N.

Normally, total lift of the whole aircraft has to be 1957 N. However, as it is seen in the Table 4, the total lift for the whole aircraft is about 1410 N and this value is lower than 1957 N. Calculating the dive speed angle of attack for wing and using this angle of attack for whole aircraft is the main reason of this difference. In order to obtain a better lift force, computational aerodynamic analysis of the whole aircraft should be performed at different angles of attack and lift coefficient versus angle of attack curve should be calculated for the whole aircraft. In that case, an angle of attack valid for whole aircraft at the dive speed can be calculated. It is obvious that, angle of attack of the tactical UAV at the dive speed and 3.8 g loadfactor should be higher than 0.43^o, because the total lift is 1410 N at 0.43^o angle of attack. In the current study, one of the main aims of the computational aerodynamic analysis is to calculate the external load to be used in the structural analysis of the wing. Therefore, an accurate dive angle of attack for the whole airplane is not calculated to reduce the computational cost associated with the aerodynamic analysis of the whole airplane. It is deemed that as long as the nodal forces are scaled so that the total lift force calculated for the wing matches the half weight of the airplane at 3.8 g flight, the external load calculated for the structural analysis of the wing will more or less represent the true aerodynamic loading on the wing.

2.6. Computational aerodynamic analysis of the whole airplane at stall angle of attack

In this section computational aerodynamics analyses performed for the whole aircraft at minimum maneuvering speed *(Va)* and the stall angle of attack are presented. External forces needed for the structural analysis are calculated by CA analysis. The stall angle of attack of NACA 63412 airfoil is 14 degrees according to the lift coefficient- angle of attack graph of the airfoil. The minimum maneuvering speed is calculated as 43.2 m/s at 3.8g loadfactor and at 14 degrees angle of attack. CA analysis of the whole aircraft is performed. Figure 15 shows the pressure distribution over the whole aircraft at the minimum maneuvering speed condition. Result shown in Figure 16 is the sea level gage pressure distribution.
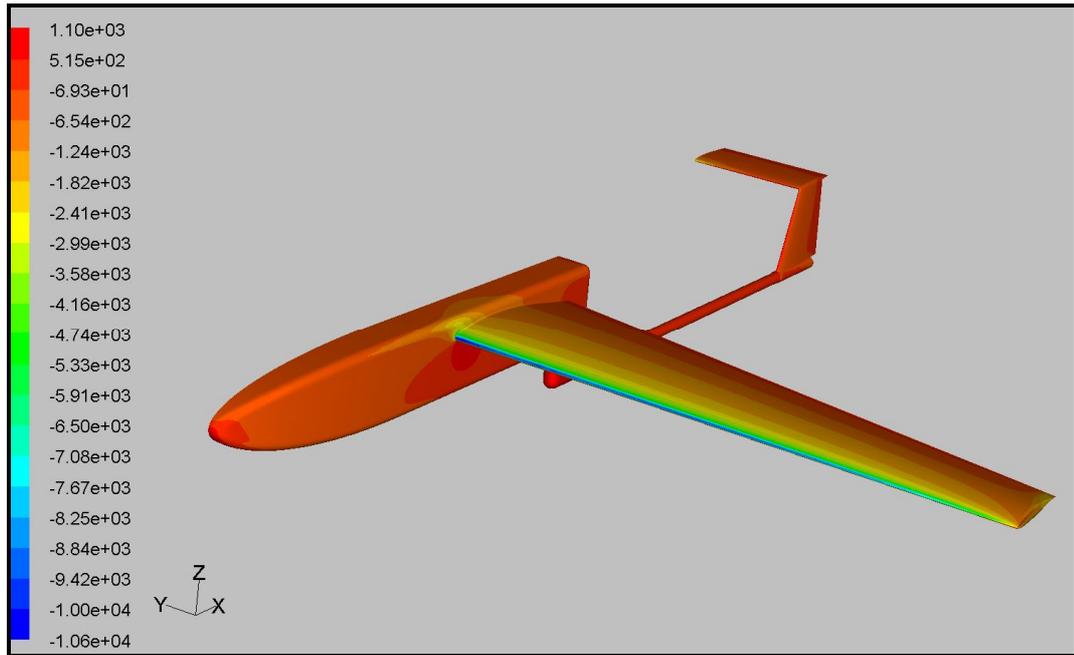
Figure 16: Pressure distribution over whole aircraft at stall speed condition (Pa)

Number of elements used in the computational aerodynamics analysis and the calculated total lift and drag forces are tabulated in Table 5. Forces presented in Table 5 are valid for the half aircraft model.

Table 5: CA results for whole airplane at stall condition

Number of Cells	3658147
Number of Faces	7401862
Number of Nodes	655010
Lift (N)	1789,82
Drag (N)	134,33

Weight of the half aircraft at the stall angle of attack is equal to the load factor times the weight of the aircraft divided by two and this value is 1957 N at 3.8 g load factor. As it is seen in Table 5, CA solution gives 1790 N lift at stall angle of attack. The Euler solution may not be sufficient at the stall condition because of the separation. The reliability of Euler solution decreases at high angle of attacks because separation may occur.

Lift and drag forces before interpolation to Patran [16] and after interpolation are tabulated in Table 6. As it is seen, lift is decreased by 1.9% and drag is increased

by 11.8% after interpolation. The lift is more critical for the structural analysis because the lift is much bigger than the drag force. The interpolation can be said to be successful because of the small change of lift during the interpolation.

Table 6: CA analysis results at stall condition

	Before interpolation	After interpolation	Error
Total Lift (N)	1789,82	1755,5	1.9%
Total Drag (N)	134,33	150,2	11.8%

Lift and drag forces of the wing, fuselage, boom and the tail after the interpolation are tabulated individually in Table 7. Lift generated by the wing at the stall angle of attack is 1587 N and this value is much smaller than 1957 N. However, all pressure values will be scaled in the structural analysis; so that, the lift generated by the wing will be 1957 N. Scaling will be performed after interpolation of the CA data to Patran.

Table 7: Lift and drag forces of the sub-structures at the stall speed after the interpolation

	Wing	Fuselage	Tail booms	Tail
Lift force (N)	1586,55	129,44	12,83	26,68
Drag force (N)	109,71	30,65	6,81	3,03

In performing the structural analysis of the wing, it is assumed that all the lift force is generated by wings. Therefore, the lift force to be used during the structural analysis should be 1957 N at 3.8 g load factor for each wing. However, computational aerodynamics analysis of the half aircraft generated a lift of 1587 N after the interpolation procedure. Therefore, by keeping the same pressure distribution, all the aerodynamic forces are scaled up by 1.23 in the structural analysis. Scale up operation is performed by "Load Case Scale Factor" option of Patran under "Load Cases" menu. The interpolation of the load data from Fluent to Nastran is explained in detail in Appendix A.

2.7. Comparison of Navier-Stokes and Euler solutions

Loads found by the Euler solution are used in structural analysis of Tactical UAV. However, in this section, Euler results and Navier-Stokes results are compared in different sections and the reliability of Euler results is investigated.

Euler computational aerodynamics results and Navier-Stokes computational aerodynamics results are compared at 3 different sections. The first section (Sec A-A) is a spanwise section at the quarter chord the wing. The second section (Sec B-B) is a chordwise section at a meter away from the wing root. The third section (Sec C-C) is a chordwise section at the wing tip. Figure 17 shows 3 sections where Euler and Navier-Stokes results are compared.
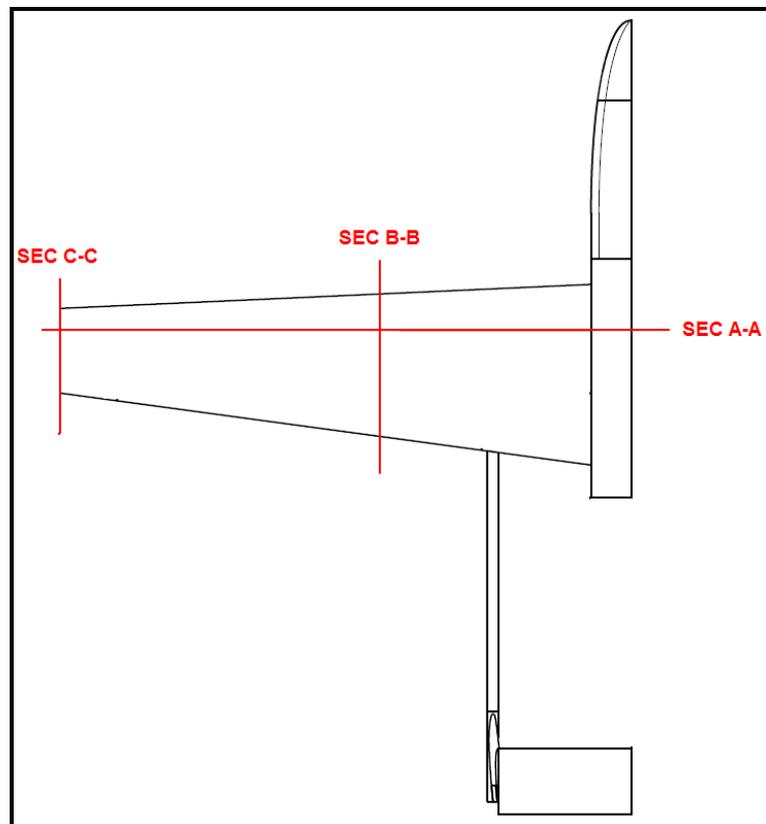
Figure 17: Sections where Euler and Navier-Stokes results are compared

Gage pressure values of Euler and Navier-Stokes solutions at section A-A can be seen in Figure 18 and Figure 19. In Figure 18 and Figure 19, red lines show the Navier-Stokes solution results and black lines show the Euler solution results. Figure

18 shows the Euler- Navier stokes comparison at the dive speed condition, and Figure 19 shows Euler- Navier stokes comparison at the stall condition at the minimum maneuvering speed. Figure 18 and Figure 19 shows that pressure values on lower surfaces of UAV are almost equal and pressure values on upper surfaces of UAV change slightly between the Euler and the Navier Stokes solutions for both dive speed and stall conditions. The peak shown in Figure 18 corresponds to the tail boom connection region under the wing. A small distortion is also seen at the same location in Figure 19, but since Figure 19 corresponds to the high angle of attack condition very near the stall region, the distortion in the tail boom region under the wing is small unlike the dive speed condition.
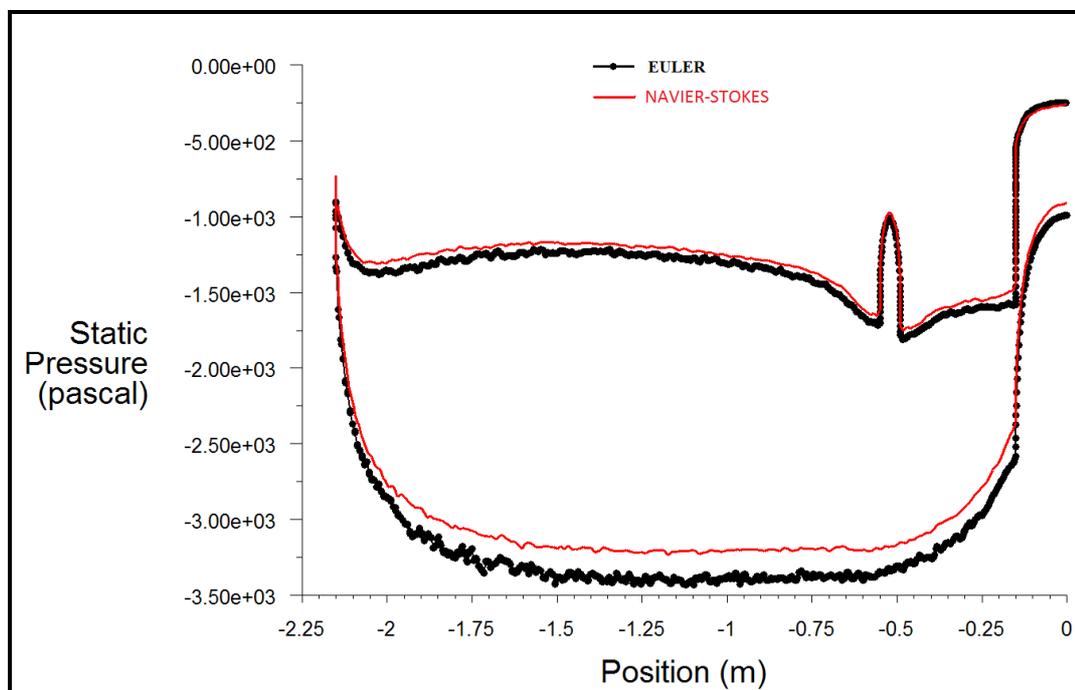
Figure 18: Dive speed pressure distributions determined by Euler and Navier Stokes solutions at Section A-A (0 m: Mid-fuselage, -2.15 m: Wing Tip)

Note: Upper curves belong to the lower surface of the wing
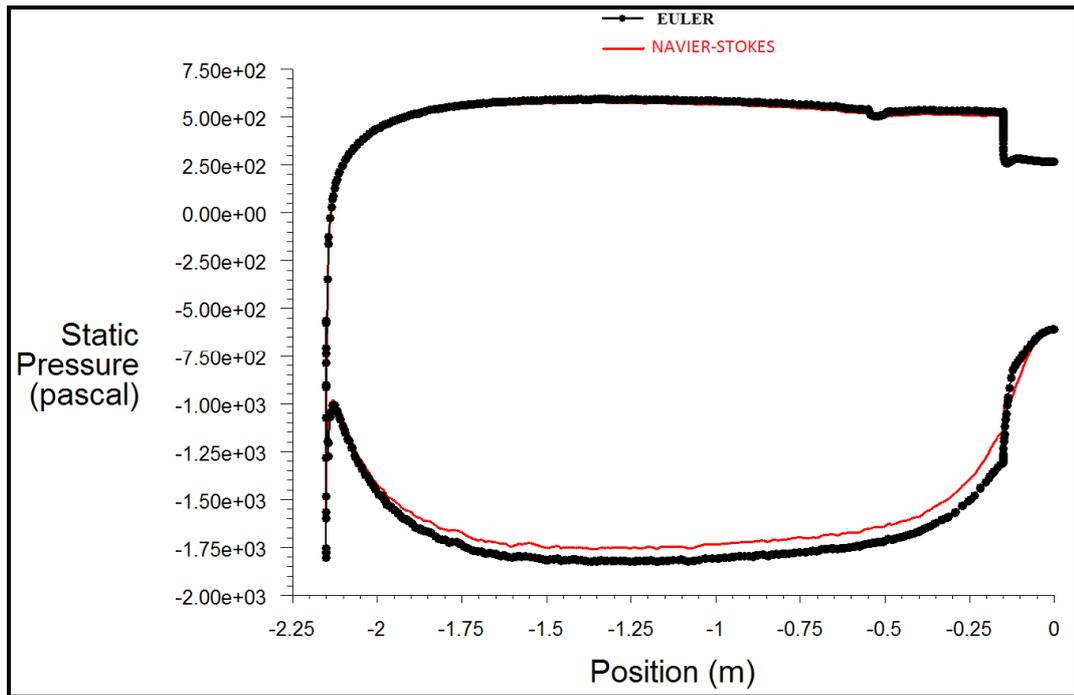
Figure 19: Stall speed pressure distributions determined by Euler and Navier Stokes solutions at Section A-A (0 m: Mid-fuselage, -2.15 m: Wing Tip)

Note: Upper curves belong to the lower surface of the wing

The pressure difference between the upper and the lower surfaces of the wing is less for the Navier Stokes solution in comparison with the Euler solution. Therefore, using pressure forces determined by the Euler solution in the structural analysis would be more conservative. In a way, the use of pressure forces of the Euler solution in the structural analysis corresponds to an additional factor of safety, assuming that the external aerodynamic loading based on Navier Stokes solution is more accurate compared to the aerodynamic loading based on Euler solution. However, it should be pointed out that for the dive speed condition, the dive speed angle of attack is obtained by the Euler solution not by the Navier Stokes solution. Therefore, for the dive speed condition it would not be appropriate to compare the magnitude of the overall lift force acting on the wing. However, for the stall condition the angle of attack is unique, and Figure 19 shows that the pressure difference between the upper and the lower surfaces of the wing is less for the Navier Stokes solution in comparison with the Euler solution.

Figure 20 and Figure 21 show the pressure distribution of the Navier-Stokes and the Euler solutions at Section B-B. Navier-Stokes and Euler solution comparison at dive condition is given in Figure 20, and Navier-Stokes and Euler solution comparison at stall condition is given in Figure 21. It is seen that gage pressure values are very close to each other at this section for both Euler and Navier Stokes solutions. In Figure 20 and Figure 21 the left side is the leading edge of the wing and the right side is the trailing edge of the wing. It is seen that at the leading edge of the wing, due to stagnation a peak in pressure is observed. On the other hand, in the trailing edge of the wing, smooth transition of the pressure between the upper and the lower surfaces of the wing is seen. Such a smooth transition of pressure between the upper and lower surfaces of the wing is a clear sign of the satisfaction of the Kutta condition. [17]
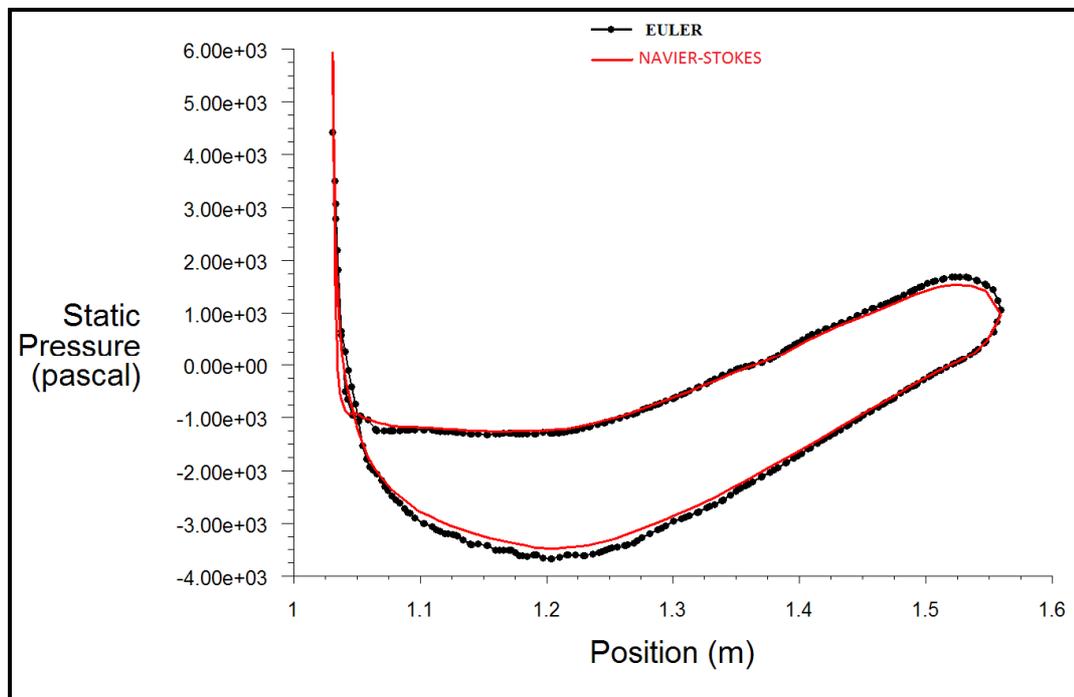
Figure 20: Dive speed pressure distributions determined by Euler and Navier Stokes solutions at Section B-B

Note: Upper curves belong to the lower surface of the wing, Left side: Leading edge, Right side: Trailing edge
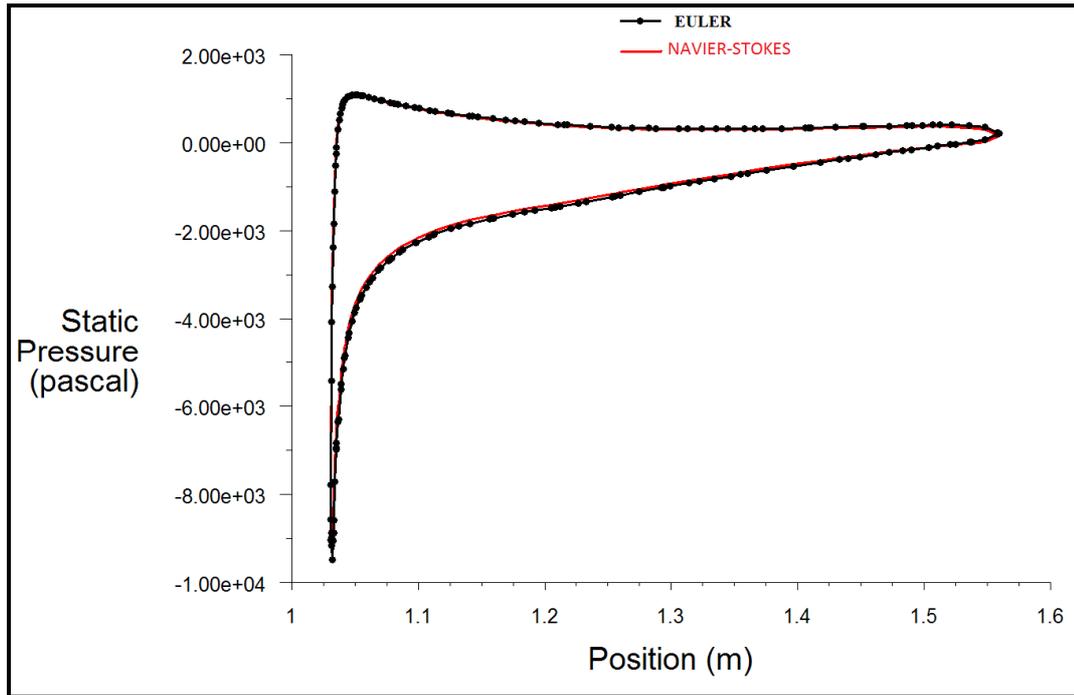
Figure 21: Stall speed pressure distributions determined by Euler and Navier stokes solutions at Section B-B

Note: Upper curves belong to the lower surface of the wing, Left side: Leading edge, Right side: Trailing edge

Gage pressure distributions obtained by the Navies-Stokes and the Euler solutions at Section C-C for the dive and stall conditions are given in Figure 22 and Figure 23, respectively. Although the difference between the Navier-Stokes and the Euler solutions is more recognizable at the wing tip, it is considered that an adequate consistency exists between two solutions.
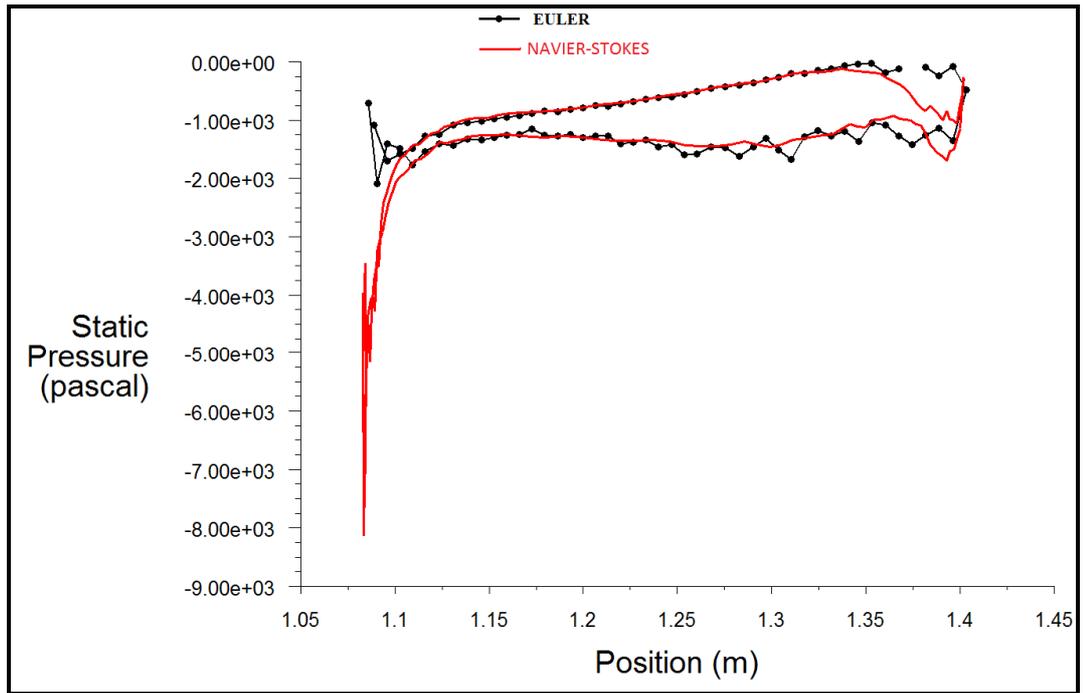
Figure 22: Dive speed pressure distributions determined by the Euler and the Navier Stokes solutions at section C-C
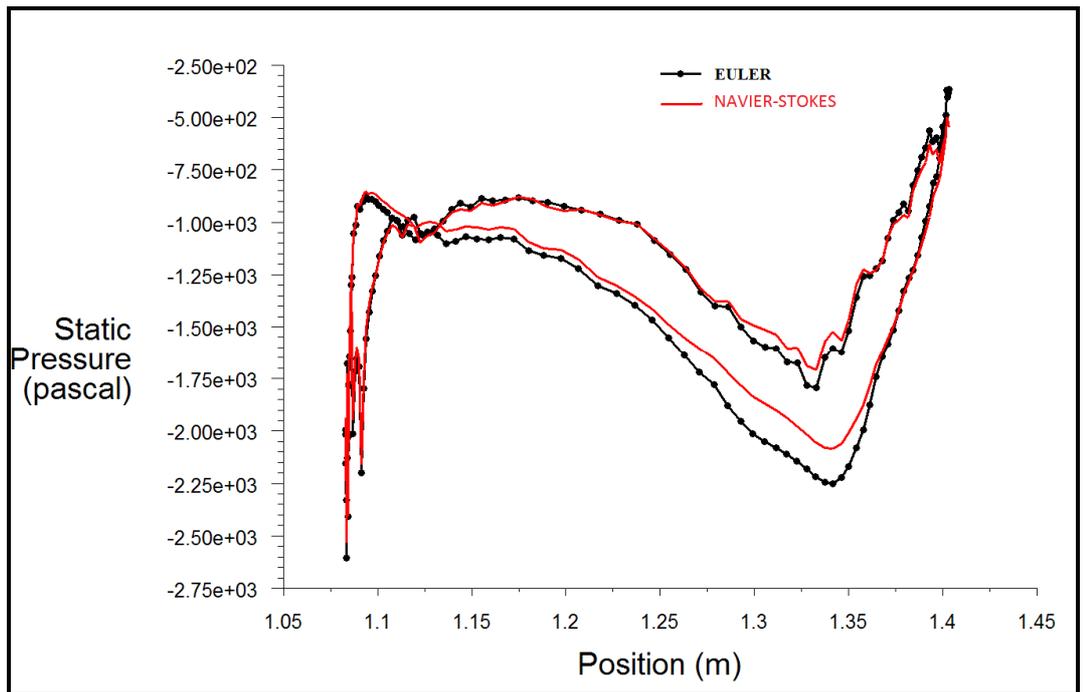
Figure 23: Stall speed pressure distributions determined by the Euler and the Navier Stokes solutions at section C-C

The total lift force and the total drag force obtained by Navier-Stokes and Euler solutions at the dive and the stall conditions are tabulated in Table 8. Lift and drag forces given in this table are valid for the half of UAV. As it is seen in Table 8, the lift force obtained by the Euler solution is higher than the one obtained by the Navier-Stokes solution. Whereas, drag force obtained by the Navier-Stokes solution is higher than the drag force obtained by the Euler solution. Since at the same angle of attack the Navier-Stokes solution gives less lift than Euler solution, in the structural analysis, pressure distribution obtained by the solution of Euler solution is used. Actually, as long as the total lift force is scaled up to the weight of the UAV, using the pressure distribution obtained by Euler solution or Navier-Stokes solutions in structural analysis does not create a significant difference in the structural analysis. However, Euler solution is preferred because Euler analysis takes less time than the Navier-Stokes analysis.

Table 8: Comparison of the Navier-Stokes and Euler results at dive and stall conditions

	Dive Speed		Stall speed	
	Navier- Stokes	Euler	Navier-Stokes	Euler
Total Lift (N)	1290,09	1409,78	1706,42	1789,82
Total Drag (N)	281,51	139,36	149,98	134,33

Comparing the Navier-Stokes and the Euler solutions, it is concluded that pressure distribution obtained by the Euler solution can be safely used in the structural analysis. Advantage of the Euler solution is its short computation time compared to the Navier Stokes solution. Comparing the pressure distribution of the Navier Stokes and the Euler solution at 3 different sections, it is observed that Euler and Navier-Stokes solutions give similar pressure distributions. Similar pressure distributions will cause similar bending and torsional moments. Therefore, as long as the shape of the pressure distribution is reliable, a lower total force is not a major problem in the structural analysis, because in order to get the necessary lift force, nodal forces can be scaled up in the Patran environment.

CHAPTER 3

STRUCTURAL ANALYSES OF TACTICAL UAV

3.1. Introduction

In this section, the sub-structures of the tactical UAV and their finite element models are explained.

Figure 24 shows the internal structural layout of the wing with color coded zones and their description. Upper and lower skins of the wing are made of a composite sandwich structure having aircraft grade Rohacell 31A [18] foam material between woven E-glass/epoxy layers. The foam core is used in all parts of the wing skin to provide an improved skin buckling resistance as well as to resist side loads due to minor impact loads or loads encountered during transportation. The two-spar configuration wing is designed to be assembled to the fuselage through the front and rear spar connections shown in Figure 24. The front spar root end, whose core was made of hornbeam wood, is extended to enter a box in the fuselage whereas the rear spar is made flush with the fuselage and it is connected to a fuselage frame by means of two bolts through the end face of the rear spar root which is made of aluminum. Front spar box used in the fuselage is manufactured from a carbon-epoxy composite by using the front spar extension as the male mold. Such a production process provided close tolerance between the spar root and its counterpart box. The two inboard ribs are closely spaced to support the hard points, which are placed between the ribs, to connect the tail plane booms under the wing.
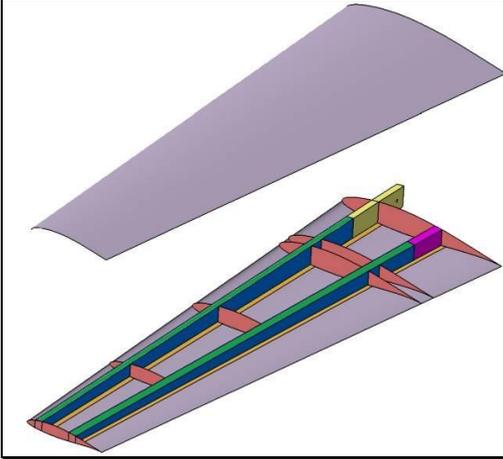
Color	Group	Material
	Front spar root	Hornbeam covered by carbon-epoxy
	Rear spar root	Al 7075-T6 covered by E-glass + carbon-epoxy
	Spar webs	Carbon-epoxy
	Upper spar flanges	Carbon-epoxy + upper skin material
	Lower and upper skins	E-Glass-epoxy + Rohacell-foam sandwich structure
	Lower spar flanges	Carbon-epoxy + lower skin material
	Ribs	Carbon-epoxy+balsa wood +foam sandwich

Figure 24: Color coded zones of the wing model and description of the sub-elements of the wing

Figure 25 shows the coarse mesh finite element model of the wing used in the aeroelastic analyses. It shows the mesh for the lower skin and the internal reinforcements without the upper skin. Finite element model of the wing structure is prepared by grouping the meshes of the sub-elements in accordance with the groups established for the geometric model given in Figure 24 by the color coded zones. Front and rear spar connections are assigned isotropic material properties. Spar webs and flanges, upper and lower skins and the ribs are assigned composite laminate properties. As it is shown in Figure 24 skin layers are also included in the laminate definition of the upper and lower flanges of the spars. Perfect bonding assumption is made for all the mating elements which are bonded to each other either by the epoxy used during the vacuum bagging operation or by the adhesive used in secondary bonding. Front and rear spar airframe connections are meshed with solid elements. The remaining sandwich sub-elements listed in Figure 24 are meshed with quadrilateral shell elements, and the laminates are defined by the order and orientation of lamina with respect to a material coordinate system using the PCOMP entry in Nastran input file.[16]
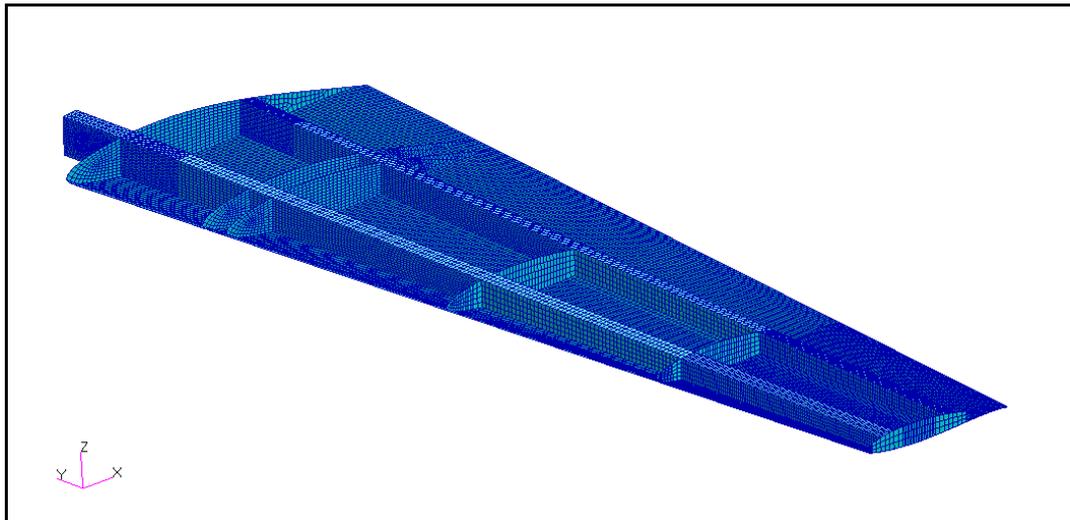
Figure 25: Finite element model of the wing structure

Figure 26 shows the boundary conditions used in the static analyses of the wing. The front spar root, which enters into its counterpart box in the fuselage, is pressed against the box by the two side bolts, as shown. Therefore, the three displacements on the face of the front spar root are fixed in the analysis of the wing. The rear spar aluminum root is flush with the side wall of the fuselage, and it is connected to the fuselage frame by two bolts as shown. During the wing-fuselage assembly when the two bolts are tightened, the wing is pulled against the side wall of the fuselage, thus preventing wing axis (y) displacements on the face of the rear spar root in contact with the side wall of the fuselage. The fuselage axis (x) and perpendicular axis (z) displacements on the face of the rear spar root depends on the friction between the aluminum root of the rear spar and the fuselage side wall. In the static analysis of the wing, the friction between the aluminum root and the fuselage side wall is neglected and the fuselage axis (x) and perpendicular axis (z) displacements on the face of the rear spar root are taken as free. In the finite element model for the static analysis the x, y, z displacements of the nodes on the surface of the two bolt holes are also fixed since the bolts provide almost a rigid connection between the rear spar root and the fuselage frame.
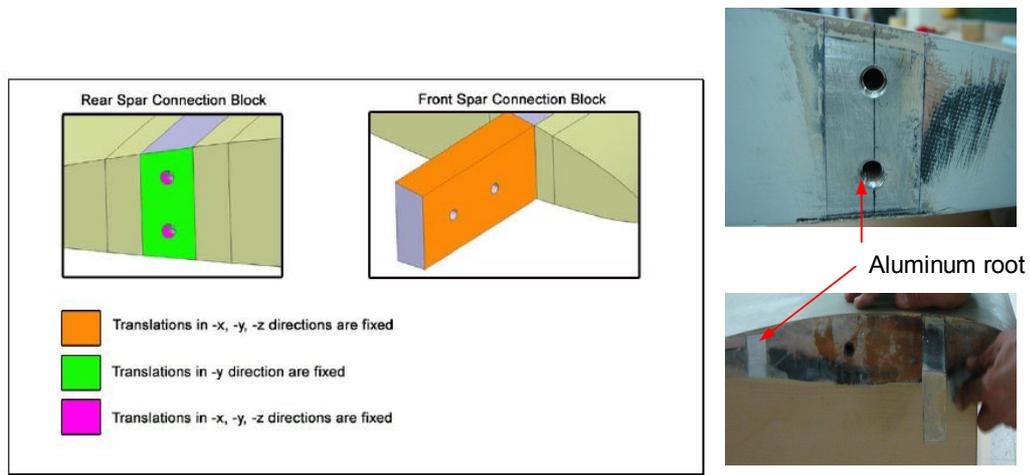
Figure 26: Spar roots and the boundary conditions used in the wing roots in the static FE analysis

Internal structure of the horizontal and vertical tail is similar to the internal structure of the wing. Skins are composed of sandwich structure consisting of Rohacell foam as the core material with E-glass woven fabric composite as the face sheets. The use of Rohacell foam as the core material in the skins eliminated the need of using ribs in the horizontal and vertical tails. Resin absorbed by the foam core gives sufficient stiffness to the skins such that local penetrations due to side loads and skin buckling are prevented by the use of Rohacell foam core. Figure 27 shows the internal structure of the horizontal and the vertical tail.
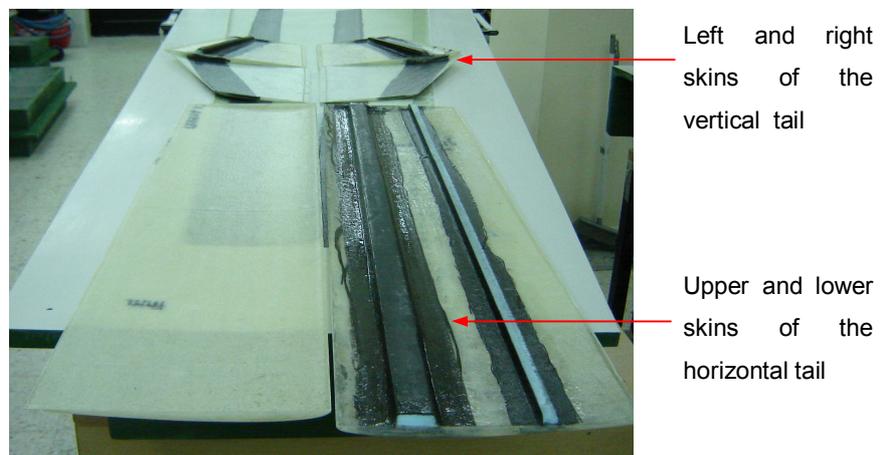
Figure 27: Internal structural layout of the horizontal and vertical tail

The picture in Figure 27 was taken before the both sides of the tail skins were bonded to each other. Upper faces of the spar in the horizontal and vertical tails

shown in Figure 27 also provide span wise support to the skins thereby no rib was required for the tails. The main spars of the horizontal and vertical tail are manufactured and bonded to one of the skins in exactly the same way as the spars of the wing. Wetted carbon fabric composite are laid over the blue styrofoam molds of the spars and vacuum bagging process is applied to consolidate the bonding between the main spars and the skin. On the horizontal tail a rear spar is used to provide backing for the larger elevator actuator which will be positioned between the two spars. The rear spar, which is composed of sandwich blue Styrofoam and carbon fabric composite, is manufactured by vacuum bagging in a separate operation, and it is cut into the required dimensions and secondary bonded to the lower skin. As in the case of the wing structure, the upper and lower skins of the tails are bonded to each other along the leading and trailing edges and faces of the spars by secondary bonding.

The horizontal and vertical tail connection is designed to be permanent to prevent any probable free play of the connection elements between the horizontal and vertical tails in case a removable connection was used. Figure 28 shows the permanently connected horizontal and vertical tails. After the adjustment of the set angle of the horizontal stabilizer, permanent connection of the horizontal and vertical tails is achieved by bonding the tails to each other by composite material along the two edges of the horizontal tail, as shown in Figure 28. To provide a stiff connection several layers of composite material are placed along the inner and outer edges of the tail plane connections.

Inner and outer edges of the tail plane connections
are covered with wetted fabric

Figure 28: Permanent connection of the horizontal and vertical tail

In the finite element model of the horizontal tail and vertical tail composite laminate properties are assigned to skins and spars appropriately. Figure 29 shows the finite element mesh of the horizontal and vertical tail connection. During the permanent assembly of the horizontal and vertical tail several layers of composite materials that are used providing a very stiff connection. Therefore in the finite element model, the horizontal and vertical tail planes are modeled conjointly.
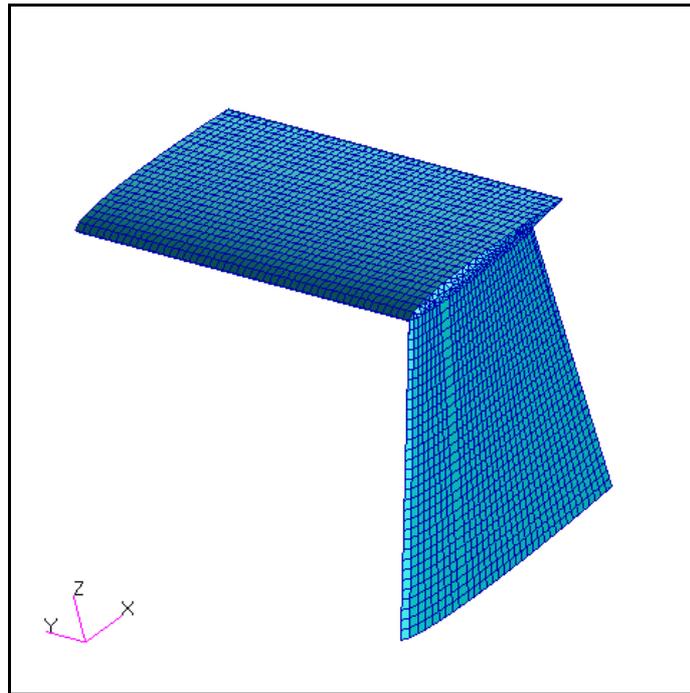
Figure 29: Finite element model of the horizontal and vertical tail and their connection

Figure 30 shows the tail boom connections at the wing and at the vertical tail. The tail boom, which is manufactured by the filament winding process, enters into its guides under the wing and under the vertical tail. On the wing side the tail boom is secured to the wing by the two bolts whose locations are shown in Figure 30. The bolts are screwed to the two hard points between the two closely spaced ribs. The hard points are also bonded to the front and rear spars so that the tail loads could be distributed to the wing structure through the stiff spars and the two closely spaced ribs. On the vertical tail side tail boom enters into a cylindrical counterpart which is bonded to the vertical tail by composite material permanently. On the vertical tail side a single bolt was used to secure the tail boom vertical tail

connection. On the wing side the boom elements, which are in line with the connection bolts, are tied to the respective hard point nodes with rigid elements which represent the bolts used in the connection.
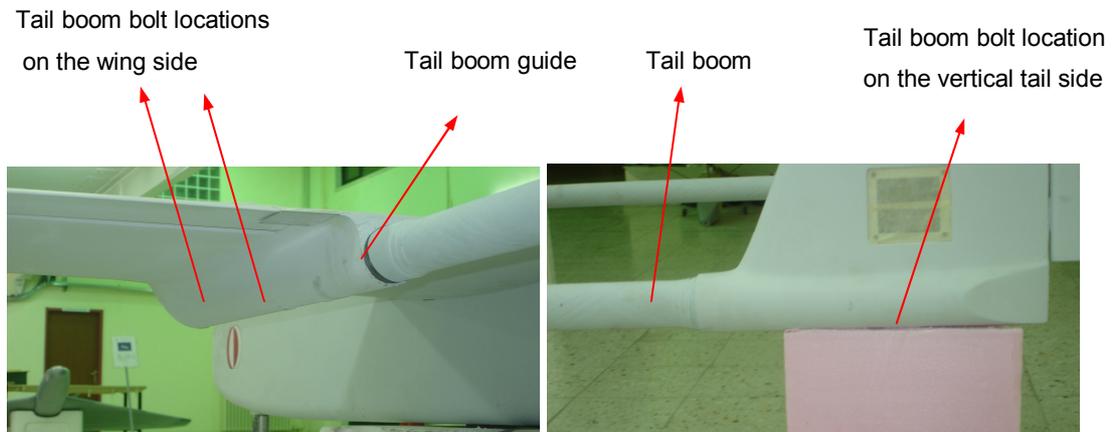
Figure 30: Tail boom bolt connection locations on the wing and the vertical tail

3.2. Structural Analysis of the Wing-Tail Plane Combination

During the structural analyses, loads acting on the wing, tail and tail boom are utilized. Aerodynamic loads on the tactical UAV are obtained by the computational aerodynamic analysis and interpolated to the structural mesh. Structural analyses of the tactical UAV are performed by MD Nastran solver. Structural analysis of the fuselage is not included in this section since main scope of the analysis section is on the structural integrity of the lifting surfaces. Figure 31 shows the finite element model used in structural analysis. Finite element model consists of half wing and tail plane of the tactical UAV with the appropriate boundary and symmetry conditions. As it is seen, front and rear spar of wing is fixed at wing root and symmetry boundary condition is applied at tail symmetry plane. By fixing the wing root it is assumed that the fuselage connection is rigid. It should be noted that fixed wing root is more critical in terms of stresses induced in the wing.
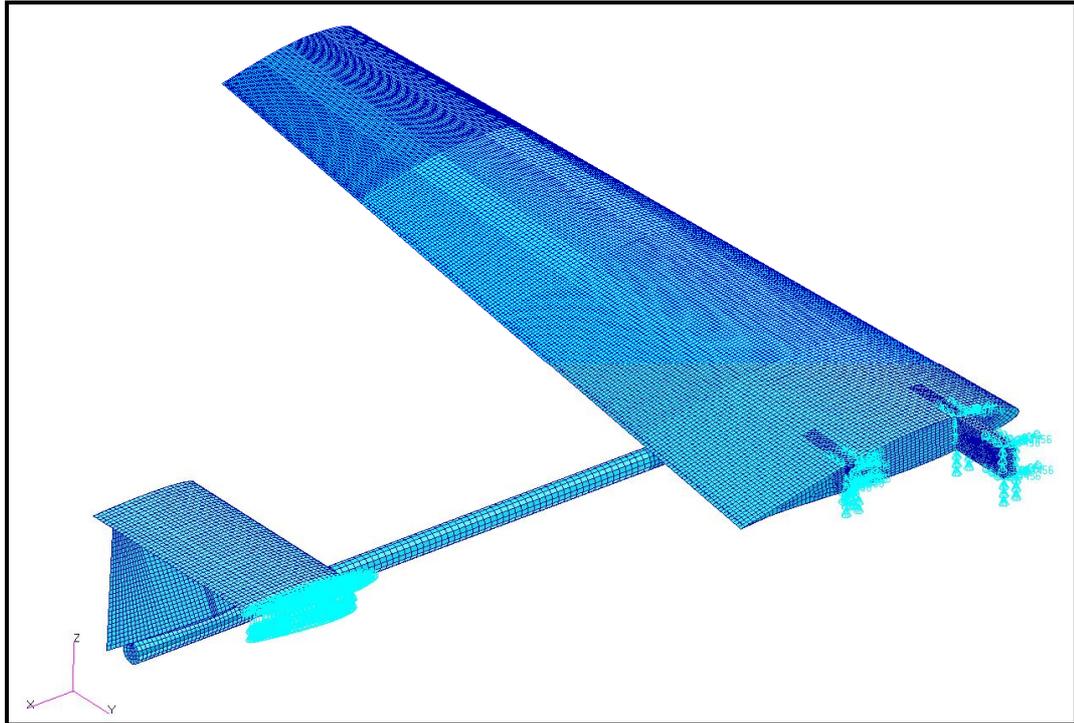
Figure 31 : Finite Element model of Tactical UAV

There are 58943 grid points and 81446 elements in the finite element model of the Tactical UAV. Element and grid point summary of the finite element model is tabulated in table below. Front spar root and rear spar root are meshed with CTETRA elements due to their complex shapes and hardpoints are modeled by CHEXA elements. Wing skin, wing webs, boom and tail are meshed with quad dominant shell elements; however, shell elements around the wing spar roots are modeled by CTRIA3 elements because of that spar roots are modeled by CTETRA elements.

Table 9: Finite element model summary

NUMBER OF GRID POINTS	58943
NUMBER OF CHEXA ELEMENTS	504
NUMBER OF CQUAD4 ELEMENTS	54964
NUMBER OF CTETRA ELEMENTS	21461
NUMBER OF CTRIA3 ELEMENTS	4509
NUMBER OF RBE2 ELEMENTS	8

During the structural analysis, Von Misses stress criterion is used for the strength check of the isotropic materials, and Tsai-Wu failure theory is employed for composite materials.

Hornbeam, stainless steel, aluminium and epoxy are isotropic materials used in manufacturing of tactical UAV. Material properties of these materials are tabulated in Table 10.

Table 10: Mechanical properties of isotropic materials

	E (MPa)	υ	σ_u (MPa)
Hornbeam	15260	0.35	48.3
Steel	200000	0.3	400
Aluminum	70000	0.33	534
Epoxy	3450	0.35	82

E-glass/epoxy and carbon/epoxy are the orthortopic materials used in manufacturing of tactical UAV . Material properties of these orthotropic materials are determined by tests [21] and tabulated in Table 11. In this thesis, Woven carbon and E-glass fabric that was procured to be used for the serial production version of the airplane are characterized for the tensile properties by the tests. Preparation procedure of test specimens and test results are described in Appendix C.

Table 11: Mechanical properties of orthotropic materials

	E11 (MPa)	E22 (MPa)	υ 12	G12 (MPa)	X (MPa)	X' (MPa)	Y (MPa)	Y' (MPa)	S (MPa)
E-Glass	26400	26400	0.125	4820	275	275	275	275	34
Carbon	47475	47475	0.0606	3393.8	403	403	403	403	103.4

3.3. Detailed description of Tactical UAV design

In the introduction chapter, general design specifications of the UAV were given. In addition, in section 3.1 description of the sub-structures of the tactical UAV and the finite element models of the sub-structures are explained. In this section, more details about the sub-structures are given. These details include the layer numbers, approximate thicknesses of each layer

Wing

Wing Skin: Wing skin is designed as sandwich structure composed of E-glass/Epoxy layers above and below the Rohacell foam core [18]. There are 2 layers of E-Glass/Epoxy under the Rohacell foam and 2 layers of E-Glass/Epoxy above the Rohacell foam. Each E-Glass/Epoxy layer has approximately 0.3 mm thickness and thickness of the Rohacell foam is 2 mm. Rohacell A coarse grid foam core is an aircraft grade closed cell rigid foam plastic which absorbs resin because the volume of cell walls made of PMI is very less in comparison to the volume of filled cells with resin. According to the foam manufacturers application of vacuum pressure soaks the foam with resin; therefore in the finite element model the recommendation is to use pure resin property for the foam core. Therefore, in the structural analysis, epoxy properties are used for Rohacell foam core in the structural analysis.

Wing Spars: There are 2 spars in wing structure. A foam mold is placed on 2 layers of carbon/epoxy and foam is covered by 5 layers of carbon/epoxy. Figure 32 shows the detail of the sandwich construction around the root of the front spar. In the wing root an hornbeam (Figure 24) is placed. But away from the wing root, the core of the spars is made of blue foam. By placing carbon epoxy layers over the foam mold hat shaped spar structures are produced. Mold foam is neglected in the structural analysis, and spars are assumed to be made up of only carbon/epoxy layers. Thickness of each carbon/epoxy layer is approximately 0.3 mm. During the finite element modeling of the spars, the skin layers are also included in the laminate definition of the upper and lower flanges of the spars. Lower and upper flanges of the front spar is shows in Figure 32. Perfect bonding assumption is made for all the mating elements which are bonded to each other either by the epoxy used during the vacuuming operation or by the adhesive used in secondary bonding.
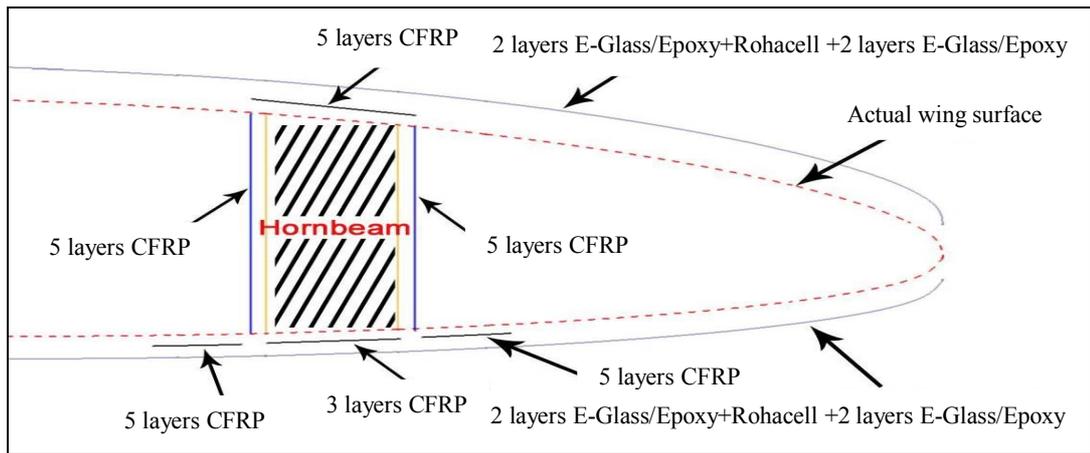
Figure 32 : Detail of the sandwich construction around the root of the front spar

<u>Wing Ribs:</u> there are 6 ribs in each wing structure. Wing ribs consist of Carbon/Epoxy, blue foam and hornbeam. Structural configuration of wing rib is shown in Figure 33 and tabulated in Table 12.
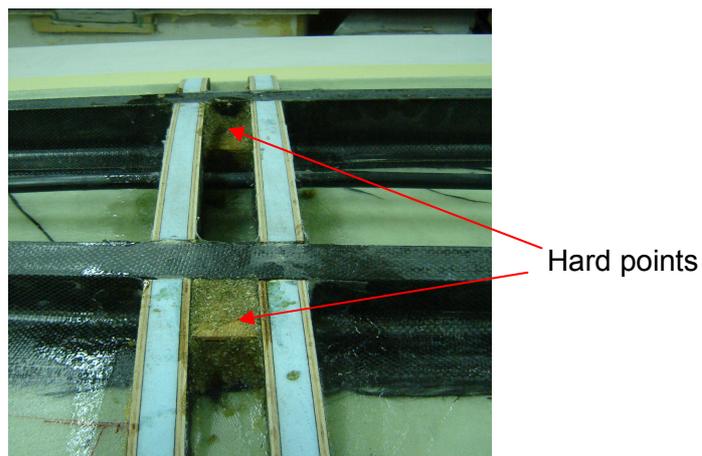
Figure 33 : Close view of the wing rib

Table 12: Wing rib structure

Layer #	Material
1	0.1 mm thick Carbon/Epoxy
2	4 mm thick hornbeam
3	0.1 mm thick Carbon/Epoxy
4	20 mm thick blue foam
5	0.1 mm thick Carbon/Epoxy
6	4 mm thick hornbeam
7	0.1 mm thick Carbon/Epoxy

Thick hornbeam and blue foam provide wing structure with torsional stiffness to the wing ribs. In addition, wider thickness of the wing ribs provides adequate surface area during the bonding of the ribs to the upper and lower surfaces of the wing. Using multi-layer theory at rib structure is not appropriate because of the high thicknesses of the hornbeam and the blue foam. However, in order to prevent thre dimensional modeling of the wing ribs, ribs are modeled as composite material to simplify the finite element model. In case of three dimensional modeling of the wing ribs, the upper and the lower surfaces of the wing would have to be split along the edges of the hornbeam and the blue foam and this would complicate the finite element model very much. Therefore, in this thesis classical lamination theory is also used in modeling the wing ribs. In this case upper and lower surfaces of the wing are split only at the rib stations by single lines. Figure 34 shows the surface models of the wing ribs used in the wing. The two closely spaced ribs near the wing root correspond to the tail boom connection region under the wing.
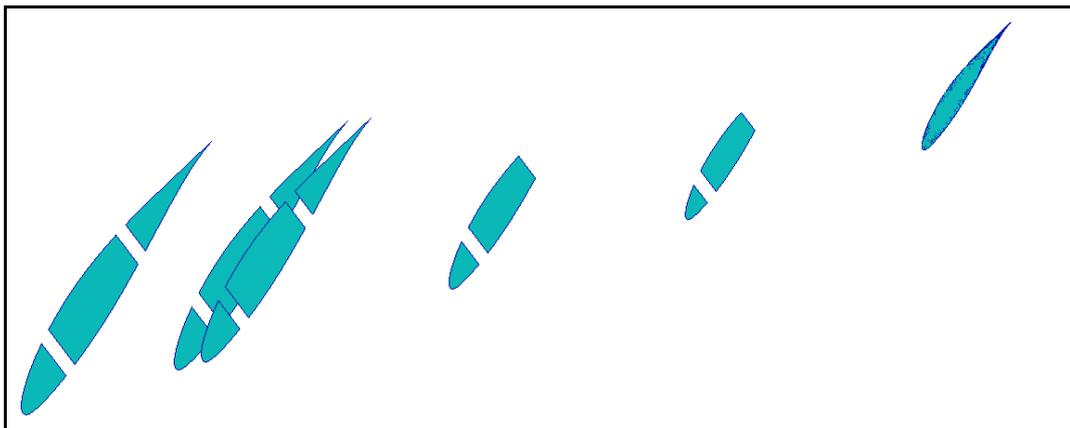
Figure 34: Surface models of the wing ribs

Wing Spar-Fuselage Connections: Front spar-fuselage connection is made up of hornbeam and it is extended to mid-fuselage. 2 bolts attach front spar-fuselage connection to fuselage from side surfaces. Rear spar-fuselage connection is made up of aluminum 7075-T6 and it is attached to fuselage by 2 bolts from the outside. Figure 35 shows spar connections and finite element model of spar connections.
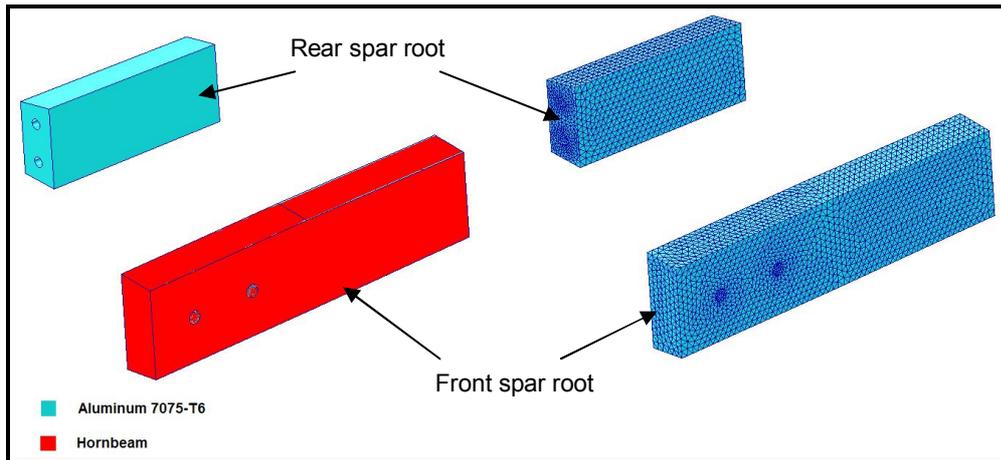
Figure 35: Wing spar-fuselage connections.

Wing-Tail boom Connections: Tail plane and wing are connected to each other by tail booms. There are 2 hard points, in each wing structure, fixing the tail boom to wing structure. Hard points are placed between 2 neighboring ribs and behind the front and the rear spars. Hard points are shown in Figure 33 in the close view of the wing rib. Figure 36 shows the finite element model of the hard points and neighboring ribs.
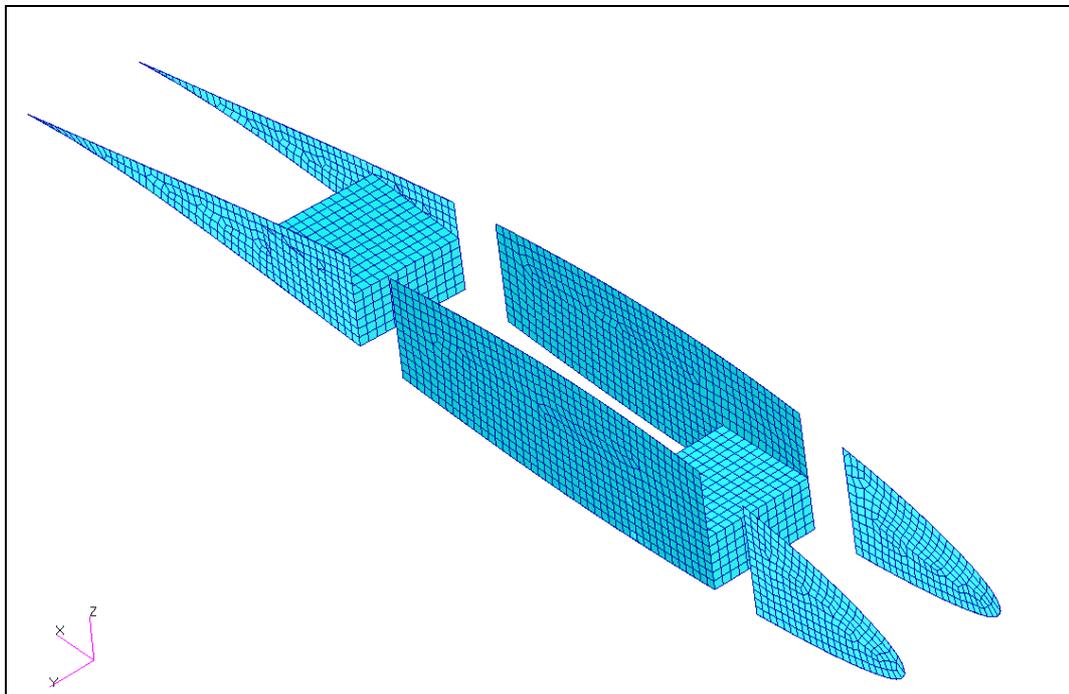
Figure 36: Finite element model of the hard points connecting the tail boom to wing

Hard points consist of a stainless steel block between 2 hornbeam blocks. Lower hornbeam block has a thickness of 4mm, upper hornbeam block has a thickness of 14 mm and stainless steel block has a thickness of 10 mm. Inner structure of the hard points is shown in Figure 37. Tail boom is fixed to the stainless steel blocks by M8 bolts. M8 bolts are modeled by 4 rigid MPC's (Multipoint Constraints) in the structural analysis, as seen in Figure 38.
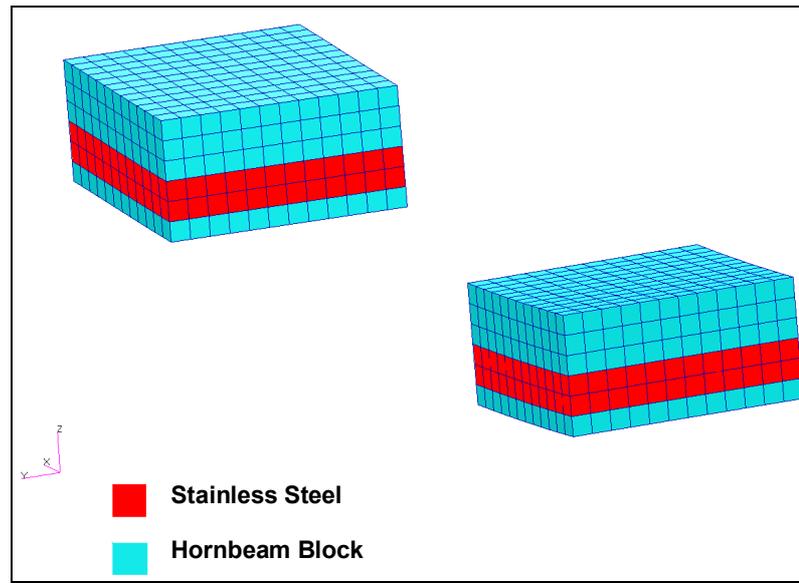
Figure 37: Inner structure of the hard points
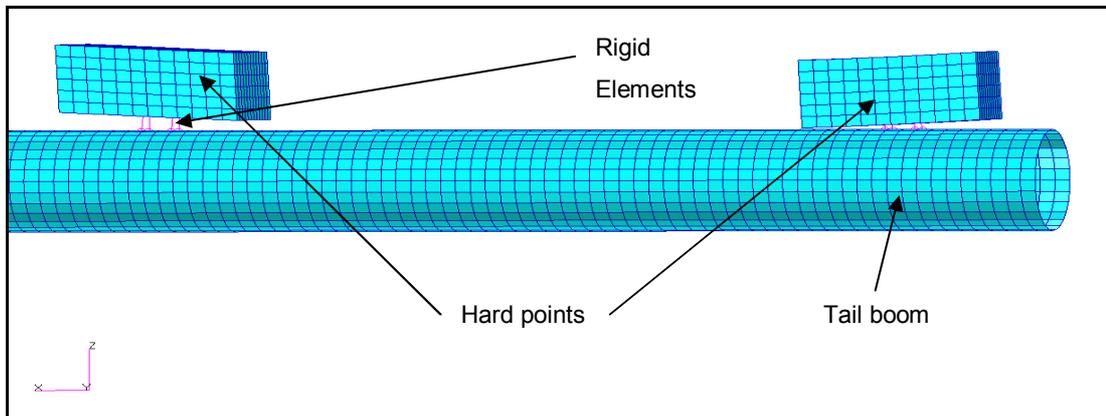
Figure 38: Multipoint constraints represensing M8 bolts

<u>Horizontal Tail</u>

Surface model of the half horizontal tail inner is given in Figure 39. Inside the horizontal tail, there are 2 spars and there are not ribs.
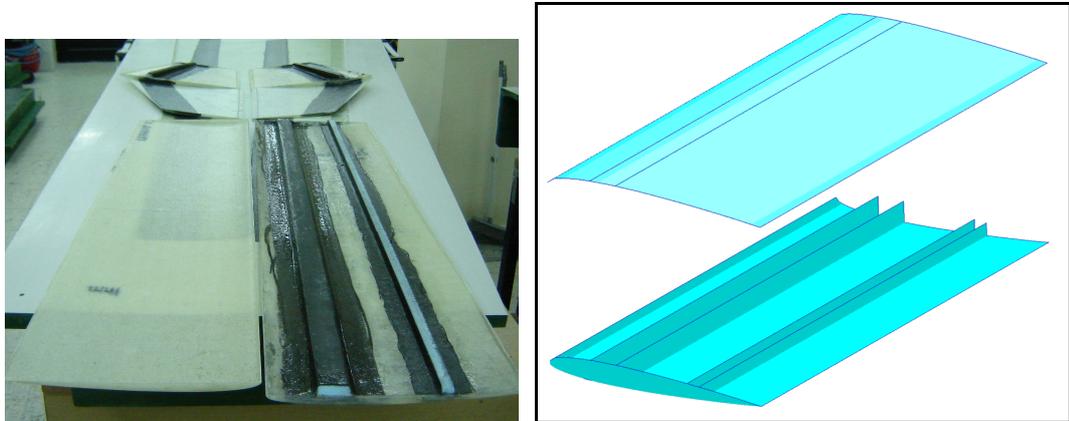
Figure 39: Inner structure of the horizontal tail

Figure 39 also shows the manufactured horizontal tail. The two spars are co-cured to the lower skin of the horizontal tail.

Horizontal tail skin: Skins of the horizontal tail are designed as a sandwich construction composed of e-glass/epoxy-Rohacell foam core. Horizontal tail skin consists of 3 layers; bottom layer is 0.3 mm thick E-glass/Epoxy woven fabric, mid layer is 2mm thick Rohacell foam and upper layer is 0.1mm thick E-glass/Epoxy woven fabric. Again, because of the epoxy sucking property of the coarse grid Rohacell foam during the vacuum operation used in the manufacturing, epoxy properties are used for the Rohacell foam core in the finite element analysis.

Horizontal tail spars: Figure 40 shows the structural mesh and materials of spars of the horizontal tail. Front spar is a hat shaped spar structure, as seen in Figure 39. A mold foam is placed on 2 layers of 0.3 mm thick Carbon/Epoxy woven fabric and foam is covered by 2 layers of Carbon/Epoxy during the vacuum bagging operation. Rear spar is consists of two L-shaped side flanges which are composed of 2 layers of 0.1mm thick Carbon/Epoxy woven fabric. It should be noted that in the structural analysis blue foam is not taken into consideration. Laminate definitions are made for

the skins of the spars. In the laminate definitions of the upper flange and side flanges of the front spar and the L shaped side flanges of the rear spar, skins are also included. Specifically, in the laminate definition of the upper flange of the front spar, upper skin is also included in the laminate definition of the upper flange. In the side flanges of the front spar, lower skin is also included in the laminate definition of the side flanges of the front spar. In the side flanges of the rear spar, lower skin is also included in the laminate definition of the of the side flange of the rear spar. In Figure 40, laminate definitions are given for the webs which do not include the skin material.
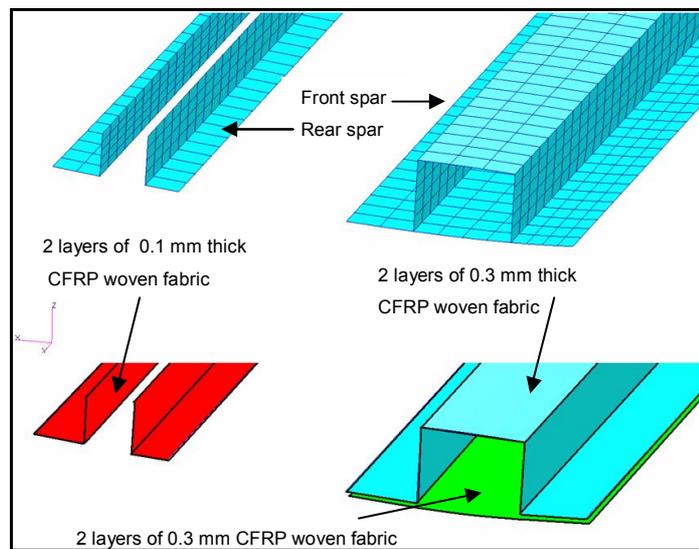
Figure 40: Spar structure of the horizontal tail

Vertical tail

Figure 41 shows vertical tail structure. Both the manufactured left and right skins and the surface model of the vertical tail are shown in Figure 41. As it is seen, there is one spar in vertical tail structure, and the upper tip of vertical tail is trimmed in order to provide vertical tail and horizontal tail connection.
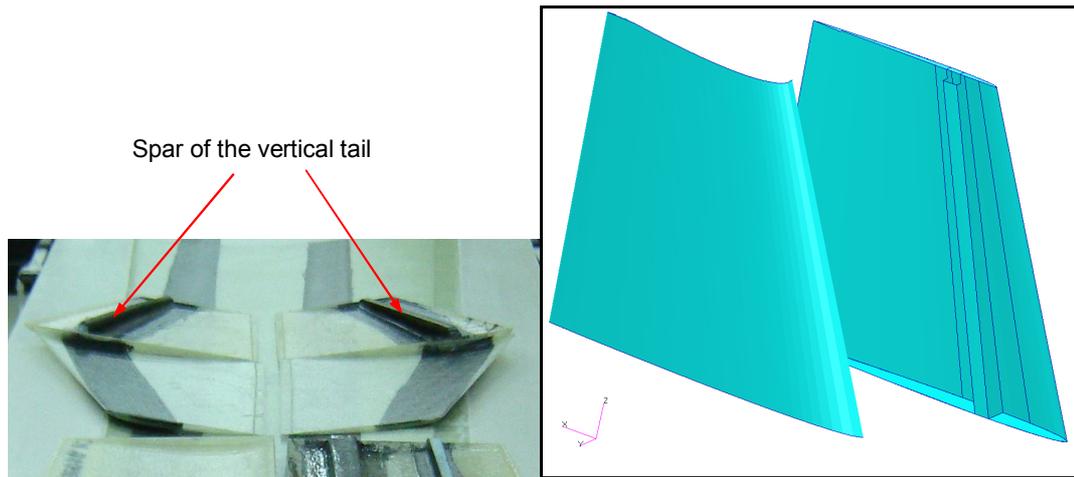
Figure 41: Vetical tail inner structure

Vertical tail skin: Vertical tail skin structure is designed as the same E-glass/rohacell sandwich structure with horizontal tail skin.

Vertical tail spar: During the manufacturing of the vertical tail a mold foam is placed on top of 2 layers of Carbon/Epoxy layers, shown in Figure 41, on the skin of the tail. Then, the foam mold is covered with two 2 layers of Carbon/Epoxy, and the vacuum bagging operation is applied. Thus, spar of the tail is fully integrated to the skin of the tail during the vacuum bagging operation resulting in a hat shaped vertical tail spar. Surface model and finite element model of the spar of the vertical tail is shown in Figure 42. Thickness of each carbon-epoxy layer which is placed over the foam mold is 0.3 mm.
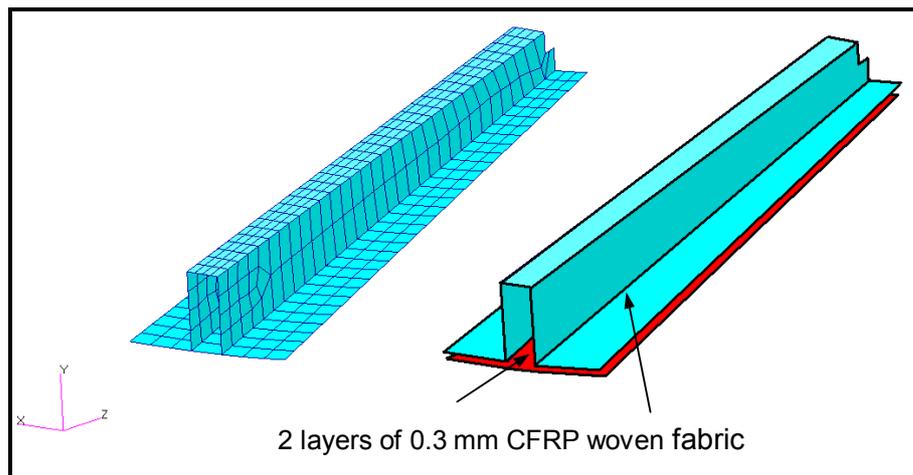
Figure 42: Vertical tail spar structure

3.4. Tsai-Wu Failure Theory

In the thesis, structural integrity of the composite parts is checked by employing the Tsai-Wu failure criterion [20]. Tsai-Wu failure index is defined in Equation 5. In this equation, FI is the failure index value and the failure is predicted when FI is equal to 1 or larger than 1. In Equation 5, σ_1 is the axial stress in fiber direction, σ_2 is the axial stress in the direction perpendicular to fiber direction and τ_{12} is the in-plane shear stress. Tsai-Wu failure criterion is defined for unidirectional composite layers. In the current study, Tsai-Wu failure criterion is also applied for woven fabric composites, assuming that strength properties in x and y directions are equal to each other for the plain balanced woven fabric composites. In addition, in the current study tensile and compressive strengths are taken as the same to be more conservative, because, in general compressive strength of the composites is higher than the tensile strengths. It should also be noted that for equal tensile and compressive strengths, when interaction term is taken as -0.5, Tsai-Wu and Tsai-Hill failure index theories give the same failure indices for woven fabric composites [20].

$$F_{11}\sigma_1^2 + F_{11}\sigma_2^2 + 2F_{12}\sigma_1\sigma_2 + F_{66}\tau_{12}^2 + F_1\sigma_1^2 + F_1\sigma_2^2 = FI \qquad (5)$$

Where:

$$F1 = \frac{1}{TX} - \frac{1}{CX} \qquad F22 = \frac{1}{TY \cdot CY}$$

$$F2 = \frac{1}{TY} - \frac{1}{CY} \qquad F12 = \frac{IXY}{\sqrt{TX \cdot CX \cdot TY \cdot CY}}$$

$$F11 = \frac{1}{TX \cdot CX} \qquad F66 = \frac{1}{SXY^2}$$

IXY = -0.5 (recommended value) [19]

TX   : Tensile strength along the x-axis
CX   : Compressive strength along the x-axis
TY   : Tensile strength along the y-axis
CY   : Compressive strength along the y-axis
SXY   : Shear strength in the XY plane

SYZ   : Shear strength in the YZ plane

SXZ   : Shear strength in the XZ plane

F12   : Interaction Term

Strength ratio (R) shows how much load can be increased until failure. In terms of strength ratio, failure is predicted when the strength ratio is less than one and material is safe when the strength ratio is greater than one. Relation between the failure index and the strength ratio is given by Equation 2.

$$\text{Strength Ratio } R = 1/\sqrt{FI} \qquad (6)$$

Figure 43 shows sample safe regions of the maximum stress theory and Tsai-Wu failure theory on the $\sigma_1 - \sigma_2$ graph. As it is seen, safe region for Tsai-Wu theory is elliptical and safe region for maximum stress theory is rectangular. When normal stresses for both fiber and transverse directions have the same sign, the maximum stress theory is more conservative than the Tsai-Wu failure criterion. However, in case of bi-axial loading with alternating signs for the fiber and transverse direction stresses, Tsai-Wu failure criterion is more conservative.
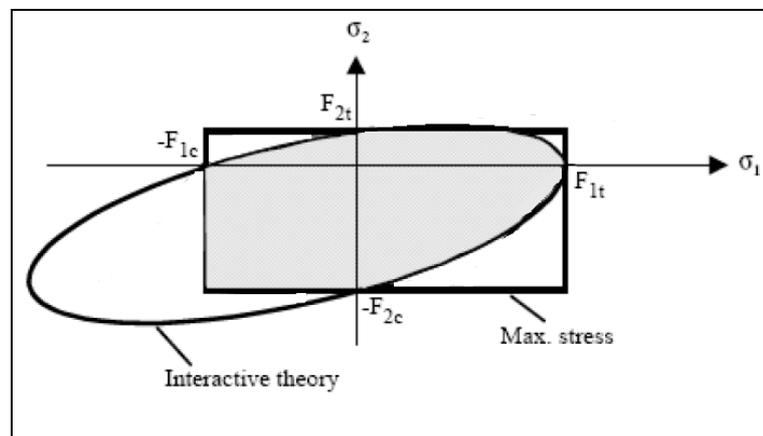
Figure 43: Comparison of the maximum stress theory and the Tsai-Wu failure index

In the structural analysis of the wing-tail plane combination, for each composite sub-regions which belong to wing-tail plane combination, the maximum failure indices are calculated and based on the maximum failure indices, a general idea is obtained with regard to the structural integrity of the composite sub-region.

In the structural analysis, equivalent stress distribution plots are presented for each composite sub-regions. Woven composite materials used in the structural analyses have equal strengths in both fiber and transverse directions. Because of that, equivalent stress distribution gives a general idea about the FI distribution in the structural analyses. As it is seen in Figure 44, equivalent stress distribution and FI distribution are similar for a rectangular plate subjected to in-plane and out-of-plane loading.
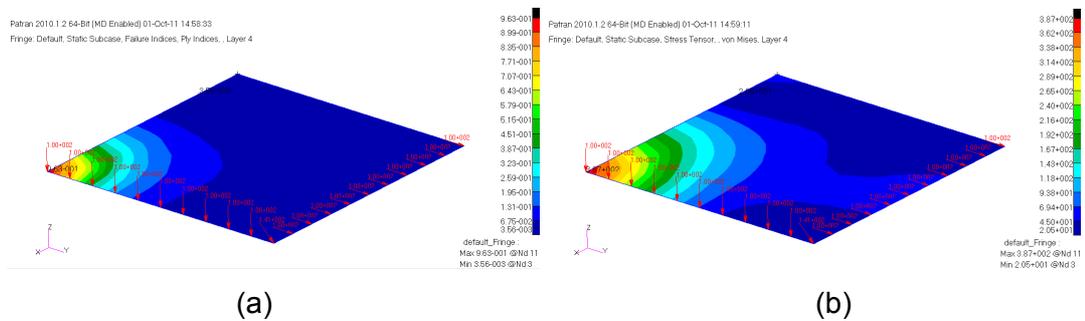
Figure 44: Comparison of (a) the FI and (b) the equivalent stress plots

3.5. Structural Analysis of the Wing at 3.8g dive and stall conditions.

The pressure distributions given in Figure 15 and Figure 16 are first transferred to the structural mesh and then scaled up. Structural analyses are then performed by MSC Nastran using the half wing tail plane combination. In this section, stress results are only presented for the wing structure. Displacement plots which are obtained for the dive and the stall conditions are shown in Figure 45-47.

Figure 45 shows the displacement plot for the wing-tail plane combination.For the dive speed condition, the maximum displacement at the tail is determined to be about 28 cm. Figure 46 shows the displacement plot of the wing only. It is seen that the maximum displacement of the wing is about 33 mm at the wing tip. It should be

noted that the tail plane is connected to the wing by tail booms. In a way, the tail plane is cantilevered to the wing by tail booms. Therefore, at the dive speed condition, displacement of the tail is very high. It should be noted that displacement plots given are magnitude plots. Due to the initial negative angle of attack of the tail plane, at the dive angle of attack the overall angle of attack of the tail plane is still negative. From Figure 45, it is seen that the tail boom bends down due to the down-lift action on the horizontal tail. On the other hand, for the stall condition, the maximum displacement is 36.9 mm at wing tip. From Figure 47 it is seen that in the stall condition, the displacement of the tail plane is less than the tip displacement of the wing. For the stall condition, the angle of attack is very high and at such a high angle of attack, fuselage may block the tail plane. However, the minimum maneuvering speed is very low compared to the dive speed and aerodynamic forces are proportional to the square of the air speed. Therefore, at the minimum maneuvering speed, the net lift force acting on the tail plane is much less compared to the net lift force acting at the dive speed condition. It is considered that the low tail plane displacement at the stall condition is due to the low speed at which the aerodynamic forces are calculated by the computational aerodynamic analysis at the minimum maneuvering speed.
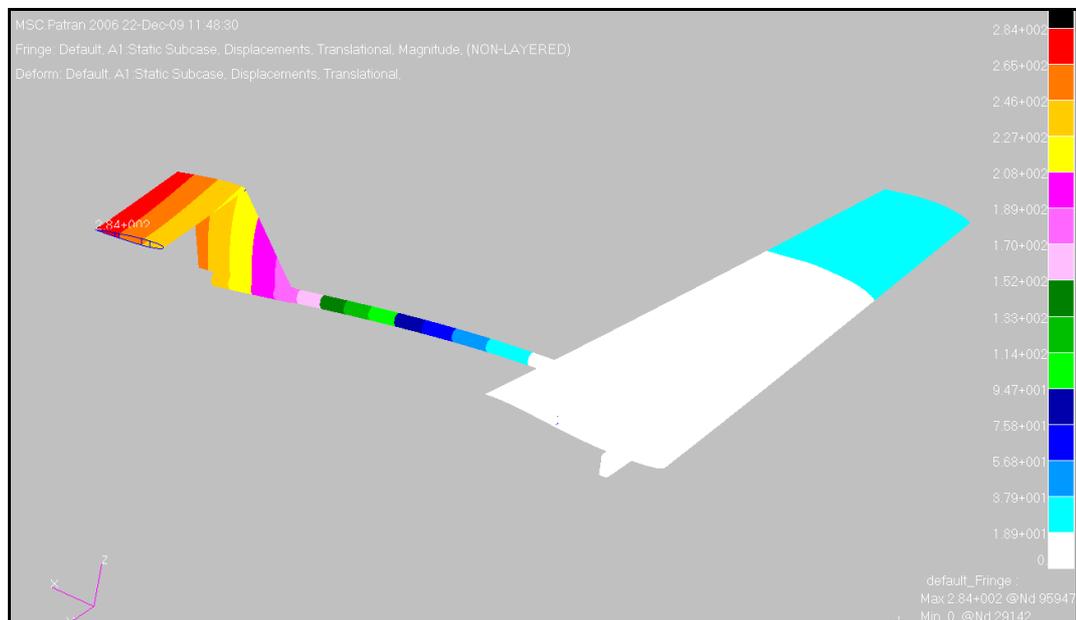
Figure 45: Displacements of the wing-tail plane combination at dive speed
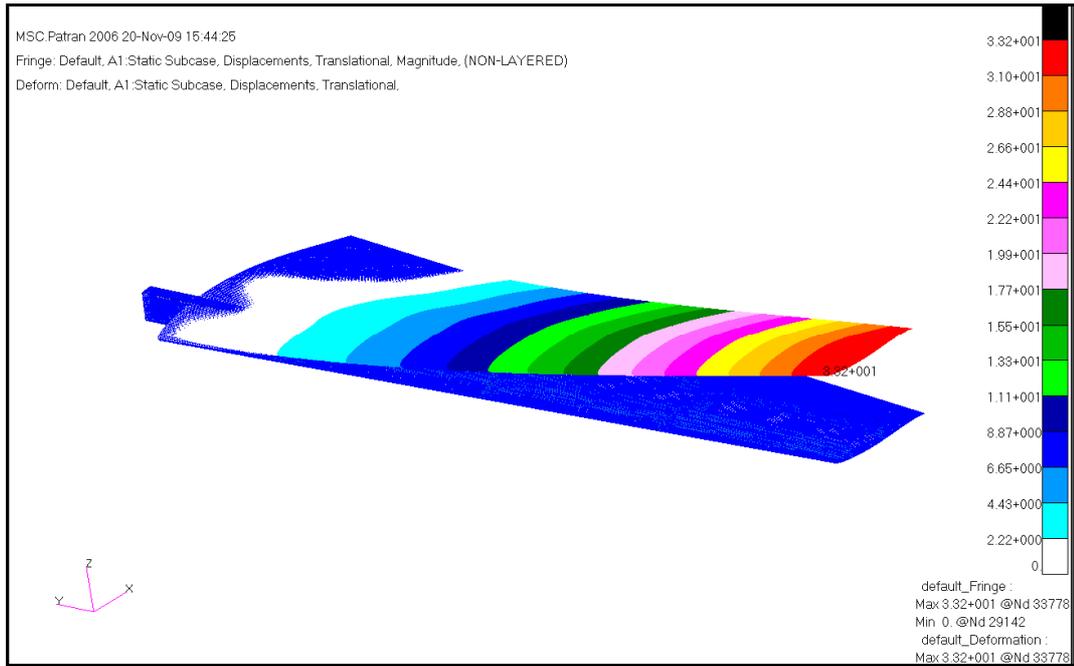
Figure 46: Displacements of the wing-only at dive speed
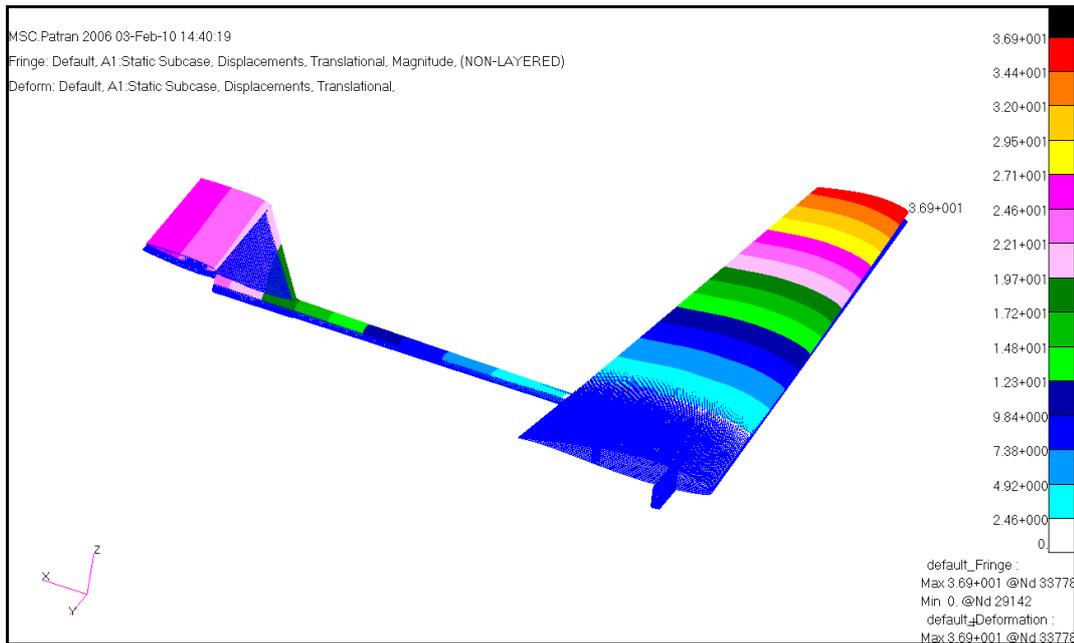
Figure 47: Displacements of the wing-tail plane combination at stall condition

<u>Stress Analysis of the Ribs</u>

Before the stress distributions on the wing ribs are presented, surface normals of the shell elements, which are used to model the ribs, are drawn to make sure that there is uniformity in the surface normals. Surface normals of the wing ribs are shown in Figure 48. Surface normal of tip rib is adjusted to be in the outward direction, whereas surface normals of the inner ribs are adjusted to point towards the wing root, as shown in Figure 48. According to the laminate definition used in the Nastran finite element program, the first layer of a composite is the layer on opposite side of surface normal and layer numbers increase one by one in the normal direction. In examining results, surface normals should be considered in order to understand layer numbering.

After the finite element analysis of the wing-tail plane combination, equivalent stresses are determined on each sub-part of the wing-tail plane combination. Figure 49 shows equivalent stresses in the 1st layer of the wing ribs at dive condition.
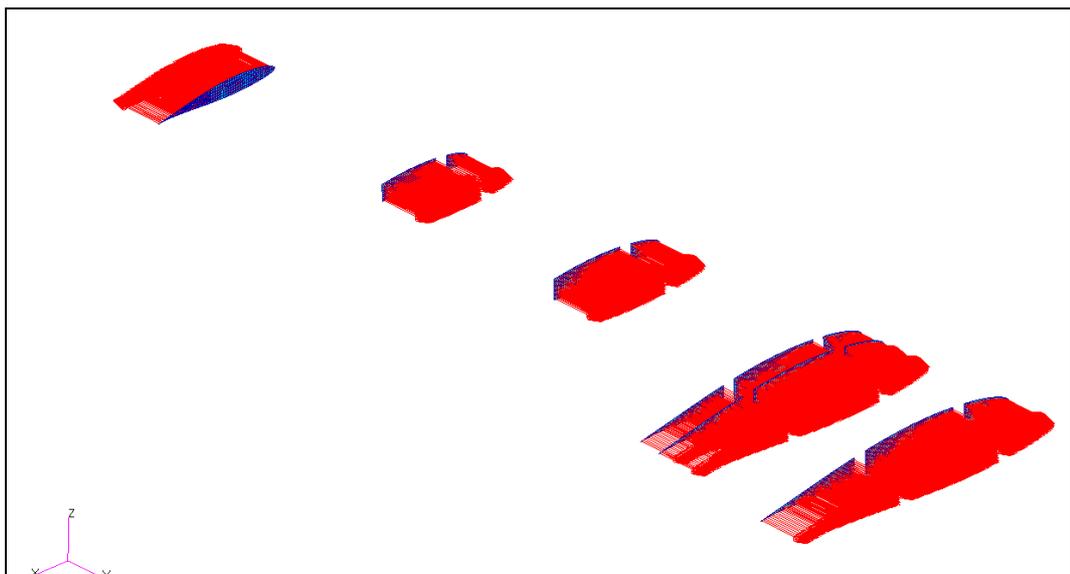
Figure 48: Surface normals of wing ribs
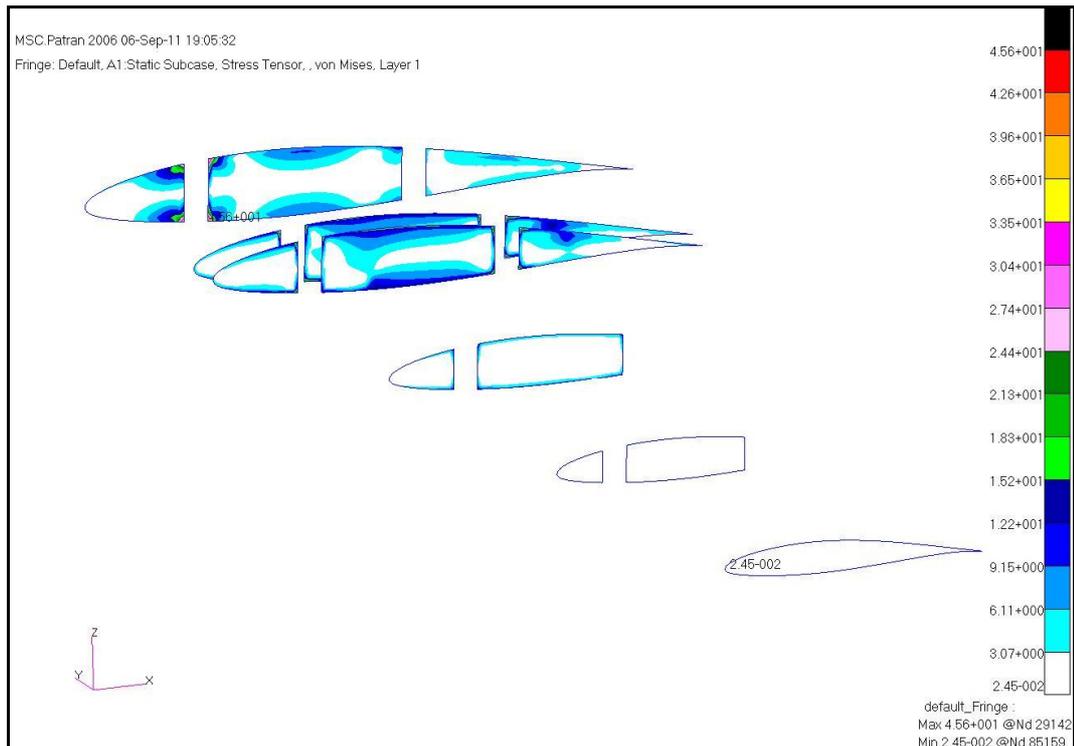
Figure 49: Equivalent stresses in the first layer of the wing ribs for dive condition

In Figure 49, equivalent stresses are plotted on all ribs in the same view to compare the stress levels on ribs. It is seen that stresses on the root rib and two ribs on the left and right side of the tail boom have higher stresses compared to the stresses on other ribs. The maximum equivalent stress occurs in the root rib. High stresses in the two ribs next to the tail boom connection in the wing, verifies that the design choice of installing two ribs near the tail boom connection has been the right choice.

Maximum failure indices and strength ratios for each layer of the ribs are tabulated in Table B1 in Appendix B. The maximum failure index value is calculated as 0.08 at the first layer of root rib at dive condition. Based on the failure index values, wing ribs can be said to be safe at dive condition.

For the minimum maneuvering speed condition, Figure 50 gives the equivalent stresses in the first layer of the ribs. For the stall condition, since the air speed is low, tail load is less compared to the dive speed condition. For this case, it is seen that the rib at the root has much higher stresses than the two ribs next to the tail boom connection. However, based on the maximum failure indices for each layer of

each rib given in Table B2 in Appendix B, the maximum failure index value is 0.006 for the stall condition. It is seen that for both flight conditions failure indices are very low, and this is an indication that even at the limit loads, ribs are not highly stressed. In addition, very stiff rib structure is also another reason for this. It should be noted that for the hornbeam layers in the sandwich rib structure, in Appendix B margins of safety are calculated based on the allowable of the hornbeam which is assumed to be isotropic material. In Appendix B, it is seen that the lowest margin of safety values for the hornbeam is at the root rib where the wing loading is the highest. From the wing root to the wing tip, margin of safety for the hornbeam layers increase. It is also noted that in the structural finite element model, the blue foam layer is included only as a thickness in the laminate definition and no material is assigned for it. Therefore, in Appendix B no margin of safety is calculated for the blue foam inside the wing ribs.
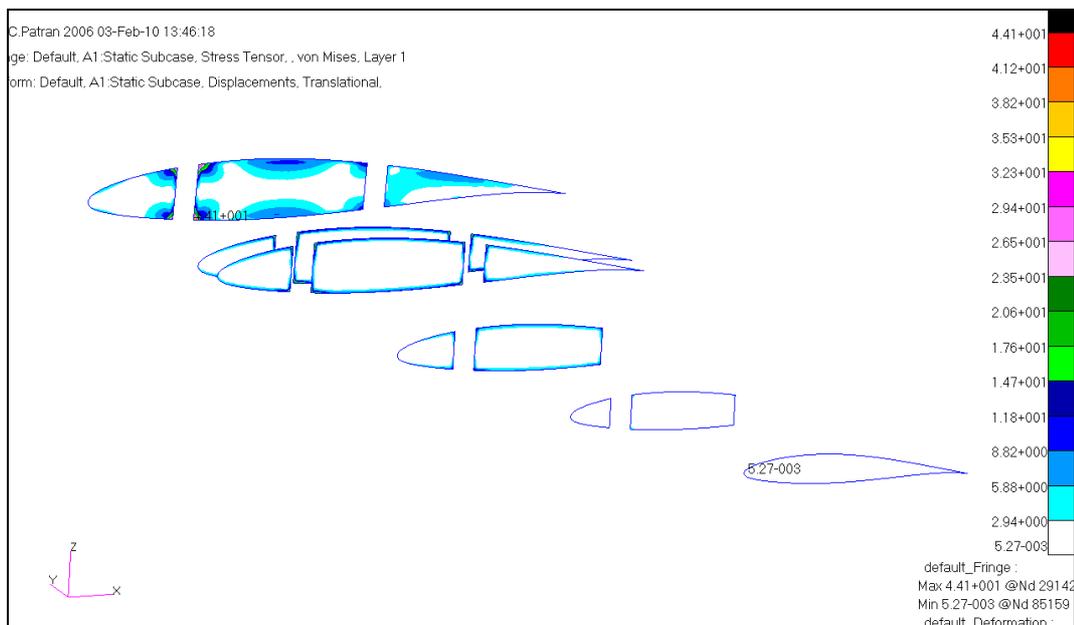
Figure 50: Equivalent stresses in the first layer of the wing ribs for stall condition

<u>Stress analysis of the spar webs</u>

Figure 51 shows equivalent stresses on the top layer of the spar webs at the dive condition. It is seen that the maximum equivalent stress in the first layer occurs in the front spar webs for the dive speed condition. Similar to the stress analysis procedure used for the wing ribs, maximum failure indices and the strength ratios in each layer of the spar webs are tabulated in Table B3 in Appendix B. The maximum failure index is determined to be 0.068 in the first layer of front spar web in the +x direction for the dive condition. Based on the failure indices, it can be concluded that spar webs are safe at the dive speed condition. As expected, the maximum stress in the front spar web is at the region where the front spar enters into the box on the main fuselage bulkhead. However, in the regions where the front spar webs enter into the box on the main fuselage bulkhead, there is no stress because in the finite element model, all nodes of the surfaces of the front spar web which are in contact with the box on the main fuselage bulkhead are constrained. In the global finite element analysis, no contact definition is made between the front spar web and the inner surface of the box on the main fuselage bulkhead. Therefore, local stresses due to contact between box on the main fuselage bulkhead and the wing root, entering into the box, are neglected. In detailed analysis, local models must be constructed to analyze the contact stresses between the front spar root and the box. At rear spar web, maximum stress occurs near the connection region of the rear spar webs and the rear spar root where the aluminium block exists. It is seen that stresses in the carbon fabric layers which are on top of the aluminum block suddenly decrease because of the stiffness of the aluminium block which reduces the stresses on spar web surfaces in contact with the aluminium block.

Figure 52 shows the equivalent stresses in the top layer of the spar webs at stall condition. Equivalent stress plot is very similar to the one for the dive speed condition. For the stall condition, maximum failure indices and strength ratios are also tabulated in Table B4 in Appendix B. Maximum failure index is determined to be 0.059 in the first layer of the front spar web in +x direction for the stall condition. Based on the failure indices, it can be concluded that spar webs are safe at the stall condition, because all failure indices are much smaller than 1.
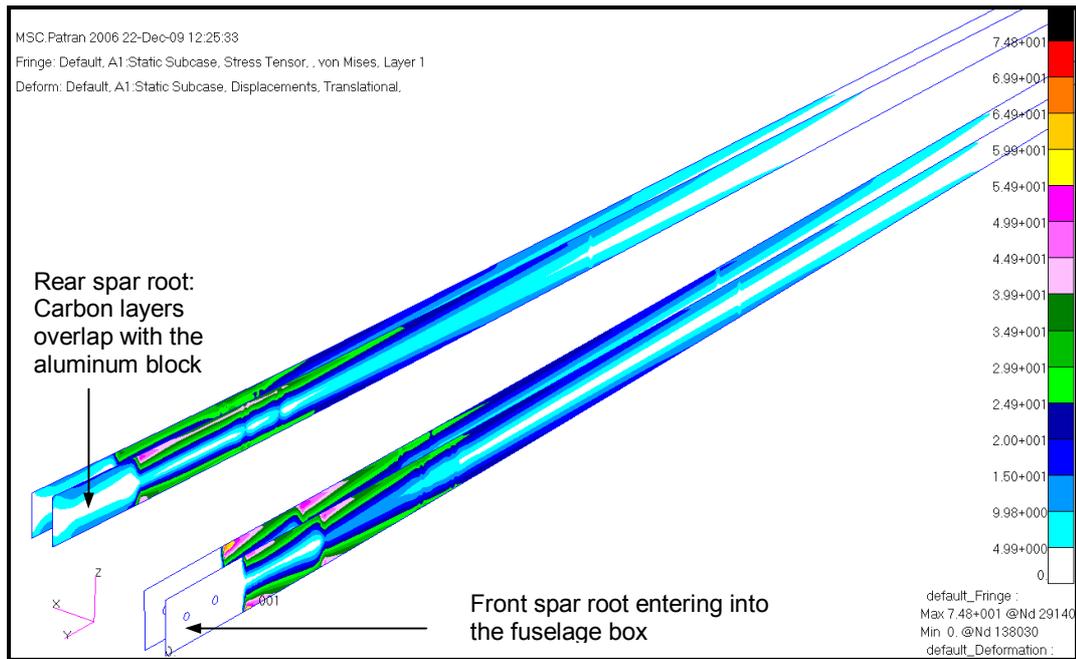
Figure 51: Equivalent stresses in the first layer of spar webs for dive condition
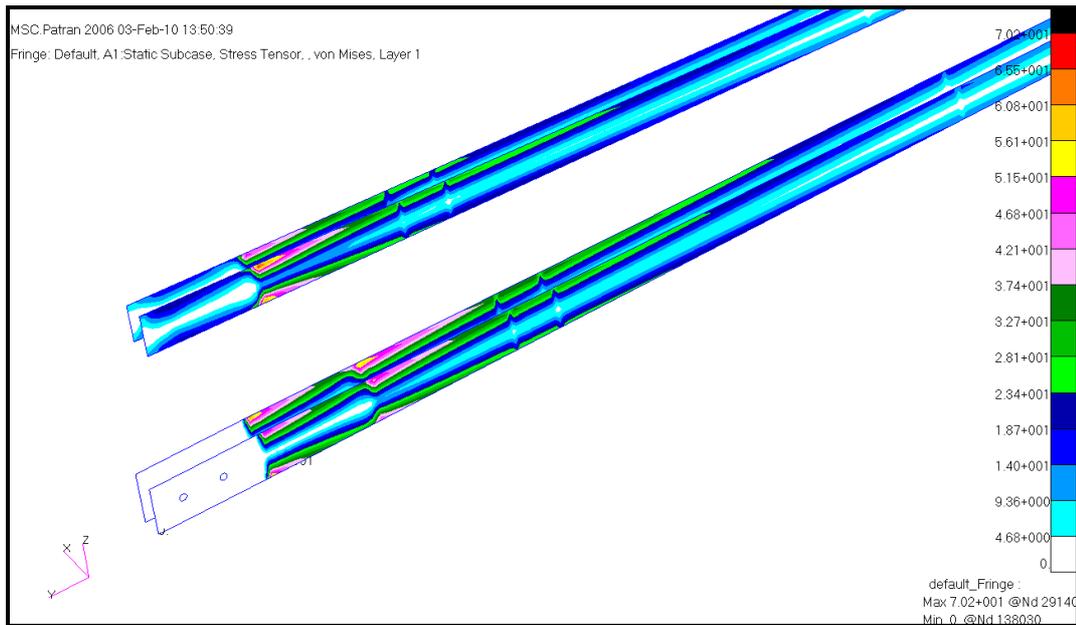
Figure 52: Equivalent stresses in the first layer of spar webs for stall condition

Stress analysis of the upper flanges of the spars

Figure 53 shows equivalent stresses in the 1th layer of the upper flanges of the spars at the dive condition. Figure 53 shows that the maximum equivalent stress occurs on the front spar flange, right before the front spar enter into the box on the main fuseage bulkhead. It is seen that in general upper flange of the front spar has higher stress than the upper flange of the rear spar.

For the upper flanges of the spars, surface normals of the upper flanges of the wing are in the outward +z direction. It is again noted that in the regions where the upper flange of the front spar enters into the box on the main fuselage bulkhead, there is no stress. Because in the finite element model, all nodes on the root of the upper flange of the front spar, which are in contact with the box on the main fuselage bulkhead, are constrained. It should be noted that root part of the upper flange of the front spar is composed of 5 layers of carbon/epoxy woven fabric composite, and since upper skin terminates at the fuselage wall, skin material is not included in the laminate definition of the upper flange of the front spar which enters into the box on the main fuselage bulkhead.
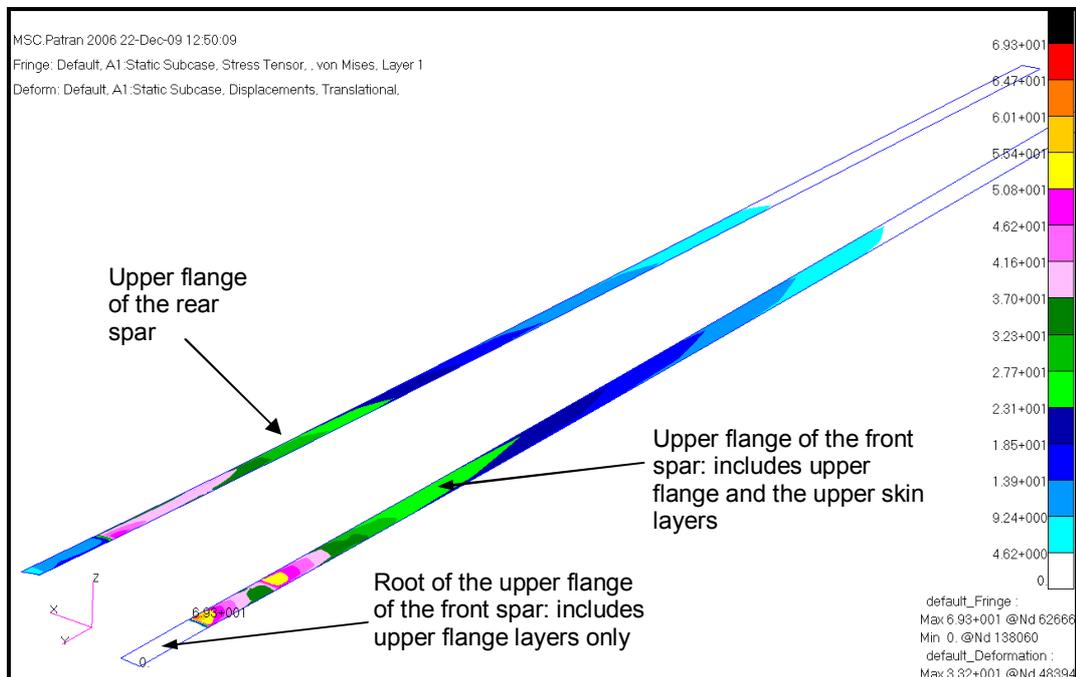
Figure 53: Equivalent stresses in the first layer of upper flanges of spars for dive condition

In the part of the upper flange of the front spar which is outside the box on the main fuselage bulkhead, upper skin material is also included in the laminate definition of the upper flanges of the spars which are composed of five layers of carbon/epoxy woven composite. During the manufacturing of the wing, upper skin of the wing is glued to the upper flanges of the spars by a strong adhesive. However, in the finite element analysis, it is assumed that upper flanges of the spars are perfectly bonded to the upper skin of the wing and the adhesive used is not considered in the laminate definition. As shown in Figure 32, the upper skin of the wing is composed of sandwich structure with a middle Rohacell foam layer and two layers of e-glass/epoxy composite above and below the Rohacell foam core. Thus, upper skin of the wing is composed of 5 layers. Since upper flanges of the spars are also composed of 5 layers, in the laminate definition of the upper flanges of the spars 10 layers are included. As long as perfect bonding is assumed, modeling the upper flanges as a laminate composed of 10 layers is considered to be a valid approach.

For the upper flanges of the spars, maximum failure indices and strength ratios in each layer are tabulated in Appendix B. It is seen that 10th layer has the highest failure index. Layers 6-10 belong to the upper skin of the wing. Failure index is not calculated for layer 8, because layer 8 is Rohacell foam which is modeled as pure epoxy, since Rohacell foam sucks too much epoxy during the vacuum bagging operation. Since pure epoxy is isotropic material, instead of failure index, margin of safety (MOS) is given for layer 8. For the carbon/epoxy layers, the fifth layer has the maximum failure index with a value of 0.044. For the e-glass/epoxy layers, the uppermost layers have the maximum failure index with a value of 0.071. As it is seen in Table B5 in Appendix B, failure indices increase from inner layers towards outer layers. This is an expected situation, since due to the bending effect, higher stresses occur in outer layers.

Figure 54 shows equivalent stresses in the 10th layer of upper flanges of the spars at the stall condition. Since the root of the upper flange of the front spar, which enters into the box on the main fuselage bulkhead, does not have the skin material in its laminate definition, the root of the front spar has a dark color and no stress is seen. For the stall condition failure indices and strength ratios are tabulated in Table B6 in

Appendix B. For the stall condition, failure indices are also very low in all composite layers.
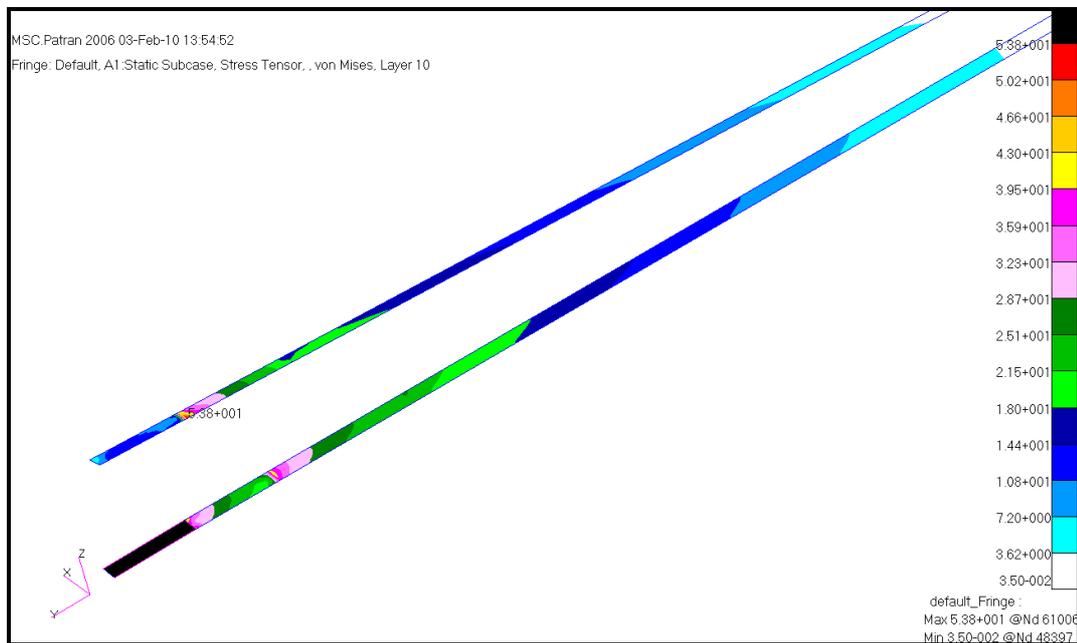
Figure 54: Equivalent stresses in the first layer of upper flanges of spars for stall condition

Finally, it should be noted that lowest margin of safety in the rohacell layer occurs in the dive condition. Rohacell layer in the upper flange of the front spar has the lowest margin of safey which is approximately 15%. It can thus be concluded that compared to the composite layers, the rohacell layer is much more critical under limit loads imposed.

Stress analysis of the upper skin of the wing

Figure 55 shows the equivalent stress plot in the first layer of the upper wing skin at the dive condition. Since all the surface normals of upper skin point in the outward +z direction, first layer of the upper skin corresponds to the innermost layer and the fifth layer is the uppermost layer. As seen in Figure 55, slices of the upper skin, which are not shown, correspond to the upper flanges of the spars whose failure indices are given under the upper flanges section. From the equivalent stress plot it can be seen that there is a concentration of the stresses along the spars which

extend in the spanwise direction along the wing. Higher stresses near spars is due to the rigidity of the spars formed by the hat shaped carbon/epoxy layers. In addition, the maximum stress occurs at the root of the front spar. It should be noted that since the wing is connected to the fuselage from the spar roots, higher stresses near spar roots are reasonable because of the stress concentration.

For the upper skin, the maximum failure indices and strength ratios are tabulated in Table B7 in Appendix B. It is again noted that upper flange regions of spars are not included in the upper wing skin surface group. For the E-glass/epoxy layers, the uppermost fifth layer has the maximum failure index with a value of 0.471. Table B7 shows that there is a gradual increase of failure indices towards the upper layers of the wing skin.
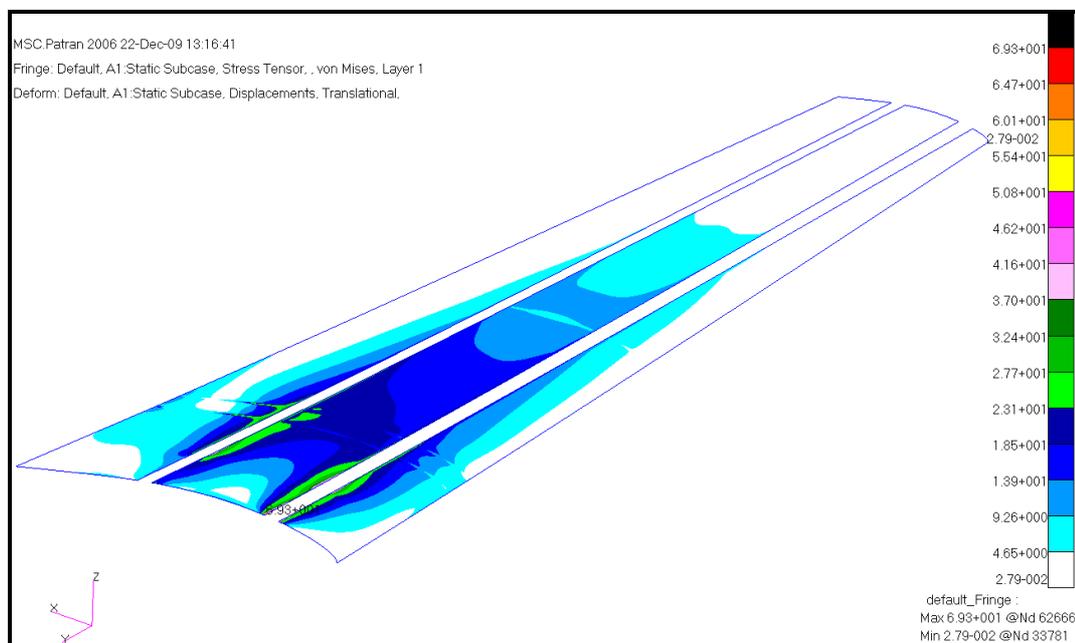
Figure 55: Equivalent stresses in the first layer of the upper skin of the wing for dive condition

Figure 56 shows the equivalent stress plot on the 5th layer of the upper skin of the wing at the stall condition. For the stall condition, maximum failure indices and strength ratios are tabulated in Table B8 in Appendix B. Maximum failure index occurs in the 5th layer and its value is 0.547.

It should be noted that for the upper wing skin, failure indices are much higher than failure indices of the upper flanges of the spars. This result is reasonable because upper flanges of the spars consist of 10 layers with 5 carbon/epoxy layers on the bottom, whereas upper skin of the wing has 5 layers with the pure epoxy layer between two layers of e-glass/epoxy on the top and bottom of the epoxy layer.
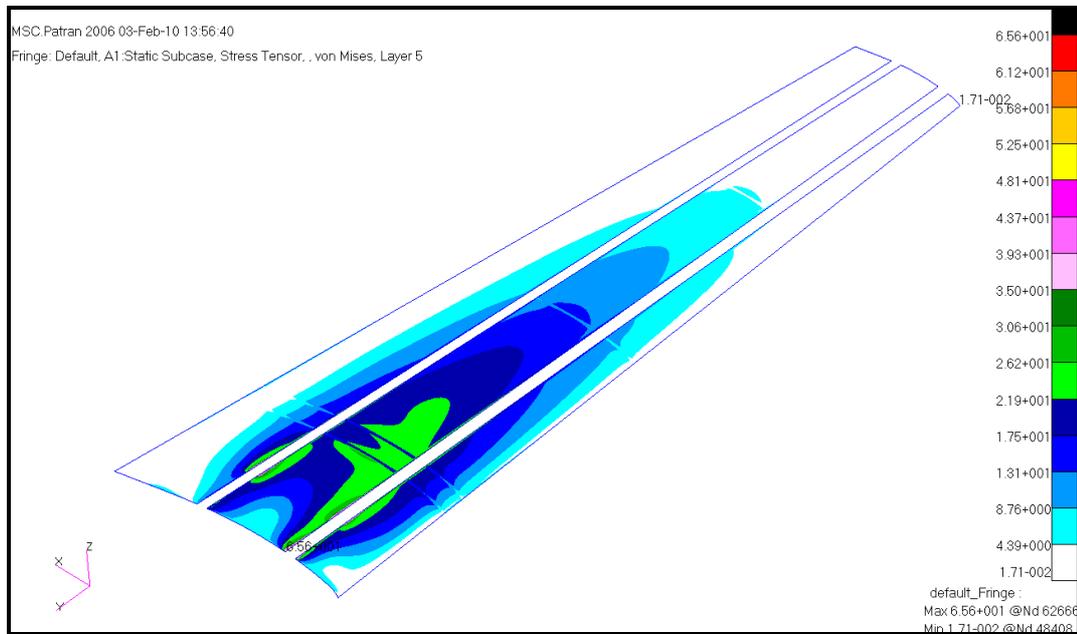
Figure 56: Equivalent stresses in the first layer of the upper skin of the wing for stall condition

Stress analyis of the lower flanges of the spars- Region 1

Region 1 of the lower flanges corresponds to the slices right under the spar mold between the two spar webs. In this region, surface normals point outwards in the –z direction. Region 1 consists of 2 layers of carbon/epoxy and wing skin layers. In this region, wing skin and two layers of carbon/epoxy are integrated to each other in a single vacuum bagging operation. Figure 57 shows the equivalent stress plot in the innermost 1th layer of the lower flange of the spars (region 1) at the dive condition. Maximum failure indices and strength ratios are tabulated in Table B9 in Appendix B.

It is seen that the for the carbon/epoxy layers, the innermost first layer of the lower flange of the rear spar has the highest failure index with a value of 0.143. For the E-glass/epoxy layers, the outermost 7th layer of the lower flange of the rear spar has the highest failure index with a value of 0.269.
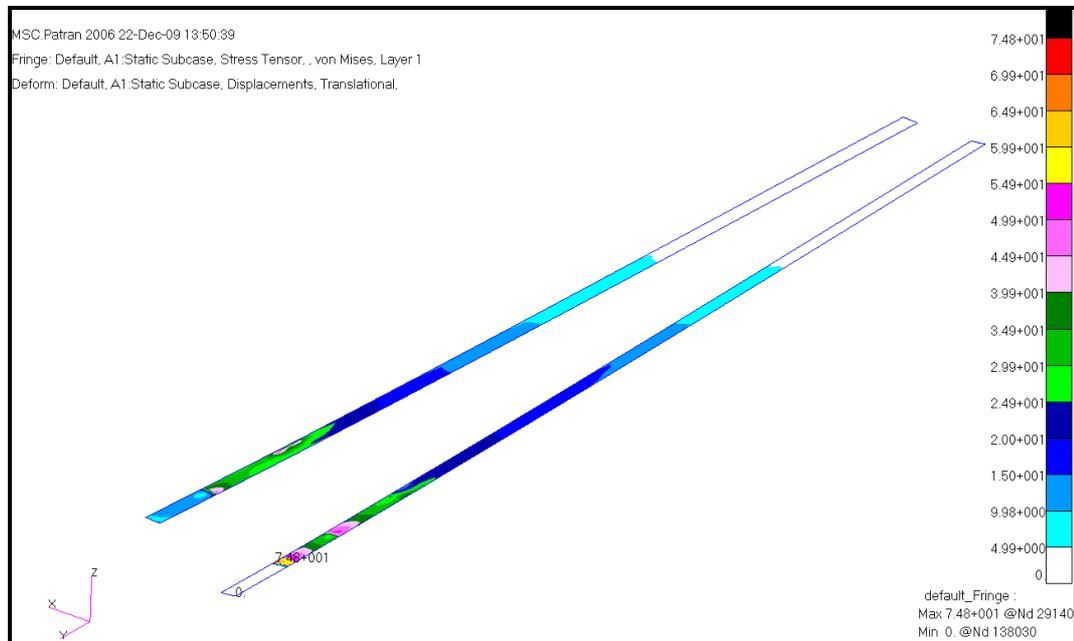
Figure 57: Equivalent stresses in the first layer of lower flanges (region 1) of spars for dive condition

Figure 58 shows the equivalent stress plot on the 7th layer of the lower flange of the rear spar (region 1) at the stall condition. For the stall condition, maximum failure indices and strength ratios are tabulated in Table B10 in Appendix B.

It is seen that the for the carbon/epoxy layers, second layer of the lower flange of the rear spar has the highest failure index with a value of 0.05. For the E-glass/epoxy layers, the outermost 7th layer of the lower flange of the rear spar has the highest failure index with a value of 0.075.

For both dive and stall conditions, margin of safeties of the pure epoxy layers are positive indicating that epoxy layers are safe at both limit load states.
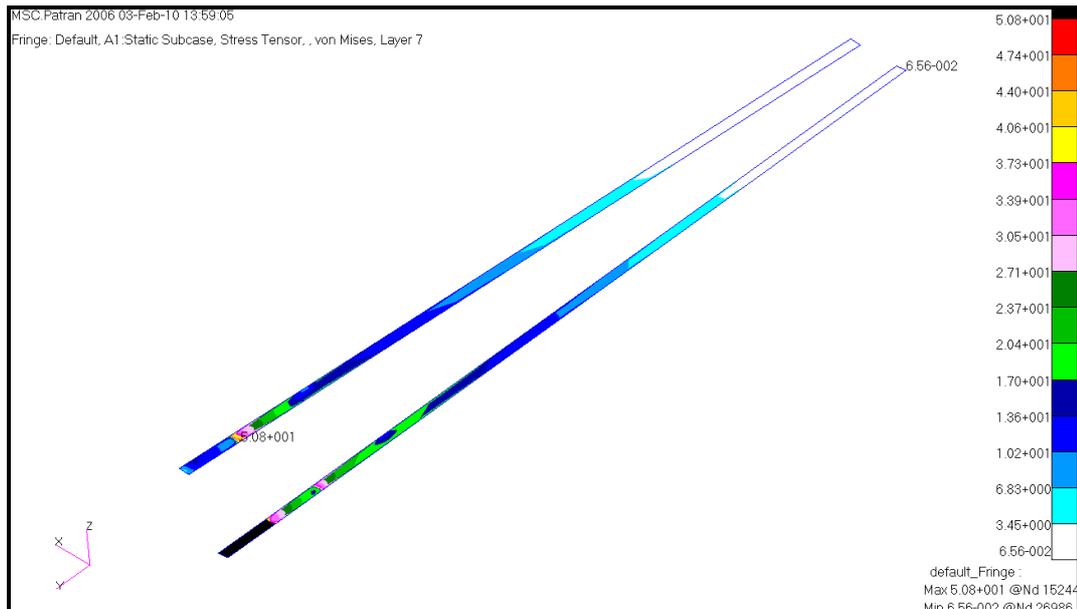
Figure 58: Equivalent stresses in the first layer of the lower flanges (region 1) of the spars for the stall condition

Stress analyis of the lower flanges of the spars- Region 2

These side flanges consist of extensions of the carbon/epoxy layers, on the lower wing skin, which are laid over the spar molds, as shown in Figure 32. Surface normals of the lower flanges of the spars (region 2) point outwards from the wing in the –z direction. The laminate definition of this region includes 7 layers of carbon/epoxy over the lower wing skin layers. Figure 32 clearly shows these layers. Lower skin is composed of 5 layers, four of which are the E-glass/epoxy fabric composite with the pure epoxy layer right in the middle. On top of the lower wing skin, 2 layers of carbon/epoxy are placed as the backing material. Finally, on top of the 2 layers of carbon/epoxy, extensions of the five layers of carbon/epoxy, which are placed over the spar molds, come.

Figure 59 shows the equivalent stress plot for the innermost 1th layer at the dive condition. For the dive condition, maximum failure indices and strength ratios are tabulated in Table B11 in Appendix B. Based on the failure indices tabulated in Table B11, 8th layer of the lower flange of the front spar has the highest failure index with a value of 0.59. It should be noted that 8th layer is the e-glass/epoxy layer of the

lower wing skin. It is also noted that all carbon/epoxy layers have lower failure indices.
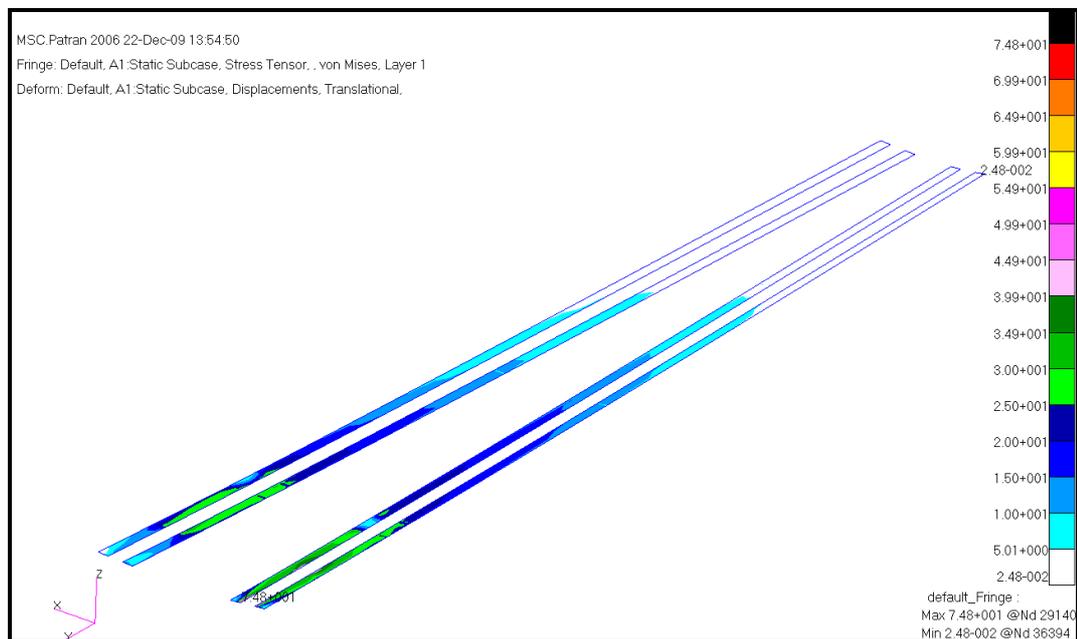
Figure 59: Equivalent stresses in the first layer of lower flanges (region 2) of spars for dive condition

For the stall condition, Figure 60 shows the equivalent stress plot for the 8th layer which has the highest failure index with a value of 0.595. For the stall condition, maximum failure indices and strength ratios are tabulated in Table B12 in Appendix B. Similar to the dive condition, failure indices of carbon/epoxy layers of the lower flanges are much lower than the failure indices of the E-glass/epoxy layers of the lower wing skin. For both dive speed and stall conditions, margins of safety of the isotropic pure epoxy layers are positive.
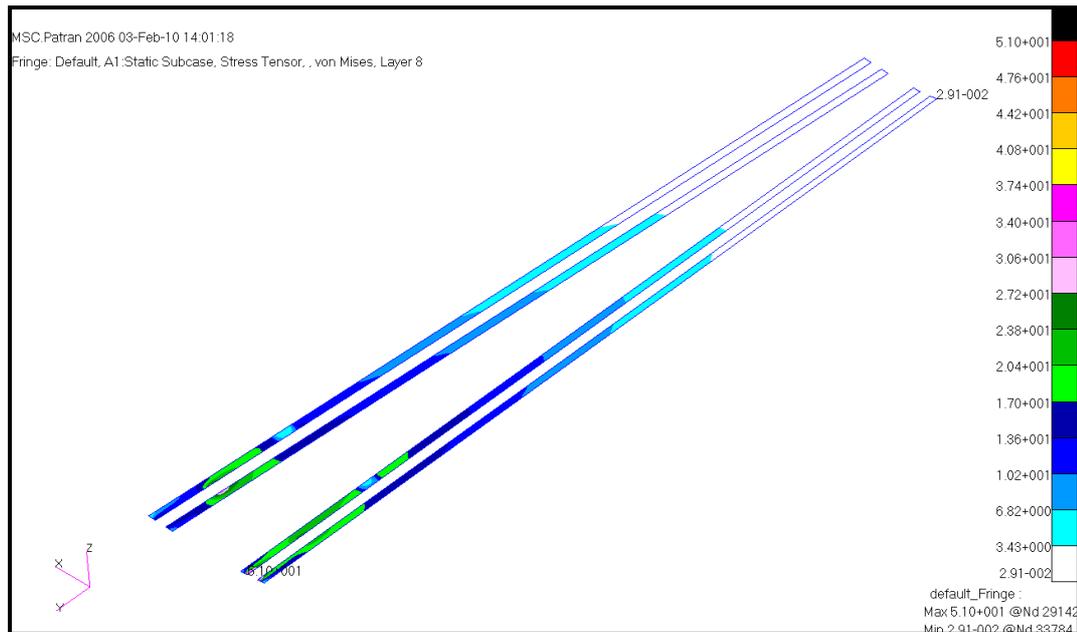
Figure 60: Equivalent stresses in the 8th layer of lower flanges (region 2) of spars for stall condition

Stress analysis of the lower wing skin

Figure 61 shows the equivalent stress plot for the fifth layer of the upper wing skin at the dive condition. Since all the surface normals of upper skin point in the outward -z direction, fifth layer of the lower skin corresponds to outer layer. As seen in Figure 61, slices of the lower skin, which are not shown, correspond to the lower flanges of the spars (regions 1 and 2) whose failure indices are given under the lower flanges sections above. From the equivalent stress plot, it can be seen that there ise concentration of the stress along the spars which extend in the spanwise direction along the wing. Higher stress near the spars is due to the rigidity of the spars formed by the hat shaped carbon/epoxy layers. In addition, maximum stress occurs near the tail boom connection hardpoints which are fixed to the lower skin of the wing.

For the lower skin maximum failure indices and strength ratios are tabulated in Table B13 in Appendix B. For the E-glass/epoxy layers, the outer layer has the maximum failure index with a value of 0.071. It should noted that for the lower skin, failure indices are much lower than the failure indices of the upper wing skin. Possible reason for the reduction of the failure indices could be due to the additional

carbon/epoxy strips which are placed over the lower skin during the manufacturing of the wing. In addition, as shown in Figure 32, side extensions of the five layers of carbon/epoxy, which are placed over the spar molds, also provide additional stiffness and strength to the lower skin. Although the additional layers are treated under the lower spar flange regions 1 and 2, these layers also provide extra stiffness to the lower skin of the wing. Table B13 also shows that there is gradual increase of failure index towards the outer layers of the lower skin of the wing.
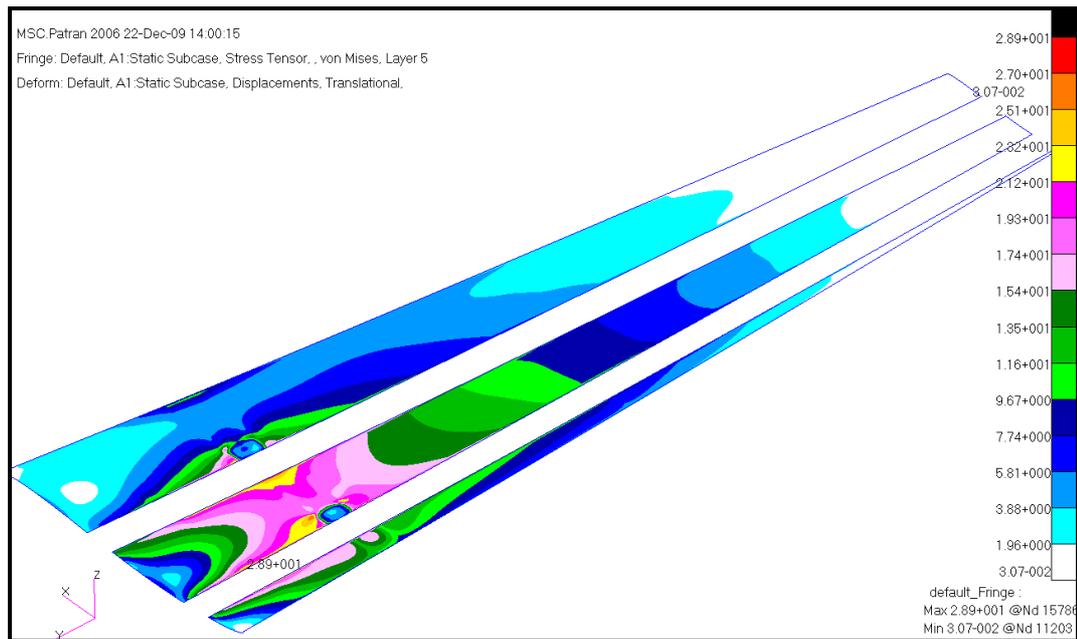
Figure 61: Equivalent stresses in the lower skin of the wing for dive condition

Figure 62 shows the equivalent stress plot for the innermost 1th layer of the lower skin of the wing at the stall condition. For the stall condition, maximum failure indices and strength ratios are tabulated in Table B14 in Appendix B. Maximum failure index occurs in the 1th layer and its value is 0.081. It is noted that for the both dive speed and stall condition, Tables B13 and B14 show that margins of safety for the pure epoxy layer is much higher than the margins of safety of the pure epoxy layer of the upper skin of the wing. The higher margin of safety is again attributed to the additional carbon/epoxy layers of the lower flange of the spars (regions 1 and 2) which provide additional stiffness and strength to the neighboring lower skin of the wing.
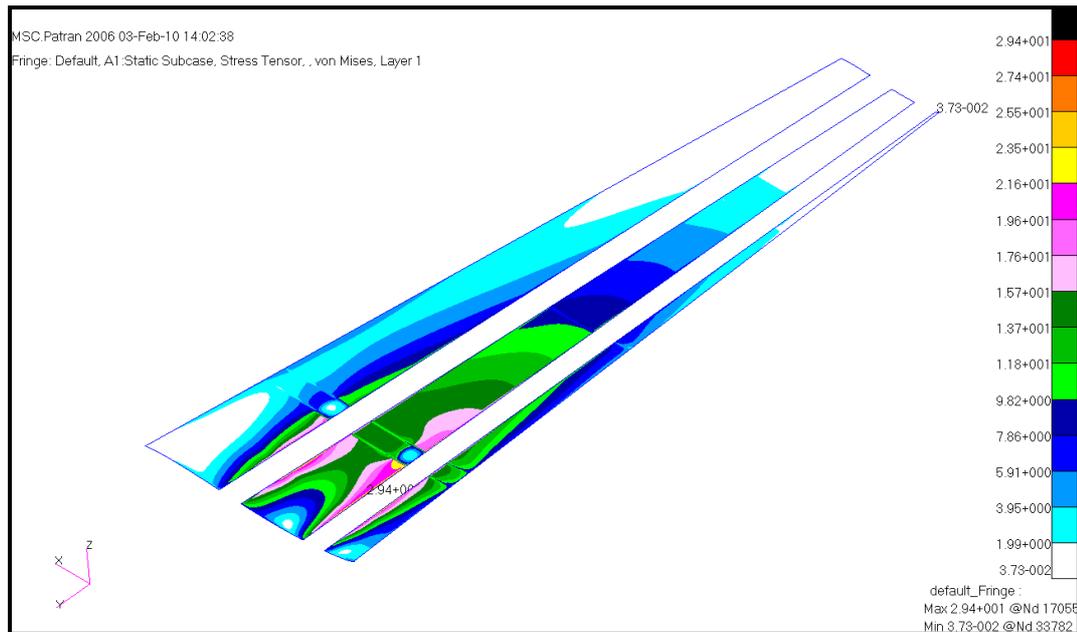
Figure 62: Equivalent stresses in the lower skin of the wing for stall condition

<u>Stress analysis of the hornbeam root of the front spar</u>

Front spar root block is made up of hornbeam. Figure 63 and Figure 64 show the Von-Mises stress plots for the hornbeam root of the front spar at the dive and stall conditions. It is noted that there is nearly no stress on the surfaces of front spar root block entering into the box on the main bulhead of the fuselage, because all nodes on the surfaces of the root are fixed in the finite element model. It is also noted that at the corner where the spar enters into the fuselage, maximum stress occurs for both stall and dive speed conditions. Such a stress concentration is inevitable because although structure is continuous, boundary conditions change right at the enterance of the spar root into the fuselage box. Table 13 shows the margins of safety for the front spar root at the dive and stall conditions. It is seen that hornbeam front spar root has positive margin of safety which indicates that front spar root block is safe, at least from a global finite element analyis point of view.
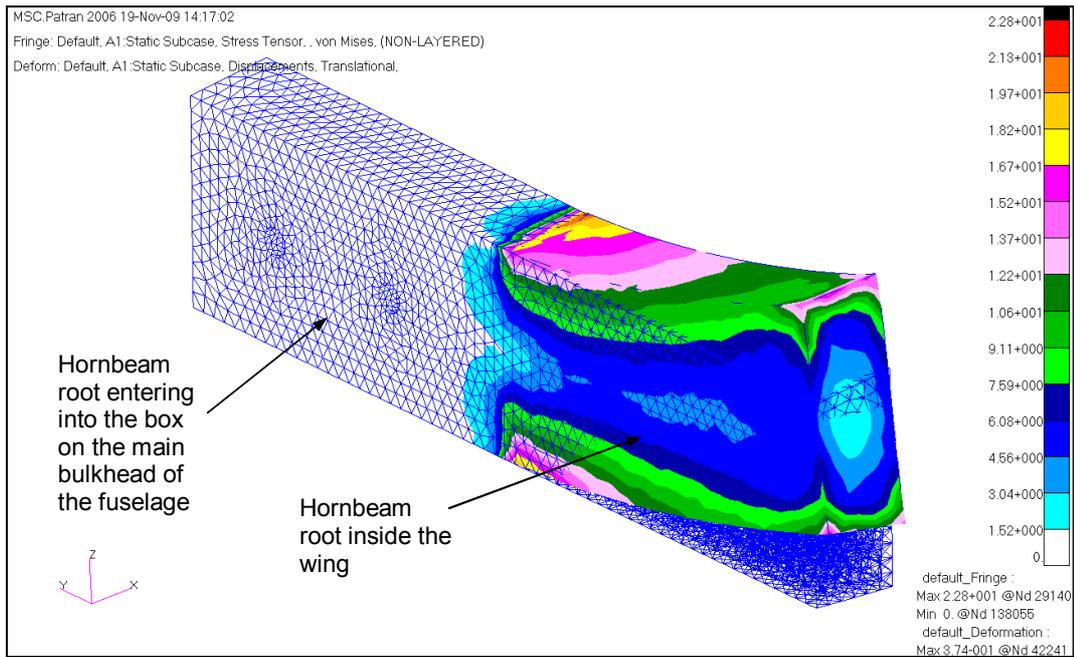
Figure 63: Von-Mises stresses in the front spar root for dive condition
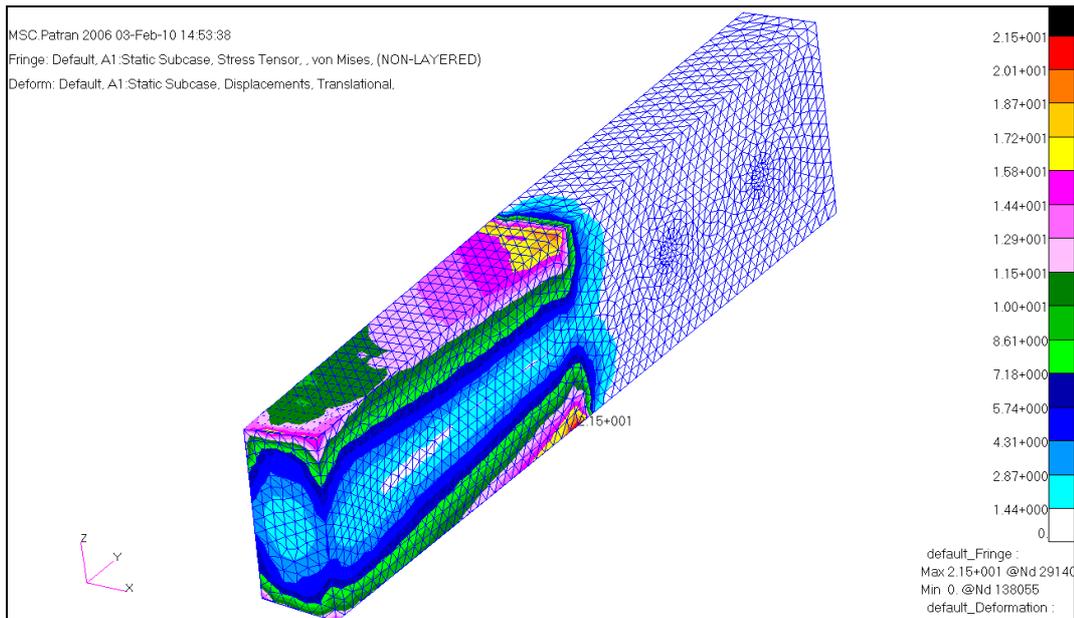
Figure 64: Von-Mises stresses in the front spar root for stall condition

Table 13: Margins of safety for the hornbeam block of the front spar root

	Margin of Safety
3.8g Dive	212%
3.8g Stall	227%

Stress analysis of the aluminum root of the rear spar

Rear spar root block is made up of aluminium. Figure 65 and Figure 66 show the Von-Mises stress plots for the aluminum root of the rear spar at the dive and stall conditions. As it is seen, sudden change of stiffness results in stress concentrations at the edges of the aluminum block where the block ends. Stress concentration occurs at the leading edge corner points of the aluminum block for both dive and stall conditions. However, the peak stress is about 70 MPa which is much less than the stress allowable for the aluminum material used which is tabulated in Table 10.
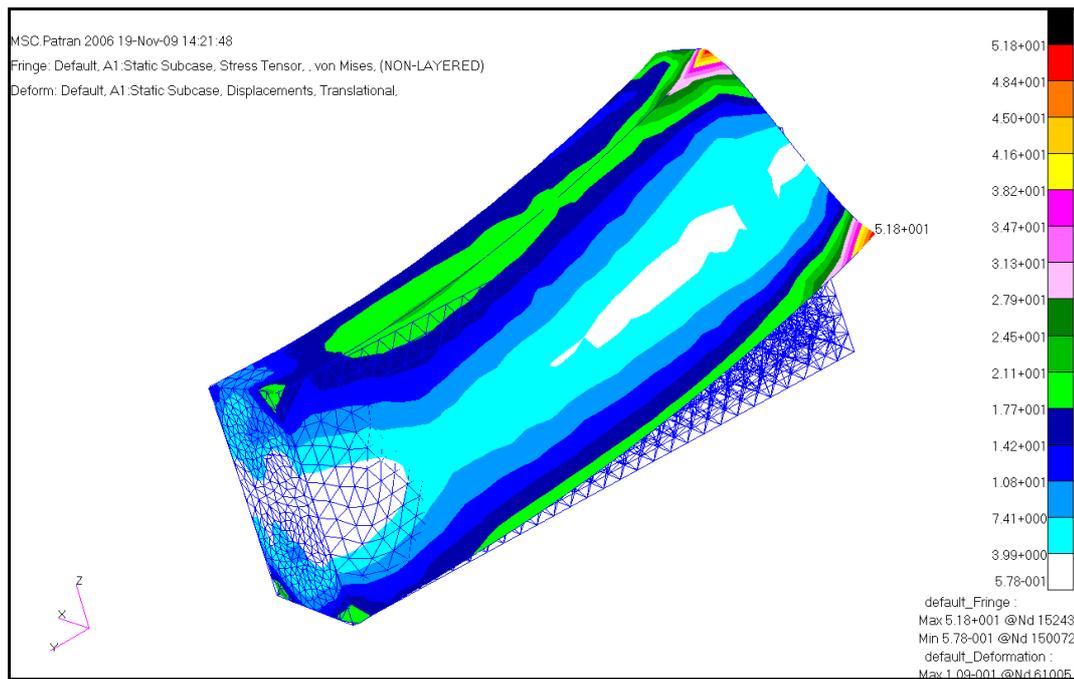
Figure 65: Von-Mises stresses in the rear spar root for dive condition
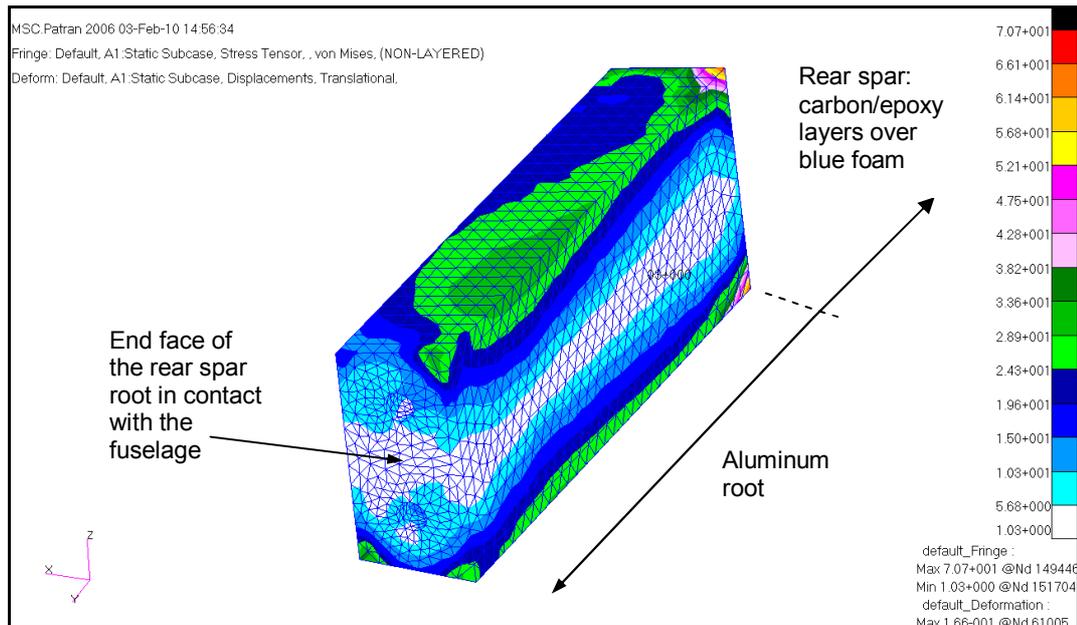
Figure 66: Von-Mises stresses in the rear spar root for stall condition

Margins of safety of the rear spar aluminum block are tabulated in Table 14. Margins of safety for the aluminum rear spar block are much higher than the margins of safety for the hornbeam root of the front spar. There are mainly two reasons for the higher margins of safety for the aluminum root of the rear spar. Firstly, the rear spar root is made of aluminum which is stronger and stiffer than the hornbeam root of the front spar. Secondly, front spar takes up higher share of the load compared to the rear spar.

Table 14: Margins of safety for aluminum rear spar root block

	Margin of Safety
3.8g Dive	1030%
3.8g Stall	761%

Stress analysis of the hardpoints of the tail booms on the wing

As it was explained before, tail boom hardpoints on the wing is composed of a steel block sandwiched between two layers of hornbeam wood. In Figure 33 hardpoints are clearly seen between the two closely spaced ribs. Figure 67 shows the Von-Mises stresses on the steel part of the hardpoint for both dive and stall conditions.

Loads are transferred to the hardpoints from the M8 bolts shown in Fig. 30, and also from the spars and the ribs with which the hardpoints have common nodes. It is seen that for the dive condition the steel block has a %240 margin of safety, whereas for the stall condition the margin of safety is about %1050. It is noted that for the dive speed condition, airspeed is much higher than the minimum maneuvering speed, therefore the tail load is higher in case of dive speed condition. In addition, for the stall condition, fuselage also blocks and disturbs the air flow passing over the horizontal tail reducing the tail load further. Lower tail load results in lower stress in the steel harpoint and therefore margin of safety is much higher for the stall condition. It should be noted that in the thesis detailed local finite element analysis is not conducted but global stress analysis is performed to make initial strength check of the critical parts.
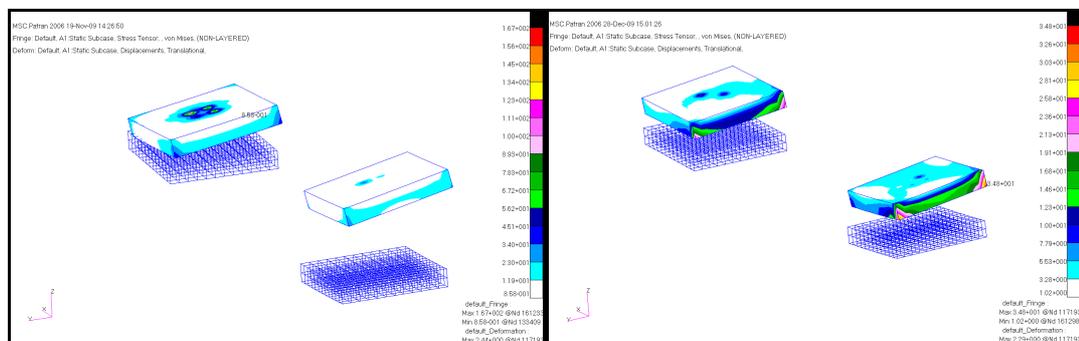
(a) dive condition   (b) stall condition

Figure 67: Von-Mises stresses in the steel part of the tail boom hardpoints on the wing

The hornbeam blocks which placed above and below the steel block have a maximum Von-Mises stress of about 35 MPa which is lower than the ultimate strength of the hornbeam which is about 48 MPa. It should be noted that during the manufacturing of the hardpoint, the steel block and the hornbeam blocks are bonded to each other by the mixture of strong adhesive and wood dust which also improves the strength of the hornbeam which is not considered in the strength value of 48 MPa. Based on the preliminary results, it can be concluded that the steel and hornbeam parts of the hardpoint are not overstressed in the extreme dive speed and stall conditions which are not expected to occur during the normal operations of the airplane.

3.6. Structural analyses of horizontal and vertical tail

3.6.1. Structural analyses of horizontal tail at 3.8g dive and stall conditions

FEM model of the horizontal tail and the surface normals are shown in Figure 68. As shown in Figure 68, surface normals of the upper skin are in the +z direction and the surface normals of lower skin are in the –z direction. As it was mentioned before, finite element analysis of the half wing-tail plane combination is performed and symmetry boundary conditions are applied at the centerline of the horizontal tail.
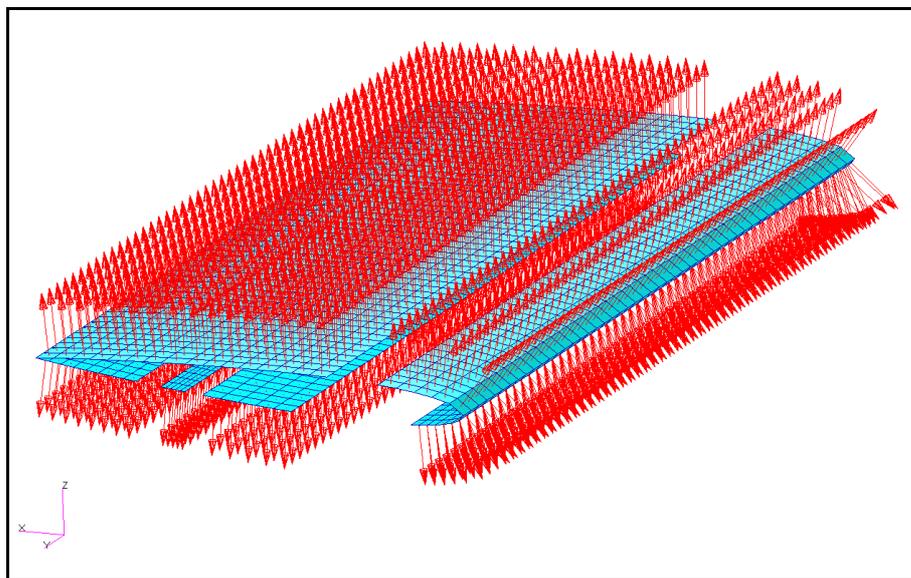
Figure 68: Surface normals of horizontal tail skin

Stress analysis of the upper skin of the horizontal tail:
For the upper skin of the horizontal tail, maximum failure indices and strength ratios are tabulated in Tables B15 and B16 in Appendix B, for the dive and stall conditions, respectively. For the dive speed condition, the inner layer of the upper skin (1st layer) has the highest failure index with a value of 0.019.

Equivalent stress plot for the 1st layer of upper skin of the horizontal tail at the dive condition is shown in Figure 69. As expected, maximum equivalent stresses occur at the symmetry plane, because horizontal tail is supported by vertical tail at the ends and maximum bending moment occurs at the symmetry plane. It should be noted

that the skin material overlapping with the upper flange of the front spar of the horizontal tail are not shown in the stress plot of the tail skins.
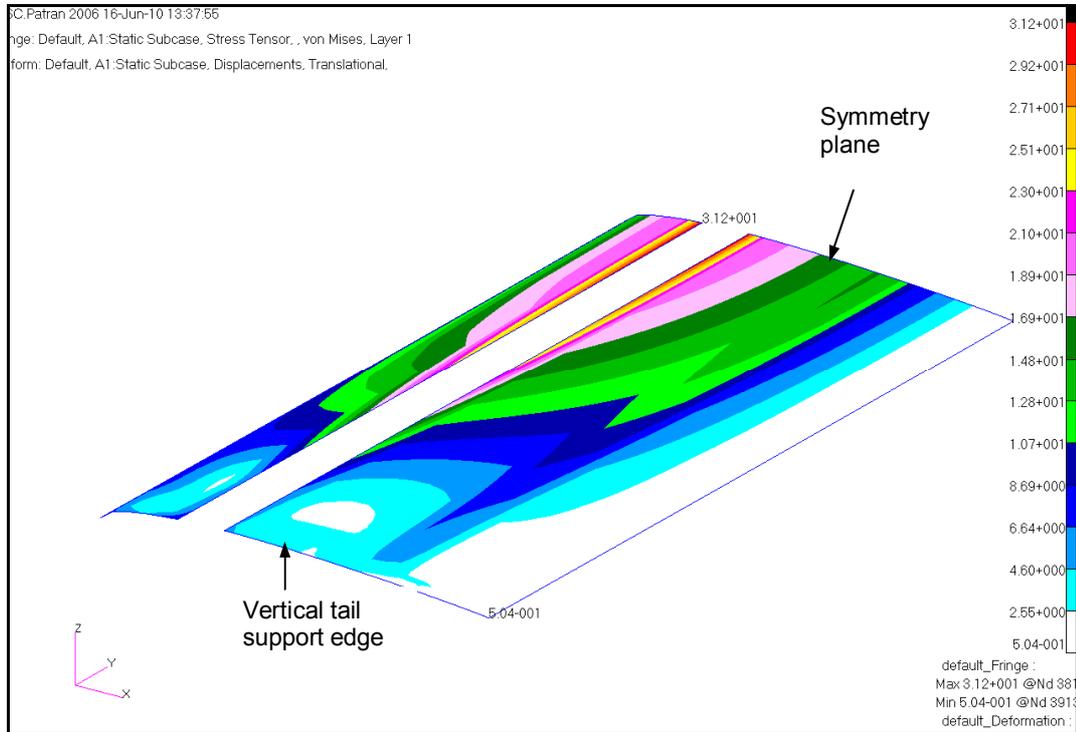
Figure 69: Equivalent stresses in the first layer of upper skin of the horizontal tail for dive condition

Equivalent stress plot for the outer (3rd) layer of the upper skin of the horizontal tail at the stall condition is shown in Figure 70. For the stall condition, maximum equivalent stresses occur at horizontal tail - vertical tail connection region. For the stall condition, the horizontal tail does not receive a clan inflow because of the separation and the fuselage blockage. Therefore, a clear bending of the horizontal tail, like the dive speed condition, does not occur for the stall condition. It is also clear from the stress values shown in Figure 69 and Figure 70 that the peak stress for the stall condition is nearly 10 times less than the peak stress for the dive speed condition. For the stall condition, the outer layer of the upper skin (3rd layer) has the highest failure index with a value of 0.00022. It is seen that for the stall condition, maximum failure index is approximately 100 times less than maximum failure index for the dive speed condition. It is noted that the ratios of the maximum failure indices and the maximum equivalent stresses are in accordance. Since failure index is

proportional to the square of the stress, 10 times higher stress corresponds to 100 times higher failure index.

Figure 69 and Figure 70 also show that there is concentration stress around the spar of the horizontal tail. The stiffer spar attracts the load paths resulting in higher stresses around on the tail skin around the the spar.
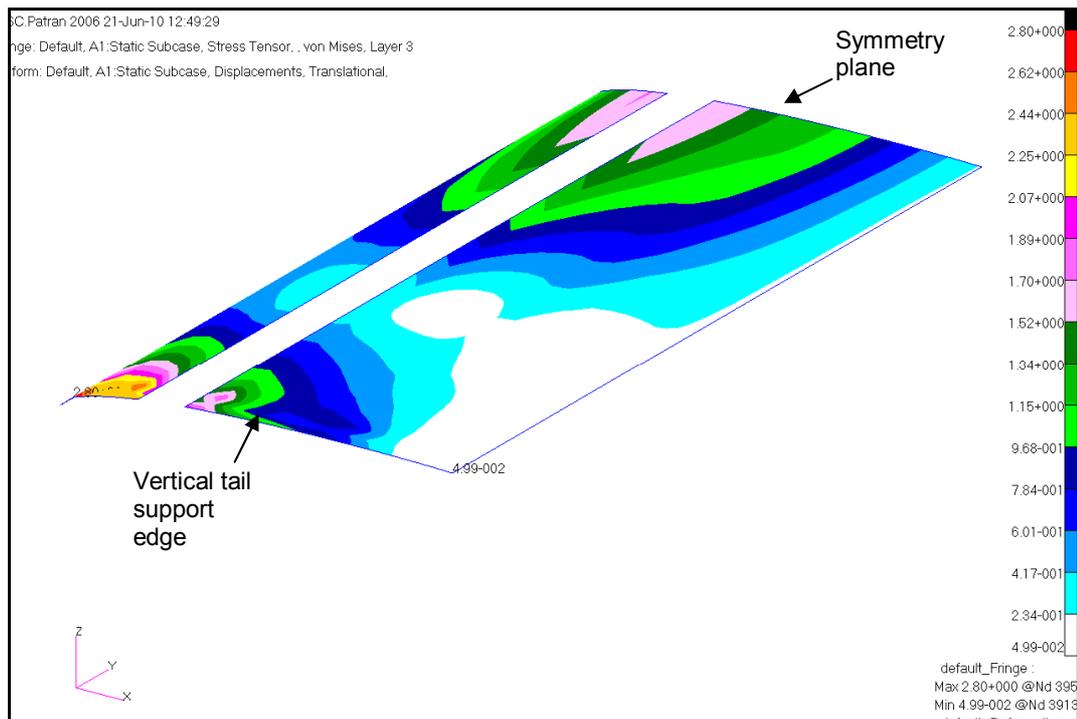
Figure 70: Equivalent stresses in the third layer of upper skin of the horizontal tail for stall condition

<u>Stress analysis of the lower skin of the horizontal tail:</u>

For the lower skin of the horizontal tail, maximum failure indices and strength ratios are tabulated in Tables B17 and B18 in Appendix B, for the dive and stall conditions, respectively. For the dive condition, the inner layer of the upper skin (1st layer) has the highest failure index with a value of 0.024. Equivalent stress plot for the 1st layer of the upper skin of the horizontal tail at the dive condition is shown in Figure 71. For the lower skin, the carbon/epoxy strips and the side extensions of the carbon/epoxy layer placed over the front spar mold are not shown in the stress plot of the lower

skin. In addition, strips of the lower skin overlapping with the side flanges of the rear spar are also not shown in the stress plot of the lower skin. Again for the dive speed condition, maximum equivalent stresses occur at the symmetry plane.

Equivalent stress plot for the inner (1st) layer of the lower skin of the horizontal tail at the stall condition is shown in Figure 72. For the stall condition, maximum equivalent stresses also occur at horizontal tail - vertical tail connection region. For the stall condition, the inner layer of the lower skin (1st layer) has the highest failure index with a value of 0.000318. For the lower skin, maximum equivalent stress ratio and the maximum failure index ratio follow the same trend as the upper skin. It should be noted that in general higher stress and failure index is observed in the inner layer of the skins not in the outer layer of the skins. The reason for this could be due to the bonding of spars through the spar flanges directly on the inner layer of the skin. The stiffer spar flanges attract the load path, so stress is more concentrated near the spar flanges. Thus, the inner layer of the skin which has direct contact with the spar flanges may be more stressed than the outer layers because of the direct contact of the inner skin layers with the spar flanges.
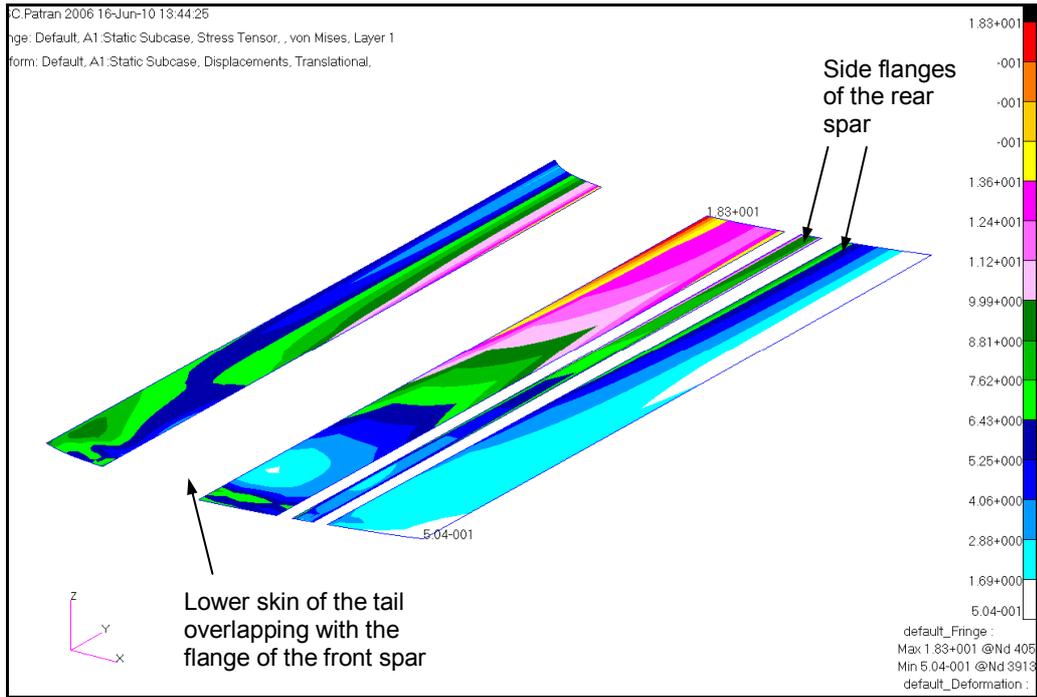
Figure 71: Equivalent stresses in the first layer of lower skin of the horizontal tail for dive condition
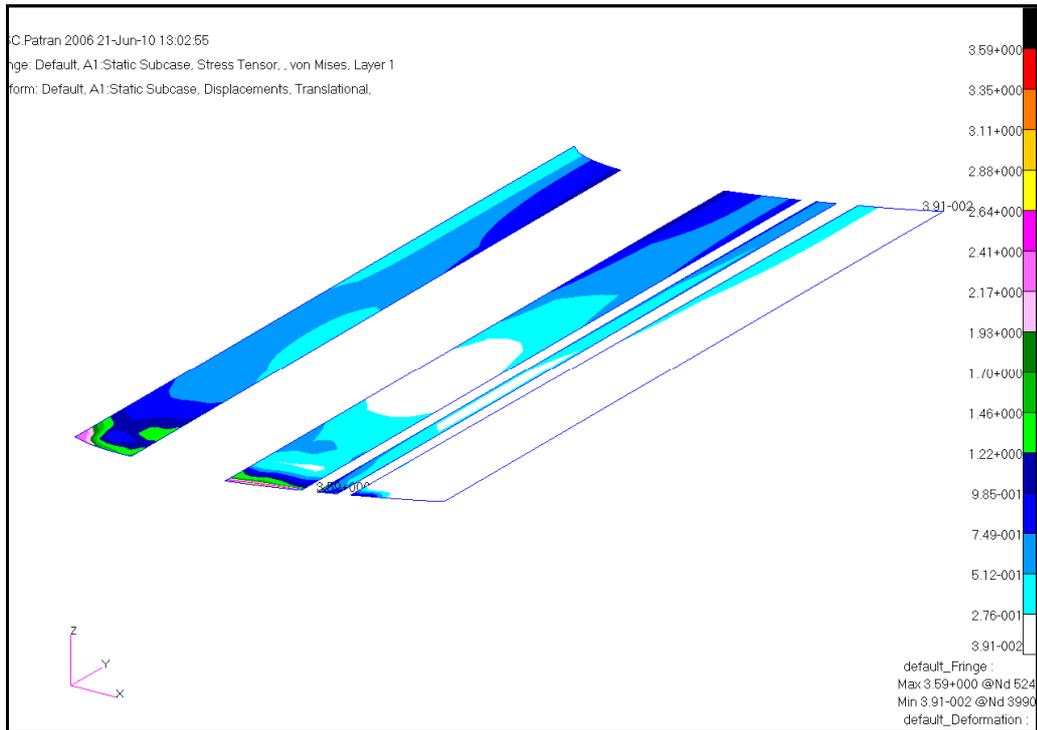
Figure 72: Equivalent stresses in the first layer of lower skin of the horizontal tail for stall condition

Stress analysis of the spar webs of the horizontal tail:

Front spar web of the horizontal tail consists of 2 layers of 0.3 mm thick carbon/epoxy fabric composite and rear spar web consists of 2 layers of 0.1mm thick carbon/epoxy fabric composite. FEM model of the horizontal tail webs and surface normal are shown below in Figure 73.
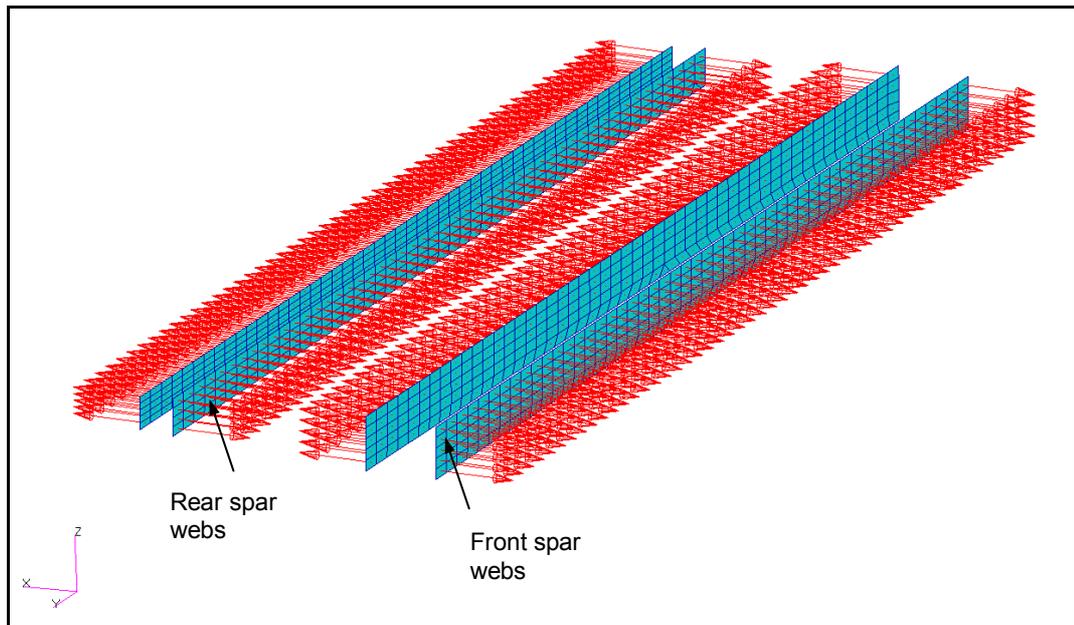
Figure 73: Surface normals of horizontal tail webs

Equivalent stresses on the 1st layer of spar webs at the dive and stall conditions are shown in Figure 74 and Figure 75, respectively. Similar to the situation for the maximum equivalent stress of the upper and lower skins of the horizontal tail, for the spar webs of the horizontal tail, maximum equivalent stresses occur at the symmetry plane for the dive speed condition and at vertical tail connection region for the stall condition. Maximum failure indices and the strength ratios are tabulated in Tables B19 and B20 in Appendix B. For the dive speed condition, maximum failure index is 0.01856, and for the stall condition maximum failure index is 0.0021. Ratio of the maximum failure indices is again in accordance with the ratio of the maximum equivalent stresses for the dive speed and the stall conditions. It is also noticed that front spar web has higher failure index than the rear spar web.
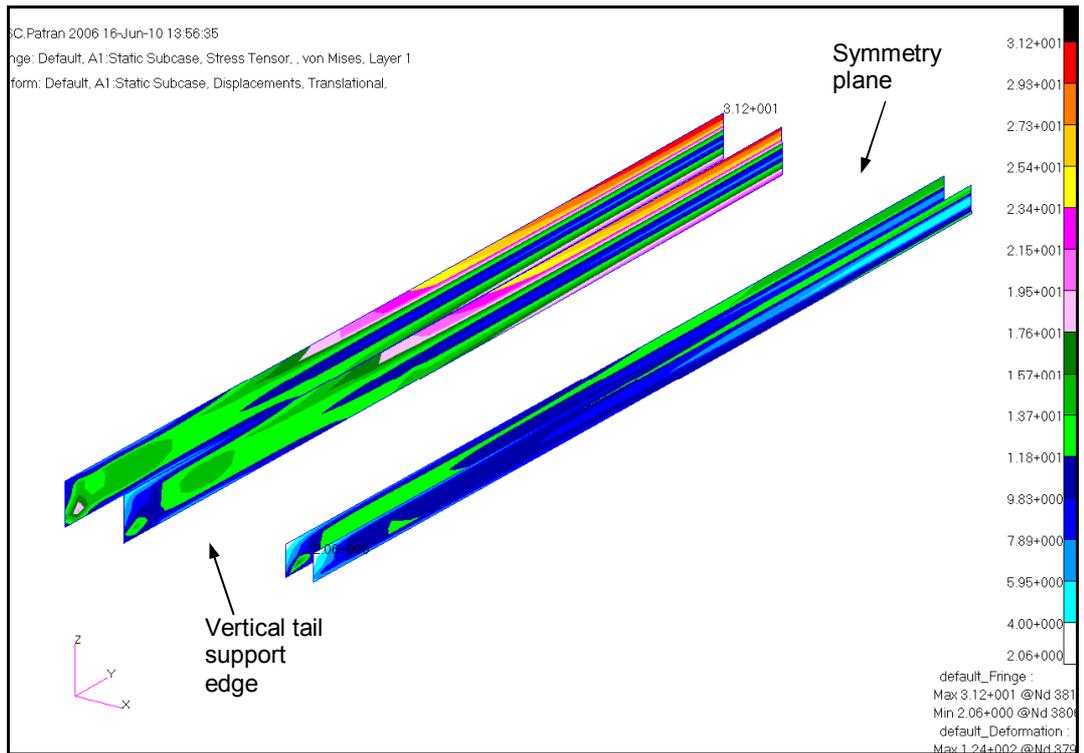
Figure 74: Equivalent stress plot for the spar webs of the horizontal tail for dive condition
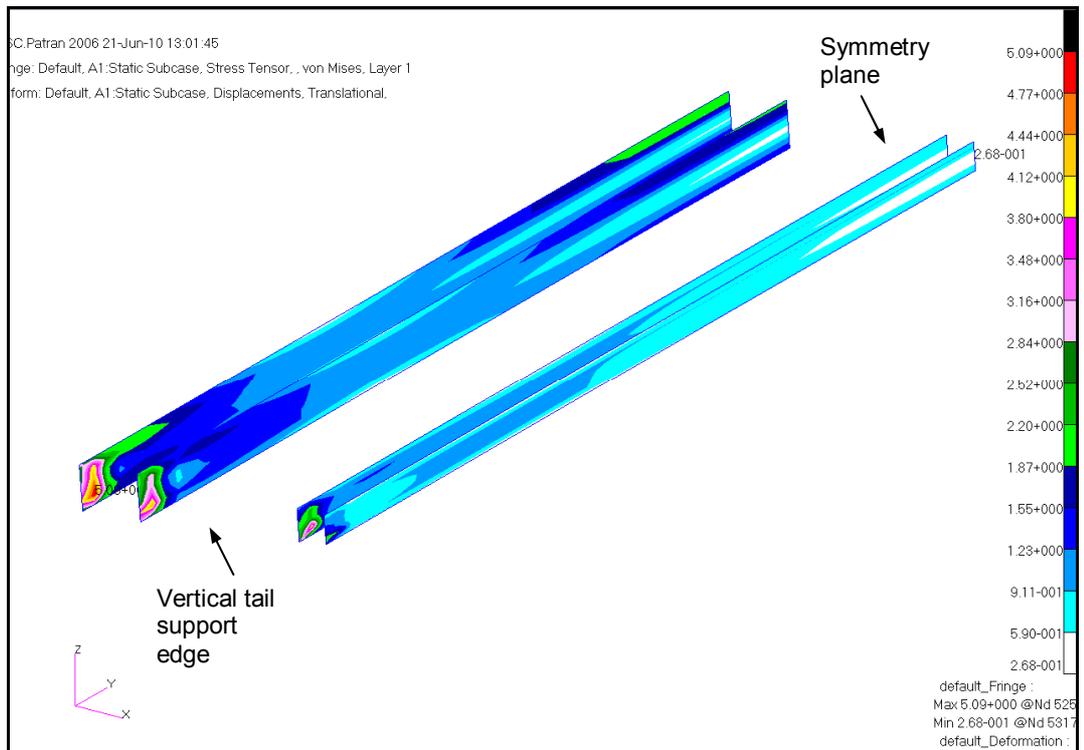
Figure 75: Equivalent stress plot in spar webs of the horizontal tail for stall condition

It should be noted that edges of the front spar webs near the upper skin of the horizontal tail has higher stress than the edges of the spar webs along the lower skin. The main reason for the lower stress on the edges of the spar webs near the lower skin is due to stronger lower skin to which spar webs have direct contact through side extensions. It should be reminded that two strips of additional carbon/epoxy fabric composite are laid over the lower skin along the front spar line during the manufacturing. These strips account for the hihger stiffness of the lower skin which in turn reduces the stresses along the edges of the front spar web near the lower skin of the horizontal tail.

Stress analysis of the upper flange of the front spar of the horizontal tail:

As Figure 40 shows upper flange of the horizontal tail is composed of two layers of carbon/epoxy fabric composite. However, in the stress analysis the upper skin material is also included in the laminate definition of the upper flange of the front spar. Thus, upper flange consists of 5 layers. First 2 layers are carbon/epoxy layers placed over the foam mold of the spar, and the remaining layers belong to the upper skin which is a sandwich structure composed of E-glass/epoxy composite fabric and Rohacell foam. Figure 76 and Figure 77 show the equivalent stress plots for the upper flange of the front spar for the dive speed and stall conditions, respectively. Surface normals of the upper flange are in the +z direction shown in Figure 76 and Figure 77.

For the dive speed condition, maximum equivalent stresses occur at the symmetry plane, as expected. Maximum failure indices and the strength ratios are tabulated in Tables B21 and B22 in Appendix B. For the dive speed condition, maximum failure index is 0.009 for the carbon/epoxy layers and 0.00938 for the E-glass/epoxy layers. For the stall condition, similar to the situation for the tail skin and the spar webs, maximum equivalent stresses occur at vertical tail connection region. For the stall condition, maximum failure index is 0.00004 for the carbon/epoxy layers and 0.00016 for the E-glass/epoxy layers.

It should be noted that critical points determined by the two different limit loads calculated at the corner points of the V-N diagram are different. The results presented in the thesis point that accurate load analysis within the flight envelope of

the airplane is very crucial to identify the different critical points which are not always obvious.
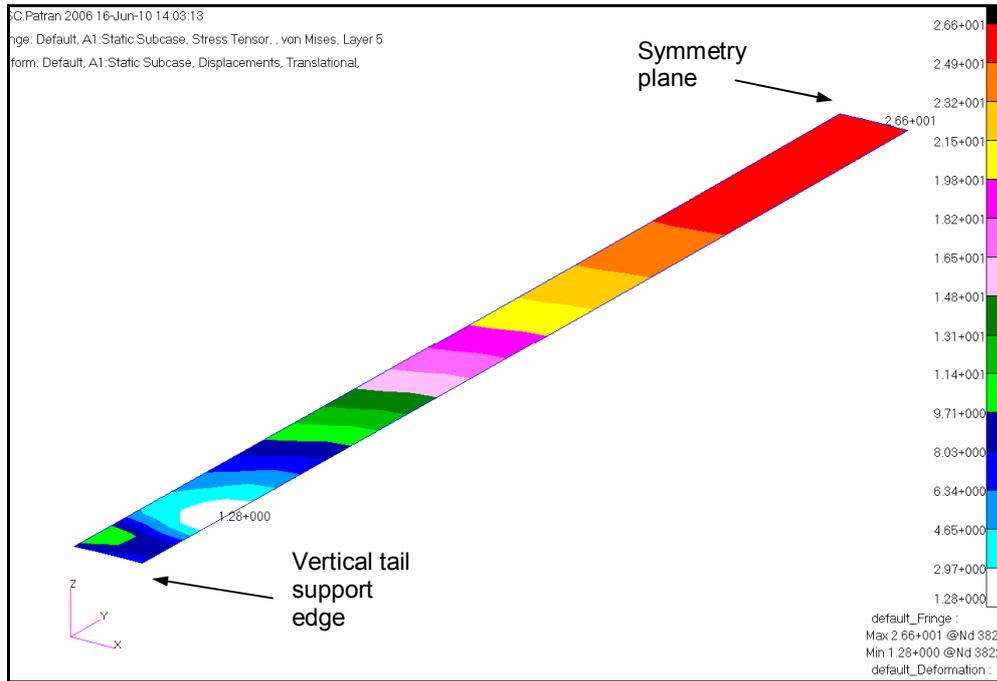
Figure 76: Equivalent stress plot in the upper flange of the front spar of the horizontal tail for dive condition
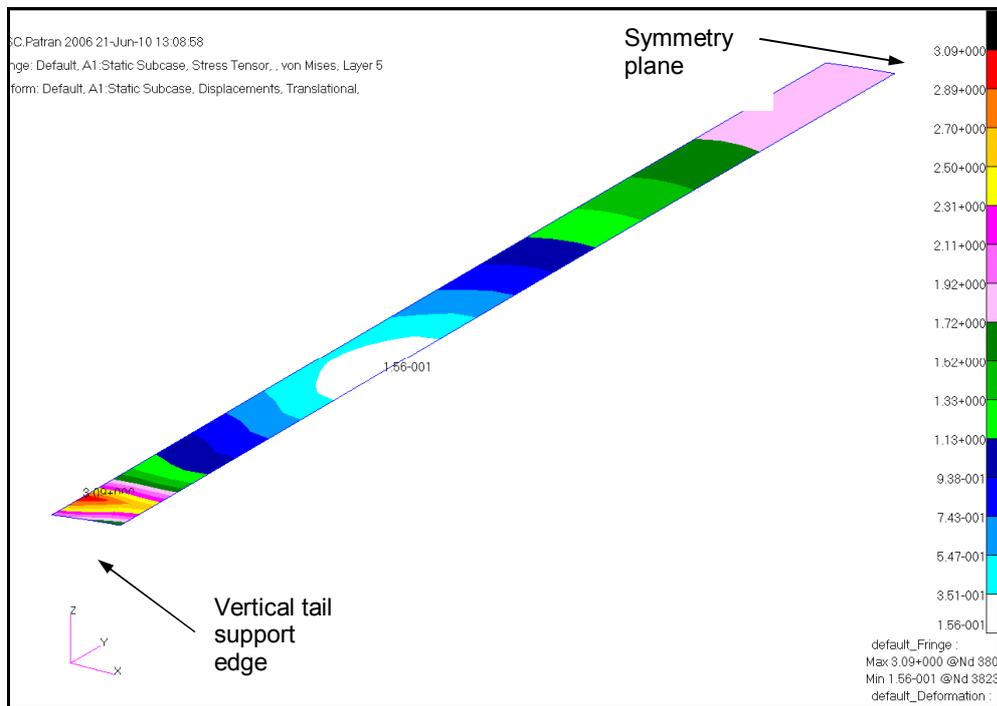
Figure 77: Equivalent stress plot in the upper flange of the front spar of the horizontal tail for stall condition

Stress analysis of the lower flange (flange 1) of the front spar of the horizontal tail:

As Figure 40 shows, lower flange 1 of the front spar is the region under the side extensions of the carbon/epoxy fabric composite layers which are placed over the foam mold of the front spar. Lower skin is also included in the laminate definition of the lower flange of the front spar (flange 1). Therefore, lower flange of the front spar (flange 1) consists of 7 layers. Counting from the layers inside the tail towards the outer layers, first 4 layers are carbon/epoxy layers, and the last three layers of E-galss/epoxy and Rohacell foam sandwich belong to the lower skin. On the other hand, lower flange of the rear spar consists of 5 layers; 2 layers of carbon/epoxy and the remaining three are the E-glass/epoxy-rohacell sandwich structure of the lower skin of the horizontal tail.

For the dive and stall conditions, equivalent stress plots for the 7th layer of the lower flange of the front spar (flange 1) are shown in Figure 78 and Figure 79, respectively. It should be noted that the 7th layer is the outer skin layer since surface normals of the lower flange of the front spar are in the -z direction. In Figure 78 and Figure 79 stress plots are generated for the 7th layer of the front spar flange, therefore rear spar flanges do not show any stress since rear spar flanges are composed of only 5 layers. In this case, for the dive speed condition, maximum equivalent stresses occur at vertical tail connection region not at the symmetry plane of the horizontal tail. It is noted that seventh layer of flange 1 is the outermost layer which is closest to the vertical tail support edge. This could be one reason for why for the dive speed condition, maximum stress occurs right above the vertical tail support but not at the symmetry plane. However, one can easily see from Figure 78 that for the dive speed condition equivalent stresses increase towards the symmetry plane but only at a very confined region near the vertical support edge, there is high stress on the 7th layer. It is again noted that for the dive speed condition equivalent stresses are higher than the one for the stall condition.

For the dive and stall conditions, maximum failure indices and the strength ratios are tabulated in Tables B23 and B24 in Appendix B. For the dive speed condition, maximum failure index is 0.01412 at the 7th layer. For the stall condition, maximum failure index is 0.00077 at the 7th layer. For both load condition, the rear spar flanges have lower failures indices than the flanges of the front spar.
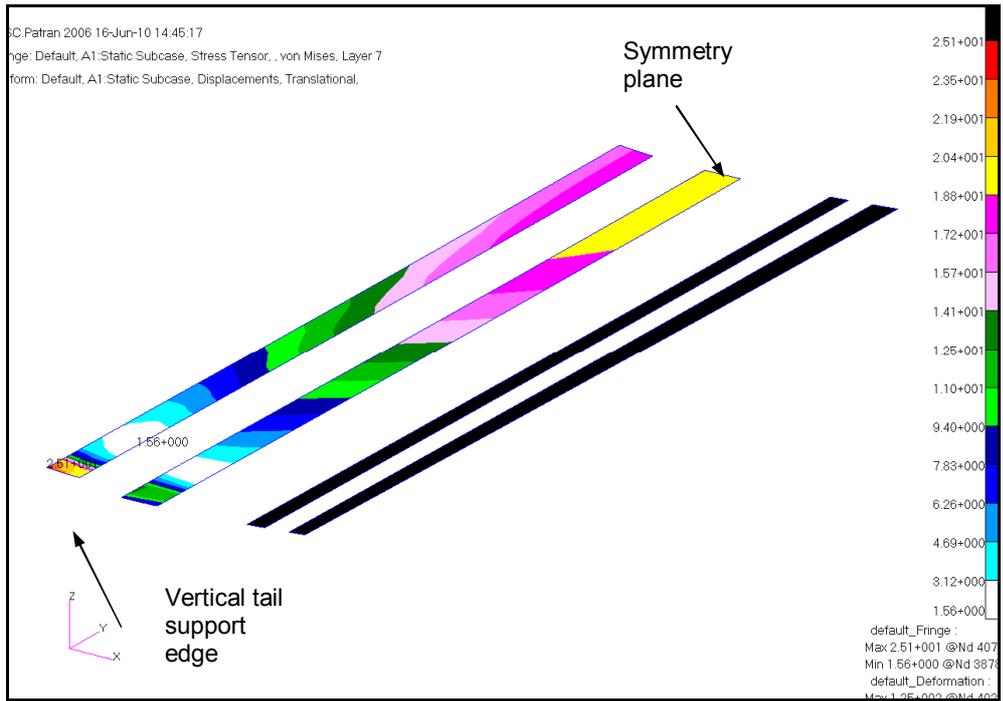
Figure 78: Equivalent stress plot in the lower flange (flange 1) of the front spar of the horizontal tail for dive condition
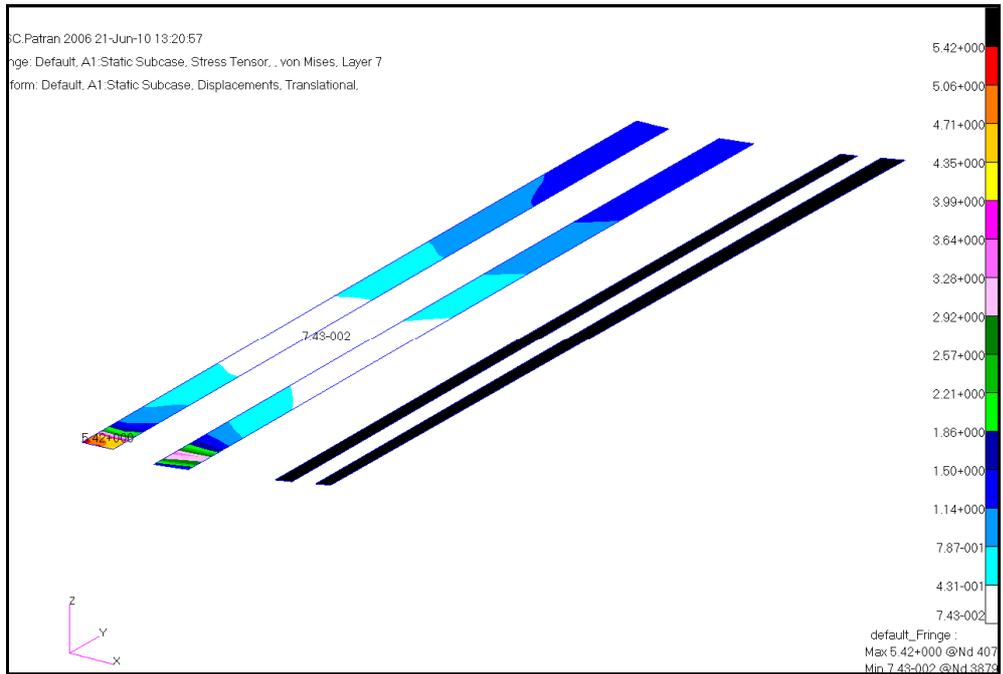
Figure 79: Equivalent stress plot in the lower flange (flange 1) of the front spar of the horizontal tail for stall condition

<u>Stress analysis of the lower flange of the front spar of the horizontal tail:</u>

Lower flange-2 of the front spar of the horizontal tail is the region right under the front spar foam. As seen in Figure 40, side extensions of the carbon/epoxy fabric composite are not included in the lower flange-2 of the front spar which consists of 2 layers of carbon/epoxy fabric composite, which are placed as the backing strips for the front spar, and the lower skin of the horizontal tail.

For the dive and stall conditions, equivalent stress plots for the outermost 5th layer of the lower flange of the front spar (flange 2) are shown in Figure 80 and Figure 81, respectively. For the dive speed condition, maximum equivalent stresses occur at the symmetry plane and at the vertical tail connection region. It is seen that locally, there is high stress at the connection region of the horizontal tail with the vertical tail. On the other hand, for the stall condition maximum equivalent stresses occur at the connection region of the horizontal tail to the vertical tail.
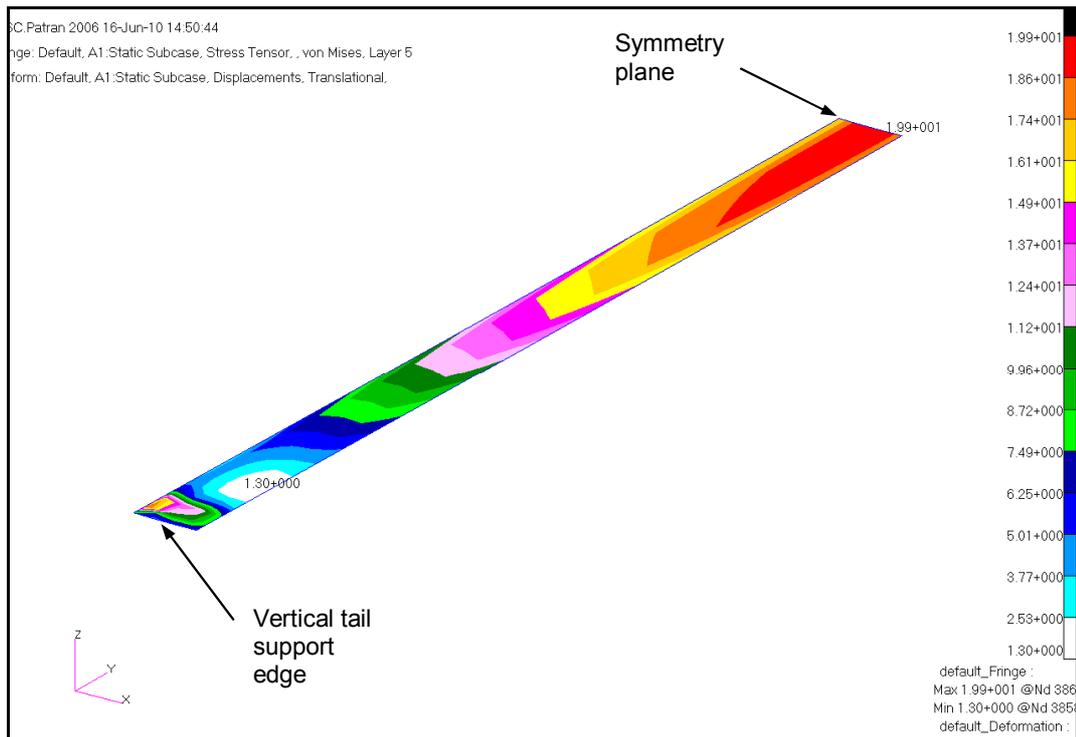
Figure 80: Equivalent stress plot in the lower flange (flange 2) of the front spar of the horizontal tail for dive condition

For the dive and stall conditions, maximum failure indices and the strength ratios are tabulated in Table B25 and B26 in Appendix B. For the dive speed condition, maximum failure index is 0.0287 at the outermost 5th layer. For the stal condition, maximum failure index is 0.0006 at the outermost 5th layer.
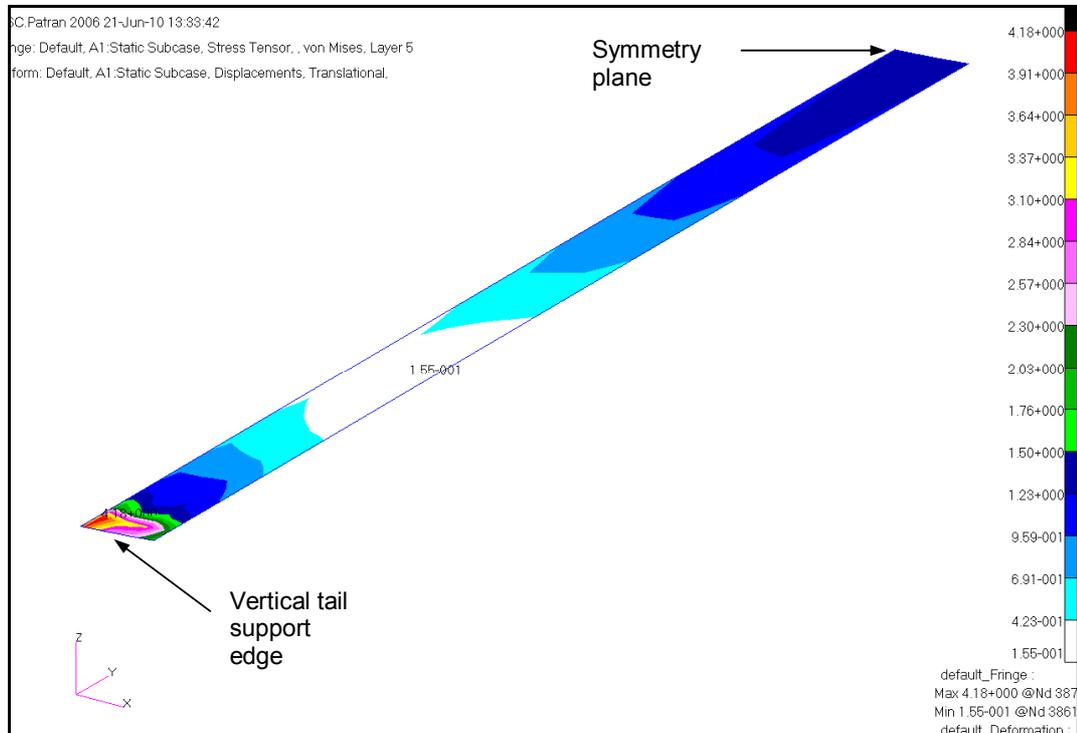
Figure 81: Equivalent stress plot in the lower flange (flange 2) of the front spar of the horizontal tail for stall condition

3.6.2. Structural analyses of vertical tail at 3.8g dive and stall conditions

Sideslip angle is not considered in the dive and stall condition analyses in current study. Thus, aerodynamic force on vertical tail structure is negligibly small for the stall condition. For stall condition, although there is a load transfer from horizontal tail, vertical tail structure is not critical in terms of structural integrity by current FE models. Because of that, a detailed result post-processing is not implemented for the stall condition of the vertical tail.

Stress analysis of the skin of the vertical tail:

For the skin of the vertical tail, maximum failure indices and strength ratios are tabulated in Tables B27 in Appendix B, for the dive condition. The inner layer of the skin (1st layer) has the highest failure index with a value of 0.022. Equivalent stress plot for the 1st layer of the skin of the vertical tail at the dive condition is shown in Figure 82. For the skin, the carbon/epoxy strips and the side extensions of the carbon/epoxy layer placed over the front spar mold are not shown in the stress plot of the skin. Maximum equivalent stresses occur along the spar which extend in the spanwise direction along the vertical tail. Higher stresses near spar is due to the rigidity of the spars formed by the hat shaped carbon/epoxy layers.
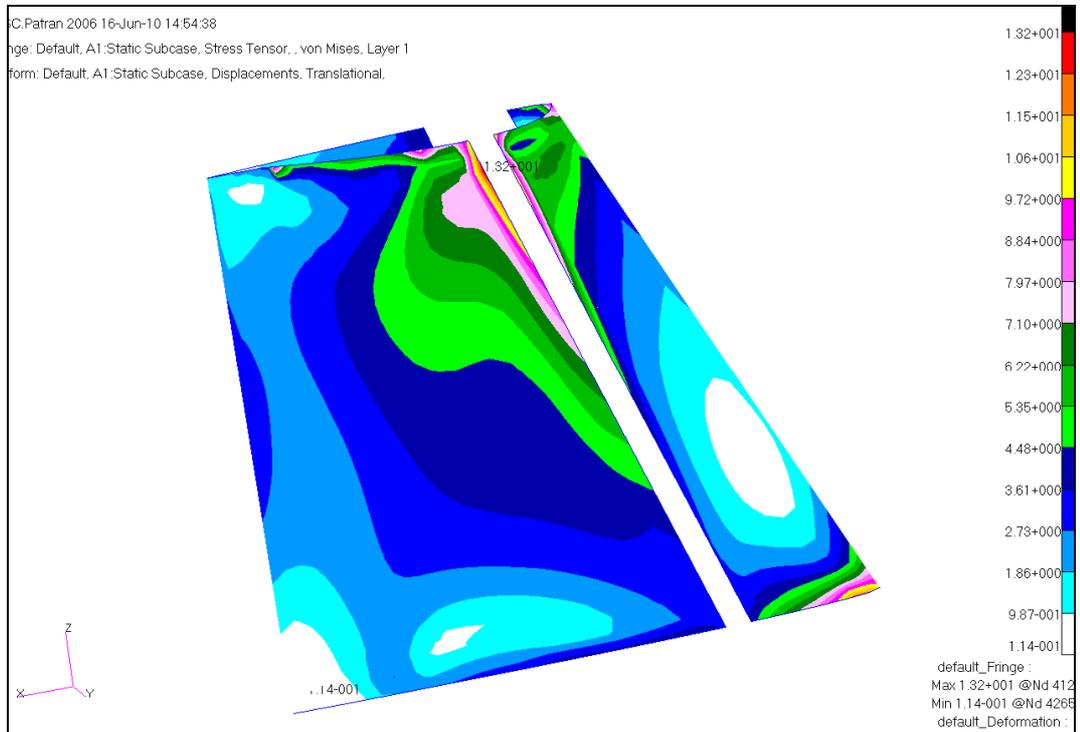
Figure 82: Equivalent stress plot in the skin of the vertical tail for dive condition

Stress analysis of the spar webs of the vertical tail:

Spar webs of the vertical tail consist of 2 layers of 0.3 mm thick carbon/epoxy fabric composite. Equivalent stresses on the 2nd layer of spar webs at the dive condition is shown in Figure 83. For the spar webs of the vertical tail, the maximum equivalent stresses occur at horizontai tail connection region. Maximum failure indices and the strength ratios are tabulated in Tables B28 in Appendix B. For the dive speed condition, maximum failure index is 0.0076. Ratio of the maximum failure indices is in accordance with the ratio of the maximum equivalent stresses for the dive condition.
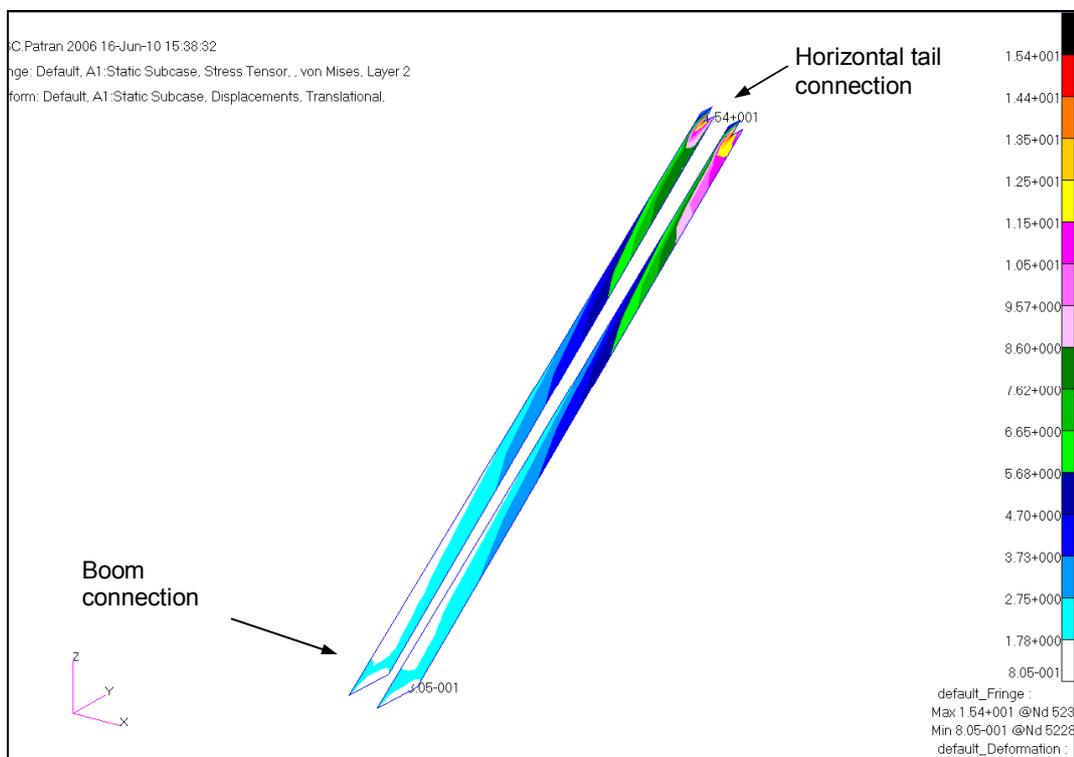
Figure 83: Equivalent stress plot for the spar webs of the vertical tail for dive condition

Stress analysis of the flange (flange 1) of the front spar of the vertical tail:

Flange-1 of the spar of the vertical tail is the region under and above the front spar foam. Skin is also included in the laminate definition of the flange of the front spar (flange 1). Therefore, flange of the front spar (flange 1) consists of 5 layers. Counting from the layers inside the tail towards the outer layers, first 2 layers are carbon/epoxy layers, and the last three layers of E-galss/epoxy and Rohacell foam sandwich belong to the skin.

For the dive condition, equivalent stress plots for the 5th layer of the flange of the front spar (flange 1) are shown in Figure 84. For the dive speed condition, maximum equivalent stresses occur at horizontal tail connection region.

Maximum failure indices and the strength ratios are tabulated in Tables B29 and in Appendix B. For the dive speed condition, maximum failure index is 0.019 at the 5th layer.
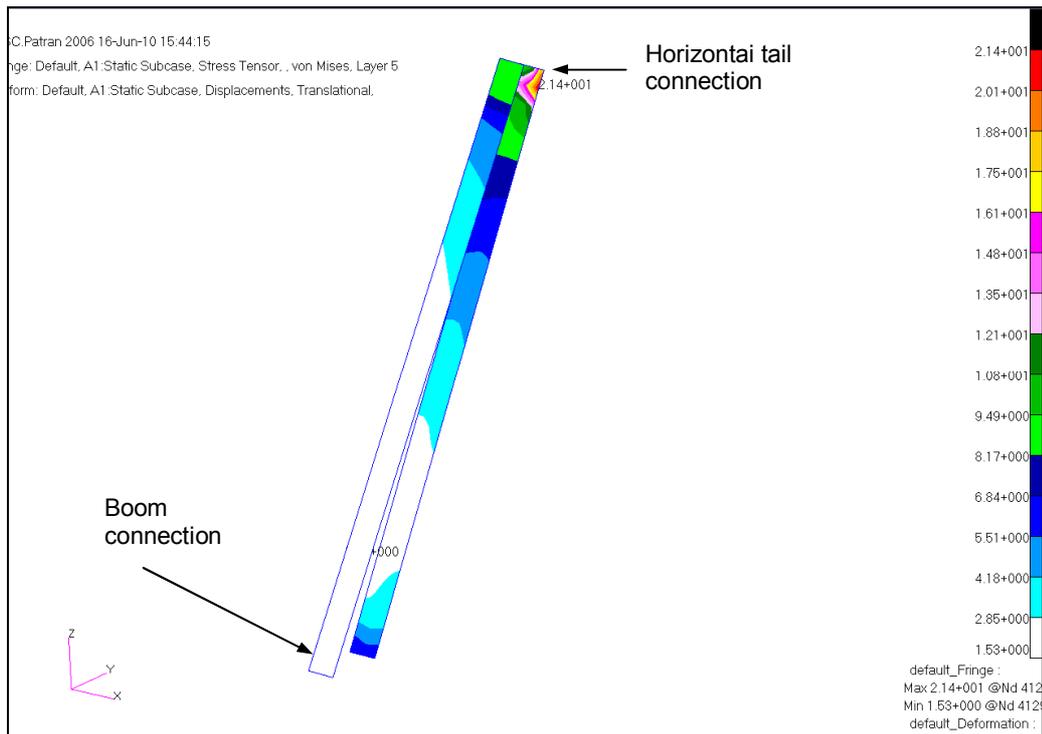
Figure 84: Equivalent stress plot in the lower flange (flange 1) of the spar of the vertical tail for dive condition

Stress analysis of the flange (flange 2) of the front spar of the vertical tail:

Lower flange-2 of the front spar is the region under the side extensions of the carbon/epoxy fabric composite layers which are placed over the foam mold of the spar. Skin is also included in the laminate definition of the flange of the front spar (flange 2). Therefore, flange of the spar (flange 2) consists of 7 layers. Counting from the layers inside the tail towards the outer layers, first 4 layers are carbon/epoxy layers, and the last three layers of E-galss/epoxy and Rohacell foam sandwich belong to the skin.

For the dive condition, equivalent stress plots for the 7th layer of the flange of the spar (flange 2) is shown in Figure 85. 7th layer is the outer skin layer. For the dive speed condition, maximum equivalent stresses occur at horizontal tail connection region. Maximum failure indices and the strength ratios are tabulated in Tables B30 in Appendix B. For the dive speed condition, maximum failure index is 0.004 at the 7th layer.
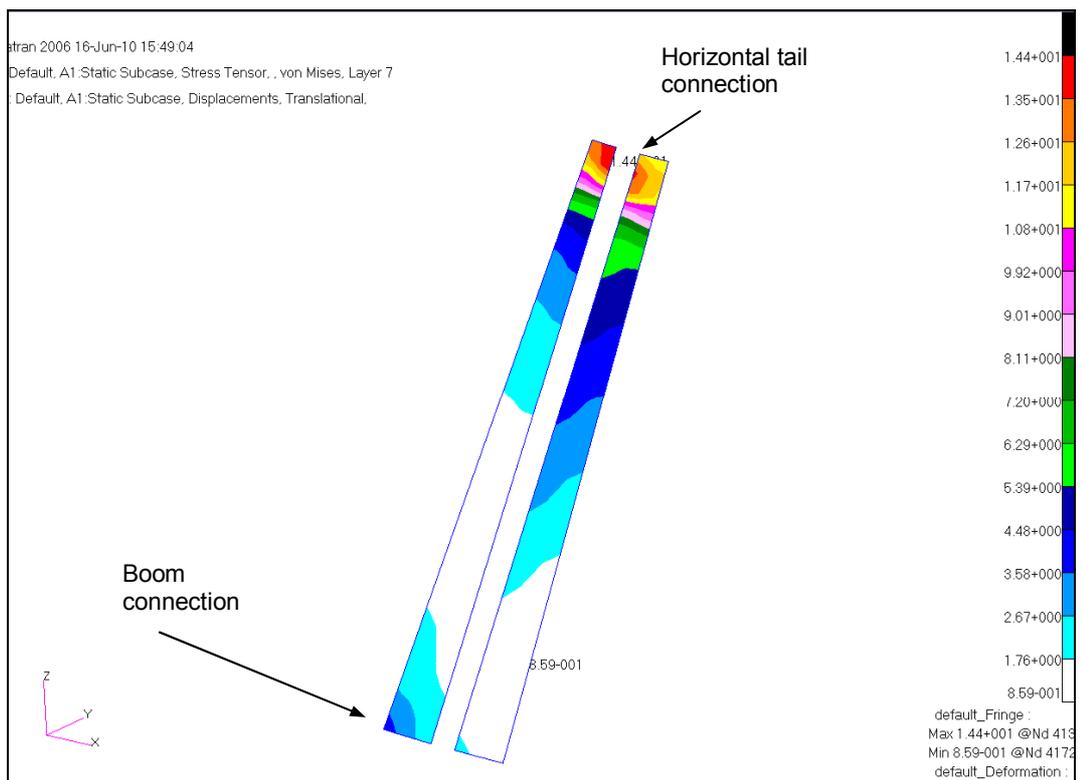
Figure 85: Equivalent stress plot in the flange (flange 2) of the spar of the vertical tail for dive condition

CHAPTER 4

AEROELATIC STABILITY ANALYSIS OF TACTICAL UAV

4.1. Introduction

In this part detailed aeroelastic stability analyses are conducted by MSC/Nastran using the Doublet-Lattice Method of aerodynamic load calculation for subsonic problems and the PK method for aeroelastic calculations. Aeroelastic analyses are performed by adding one sub-structure at a time to the aeroelastic model, and the analyses that are conducted include the "wing only", wing-tail plane combination and full air vehicle with and without wing control surfaces. With such a study, it is intended to address the effect each sub-structure added to the aeroelastic model on the critical aeroelastic stability modes and speeds, and to see how sensitive the aeroelastic stability modes and speeds are to model fidelity. During the course of aeroelastic analyses different splining methods, aerodynamic modeling alternatives, the choice of spline points, structural and aerodynamic grid refinement effects and the effect of uncertainties in the material properties are also evaluated.

Aeroelastic stability analysis method

PK method that is used in the aeroelastic stability analyses is an extension of the K method such that it is based on conducting a P method type of analysis with the restriction that the unsteady aerodynamics matrix is for simple harmonic motion. In the PK method the fundamental equation is cast into an eigenvalue problem in modal coordinates such that the real part of the aerodynamic stiffness is considered as stiffness and the imaginary part of the aerodynamic stiffness is considered as viscous damping [22].

$$\left[M_{hh}p^2 + \left(B_{hh} + \frac{1}{4}\rho\overline{c}VQ_{hh}^I/k \right)p + \left(K_{hh} + \frac{1}{2}\rho\overline{c}V^2Q_{hh}^R \right) \right]\{u_h\} = 0 \qquad (7)$$

Where:

M_{hh} : Modal mass matrix

B_{hh} : Modal damping matrix

K_{hh} : Modal stiffness matrix

u_{hh} : Modal amplitude vector

Q_{hh}^{I} (M,k)=modal aerodynamic damping matrix

Q_{hh}^{R} (M,k)=modal aerodynamic stiffness matrix

p=eigenvalue=$\omega(\gamma \pm i)$

$\gamma = 2g = $ Transient decay rate

In PK method of solution Eqn 7 is rewritten in state space form including the modal displacements and modal velocities as [22]:

$$[A - pI]\{u_h\} = 0 \tag{8}$$

Where is the real matrix given by Eqn 9:

$$[A] = \begin{bmatrix} 0 & I \\ -M_{hh}^{-1}\left[K_{hh} + \dfrac{1}{2}\rho V^2 Q_{hh}^R\right] & -M_{hh}^{-1}\left[B_{hh} + \dfrac{1}{4}\rho \bar{c} V Q_{hh}^I / k\right] \end{bmatrix} \tag{9}$$

and $\{\bar{u}_h\}$ includes both modal displacements and velocities. The eigenvalues of Eqn 8 are mostly complex conjugate pairs and the solution requires iteration for the oscillatory part. Static structural divergence roots require no iteration and are found by setting the reduced frequency to zero. The complex eigenvalues are determined through an iteration process such that first reduced frequency is assigned zero value and the real and imaginary parts of the aerodynamic matrix are determined by extrapolating to k = 0 from the available value of the aerodynamic matrix Q_{hh} (Mach number, k) which are obtained at the beginning of the solution process by the mach number/reduced frequency sets that are input by the user. After the determination of the complex eigenvalue p, the next estimate of the reduced frequency is calculated by using the frequency of oscillation just determined at the velocity specified. With the new reduced frequency, the aerodynamic matrices are recalculated and the same sequence of operations continues until the reduced frequencies calculated at two consecutive iteration steps are within a prescribed tolerance. Thus, PK method produces results only at the velocities of interest to the analyst and the stability at a specified velocity can be determined. However, the disadvantage of the PK method

is that calculated damping is only good for low levels of damping. Plots of g versus the speed allow to find the velocities where the decay coefficient goes through zero from negative to positive values. These crossing points indicate possible flutter speeds. Finally, to determine the matched point at the specified altitude the consistency of the crossing speed, Mach number and the density ratio has to be checked. Flowchart of PK method is given in Figure 86.
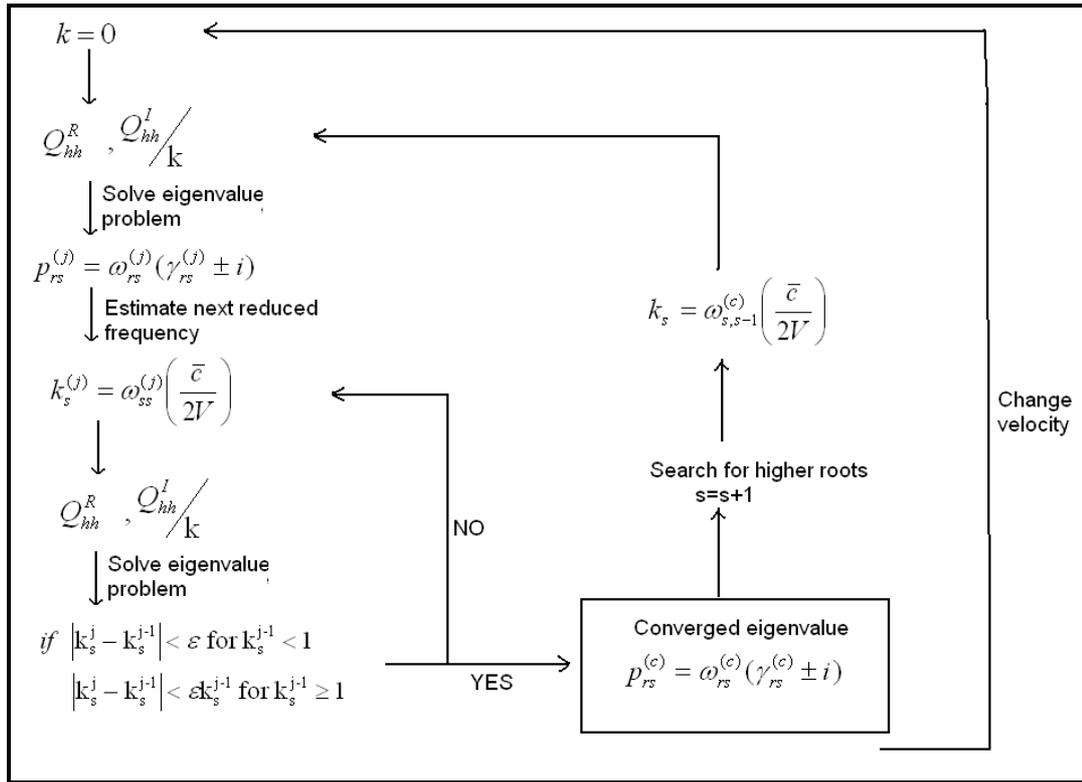
Figure 86: Flowchart of PK method

Coupling of structural and aerodynamic meshes

The coupling of the structural and aerodynamic grids is achieved by interpolation using surface splines. In the present study the infinite plate and finite plate splines are used to generate the coupling of aerodynamic and structural grids. The splining methods lead to an interpolation matrix $\left[G_{as} \right]$ that relates the components of structural grid point deflections $\{u_s\}$ to the deflections of the aerodynamic grid points $\{u_a\}$.

$$\{u_a\} = \left[G_{as} \right]\{u_s\} \tag{10}$$

Transformation between the aerodynamic and structural force systems is based on the concept of structural equivalence such that the aerodynamic forces $\{F_a\}$ and their structurally equivalent values $\{F_s\}$ acting on the structural grid points do the same virtual work in their respective deflection modes. Equality of the virtual work by the aerodynamic and structural forces leads to:

$$\{F_s\} = \left[G_{as}\right]^T \{F_a\} \tag{11}$$

The coupling of the structural and aerodynamic models thus requires the determination of the so-called spline matrix $\left[G_{as}\right]$.

1. Infinite plate spline

The infinite plate spline interpolation method, which is also used in MSC Nastran, is based upon the small deflection equation of an infinite plate. The mathematical analysis involves the finding of the point loads at a set of points given the deflections at the same set of points by utilizing the vertical deflection solution of a plate due to a transverse point load. In a typical aeroelastic analysis, the set of know deflections would be the deflections at the structural grid points. For a set of N point loads the vertical displacement $w(x, y)$ of the infinite plate can be written as [22, 23]:

$$w(x,y) = \sum_{i=1}^{N}\left(A_i + B_i r_i^2 + \left(P_i / 16\pi D\right)r_i^2 \ln r_i^2\right) \tag{12}$$

where P_i are points loads applied at N number of points, A_i and B_i are the arbitrary constants, D is the bending stiffness of the plate and r_i is the distance from the ith applied load to the point (x,y) where the vertical deflection is desired. It is stipulated that radial lines originating from the loaded points will appear to be straight lines at long distances from the applied loads. Therefore, to satisfy the boundary conditions at infinity Eqn 12 is expanded for large radial distances from the origin and only the terms of order $x = r\cos\theta, y = r\sin\theta, \ln r^2, 1$ etc. are retained. After the simplifications, a general solution for the vertical displacement can be written as:

$$w(x, y) = a_0 + a_1 x + a_2 y + \sum_{i=1}^{N} K_i(x, y) P_i \qquad (13)$$

Where a_0, a_1, a_2 are arbitrary constants and $K_i(x, y) = (1/(16\pi D)) r_i^2 \ln r_i^2$. The N+3

unknowns a_0, a_1, a_2 and P_i are determined from N known displacements of the

structural grids and 3 equilibrium equations $\sum P_i = \sum P_i x_i = \sum P_i y_i = 0$. Once all the

unknowns in Eqn 13 are determined, the vertical displacements at the aerodynamic

grid locations can be determined from Eqn 13 by entering the (x,y) coordinates of

the aerodynamic grids and finally these equations can be cast into the form given by

Eqn 10 completing the coupling of the structural and aerodynamic deflections.

2. Finite plate spline

In the finite plate spline method interpolant is based on structural behavior similar to

the infinite plate spline, but the equations are discretized approximation of a finite

structural component. Finite plate spline method uses a mesh of elemental

quadrilateral plates to compute the interpolation function [22]. A set of constraint

conditions using shape functions that are employed in the determination of the

stiffness matrix of the plate element are established such that the deformed plate

passes through the given data points. A virtual mesh is constructed on the

aerodynamic surface such that the transverse displacements and out-of-plane

rotations of the structural and aerodynamic grids can be expressed as functions of

the virtual FE mesh displacemens [24, 25]:

$$\{u_s\} = [\psi_s]\{u\} \qquad (14)$$

$$\{u_a\} = [\psi_a]\{u\} \qquad (15)$$

where $\{u_s\}$ and $\{u_a\}$ are the structural and aerodynamic point displacements,

respectively, $\{u\}$ is the overall FE mesh displacements of the virtual mesh and

$[\psi_s]$ and $[\psi_a]$ are the matrices in terms of the shape function matrices used to

interpolate the displacement field within the element in terms of nodal displacements

and the connectivity matrices relating the element nodal displacements to overall FE

mesh displacements. Since the virtual surface described by the FE mesh is required to pass through a set of structural points, a penalty method is employed to express the equilibrium state of the virtual surface [26].

$$[K]\{u\}+[\alpha][\psi_s]^T \left([\psi_s]\{u\}-\{u_s\}\right)=0 \tag{16}$$

where [K] is the free-free stiffness matrix of the finite plate and $[\alpha]$ is a diagonal weighting matrix used in scaling such that maximum diagonal elements of matrices [K] and $[\psi_s]^T[\psi_s]$ are in the same order of magnitude. Solving for {u} from Eqn 15 and substituting into Eqn 16 yields the desired splining relationship.

$$\{u_a\}=[G_{as}]\{u_s\} \tag{17}$$

where the interpolation matrix [Gas] is given by:

$$G_{as}=[\psi_a]\left\{[\alpha]^{-1}[K]+[\psi_s]^T[\psi_s]\right\}^{-1}[\psi_s]^T \tag{18}$$

4.2. AGARD 445.6 case

As a verification study, aeroelastic stability analysis of AGARD 445.6 wing is performed and results are compared with experimental results of Yates [28]. Airfoil profile of AGARD 445.6 is NACA 65A004. Wing geometry and thickness distribution of AGARD 445.6 is shown in Figure 87.
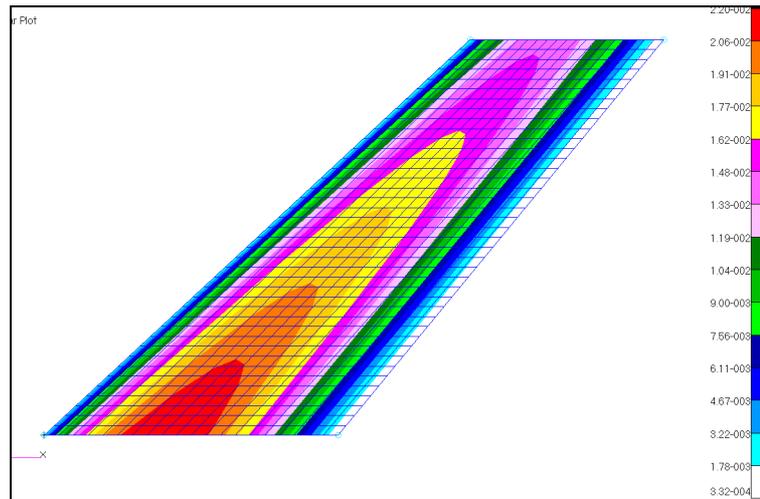
Figure 87: AGARD 445.6 wing geometry

Aeroelasticity verification study is performed for Agard weakened model 3. Results are compared with experimental results [28] and Kolonay's results [29]. Orthotropic material properties for Agard 445.6 weakended model 3 are tabulated below [29]:

E11=3.1511e9 Pa
E22=0.4162e9 Pa
v=0.31
G=0.4392e9 Pa
ρ = 381.98kg/m3

Comparison of Agard wing natural frequencies calculated by Nastan 103 modal analysis and experimental results are tabulated in Table 15.

Table 15: Natural Frequencies of AGARD 445.6

	Calculated (Hz)	Experimental (Hz) [28]
Mode 1 (1. bending)	9,55	9,6
Mode 2 (1. torsion)	39,92	38,1
Mode 3 (2. bending)	50,06	50,7
Mode 4 (2. torsion)	96,1	98,5
Mode 5	124,54	-

Lifting surface of Agard wing modeled with 800 aerodynamic panels and fluid-structure interface is performed by infinite spline method. Aerodynamic elements are shown at Figure 88 below.
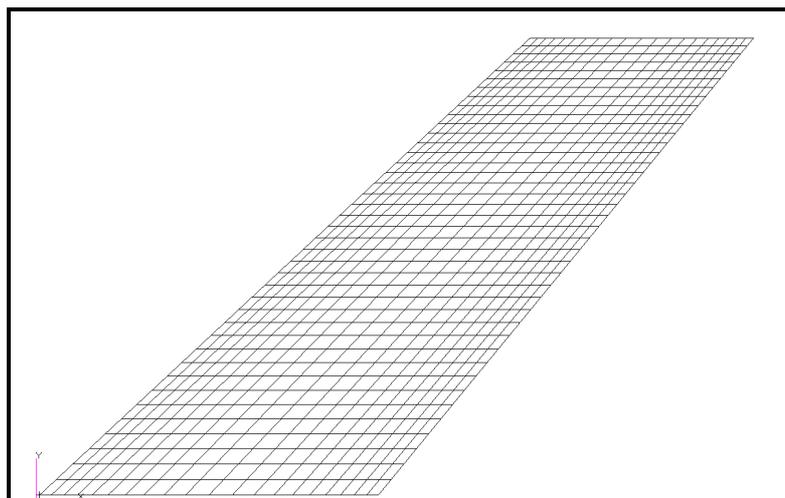
Figure 88: Aero Model for AGARD 445.6

It should be noted that the aerodynamic grid used in the verification study satisfies the MSC's recommendation of maximum aspect ratio criteria of 3 and minimum boxes per wavelength criteria of 15 [22,24].

In order to verify fluid-structure interface (spline method), moves of aerodynamic elements and structural elements are investigated at normal modes of vibration. As it is seen in Figure 89, aerodynamic and structural elements are well-matched at first normal mode. Red elements are aerodynamic panels and blue elements are structural elements in Figure 89. Aerodynamic and structural elements move well-matched at first 4 normal modes but structural and aerodynamic elements separate at high slope regions at fifth normal mode as shown in Figure 89(b).

(a)   (b)
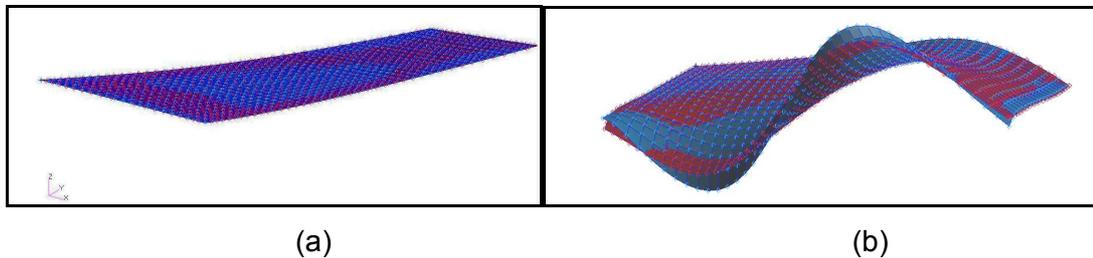
Figure 89: Spline verification (a): Mode 1, (b): Mode 5

Aeroelastic analysis for the verification case is performed for three different cases. In the first case an aerodynamic mesh of 20x10 is used and infinite plate spline and finite plate splines are employed. In the third case, an aerodynamic mesh of 40x20 is used together with the finite plate spline method for the fluid-structure coupling. Since the third case gave the closest results to the experimental results, in the thesis only the results of the third case is given for the verification study. Figure 90 shows the damping-velocity and Figure 91 shows frequency-velocity curves of the "Agard 445.6 weakened model 3". Damping of first mode becomes positive at a velocity of about 300 m/s. Positive damping shows that structure is instable and flutter will occur. In should be noted that in the aeroelastic analysis conducted, structure damping is neglected.
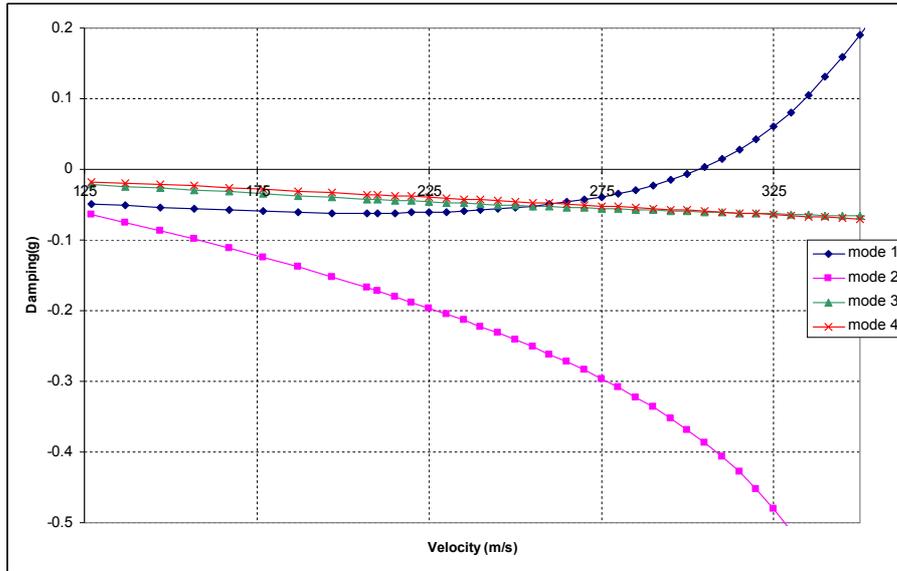
Figure 90: Agard 445.6 Damping-Velocity graph
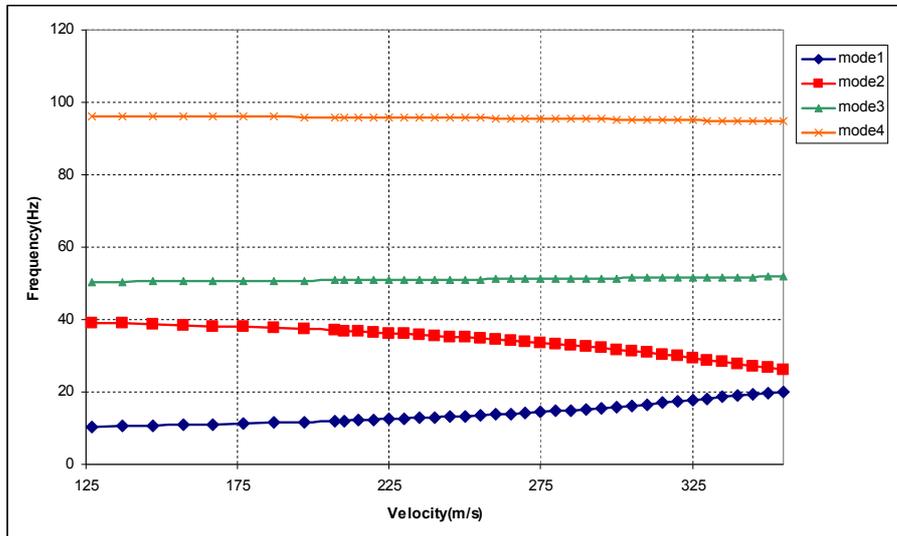
Figure 91: Agard 445.6 Frequency-Velocity graph

Linear interpolation is applied to find the exact flutter speed and flutter frequency. Flutter speed is determined as 303.5 m/s and flutter frequency is determined as 16.02 Hz according to aeroelastic analysis.

Aeroelastic analysis results and experimental results are compared in Table 16. Initially, assumed flutter Mach number is taken as 0.926 in the aeroelastic analysis and the flutter Mach number is determined as 0.922. This result shows that a matched point solution is determined and no more iteration is required.

Table 16: Comparison of Agard wing aeroelastic analysis results with the
experimental results

	Calculated	Experimental [28]
Splining	FPS	
Aerodynamic mesh	40x20	
Input Mach Number	0,926	
Flutter speed (m/s)	303,5	296,7
Flutter Mach number	0,922	0,901
Flutter frequency (Hz)	16,016	16,091

Aeroelastic analysis results of "Agard 445.6 weakened model 3" with 40x20 aerodynamic panels are compared with the experimental results [28] and Kolonay's results [29] in Table 17. The main goal of this study was to verify reliability of results of Nastran aeroelasticity module 1, and as it is seen in Table 17, flutter speed and and flutter frequency results obtained by the Nastran are close to both experimental results and results obtained by Kolonay in an independednt study [29]. It should be noted that the difference in the flutter speed could be due to not considering the transonic effects near the flutter Mach number of 0.9. In the linear aeroelastic analysis of Nastran, although correction due to compressibility is included, aerodynamic forces are calculated by the Doublet-Lattice method. However, Kolonay's study is based on solving the transonic small disturbance equations in determining the aerodynamic forces.

Table 17: Agard wing calculated, experimental and Kolonay's flutter speed and
flutter frequency

	Present study	Experimental [28]	Kolonay [29]
Flutter speed (m/s)	303,5	296,69	300
Flutter frequency (Hz)	16,016	16,09	15,28

Damping-velocity and frequency-velocity graphs obtained by Kolonay [29] for the Agard 445.6 wing are shown in Figure 92 and Figure 93. These graphs are very

similar to damping-velocity and frequency-velocity graphs of the present study which are given in Figure 90 and Figure 91.

Based on the comparisons provided with the experimental and an independent aeroelastic analysis by Kolonay, it can be concluded that flutter analysis of the Agard Wing 445.6, which is performed by the Nastran sub-sonic aeroelasticity module gives reliable results. It is considered that Nastran sub-sonic aeroelasticity module can also be used to check the aeroelastic stability speeds of the tactical unmanned air vehicle. It should be noted that the tactical UAV has a dive speed of 100 m/s which is much lower than the speed of sound at the sea level. Therefore, it is considered that sub-sonic aeroelastic analysis of the tactical UAV is sufficient show that the airplane is free of any aeroelastic instability within the flight envelope.
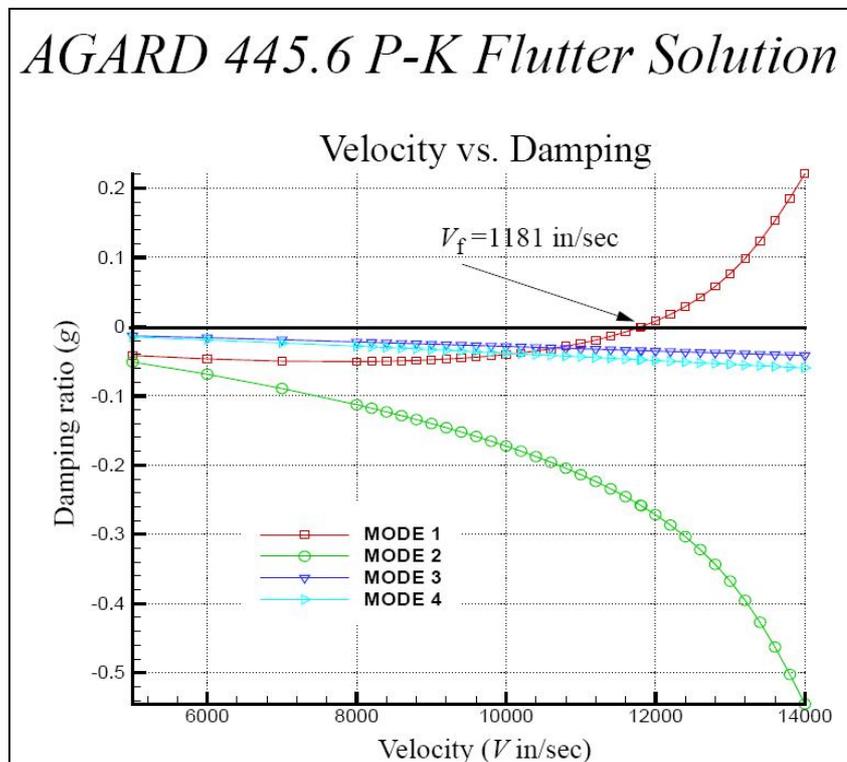
Figure 92: Damping versus velocity curve of Kolonay for the Agard 445.6 wing
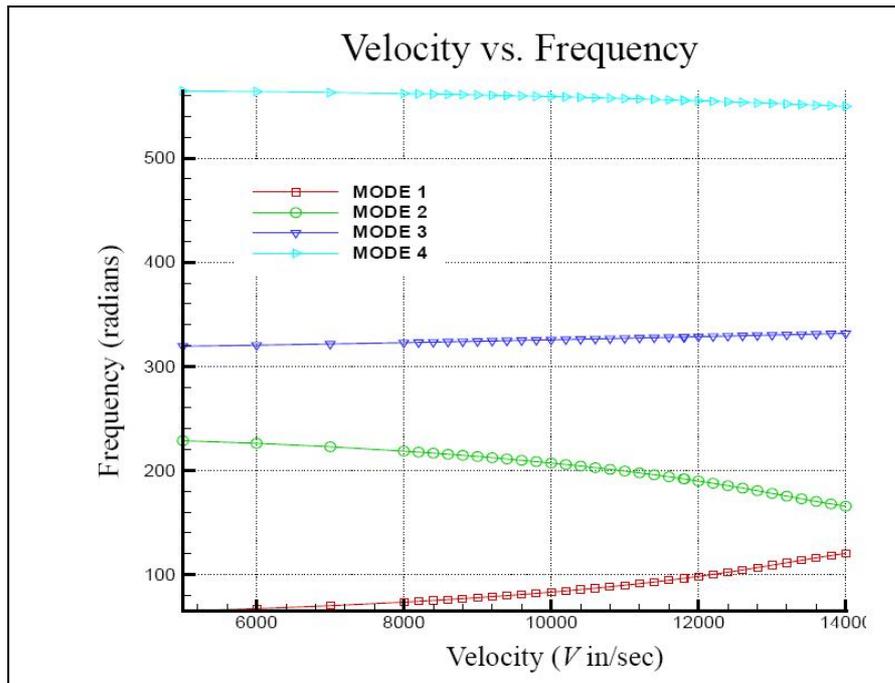
Figure 93: Frequency versus velocity curve of Kolonay for the Agard 445.6 wing

4.3. Aeroelastic analysis of Wing

Aeroelastic stability analyses of the "wing only" model has been performed for seven different cases corresponding to different spline methods, structural and aerodynamic mesh sizes and spline points off the structural model. These cases are summarized in Table 18. Before presenting the results it should be noted that for the original configuration of the wing, the flutter speed is determined to be about 330 m/s which corresponds a flutter Mach number which is very close to 1. Considering that the dive speed of the airplane is 100 m/s, wing is considered to be very rigid since the margin of safety is very high. Therefore, the in present study aeroelastic analysis is preformed for a modified wing configuration. In the modified configuration, two layers of E-glass/epoxy on the top and on the bottom of the Rohacell foam used in the wing skins are reduced to single layer of E-glass/epoxy. In addition, 5 layers of carbon/epoxy fabric composite, which are laid over the blue foam of the spars, are reduced 3 layers. Thus, in the future productions weight reduction and material cost saving can also be achieved by reducing the the layer numbers of wing skin and the spar webs. In the following, in all the aeroelastic models the modified wing is used. Therefore, the true aeroelastic stability speeds, determined by different aeroelastic models, are higher than what is reported in this

Chapter. As noted above, for the original wing configuration flutter speed is determined to be about 330 m/s.

Table 18: Properties of the seven different aeroelastic models of the "wing only" model of the UAV

	Case 1	Case 2	Case 3	Case 4	Case 5	Case 6	Case 7
Spline method	IPS[a]	IPS	FPS[b]	FPS	FPS	FPS	FPS
Structural grid	Course	Course	Course	Fine	Course	Course	Fine
Spline points	Ribs+ Webs	Ribs+ Webs+ Leading edge	Ribs+ Webs+ Leading edge	Ribs+ Webs	Ribs+ Webs	Ribs+ Webs	Ribs+ Webs
Aero grid (Spanwise x Chordwise Panels)	40x15	40x15	40x15	40x15	40x15	85x40	85x40

[a]Infinite plate spline, [b]Finite plate spline

Course mesh of the structural finite element model of the wing has 1913 elements and 1678 nodes whereas fine mesh of the finite element model has 9467 elements and 8605 nodes. Figure 94 shows the course and fine mesh of the structural finite element model. The two different spline point selections off the structural model are shown in Figure 95. The aerodynamic surface is passed through the chord line and the structural grids of the stiff elements such as spar webs, ribs, and/or leading edge at the intersection with the aerodynamic surface or the structural grids which are closest to the aerodynamic surface are grouped as the spline points. For cases 4 and 7 since the structural finite mesh is fine, in Figure 95 spline points used for the coarse mesh is shown for better visualization of the spline points. Figure 95 also shows the inner layout of the wing showing the spline points taken off the leading edge, ribs and two edges of spar webs of the front and rear spar.

(a)   (b)
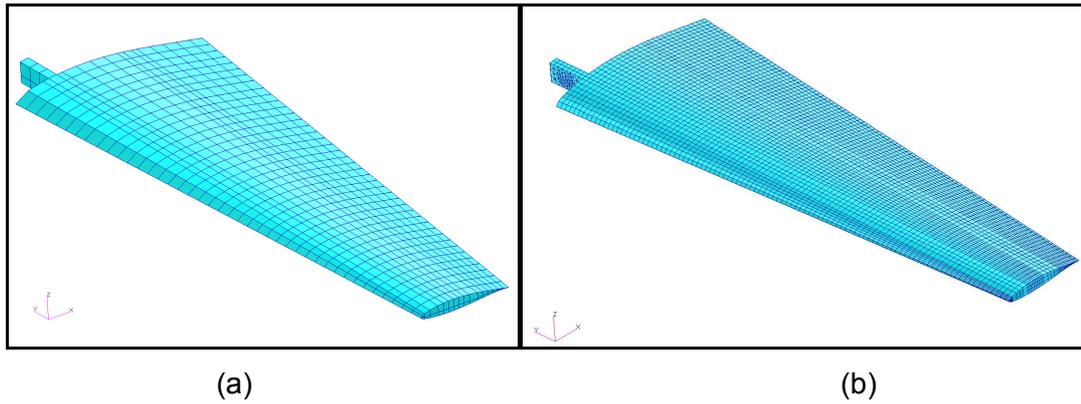
Figure 94: FE mesh a) Course, b) Fine

<u>Aeroelastic analysis of the wing without the root aero panels bridging the two wings</u>

In the initial aeroelastic analyses of the "wing-only" model the aerodynamic surface is taken as the wing planform outside the fuselage and the wings are not connected by a body and only one half of the wing is used in the aeroelastic calculations. In this case a gap forms between the right and the left wings whereas in a realistic configuration the right and the left wings are connected by a body located along the body axis. Due to the absence of an adjacent strip, a strong vortex is generated at the inboard edge which is not physical and leads to an incorrect aerodynamic force distribution [31]. However, to see the effect of such a modeling on the aeroelastic stability speeds the gap between the wings is not bridged by additional aerodynamic panels.
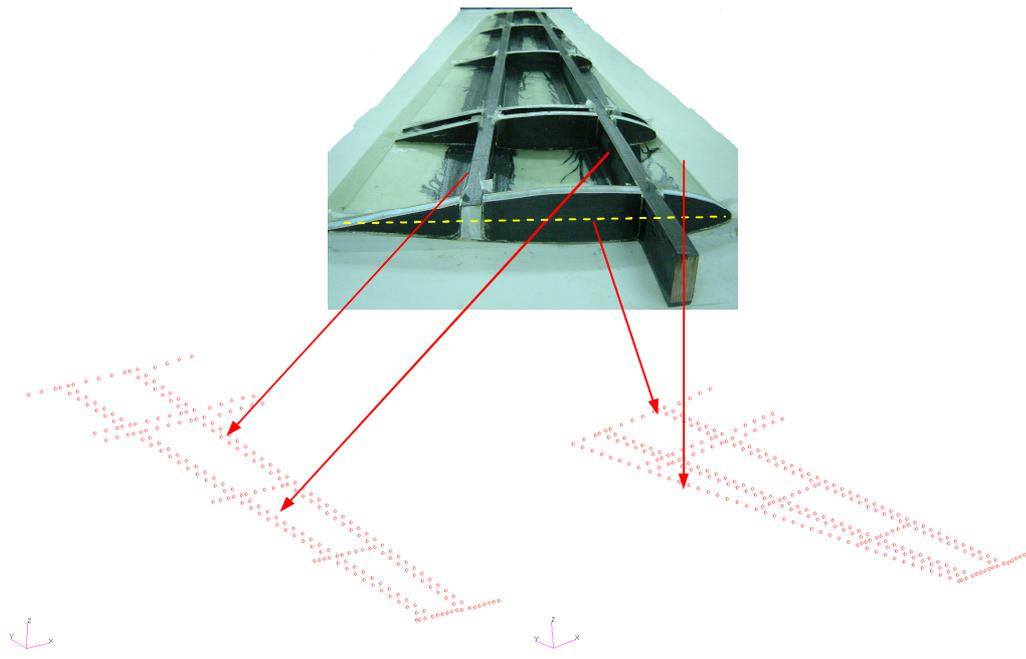
Spline points used for cases 1,4 -7   Spline points used for cases 2,3

Figure 95: Two different spline point selections off the structural model

For the wing planform outside the fuselage Figure 96 and Figure 97 show the aspect ratio distribution for the coarse and fine aerodynamic meshes. Aerodynamic mesh is two-way biased such that panel concentration is higher towards the leading and trailing edge to capture the high pressure gradients better. The fine aerodynamic grid used for cases 6 and 7 satisfies the MSC's recommendation of maximum aspect ratio criteria of 3 and minimum boxes per wavelength criteria of 15. However, for the coarse aerodynamic mesh the boxes per wavelength range is 6-35, and minimum boxes per wavelength criteria is not satisfied everywhere on the wing surface.
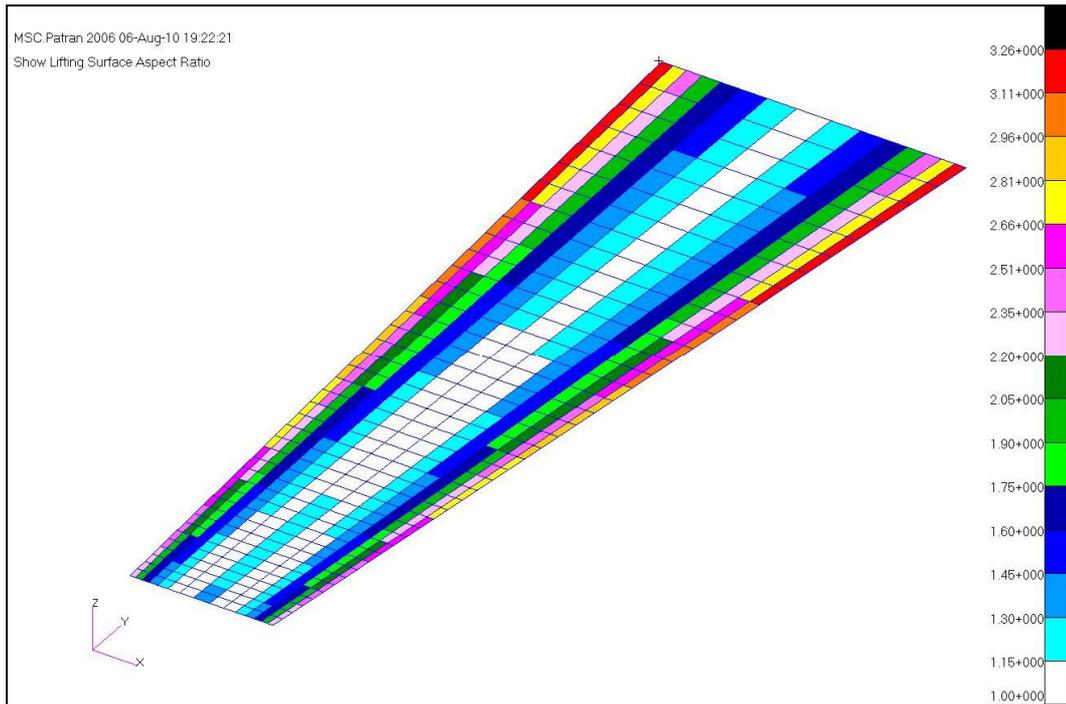
Figure 96: Aspect Ratio plots of Aero mesh
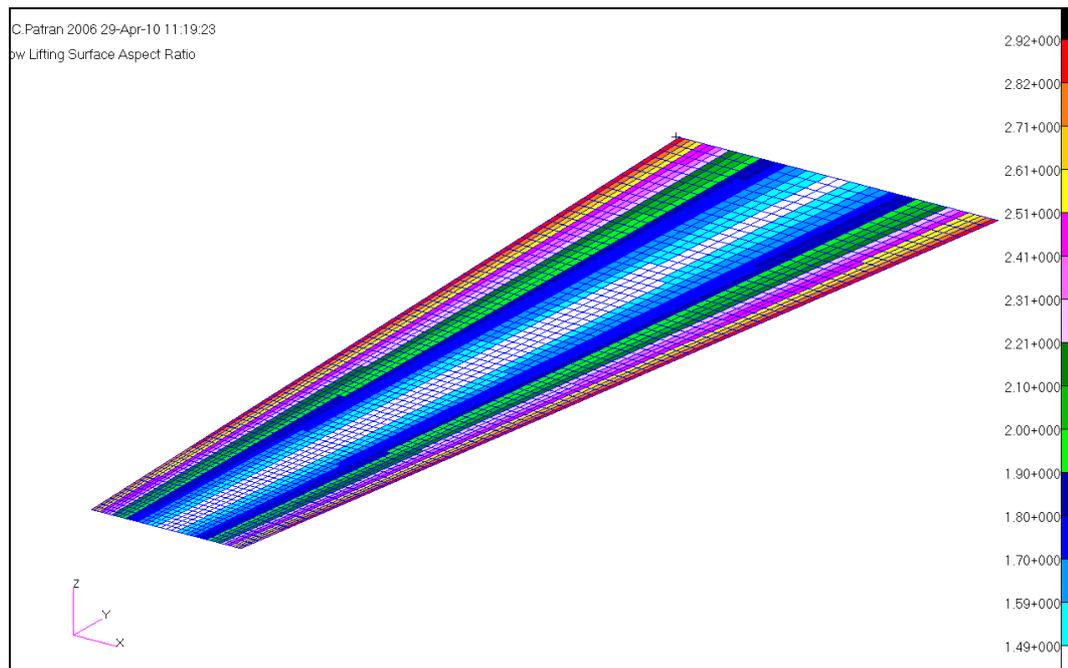
Figure 97: Aspect Ratio plots of Aero mesh

Aeroelastic stability analysis of the wing is performed at the sea level in the velocity range of 20-300 m/s. The three displacements on the face of the front spar root,

entering into its box in the fuselage, are fixed. On the rear spar side the displacements on the face of the rear spar root in contact with the fuselage are also fixed. In addition, the Rohacell foam, which is used as the core material in the wing skins, is assigned the property of pure epoxy and modal analysis is performed by the solution sequence 103 of Nastran. For the first four free vibration modes of the wing the natural frequencies, which are determined by the course and fine structural meshes are compared in Table 19 and good agreement is observed.

Table 19: Natural Frequencies of FE models

Modes	Frequencies Determined by the course mesh (Hz)	Frequencies determined by the fine mesh (Hz)
1	13.06	13.23
2	56.15	56.99
3	67.42	67.32
4	68.98	69.59

The first four still air modes shapes of the wing are shown in Figure 98 and Figure 99. The first mode is a pure bending mode and the second mode is primarily second bending mode of the wing distorted by some twisting action. The third and fourth modes are close modes which are predominantly torsional modes of vibration. Aeroelastic stability analysis results indicated that the critical modes were the first and the fourth modes.
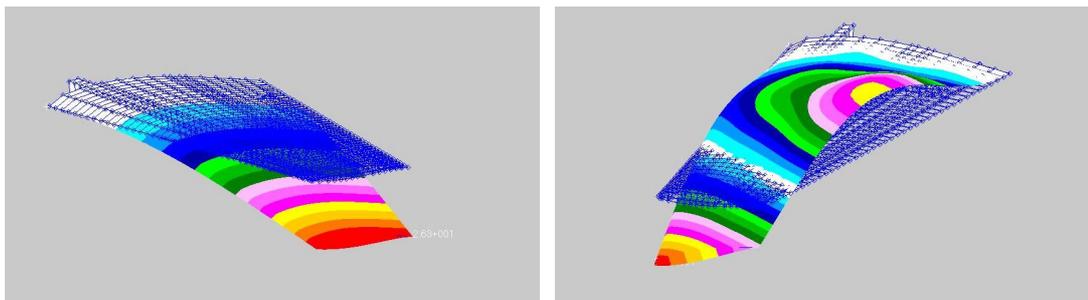
Figure 98: First and second mode shapes of the "wing-only" model
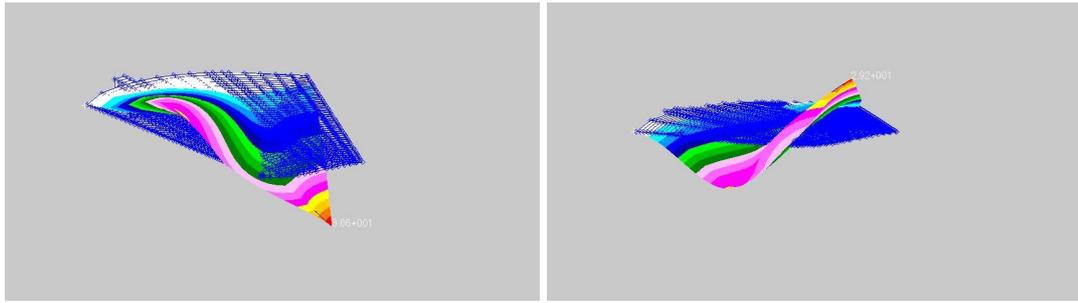
Figure 99: Third and fourth mode shapes of the "wing-only" model

Aeroelastic stability analyses are performed at the density ratio of one corresponding to the sea level, and sixteen modes are used in the PK method during the analysis performed by Nastran. In the PK method iterations have been performed until the input Mach number and the Mach number at the flutter speed agreed with each. Table 20 summarizes the results of aeroelastic stability analyses for the seven different aeroelastic models of the "wing only" model of the UAV.

Table 20: Symmetric aeroelastic stability analysis results of the "wing only" model[C]

	Case 1	Case 2	Case 3	Case 4	Case 5	Case 6	Case 7
Input Mach number	0.76	0.76	0.78	0.82	0.78	0.78	0.82
Computation time (min)	~1	~1	~1	~2	~1	~80	~90
Flutter speed (m/s)	261.3	260.8	269.4	283.9	268.5	268	284.7
Flutter frequency (Hz)	27.1	27.06	28.22	27.7	28.14	27.79	27.46
Flutter Mach number	0.761	0.759	0.784	0.826	0.781	0.78	0.828
Divergence speed (m/s)	293.4	294.7	> 300	> 300	>300	>300	>300

[c] Rohacell foam used is assigned pure epoxy property and the gap between the wings is not bridged by aero panels

For the symmetric aeroelastic analysis Figure 100 and Figure 101 give the damping and frequency versus speed curves for cases 1 and 5. Both figures show that that the flutter speed mode is the first wing bending mode and the divergence speed mode is the fourth mode which is predominantly the torsional mode and for the other cases listed in Table 20 the flutter and divergence speed modes did not change. For case 1, which uses infinite plate spline, divergence instability below 300 m/s is evident by the fact that frequency is zero and damping crosses the zero damping

line and becomes positive. For case 5, which uses finite plate spline, divergence occurs above 300 m/s which is the upper speed limit used in the analyses.
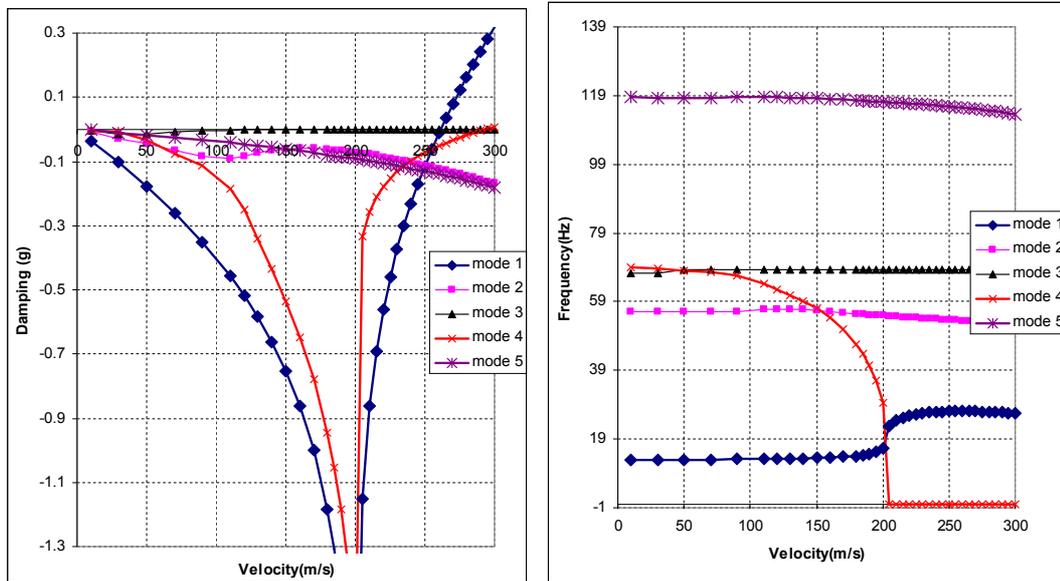
Figure 100:Damping and frequency versus speed curves for case 1-Symmetric analysis
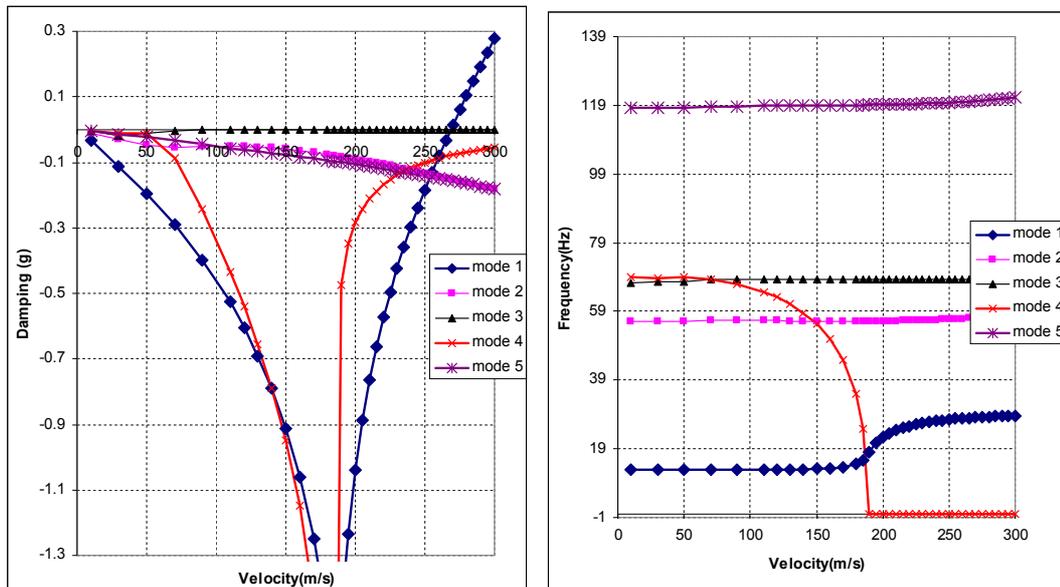
Figure 101: Damping and frequency versus speed curves for case 5 –Symmetric analysis

For case 5 antisymmetric aeroelastic analysis is also performed. For case 5 damping/frequency versus speed curves for the antisymmetric aeroelastic stability analysis is given in Figure 102. Figure 102 shows that for the antisymmetric analysis the flutter speed mode is mode 4 which is the wing torsional mode whereas the divergence speed mode is first wing bending mode.
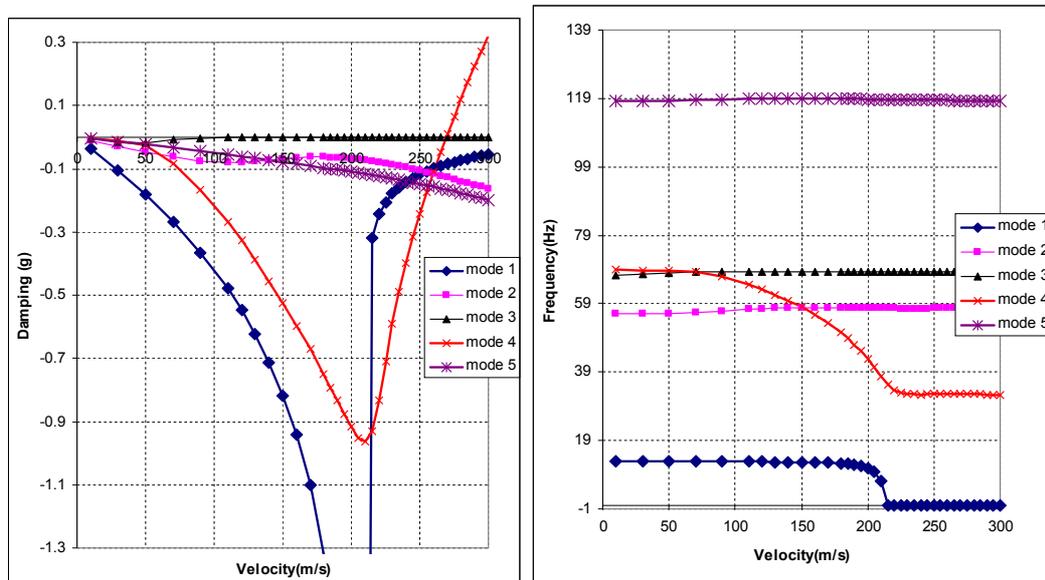
Figure 102: Damping and frequency versus speed curves for case 5 –Antisymmetric analysis

Table 21 compares the symmetric and antisymmetric analysis results for case 5. For both symmetric and antisymmetric analyses divergence instability is predicted above 300 m/s which is the upper speed limit used in the analyses.

Table 21: Comparison of symmetric and antisymmetric analysis results for case 5[d]

	Symmetric analysis	Antisymmetric analysis
Flutter speed (m/s)	268.5	269.2
Flutter frequency (Hz)	28.14	32.58
Flutter mode	Mode 1: Wing bending	Mode 4: Wing torsion

[d] Rohacell foam used is assigned pure epoxy property and the gap between the wings is not bridged by ay aero panels

<u>Aeroelastic analysis of the wing with the root aero panels bridging the two wings</u>

In the second party of aeroelastic analyses the gap between the left and the right wings is bridged by aerodynamic panels as shown in Figure 103.
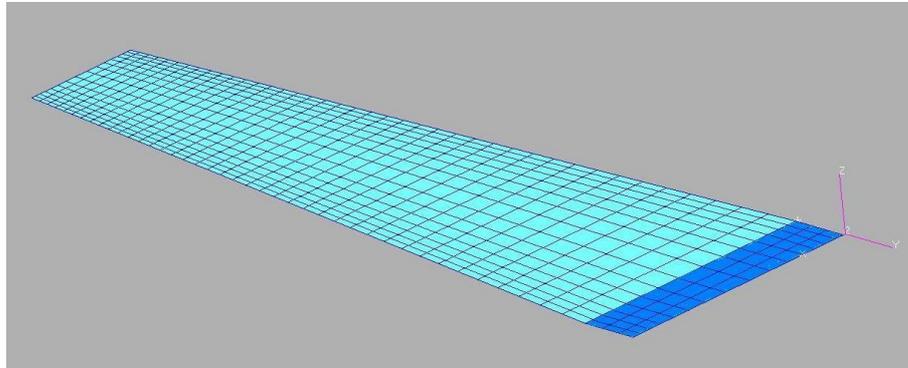
Figure 103: Additional aerodynamic panels between the right and left wings to avoid the gap

Before the aerodynamic panel configuration seen in Figure 103 is decided on, several trial aeroelastic analyses are performed with different size aerodynamic panels bridging the wings. When the single aerodynamic panel is used it is seen that mode shifting occurs between modes 1 and 4. Therefore, the configuration shown in Figure 103 is used as the aerodynamic surface in the aeroelastic analyses. Aerodynamic panels bridging the left and the right wings are not splined to the structural mesh, however it is also observed that using appropriate spline definitions through the front spar and the root rib has almost no effect on the aeroelastic stability speeds due to the fact that the three displacements of the front spar are fixed and the nodes along the root rib are almost stationary.

Table 22 gives the symmetric aeroelastic stability analysis results of the "wing only" model after the gap between the left and right wings is bridged by aerodynamic panels. Aerodynamic model shown in Figure 103 is the correct modeling approach which partially cancels the strength of the inboard vortex generated by the additional bridging aerodynamic panels which are in immediate vicinity of the inboard vortex line. Comparison of the results summarized in Table 20 and Table 22 reveal that by bridging the gap between the left and the right wings by additional aerodynamic panels, critical aeroelastic stability speeds increase slightly for the seven different cases studied. The slight increase in aeroelastic stability is considered to be due to

the partial cancellation of the strong vortex line at the inboard edge which leads to incorrect aerodynamic force distribution. It is also observed that the effect of bridging the gap between the right and the left wings by aerodynamic panels on the critical aeroelastic stability speeds is more for cases 1 and 2 which use infinite plate spline method as the aerodynamic structural coupling method.

Table 22: Symmetric aeroelastic stability analysis results of the "wing only" model[e]

	Case 1	Case 2	Case 3	Case 4	Case 5	Case 6	Case 7
Input Mach Number	0.78	0.78	0.78	0.83	0.78	0.78	0.83
Computation Time (min.)	~1	~1	~1	~2	~1	~80	~90
Flutter Speed (m/s)	267.80	267.25	270.15	286.59	269.14	268.77	287.51
Flutter Frequency (Hz)	26.54	26.51	28.41	26.29	28.31	28.54	26.44
Flutter Mach number	0.779	0.778	0.786	0.834	0.783	0.782	0.837
Divergence Speed (m/s)	299.62	>300	>300	>300	>300	>300	>300

[e] Pure epoxy property is assigned to Rohacell foam core and the gap between the wings is bridged by aero panel

From the results summarized in Table 22 several conclusions can be inferred:

-For the "wing only" model the flutter speeds are lower than the divergence speeds for the seven different cases studied. For the seven cases, it is seen that the critical symmetric flutter mode is the wing bending mode 1 and the critical divergence mode is the wing torsion mode 4.

-The results of cases 1, 2 and 3, 5 indicate that for the infinite plate spline and finite plate spline methods, the selection of the spline points off the leading edge of the wing, as in cases 2 and 3, does not significantly affect the flutter speeds.

-In the analysis that are performed finite plate spline method gave consistently higher critical speeds compared to the infinite spline method. It is also observed that when the correct aerodynamic modeling is used at the wing root the differences in the critical aeroelastic stability speeds determined by the infinite and finite plate methods decreased.

-The results of case 4 and case 7 indicate that the use of finer structural mesh has the highest impact on the critical speeds. Flutter speeds calculated by the fine structural mesh are approximately 5% higher than the flutter speed calculated by the coarse structural mesh which uses finite plate spline. Based on the comparison of the results of cases 5 and 6 or 4 and 7, it can also be concluded that the use of finer aerodynamic mesh, as in cases 6 and 7, has less influence on the critical speeds as long as an acceptable coarse mesh is used on the lifting surfaces. In addition, the solution time is drastically higher for the model using the finer aerodynamic mesh because of the preparation of aerodynamic matrices used in the frequency domain solution of Nastran. The results obtained by the coarse and the fine structural meshes show that natural frequencies and modes obtained by the coarse mesh are close to those from a structural model with finer mesh and the use of coarse structural mesh results in flutter speeds that tend to be conservative. Such a conclusion was also reported by Striz and Venkayya [27].

-Considering that the dive speed of the UAV is 100 m/s, flutter speeds, predicted by the aeroelastic analysis of the "wing only" model at the sea level, have large margins of safety. Although the aeroelastic analysis of the more accurate entire UAV model will give more insight about the critical speeds, at this stage the high critical speeds can be attributed to the high bending and torsional stiffness of the wing due to the use of two spars each with hat shaped spar web and flanges during the manufacturing.

For the wing only model another case study (Case 8) is performed by using pure Rohacell foam properties[18] for the core material used in the wing skins. Case 5, which uses finite plate spline method using coarse structural and aerodynamic mesh, is modified and pure foam material properties specified by the foam manufacturers are assigned to the core material used in the wing skins and the aeroelastic stability analysis is repeated.
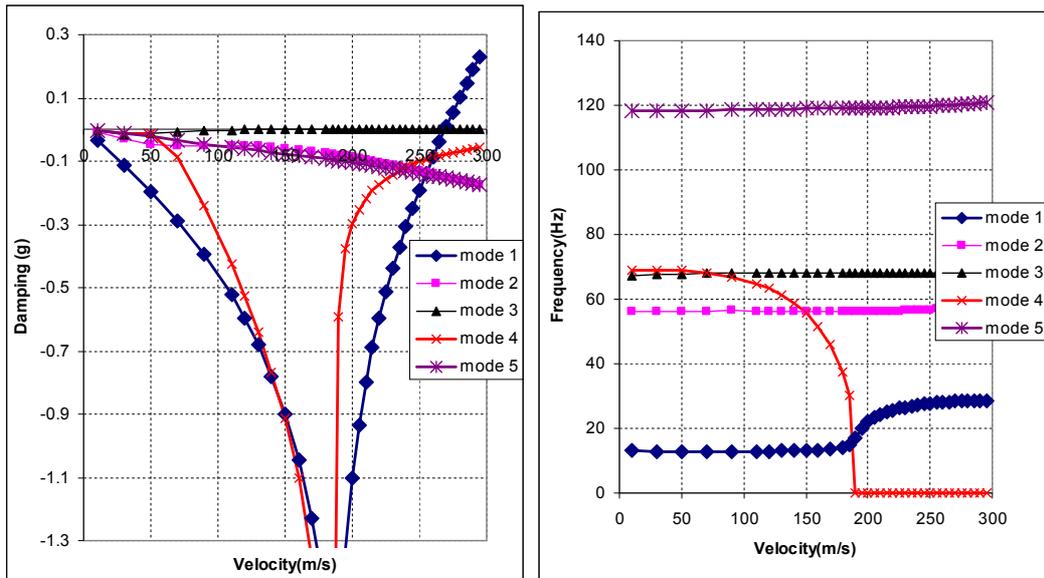
Figure 104:Damping and frequency versus speed curves for case 5 - gap is bridged by aero panels, symmetric analysis, pure epoxy property is assigned to Rohacell foam core
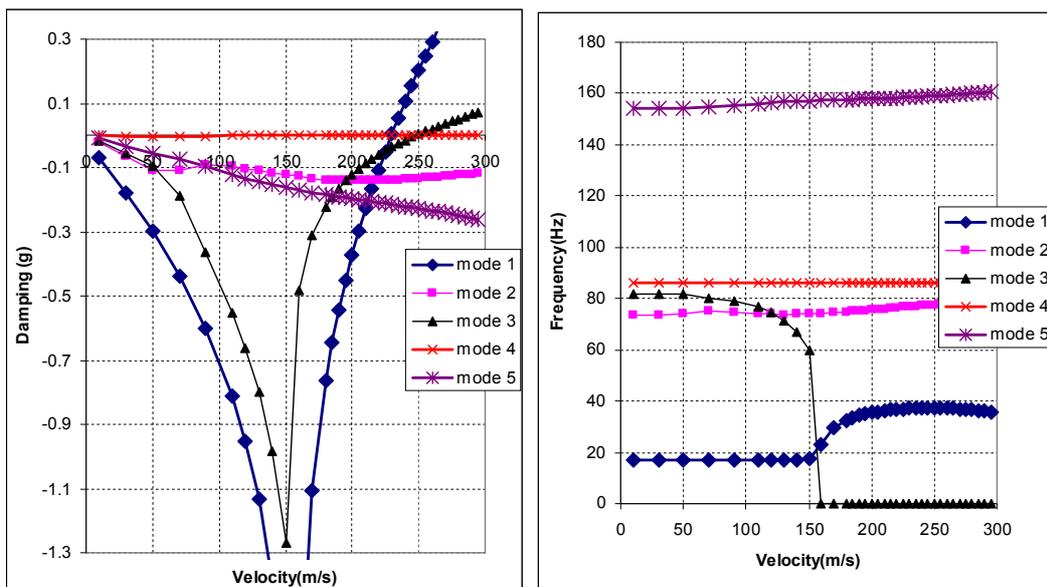
Figure 105:Damping and frequency versus speed curves for case 8 - gap is bridged by aero panels, symmetric analysis, pure foam property is assigned to Rohacell foam core

Figure 104 and Figure 105 show the damping and the frequency versus speed curves for cases 5 and 8. Figure 105 shows that for case 8 the flutter speed mode is still the first wing bending with a flutter speed below 250 m/s. In addition, the

divergence speed is seen to drop to about 250 m/s and the divergence speed mode became mode 3. Table 23 summarizes the critical speeds and flutter frequencies for cases 5 and 8. The flutter speed is approximately %15 lower when the foam core material used in the wing skins is assigned pure foam material property. It is noted that although the mode of flutter, which is the first wing bending mode, did not change the flutter frequency is seen to increase to about 37 Hz from 28 Hz. It is also noted that the reduction in the divergence speed is higher than %15 when the pure foam material property is assigned to the foam core material. This study shows that in composite air vehicles such as UAVs proper characterization of the materials used in the manufacturing is important and should not be overlooked. In the preliminary design material properties, which are highly dependent on the manufacturing method used, should either be characterized accurately or be assigned two extreme properties to determine a range for the critical aeroelastic stability speeds.

Table 23: Comparison of the aeroelastic stability analysis results

	Case 5	Case 8[f]
Input Mach number	0.78	0.67
Flutter speed (m/s)	269.2	229.7
Flutter frequency (Hz)	28.31	37.12
Flutter mode	Mode 1:Wing bending	
Flutter Mach number	0.783	0.668
Divergence speed (m/s)	> 300	247.8
Divergence mode	Mode 3: Wing torsion	

[f] Case 5 with pure Rohacell foam core material property assigned to the foam core

4.4. Aeroelastic analysis of Wing-Tail Plane Combination

In the second aeroelastic model tail boom and tail plane are added to the "wing only" model and aeroelastic stability analyses of the wing-tail plane combination has been performed for two different cases corresponding to course and fine aerodynamic meshes. In both cases course structural mesh and finite plate spline methods are used. Figure 106 shows the structural model use in the aeroelastic stability analysis of the wing-tail plane combination. In the aeroelastic stability analyses full model shown in Figure 106 is used to allow for possible future design modifications which

may destroy the symmetry of the structural model. One such modification could be the overlapping left and right wing front spar roots in the fuselage. To provide such an overlap, spars have to be offset in the aft and fore directions, thereby destroying the symmetry with respect to the centerline.
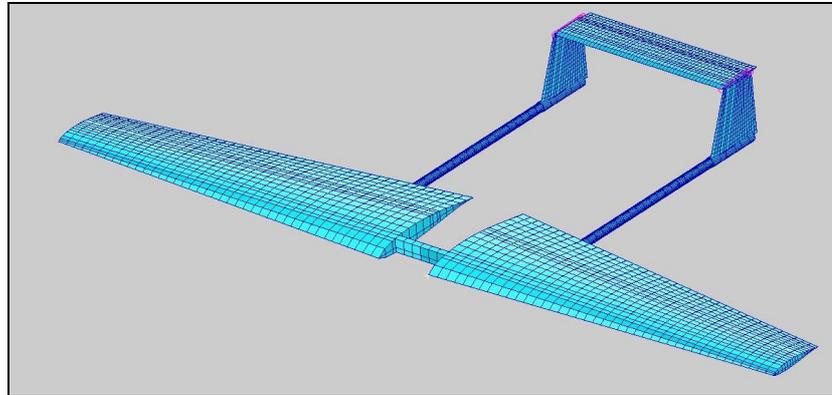
Figure 106: Wing-tail plane combination model used in aeroelastic stability analysis

Aeroelastic stability analysis of the wing-tail combination is performed at the sea level in the velocity range of 20-300 m/s. In the initial calculations, the Rohacell foam, which is used as the core material in the skins of the wing and tail, is assigned the property of pure epoxy and modal analysis is performed by the solution sequence 103 of Nastran. In the wing-tail combination structural finite element model boundary conditions at the spar roots are applied as described before.

Mode 1 ; 6.56 Hz   Mode 2 ; 8.20 Hz   Mode 3 ; 11.66 Hz   Mode 4 ; 13.07 Hz

Mode 5 ; 13.09 Hz   Mode 6 ; 35.37 Hz   Mode 7 ; 41.87 Hz   Mode 8 ; 47.34 Hz
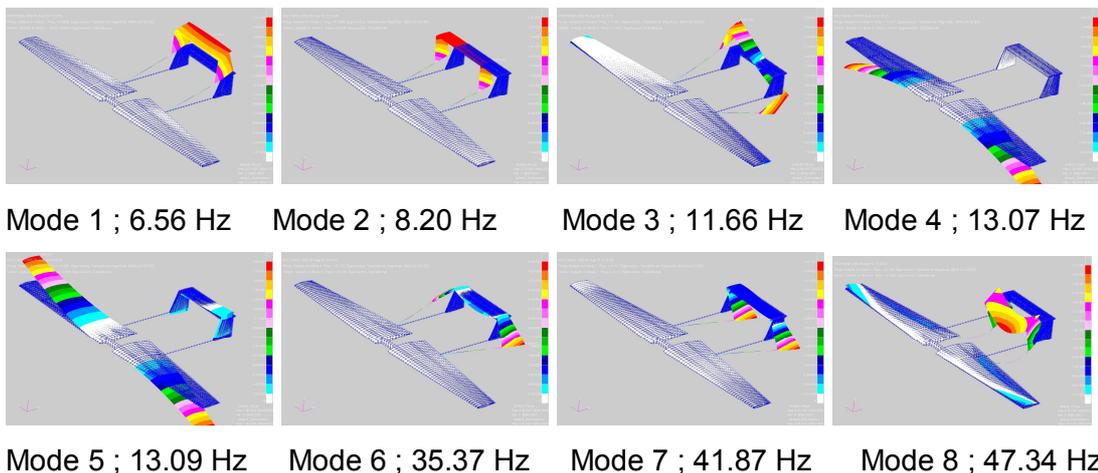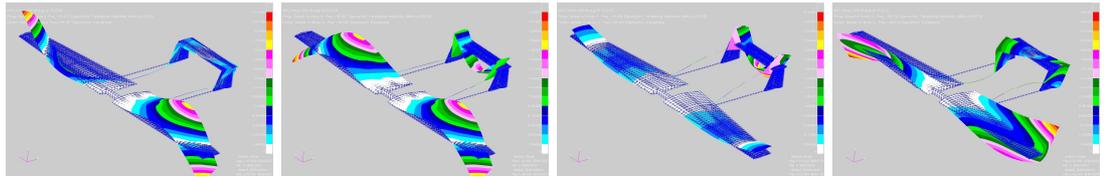
Mode 9 ; 56.16 Hz   Mode 10 ; 56.30 Hz   Mode 11; 58.46 Hz   Mode 12; 66.57 Hz
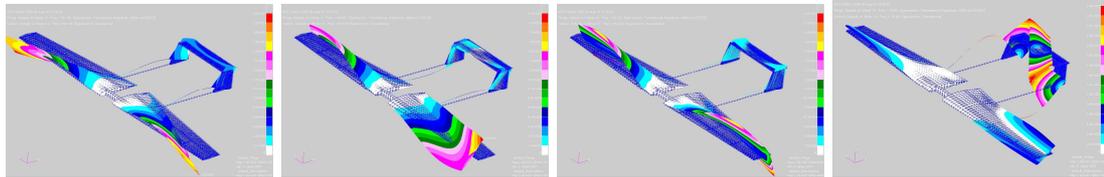
Mode 13 ; 68.15 Hz   Mode 14 ; 69.04 Hz   Mode 15 ; 69.33 Hz   Mode 16 ; 76.86 Hz

Figure 107: Modes shapes of the modes 1-16 of the wing tail plane combination

Table 24: First sixteen free vibration modes of the wing-tail combination

Mode #		Frequency (Hz)
1	6.56	Tail boom symmetric bending in the vertical direction
2	8.20	Tail boom symmetric bending in the horizontal direction
3	11.66	Tail boom antisymmetric bending in the vertical direction
4	13.07	Wing first symmetric bending
5	13.09	Wing first antisymmetric bending
6	35.37	Tail boom bending in the horizontal direction , horizontal and vertical tail bending
7	41.87	Tail boom bending in the horizontal direction and vertical tail bending
8	47.34	Tail boom bending in the vertical direction, horizontal tail bending
9	56.16	Wing second antisymmetric bending
10	56.30	Wing second symmetric bending, horizontal tail bending
11	58.46	Horizontal tail bending, tail boom bending in the vertical direction, wing symmetric bending
12	66.57	Wing antisymmetric torsion, horizontal tail torsion, tail boom bending in the vertical direction
13	68.15	Wing symmetric in-plane bending, wing antisymmetric torsion
14	69.04	Wing antisymmetric torsion, tail boom bending
15	69.33	Wing symmetric torsion
16	76.86	Tail plane torsion, tail boom bending in the vertical direction coupled with wing torsion

Figure 107 shows the first sixteen still air modes shapes of the wing-tail combination and the descriptions of the modes are tabulated in Table 24. Figure 107 shows that in some lower modes, wing and tail motions are almost uncoupled. It is also

118

observed that tail boom plays an effective role in most of the free vibration modes, as expected.

For the wing-tail plane combination fuselage is not included in the aeroelastic model as a body surface. Therefore, a gap forms between the left and the right wings similar to the "wing only" model. For the wing-tail plane model the effect of bridging the left and right wings by additional aerodynamic panels is also investigated, and for this reason two different aerodynamic models are prepared one with the gap and one with the bridging aerodynamic panels between the left and the right wings as shown in Figure 108.

(a) Aerodynamic model with a gap between the left and the right wings

(b) Aerodynamic model with bridging aerodynamic panels between the left and right wings
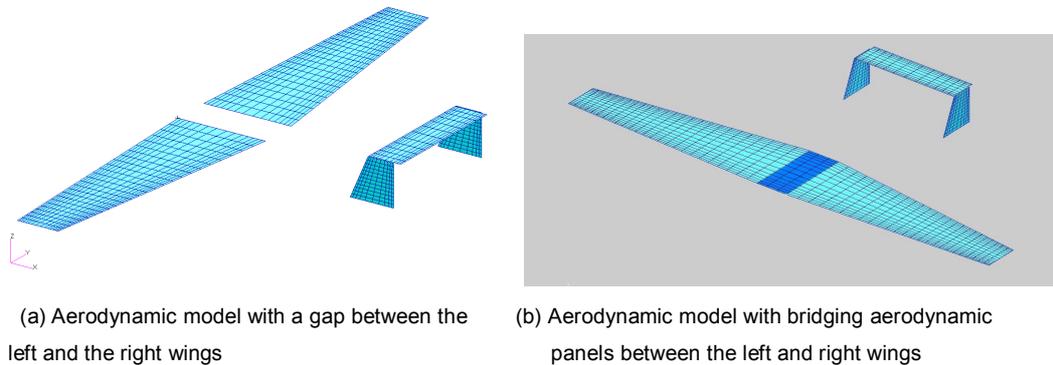
Figure 108: Aerodynamic models used in the aeroelastic model of the wing-tail plane combination

It should be noted that with the bridging aerodynamic panels, as shown in Figure 108 b, the aerodynamic model is still not realistic because the vortex lines from bridging aerodynamic panels pass through the tail plane. Although the strong vortex lines at the root chord lines of the wings are eliminated, vortex lines emanating from the bridging aerodynamic panels are not physical since in a realistic configuration fuselage body exists between the left and the right wings. However, since the horizontal tail is not co-planar with the wing surface, it is considered that the bridging aerodynamic panels will affect the aeroelastic analysis results significantly.

Another consideration with regard to aerodynamic modeling is the alignment of spanwise divisions between aerodynamic panels on the wing and on the horizontal tail. If the wing and tail are located in the same plane, all spanwise divisions of the tail must be aligned with those of the wing as shown in Figure 109. [31] It is noted in Ref. 31 that a violation of this requirement results in the vortex lines shed from the

wing cutting through the aerodynamic boxes of the tail. Since at the vortex line the aerodynamic influence is singular, this yields an unrealistically large downwash effect on the tail. This modeling restriction is also required if the distance d along the normal direction between the tail and the wing is less than the width (w) of the strip.
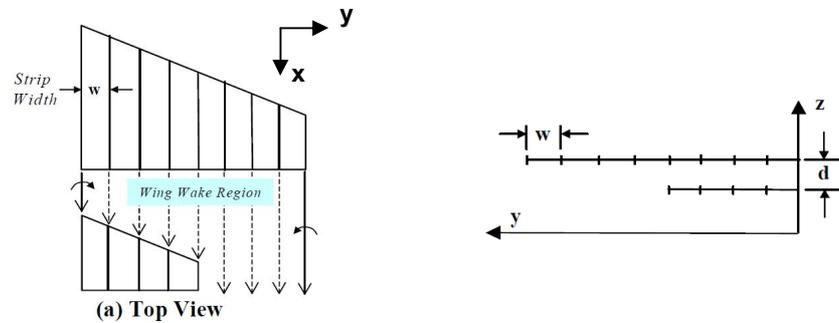
Figure 109: Alignment of spanwise divisions of wing-tail configuration

In the current design the distance between the horizontal tail plane and the wing surface is higher than the spanwise divisions used on the wing. Therefore, the alignment requirement can be relaxed and spanwise divisions on the wing and on the tail may not be aligned. In the present study, the effect of different aerodynamic modeling approaches on the aeroelastic analysis results is investigated by using four different aerodynamic models. These models are:

Model 1: Bridging aerodynamic panels do not exist between the wings and spanwise divisions are not aligned

Model 2: Bridging aerodynamic panels exist between the wings and spanwise divisions are not aligned

Model 3: Bridging aerodynamic panels do not exist between the wings and spanwise divisions are aligned

Model 4: Bridging aerodynamic panels exist between the wings and spanwise divisions are aligned

In the wing-tail plane combination model horizontal and vertical tail surfaces as well as wing surfaces are defined as the lifting surfaces as shown in Figure 108, and for each aerodynamic model aeroelastic analysis is performed using the course and the fine aerodynamic meshes. In the coarse aerodynamic mesh wing, horizontal tail and vertical tail surfaces have 25X15, 12X10 and 12x10 panels, respectively. In the fine aerodynamic mesh wing, horizontal tail and vertical tail surfaces have 40X20, 20X15 and 15x15 panels, respectively.

The spline points off the wing-tail combination model are shown in Figure 110. On the horizontal tail and vertical tail, the spline points are selected on the spars, tail boom-vertical tail connections and stiff horizontal-vertical tail intersections as shown in Figure 110. At this point it should be noted that since in the Doublet Lattice Method aerodynamic grids have only two degrees of freedom, possible in-plane translational or in-plane rotational motion of the tail plane will not be connected to the aerodynamic mesh.
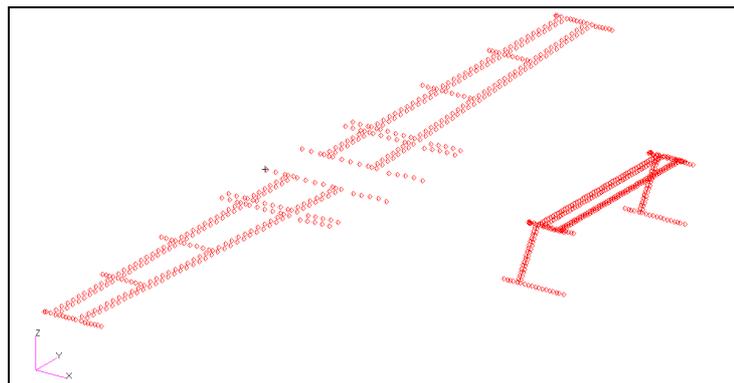
Figure 110: Spline point selection off the structural model for the wing-tail plane combination

In the aeroelastic stability analysis of the wing-tail plane combination twenty two modes are used in the PK method during the analysis performed by Nastran. Aeroelastic analysis solutions are presented for the four different aerodynamic modeling approaches. The summary of critical modes and speeds below 300 m/s is given in Table 25 for both coarse and fine aerodynamic meshes.

Table 25: Summary of critical modes of the wing-tail plane combinationg;Models 1-4

Model	Model 1 : Bridging panels <u>do not exist</u> and spanwise divisions <u>are not</u>					
Mesh	Coarse aero mesh			Fine aero mesh		
Flutter mode	Mode 1	Mode 8	Mode 15	Mode 1	Mode 8	Mode 15
Flutter speed (m/s)	272.5	239.6	269.7	272.2	240.8	269.3
Flutter frequency	30.55	36.74	33.9	30.4	36.5	33.7
Model	Model 2: Bridging panels <u>exist</u> and spanwise divisions <u>are not aligned</u>					
Mesh	Coarse aero mesh			Fine aero mesh		
Flutter mode	Mode 5	Mode 8	Mode 15	Mode 5	Mode 8	Mode 15
Flutter speed (m/s)	266	251.3	269.1	265.2	253	268.7
Flutter frequency	29	35.6	33.3	28.85	35.2	33.05
Model	Model 3: Bridging panels <u>do not exist</u> and spanwise divisions <u>are</u> <u>aligned</u>					
Mesh	Coarse aero mesh			Fine aero mesh		
Flutter mode	Mode 1	Mode 8	Mode 15	Mode 1	Mode 8	Mode 15
Flutter speed (m/s)	270.1	241.7	269.3	270.4	244.3	269.7
Flutter frequency	29.9	36.6	33.1	29.7	36.4	32.8
Model	Model 4: Bridging panels <u>exist</u> and spanwise divisions <u>are aligned</u>					
Mesh	Coarse aero mesh			Fine aero mesh		
Flutter mode	Mode 5	Mode 8	Mode 15	Mode 5	Mode 8	Mode 15
Flutter speed (m/s)	266	251.4	268.8	266.1	253.7	269
Flutter frequency	28.2	35.7	32.5	28	35.5	32.17

[9] Pure epoxy property is assigned to Rohacell foam core

For the first 8 modes, Figure 111- 114 show the damping and frequency versus speed curves of four models and Figure 115 shows the damping and frequency versus speed curves of modes 9-16 of model 4 which is considered to be the most appropriate aeroelastic model. In Figure 111-115, plots are given for the aeroelastic models with the fine aerodynamic mesh.
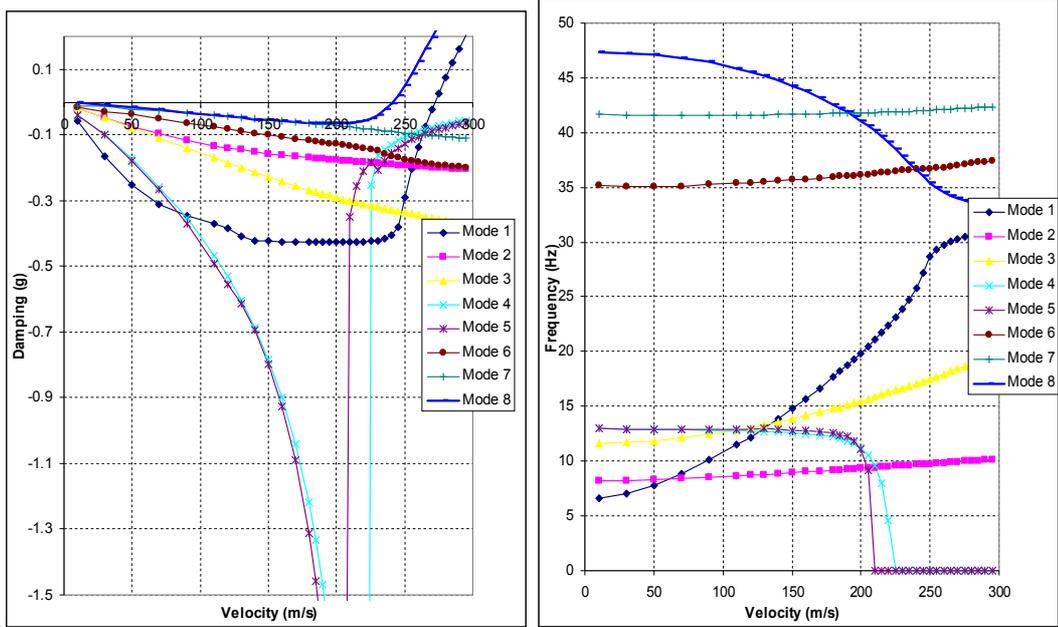
Figure 111: Damping and frequency versus speed curves for modes 1-8; Model 1
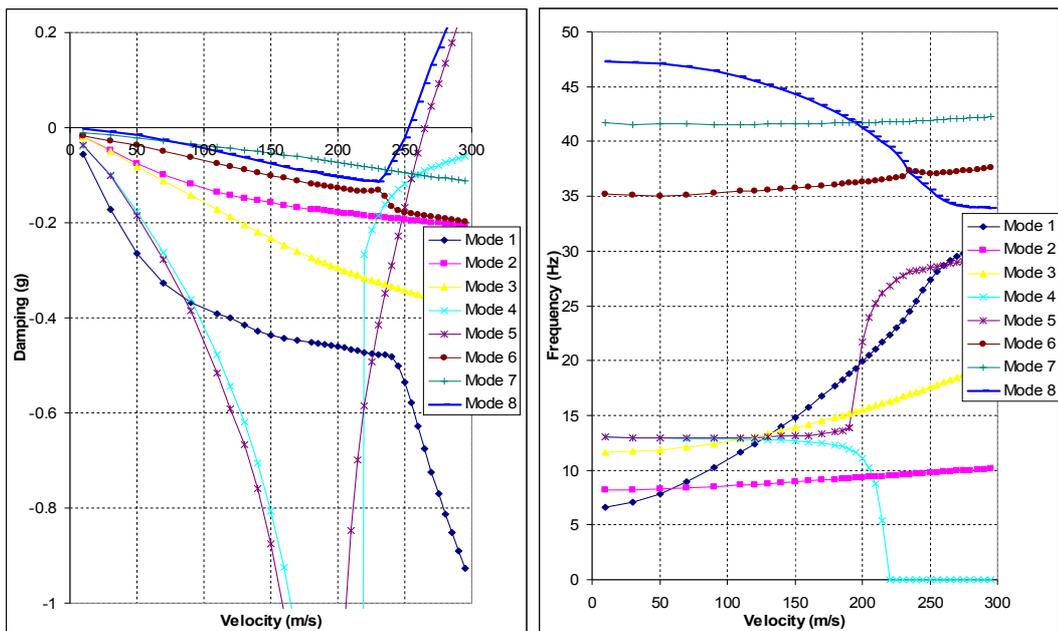
Figure 112: Damping and frequency versus speed curves for modes 1-8; Model 2
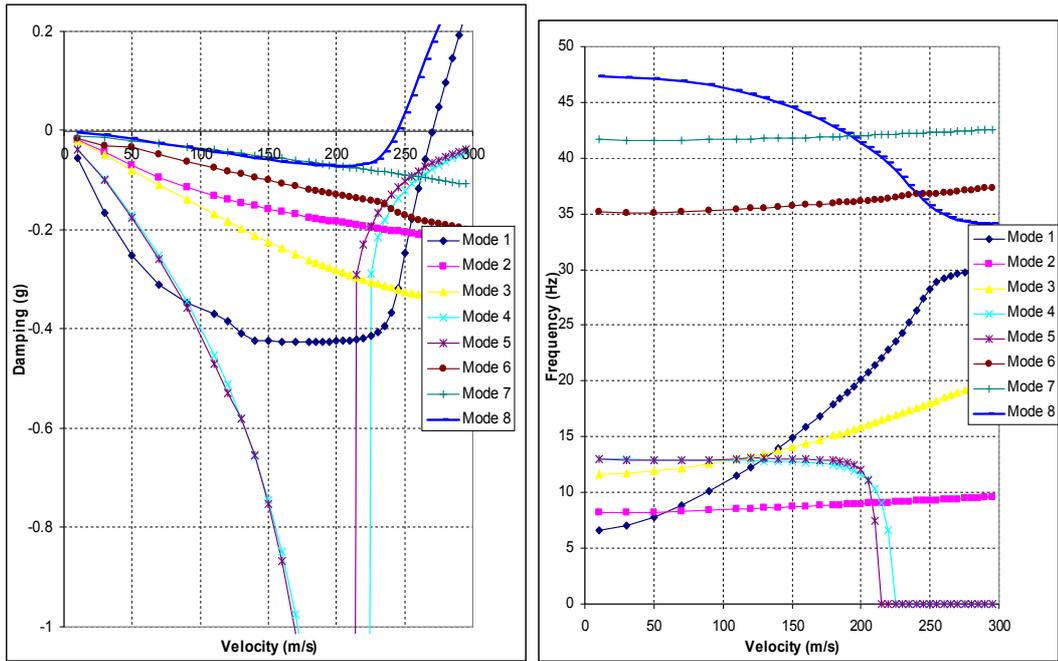
Figure 113: Damping and frequency versus speed curves for modes 1-8; Model 3
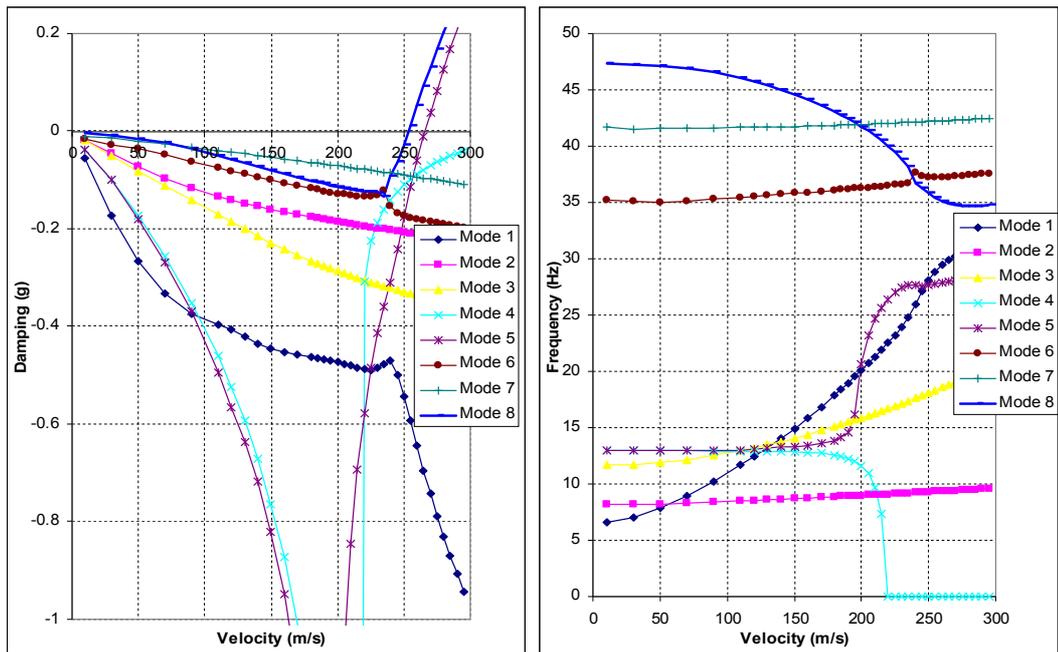
Figure 114: Damping and frequency versus speed curves for modes 1-8; Model 4
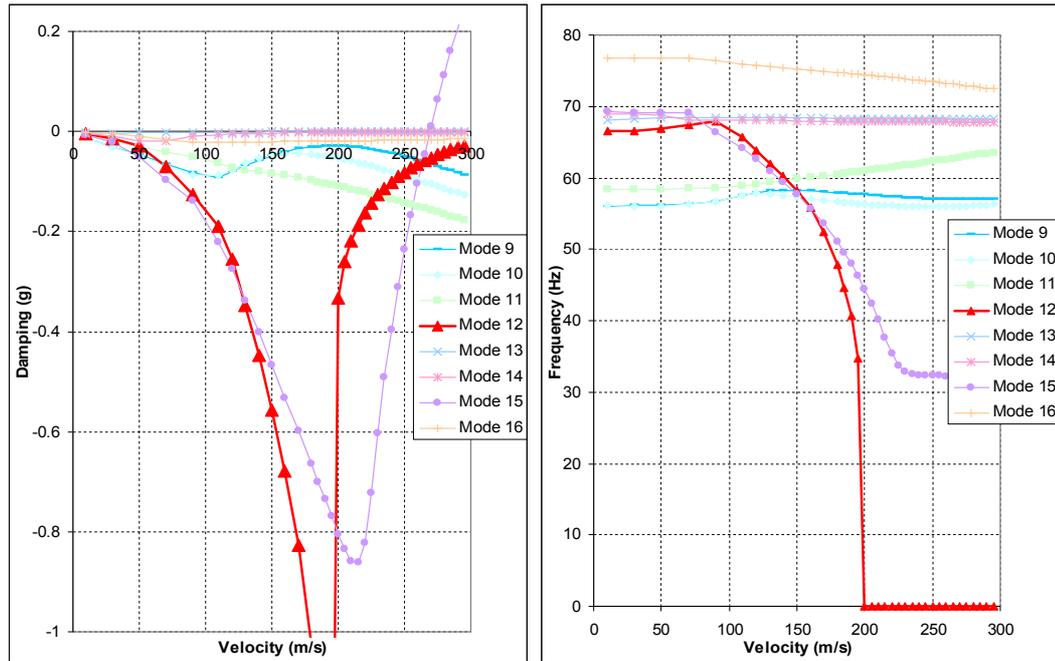
Figure 115: Damping and frequency versus speed curves for modes 9-16; Model 4

Based on the results summarized in Table 25 and damping/frequency versus speed curves shown in Figure 111-115, the following conclusions can be drawn:

-Aeroelastic models using the course and the fine aerodynamic meshes predicted the same flutter modes below 300 m/s, and flutter speeds and frequencies determined by the course and the fine aerodynamic meshes are very close to each other. Flutter speeds predicted by the aeroelastic model using the fine aerodynamic mesh are slightly higher than the flutter speeds predicted by the aeroelastic model using the coarse aerodynamic mesh.

-Modes 8 and 15 are predicted by the four models as the common flutter modes below 300 m/s. It is observed that flutter speed and frequency of mode 15 of the four models did not change appreciably.

-From the comparison of the results of model 2 and model 4, it can be concluded when the gap between the left and right wings are bridged with aerodynamic panels, the alignment of spanwise divisions on the wing and the horizontal tail does not

125

cause appreciable differences in flutter speeds. Both models predict the same critical modes below 300 m/s. Similarly, comparison of the results of models 1 and 3 show that the alignment of the spanwise divisions on the wing and the horizontal tail has no significant effect on the critical flutter modes and flutter speeds below 300 m/s. Both models predict the same critical modes below 300 m/s. The present finding supports the comment that if the distance between the horizontal tail plane and the wing surface is higher than the spanwise divisions used on the wing, the alignment requirement can be relaxed and spanwise divisions on the wing and on the tail may not be aligned.

-Comparison of the results of models 1 and 2 or 3 and 4 shows that the use of bridging panels between the wings has an effect on the flutter modes and speeds. The highest difference in the flutter speed is predicted for mode 8 for which the flutter speed increases by approximately %4 when bridging panels are used between the left and the right wings. When the bridging panels are not used, models 1 and 3 predict mode 1 as one of the flutter mode whereas when the bridging panels are included models 2 and 4 predict mode 5 as one of the flutter mode.

-Divergence instability is not predicted by any of the aeroelastic models below 300 m/s. For model 4 Figure 114 and Figure 115 show that the frequency of modes 4 and 12 become zero at about 200 m/s but with negative damping until above 300 m/s. When the damping trends of modes 4 and 12 are traced it can be commented that mode 12 will cross the zero damping line first and most likely mode 12 will be the divergence mode with a divergence speed higher than 300 m/s.

For the wing-tail combination model another case study (model 5) is performed by using pure Rohacell foam properties for the core material used in the skins of the wing, horizontal and vertical tail. Aeroelastic analysis is performed by using the coarse aerodynamic mesh, and model 4 is modified and pure foam material properties specified by the foam manufacturers are assigned to the core material used in the skins of the wing, horizontal and vertical tail. Table 26 summarizes the critical speeds and flutter frequencies for models 4 and 5 below 300 m/s. For the new model 5 natural frequencies and corresponding mode shapes changed, therefore mode numbers are shown by an asterisk near the mode numbers.

However, both models predicted the same mode (mode 8 of model 4 and mode 8* of model 5) as the mode with the lowest flutter speed. When the foam core material used in the wing skins and tails is assigned pure foam material property, flutter speed decreased by approximately %12. Figure 116 and Figure 117 show the damping and the frequency versus speed curves for model 5. From Figure 116 it can be seen that for model 5 flutter mode is 8, which is coupled tail boom bending in the vertical direction and horizontal tail bending. Modes 11* and 12* of model 5 are the symmetric and anti-symmetric torsional wing modes, respectively. It is seen that when the foam core is assigned pure foam material property, the critical wing anti-symmetric bending mode 5 of model 4 is no longer predicted by model 5 as one of the critical modes below 300 m/s.

It is noticed that model 5 also does not predict divergence instability below 300 m/s. However, from the damping trend of mode 4, which has zero frequency above 150 m/s mode 4 will likely be the divergence instability mode with a divergence speed slightly higher than 300 m/s.

Table 26: Comparison of the aeroelastic stability analysis results

Model	Model 4			Model 5[h]		
Flutter mode	Mode 5	Mode 8	Mode	Mode 8*	Mode	Mode
Flutter speed (m/s)	266	251.4	268.8	221.3	243.6	243.6
Flutter frequency	28.2	35.7	32.5	57.1	40.9	36.6

[h] Model 4 with pure Rohacell foam core material property assigned to the foam core
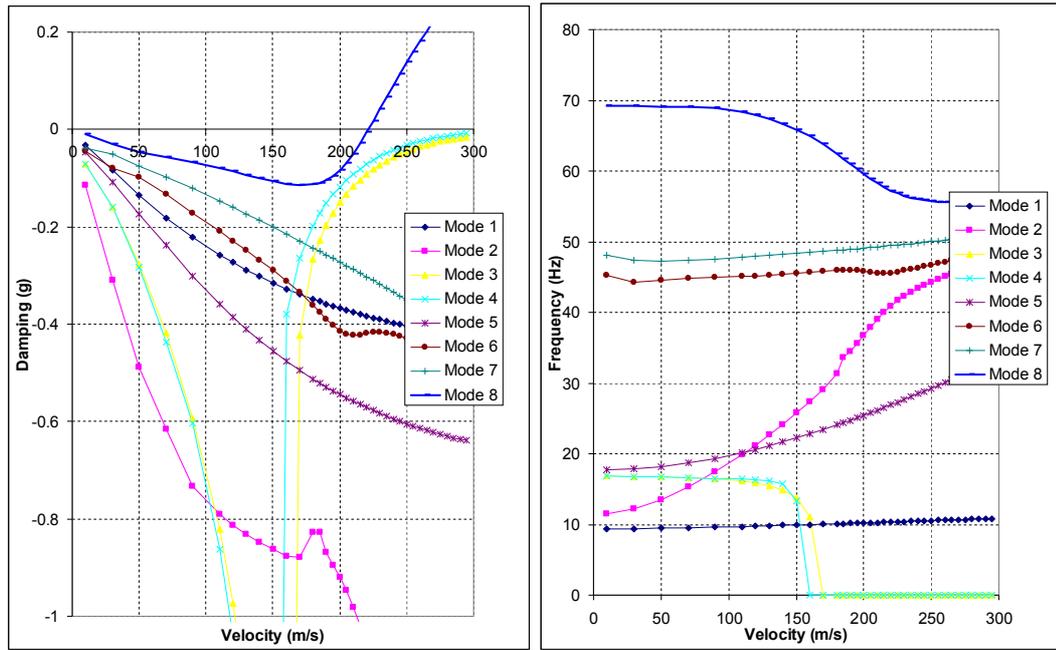
Figure 116: Damping and frequency versus speed curves for modes 1-8; Model 5-pure foam property is assigned to Rohacell foam core
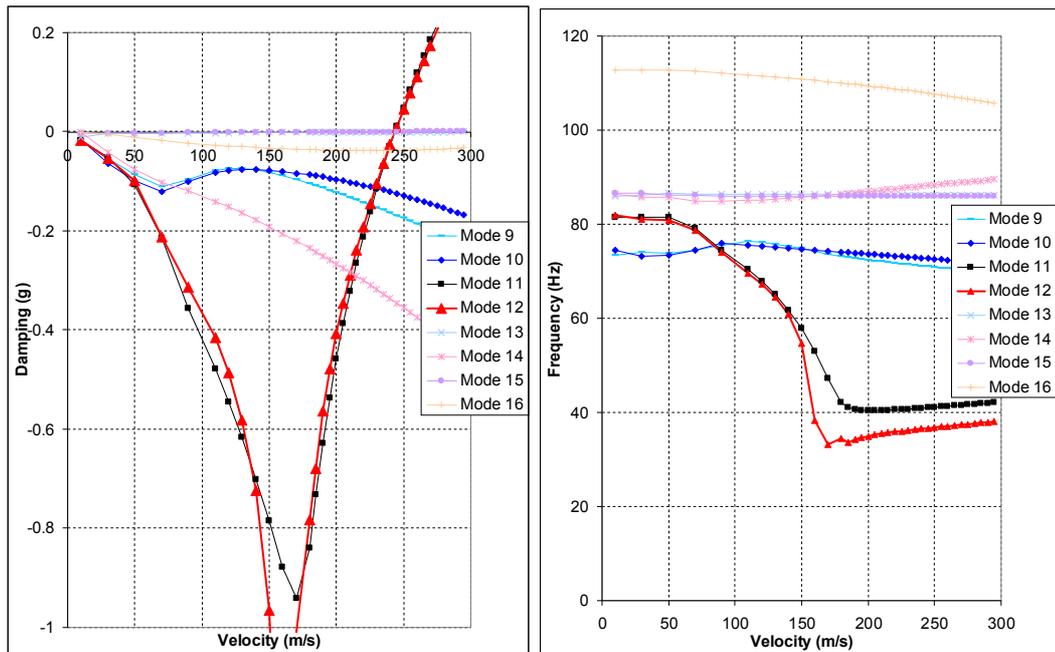
Figure 117: Damping and frequency versus speed curves for modes 9-16; Model 5-pure foam property is assigned to Rohacell foam core

Based on the aeroelastic stability analysis results obtained by the "wing only" and wing-tail combination models the following conclusions can be inferred:

-The addition of the tail boom and the tail plane into the aeroelastic model introduces tail plane modes which are highly coupled with the tail boom motion. The most critical aeroelastic instability mode is associated with mode 8 which is predominantly tail boom bending in the vertical direction coupled with horizontal tail bending. Lowest flutter speed, associated with mode 8, decreased by approximately %7 compared to the lowest flutter speed calculated by the "wing only" model.

-Figure 104 and Figure 114 show that sub-critical damping trends of the symmetric wing bending modes, mode 1 in "wing only" and mode 4 in wing-tail combination models, are similar. However, Figure 114 clearly shows that with the inclusion of the tail boom and tail plane into the aeroleastic model, the critical aeroelastic stability speed associated with the wing bending mode increases. In addition, based on the damping and frequency trends of mode 4 of the wing-tail combination model, the instability associated with the symmetric wing bending mode will no longer be flutter but instead divergence.

-Figure 104 and Figure 115 show that sub-critical damping trends of the symmetric wing torsion modes, mode 4 in "wing only" and mode 15 in wing-tail combination models, are similar in the "wing only" and wing tail plane combinations models. However, Figure 115 clearly shows that with the inclusion of the tail boom and tail plane into the aeroleastic model, the critical aeroelastic stability speed associated with the symmetric wing torsion mode decreases. In addition, based on the damping and frequency trends of mode 15 given in Figure 115, the instability associated with the symmetric wing torsion mode is longer divergence but instead flutter.

-Figure 102 and Figure 114 show that sub-critical damping trends of the anti-symmetric wing bending modes, mode 1 in "wing only" and mode 5 in wing-tail combination models are similar. However, Figure 114 clearly shows that with the inclusion of the tail boom and tail plane into the aeroleastic model, the critical aeroelastic stability speed associated with the first wing anti-symmetric bending mode decreases. In addition, based on the damping and frequency trends of mode 5 of the wing-tail combination model, the instability associated with the first anti-symmetric wing bending mode will no longer be divergence but instead flutter.

-Figure 102 and Figure 114 show that sub-critical damping trends of the anti-symmetric wing torsion modes, mode 4 in "wing only" and mode 12 in wing-tail combination models are similar. However, Figure 115 clearly shows that with the inclusion of the tail boom and tail plane into the aeroleastic model, the critical aeroelastic stability speed associated with the first wing anti-symmetric torsion mode increases. In addition, based on the damping and frequency trends of mode 12 of the wing-tail combination model, the instability associated with the first anti-symmetric wing torsion mode will no longer be flutter but instead divergence.

4.5. Aeroelastic analysis of Whole UAV

Aeroelastic analysis of the wing-fuselage-tail combination is performed for the free airplane model. Figure 118 shows the structural finite element models of the unmanned air vehicle. Figure 118 shows the full airplane model with the fuselage modeled by beam elements. For sections of the fuselage which is composed of skins made of woven fabric composite materials, equivalent Young's moduli along the fuselage axis are determined by Nastran automatically when creating composite laminate definitions for the skins. Since frames are either full or very thick compared to the composite skin, frame sections are assigned appropriate wood material properties. Beam sections of the fuselage are created by the Patran preprocessor by referencing the sectional cuts taken from the fuselage. In the beam fuselage model of the airplane, fuselage is connected to the wing using RBE2 [30] elements which provide rigid connections between the selected degrees of freedom. Rigid connections are made between appropriate nodes on the spar roots and the nodes of the beam elements which represent the main bulkheads on the fuselage.
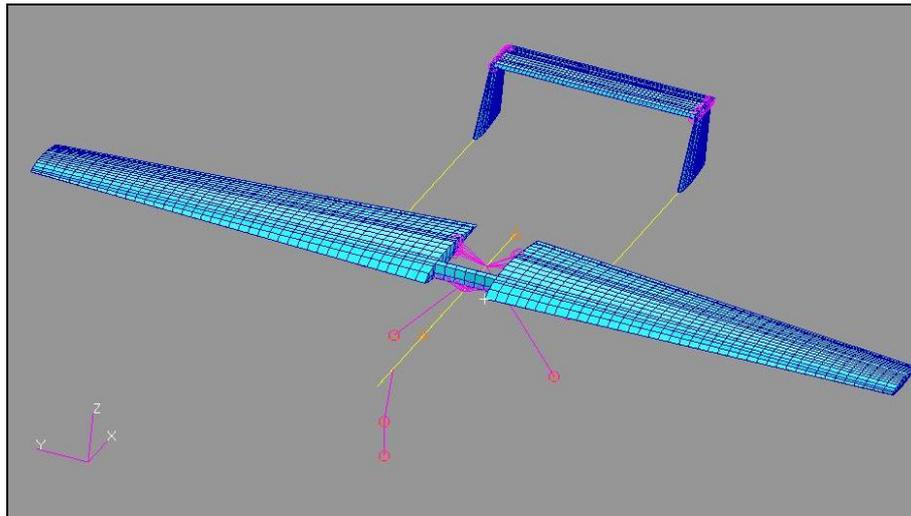
Figure 118: Structural finite element model of the wing-fuselage-tail combination

Aeroelastic analysis of the wing-fuselage-tail combination is performed by including the rigid body modes of the airplane. In the finite element model Rohacell foam, which is used as the core material in the skins of the wing and tail plane, is assigned pure epoxy property and modal analysis is performed. Figure 119 shows the first sixteen flexible vibration modes of the aircraft model. During the modal analysis to capture similar flexible modes as the wing-tail plane combination model, the upper frequency limit is adjusted accordingly during the modal analysis of the full airplane model. Comparison of still air vibration modes of the wing - tail plane combination model (Figure 107) and full airplane model (Figure 119) shows that both models predict similar vibration modes with some differences in the natural frequencies and the mode shapes. From the mode shapes it is clearly seen that fuselage motions are small due to the high inertia and stiffness of the fuselage and only in modes 1 and 10 one can distinguish the motion of the fuselage clearly. However tail booms, which have very small inertia compared to the fuselage, show significant motion in almost all vibration modes of the airplane.

| Mode 1 ; 8.08 Hz | Mode 2 ; 9.13 Hz | Mode 3 ; 11.68 Hz | Mode 4 ; 13.75 Hz |

| Mode 5 ; 29.85 Hz | Mode 6 ; 35.38 Hz | Mode 7 ; 41.92 Hz | Mode 8 ; 48.22 Hz |

| Mode 9 ; 57.27 Hz | Mode 10 ; 57.57 Hz | Mode 11 ; 58.38 Hz | Mode 12 ; 64.98 Hz |

| Mode 13 ; 68.03 Hz | Mode 14 ; 72.98 Hz | Mode 15 ; 73.14 Hz | Mode 16 ; 78.9 Hz |
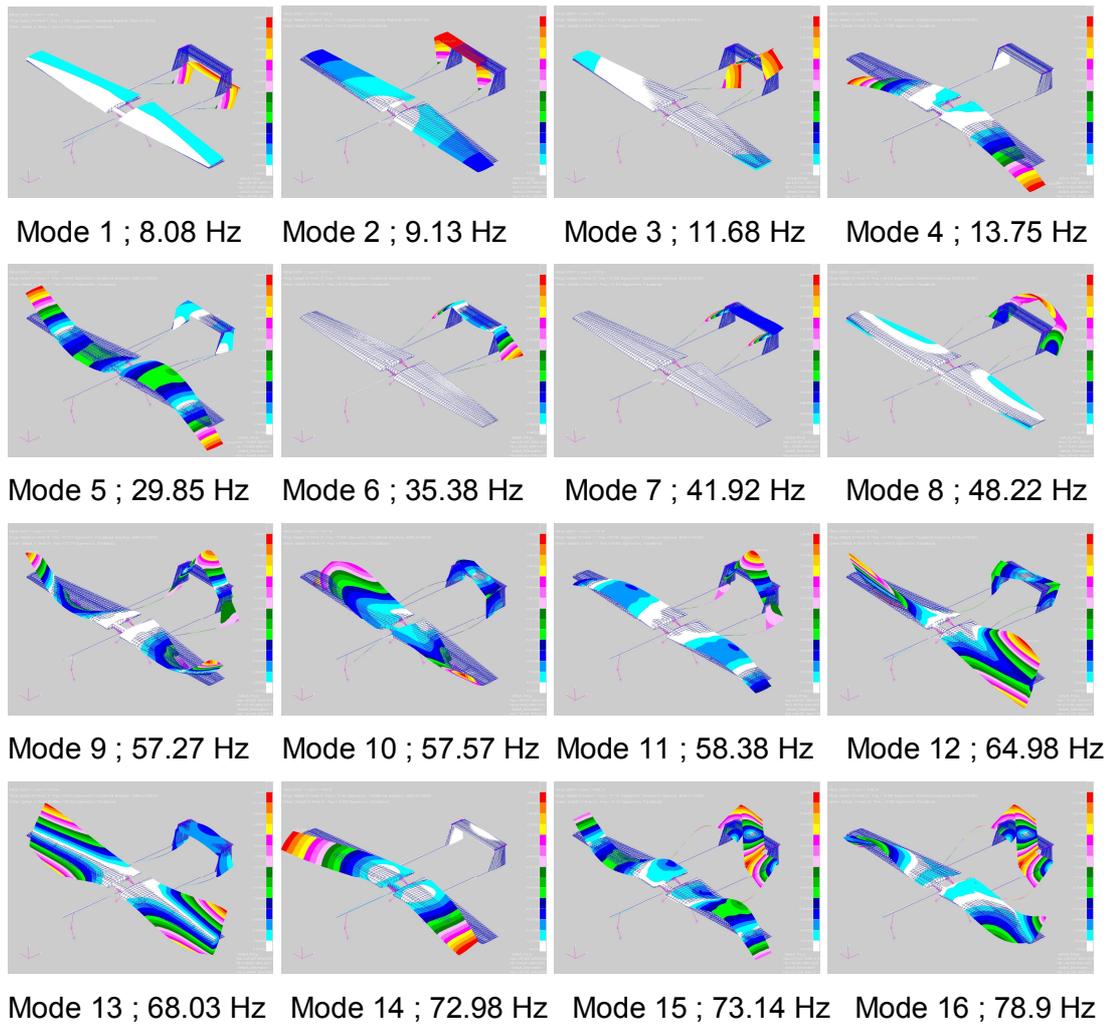
Figure 119: Modes shapes of the modes 1-16 of the wing-fuselage-tail plane combination

In the aerodynamic model of the full airplane, fuselage body is idealized as slender and interference elements in combination and subsonic wing-body interference theory is used. [24] Slender body elements account for the forces arising from the motion of the body and it is used to represent the lifting characteristics of the body. Interference body elements are used to account for the interference among all bodies and panels by providing a surface through which the boundary condition of no flow is imposed. The primary wing-body interference is approximated by a system of images of the Doublet-Lattice-Method trailing vortices and doublets within a cylindrical interference body that circumscribes each slender body. The secondary wing-body interference that results from the Doublet-Lattice-Method bound vortices

and doublets is accounted for by a line of doublets located on the longitudinal axis of each slender body.[22] Constant cross-section interference tube in the calculation of the velocities induced by the residual doublets, which are located along the axis of the body, is found to be sufficient based on the experience that residual flow is small compared to slender body flow field. The details of the slender body theory and wing-interference theory are given in [22] and [24]. Figure 120 shows the idealization of the aerodynamic model of the air vehicle with aerodynamic panels and body surfaces. In the aerodynamic model body elements and wing panels are aligned as shown in Figure 120, therefore mesh density of the body elements is increased along the wing-body junction. Since tail booms have small diameter they are not included in the aerodynamic model as body surfaces.
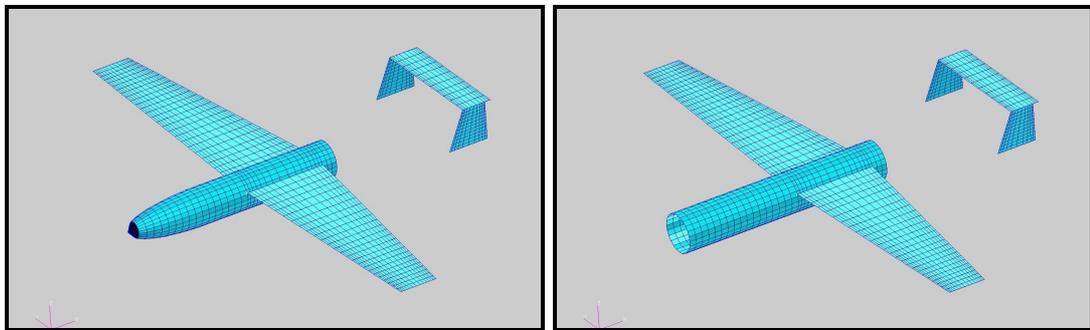
(a) Slender body elements and wing panels   (b) Interference body elements and wing panels

Figure 120: Slender body and interference body elements for the fuselage

To couple the fuselage body to the beam finite element model of the fuselage structure infinite beam splines are used. Figure 121 shows the grids, used in the definition of beam spline grids, on the beam finite element model of the fuselage and on the slender body.
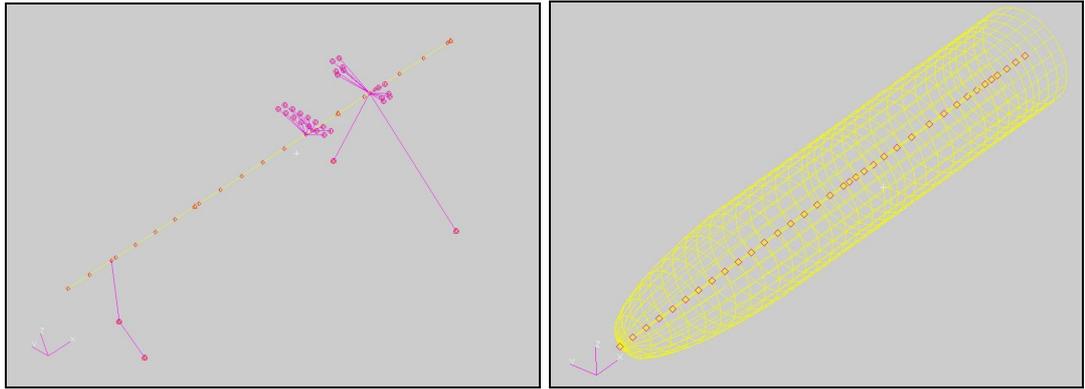
(a) Structural grids of the beam model   (b) Aerodynamic grids of the slender body

Figure 121: Beam spline grids on the structural and aerodynamic model of the fuselage

In the aeroelastic stability analysis of the wing-fuselage-tail plane model twenty two modes, including the rigid body modes, are used in the PK method during the analysis performed by Nastran. The summary of critical modes and speeds below 300 m/s is given in Table 27. Figure 122-124 show the damping/frequency versus speed curves for the first 16 modes. The most critical mode is identified as mode 4 which is symmetric wing bending.

Table 27: Summary of critical modes of the wing-fuselage-tail plane combination

Flutter mode	Mode 4	Mode 5	Mode 8	Mode 13
Flutter speed (m/s)	256	266.1	259.6	268.5
Flutter frequency (Hz)	7.46	30.22	36.49	27.93
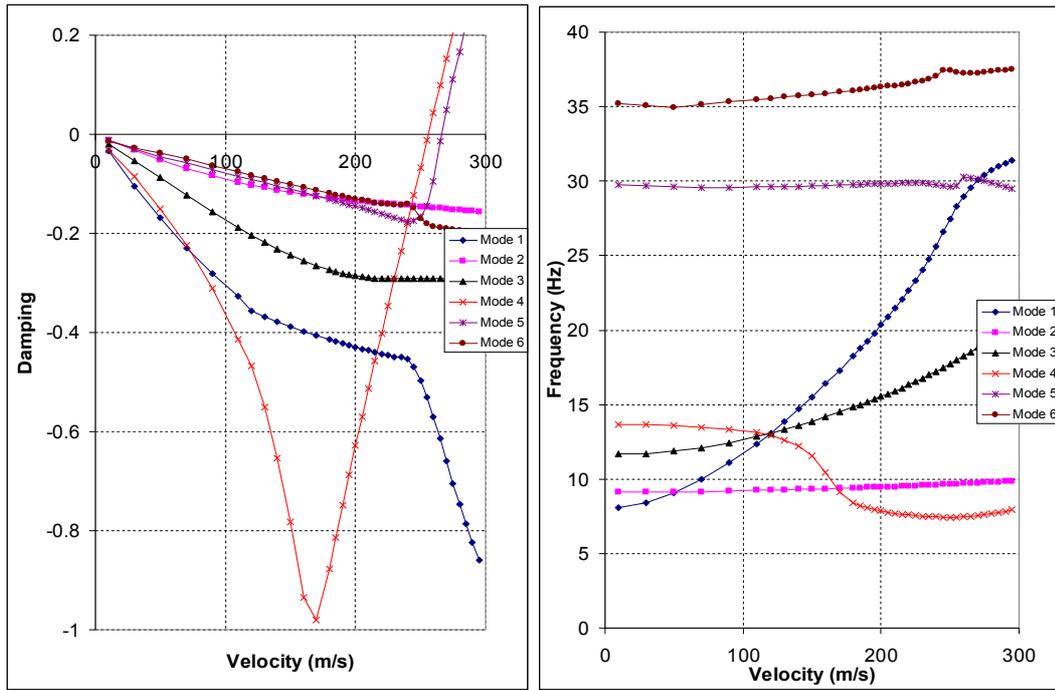
Figure 122: Damping and frequency versus speed curves for modes 1-6 of full airplane model
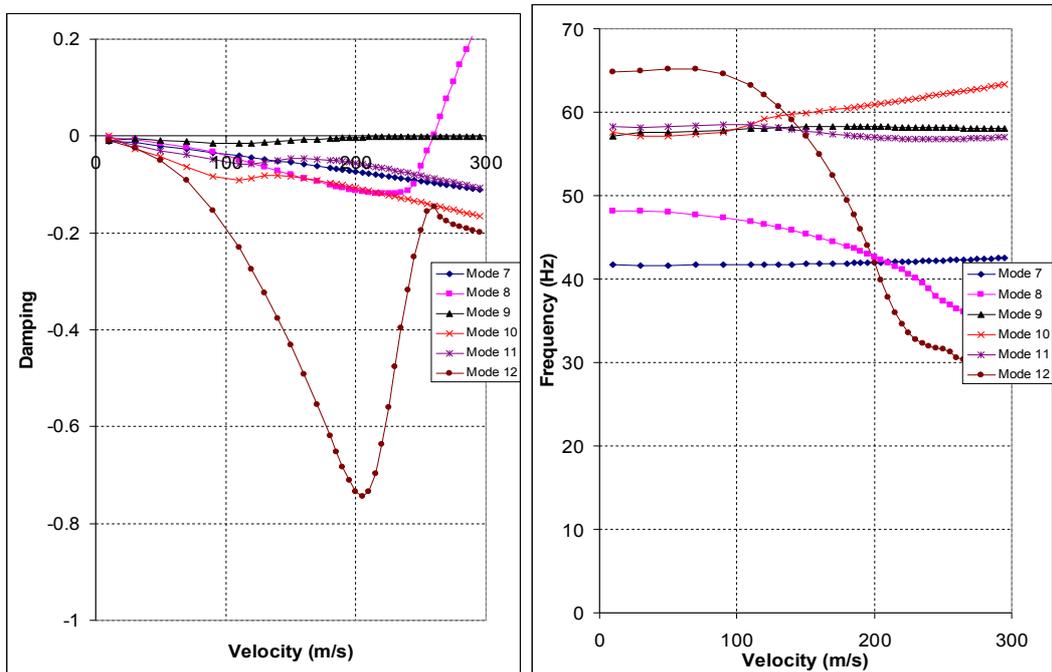
Figure 123: Damping and frequency versus speed curves for modes 7-12 of full airplane model
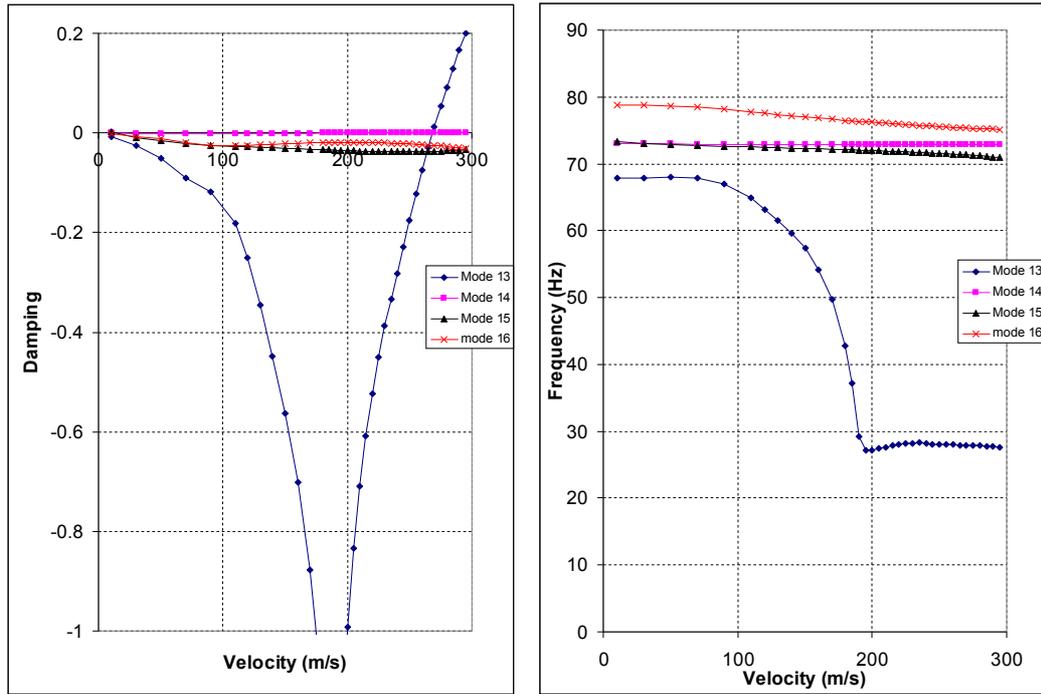
Figure 124: Damping and frequency versus speed curves for modes 13-16 of full
airplane model

Figure 125 compares the critical flutter modes, speeds and frequencies for the wing-
tail plane combination and full airplane models. Figure 125 shows that anti-
symmetric wing bending, horizontal tail/tail boom bending and wing symmetric
torsion modes are predicted by both aeroelastic models as the common critical
modes below 300 m/s. Aeroelastic model of the full airplane also predicts first wing
bending mode (mode 4) as the additional critical flutter mode below 300 m/s. First
wing bending mode was also predicted as the critical flutter mode of the "wing only"
model in symmetric aeroelastic analysis. For the wing-tail plane combination model,
first wing bending mode was predicted as the divergence instability mode with a
divergence speed above 300 m/s. The reason for the common flutter modes, which
are predicted by the wing-tail plane combination and full airplane aeroelastic models
with very close flutter speeds, is attributed to the low flexibility of fuselage structure.
Low flexibility of the fuselage structure is evident from the still air mode shapes of
the full airplane, as shown in Figure 119. Most of the still air mode shapes show very
little fuselage motion compared the rest of the airplane structure and this is an
indication of the rigidity of the fuselage structure.

Mode 8 of both models is the tail boom bending coupled with horizontal tail bending vibration. The flutter speed and flutter frequency associated with mode 8 is seen to increase slightly when fuselage is added to the aeroelastic model. The reason for the slight increase of the flutter speed could be due to the additional positive damping provided by the elastic fuselage structure. However, it should be noted that in mode 8 of vibration vertical tails exhibit in-plane motion which is not coupled to the aerodynamic mesh because in the Doublet Lattice Method aerodynamic grids have only two degrees of freedom and in-plane translational or in-plane rotational motion of vertical tail structure is not connected to the aerodynamic mesh. Therefore, mode 8 results may have more error compared to the other flutter modes.

Mode 5 of both models is the anti-symmetric wing bending mode. However, for the wing-tail plane combination model anti-symmetric wing bending mode does not have a nodal line whereas full airplane model has a chord-wise nodal line. The reason for the disappearance of the nodal line in the wing-tail plane combination model could be due to rigid end connections at the spar roots. When fuselage is added to the aeroelastic model, wing root connection nodes are tied to the fuselage by multi point constraint elements. Therefore, wing root is more flexible because fuselage is an elastic beam and wing is allowed to bend more freely near the root. The consequence of increased flexibility at the wing root is the occurrence of chord-wise nodal line for the anti-symmetric wing bending mode. Whereas in the wing-tail plane combination model nodes on the front and rear spar ends are fixed as explained before, therefore wing root is not allowed to bend easily. Restriction of the bending of the wing root prevents the formation of nodal line in the anti-symmetric wing bending vibration mode.

(a)

Mode 5	Mode 8	Mode 15
Flutter speed: 266.1 m/s	Flutter speed: 253.7 m/s	Flutter speed: 269 m/s
Flutter Freq. : 28 Hz	Flutter Freq. : 35.5 Hz	Flutter Freq. : 32.17 Hz

(b)

Mode 4	Mode 5	Mode 8	Mode 13
Flutter speed: 256 m/s	Flutter speed: 266.1 m/s	Flutter speed: 259.6 m/s	Flutter speed: 268.5 m/s
Flutter Freq. : 7.46 Hz	Flutter Freq. : 30.22 Hz	Flutter Freq. : 36.49 Hz	Flutter Freq. : 27.93 Hz
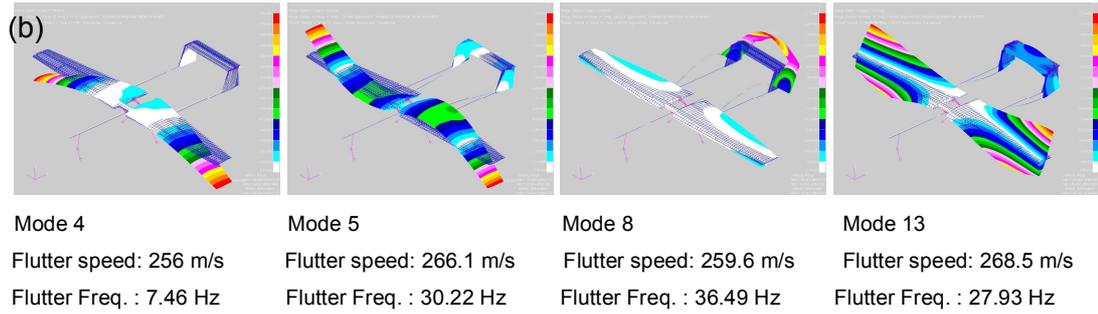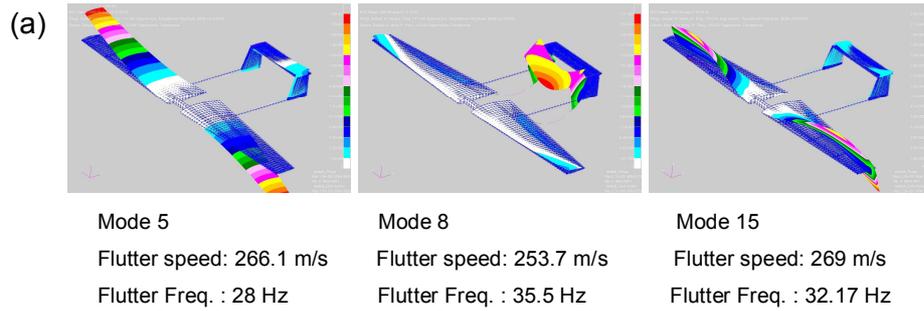
Figure 125: Comparison of critical flutter modes (a) wing-tail plane combination model (b) full airplane model

4.6. Aeroelastic analysis of Whole UAV with Control Surfaces

The last aeroelastic analysis is performed for the full airplane with the wing control surfaces included. Finite element model of the wing control surfaces which have continuous hinge axis is shown in Figure 126. Hinges are modeled by MPC [30] elements which are defined between the coincident nodes on the control surface and the wing along the hinge axis. The analysis coordinate frame of the coincident nodes on the control surface is selected as the local coordinate system which has one of its axis aligned with the hinge axis, as shown in Figure 126. Hinge axis (y1) rotation is taken as the independent degree of freedom and the remaining degrees of freedom are taken as dependent. To simplify the modeling, servo actuator-control arm-operating point combination is modeled by an equivalent torsional spring with a very high spring constant to simulate the effect of the torque provided by the servo actuator which keeps the control surface at the desired angular position. It is also assumed that the stall torque of the servo actuator is large enough to resist the aerodynamic torque at the high speed regime where aeroelastic instabilities occur.

To decide on the high stiffness constant of the torsional spring an experiment is performed to determine a reference torsional spring constant of the actuator-control arm-operating point combination to by placing weights on the control surface and measuring the rotation of the control surface when the servo actuator is powered up but when no attempt is made to prevent the rotation of the control surface by driving the servo actuator. This reference value is then multiplied by a large factor to give a constant torsional stiffness constant which is used to model servo actuator-control arm-operating point combination by a simplified first order system. As shown in Figure 126 torsional spring is modeled by the CBUSH element which is created between the two coincident nodes on the wing and on the control surface at the servo actuator arm - operating point location.

Coupling of aerodynamic and structural meshes on the control surfaces is accomplished by creating finite plate spline between the aerodynamic panels on the control surface and the structural grids on the upper surface of the control surface, as shown in Figure 127 for the flap. It should be noted that coincident nodes existing on the control surface along the hinge line are used in the spline definition for the control surface and coincident nodes existing on the wing surface along the hinge line are used in the spline definition for the particular wing section.
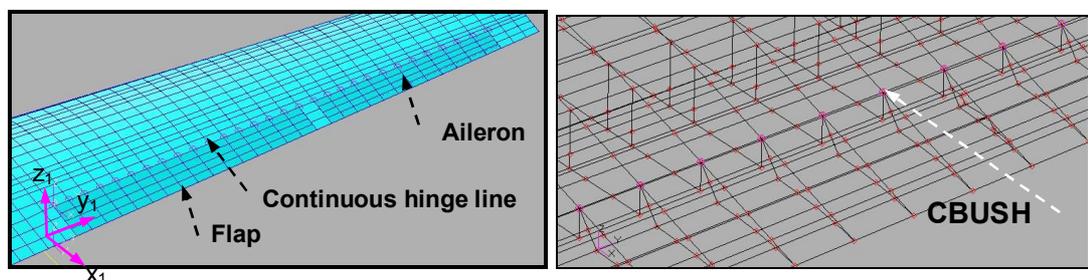
Figure 126: Description of control surface model (a) Continuous hinge line (b) Torsional spring
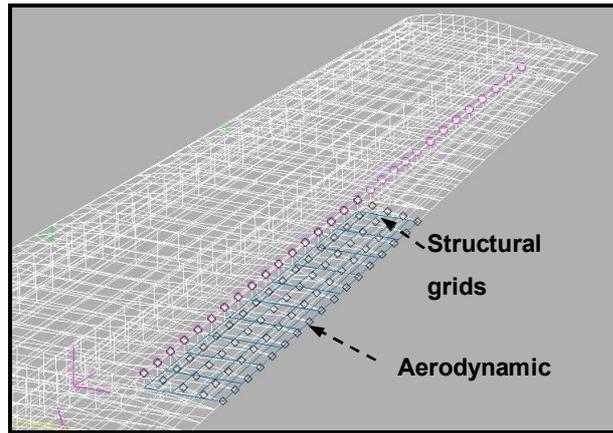
Figure 127: Spline definition for the control surfaces

In the aeroelastic stability analysis of the full airplane with the wing control surfaces twenty four modes are included. The summary of critical modes and speeds below 300 m/s is given in Table 28.

Table 28: Summary of critical modes of the full airplane with wing control surfaces

Flutter mode	**Mode 4**	**Mode 5**	**Mode 6**	**Mode 10**	**Mode 13**
Flutter speed (m/s)	261.3	253.9	288.2	289.8	112.4
Flutter frequency (Hz)	7.81	29.77	35.73	31.57	56.86

Figure 128-130 give the damping and frequency plots for the first 18 flexible modes. The critical modes below 300 m/s are identified as modes 4,5,6,10 and 13. For the most critical four modes 4,5,6 and 13, Figure 131 and Figure 132 show the spline verification at the still air vibration modes. In Figure 131 and Figure 132 red lines show the motion of the aerodynamic mesh and white lines show the motion of the structural mesh. Among the critical modes mode 13 is predominantly flap rotation coupled with wing bending. The damping-velocity curve of mode 13 given in Figure 130 shows that although the damping curve crosses the zero damping at a speed slightly over the dive speed of the airplane, damping increase is mild and damping

value is below 0.2 until 300 m/s. Therefore, a mild flutter situation is expected to occur. However, considering that the aeroelastic analysis is performed with no structural damping and no damping is included in the servo actuator model, it is probable that mode 13 will have sufficient damping to suppress flutter if structural damping and servo actuator damping is included in the aeroleastic model.
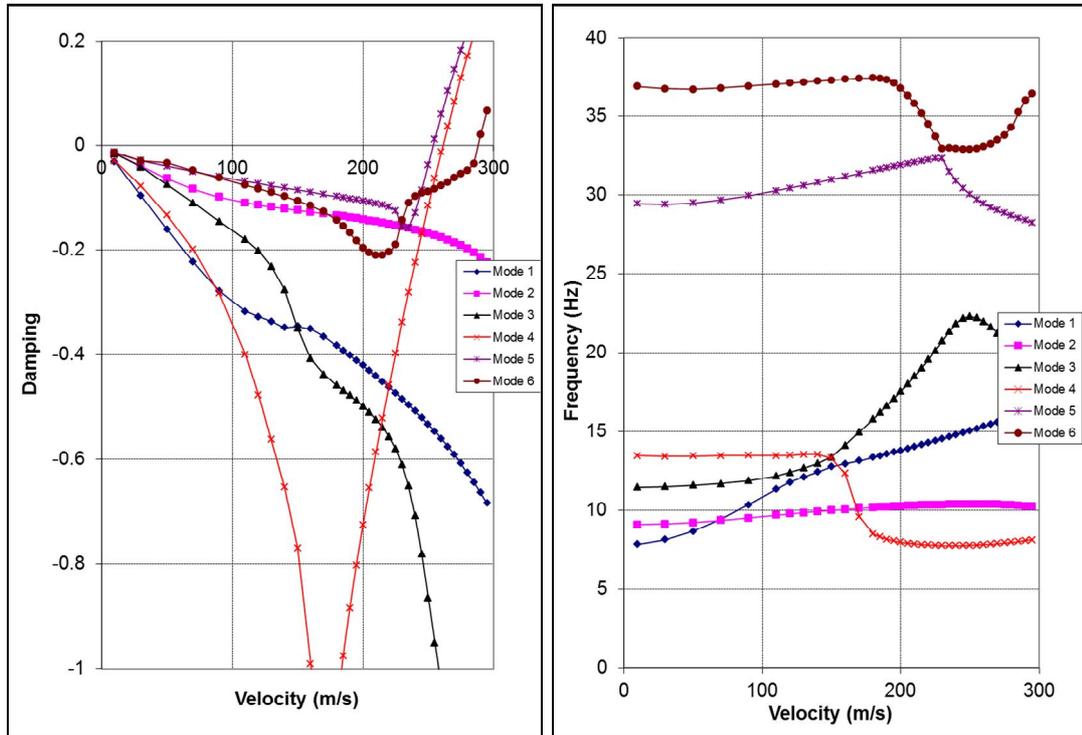
Figure 128: Damping/frequency versus speed curves for modes 1-6 of airplane with wing control surfaces
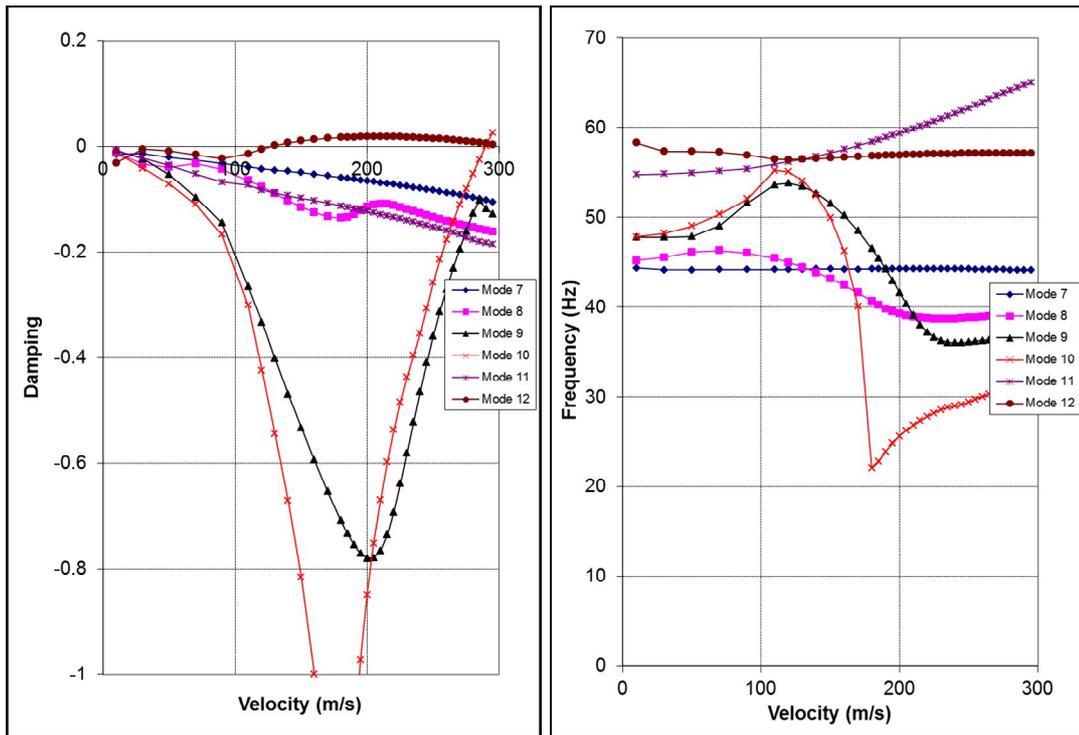
Figure 129: Damping/frequency versus speed curves for modes 7-12 of airplane with wing control surfaces
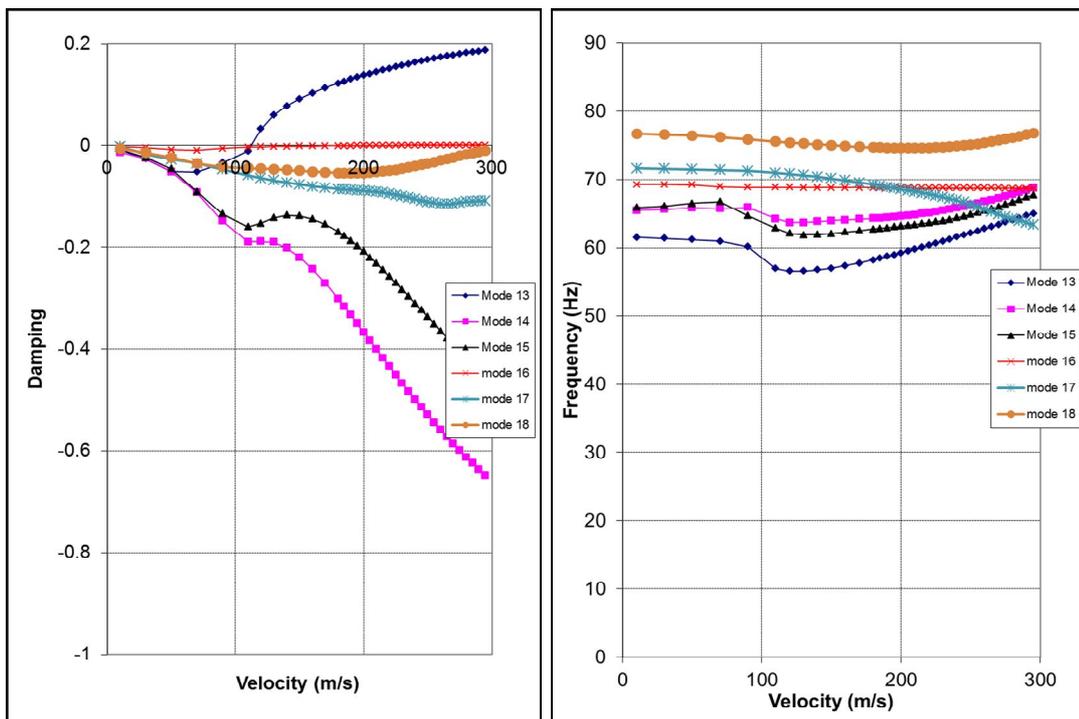
Figure 130: Damping/frequency versus speed curves for modes 13-18 of airplane with wing control surfaces
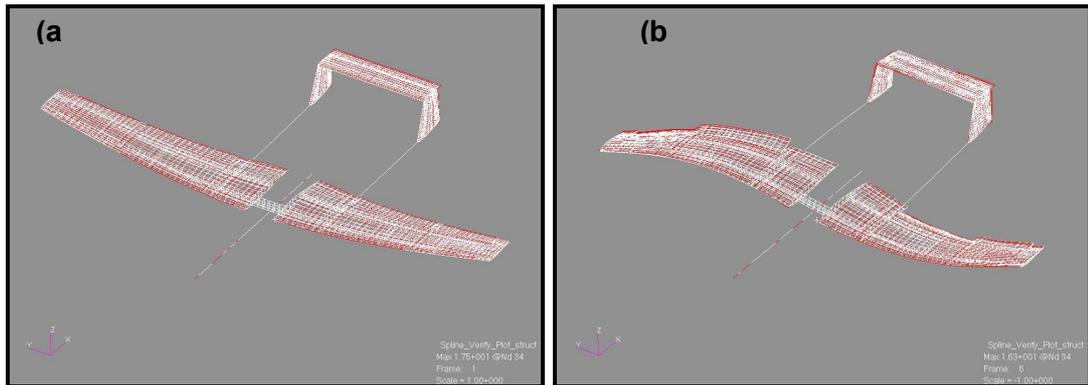
Figure 131: Spline verification of critical modes (a) Mode 4 (b) Mode 5
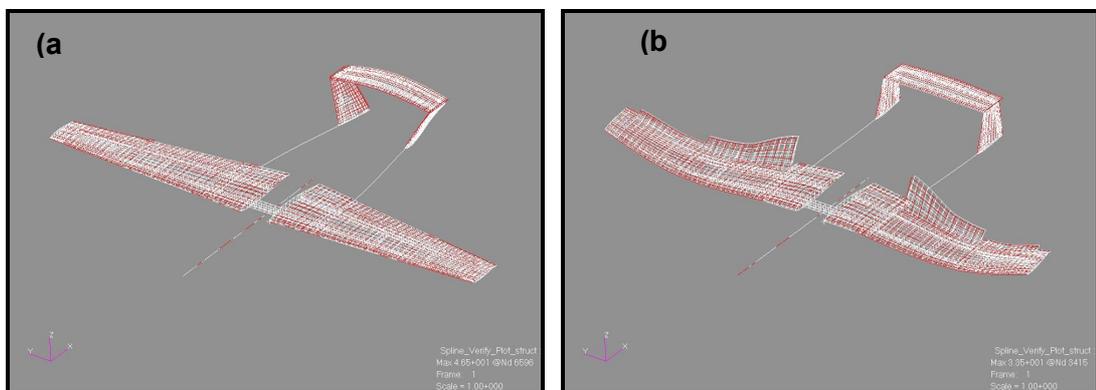
Figure 132: Spline verification of critical modes (a) Mode 6 (b) Mode 13

Based on the comparison of the critical modes of the full airplane with wing control surfaces and without wing control surfaces the following conclusions can be drawn:

·Wing bending and wing anti-symmetric bending modes of the full airplane with wing control surfaces (modes 4 and 5) are still the critical modes with close flutter speeds to the flutter speeds of wing bending and wing anti-symmetric bending modes of the full airplane without wing control surfaces (modes 4 and 5). Due to the high stiffness used in the CBUSH element which is used to model the servo actuator, wing bending and wing anti-symmetric bending modes are not affected significantly.

·Mode 8 of the aeroelastic model without wing control surfaces and mode 10 of the aeroelastic model with wing control surfaces are essentially the same mode of vibration which is tail boom bending in the vertical direction coupled with horizontal

143

tail bending. With the addition of wing control surfaces into the aeroelastic model flutter speed associated with this particular mode is seen to increase about %11.

·Mode 6 of aeroelastic models of the full airplane with and without wing control surfaces is the flapping motion of the vertical tails coupled with bending of the tail booms in the horizontal direction. Mode 6, which is not a critical mode of the airplane without wing control surfaces, is predicted as one of the critical modes for the airplane with wing control surfaces. It should be noted that the cut-out for the inboard flap causes discontinuity in the structure with associated stiffness loss in the region where tail booms are connected. Therefore, flap cut-out could have triggered mode 6 to turn into a critical mode.

·Symmetric wing torsion mode (mode 13) of the aeroelastic model of the airplane without wing control surfaces is one of the critical flutter modes. In the airplane model with wing control surfaces symmetric wing torsion mode is mode 15. From the damping trend of mode 15 given in Figure 130, it is observed that with the inclusion of the control surfaces into the aeroelastic model the symmetric torsion mode becomes highly damped.

·Studies on the aeroleastic analysis of the airplane with wing control surfaces showed that flutter modes and speeds are sensitive to the torsional stiffness constant assigned to the CBUSH element which is used to model the servo actuator. A low torsional stiffness value results in instabilities associated with control surface motion dominated modes at low speeds. Therefore, it is concluded that an accurate model of the servo actuator has to developed and incorporated into the aeroleastic model.

CHAPTER 5

CONCLUSION

In this study, the computational aerodynamics analyses for a fully composite twin wing-tail boom configuration unmanned air vehicle are performed. Angle of attacks at the static limit conditions are calculated according to only wing computational aerodynamics analyses results, and computational aerodynamic analyses of full UAV are performed at the calculated angles of attack. Pressure distributions calculated by the Euler solution and the Navier-Stokes solution are compared, and it is observed that both methods gave similar pressure distribution.

The lift curve slope determined by the Euler solution performed by Fluent is compared with the lift curve slope obtained by the ESDU95010 code which is based on the steady lifting-surface theory based on the Multhopp-Richardson solution. It is observed that, the lift-curve slope determined by the computational aerodynamic analysis and ESDU95010 code are close to each other, and the lift curve slope determined by the ESDU code approaches the lift-curve slope determined by the computational aerodynamic analysis when the number of camber points, approximating the mean camber of the wing, is increased. This study further verified the accuracy of the computational aerodynamic analysis performed by Fluent.

The computational aerodynamics based load extraction and interpolation of the aerodynamic loads to the structural mesh is accomplished successfully, and structural analyses are performed at static limit loads which are calculated at the maximum positive load factor for the minimum maneuvering speed and the dive speed. In the thesis, detailed structural analyses of the lifting surfaces are performed only. For the isotropic materials, Von-Mises stresses are compared with the material strength, and Tsai-Wu failure theory is employed to calculate the failure indices for the composite parts. Detailed structural analyses showed that the lifting surfaces have sufficient structural integrity under the action of static limit loads calculated at the corner points of the V-N diagram.

In the last part of the thesis, detailed aeroelastic stability analyses of a twin wing-tail boom configuration unmanned air vehicle are conducted at the sea level by different aeroelastic models which are created by adding one sub-structure at a time to the aeroelastic model and no aeroelastic instability is expected to occur within the flight envelope of the airplane.

During the course of aeroelastic analyses different splining methods, aerodynamic modeling alternatives, the choice of spline points, structural and aerodynamic grid refinement effects and the effect of uncertainties in the material properties are also evaluated. Results suggest that flutter speeds obtained with a reasonably coarse structural/aerodynamic grid tend to be conservative and the use of infinite plate spline method gives consistently lower critical speeds compared to the finite plate spline method. The use of bridging aerodynamic panels between the left and right wings has an effect on the flutter modes and speeds. The correct modeling approach partially cancels the strength of the inboard vortex generated by the additional bridging aerodynamic panels. By bridging the gap between the left and the right wings by additional aerodynamic panels, critical aeroelastic stability speeds increase slightly. The slight increase in aeroelastic stability is considered to be due to the partial cancellation of the strong vortex line at the inboard edge which leads to more correct aerodynamic force distribution.Results show that pure foam and pure epoxy modeling of the Rohacell foam core that is used during the manufacturing of the skins of the lifting surfaces has an appreciable effect on the flutter speeds. Material properties, which are highly dependent on the manufacturing method used, should either be characterized accurately or be assigned two extreme properties to determine a range for the critical aeroelastic stability speeds. Present study also shows that for the particular UAV, addition of the flexible tail boom-tail plane combination into the aeroelastic model introduces new flutter modes in the speed regime of interest, whereas inclusion of the stiff fuselage structure into the aeroelastic model does not affect the flutter modes and speeds appreciably. Finally, it is seen that addition of wing control surfaces into the aeroelastic model creates control surface coupled with wing bending mode with low flutter speed when the servo actuator is modeled by a simplified first order system which is a torsional spring with a very high spring constant.

Considering that the dive speed of the UAV is 100 m/s, sea level flutter speeds, predicted by the different aeroelastic models have large margins of safety. This conclusion shows that the tactical unmanned air vehicle is expected to be free of aeroelastic instability within its flight envelope.

Tail boom bending mode of the UAV has the lowest natural frequency and high frequency harmonic forces may lead to resonance in the tail of the UAV in flight. The UAV should avoid maneuvers like "short-period mode", which can produce high amplitude vibrations on the tail and cause instabilities in the control of the UAV. The UAV should also avoid maneuvers outside of flight envelope.

For the future work, aeroelastic analyses can be repeated at different altitudes, and aeroelastic stability character of the airplane can be determined at different altitudes. Low flutter speed caused by flap rotation coupled with wing bending mode can be prevented by design change on control surfaces. Aeroelastic model can also be improved by combining computational aerodynamics and structural finite element analysis for more accurate determination of the fluid-structure interaction. Nonlinear aerodynamics based aeroelastic analysis of the full airplane is a challenging job which can be studied in the future. In addition, nonlinear aerodynamics can be coupled with nonlinear structural analysis to better estimate the aeroelastic behavior of flexible aerospace structural systems. It is also considered that an accurate model of the servo actuator has to developed and incorporated into the aeroelastic model. Aeroelastic analysis of lifting surfaces control surfaces require the incorporation of accurate servo actuator models in the aeroelastic model.

REFERENCES

1. Fahlstrom, P.G., and Gleason, T.J., Introduction to UAV Systems., MD, USA, 1994.

2. French MoD (DGA) USAR Working Group, UAV Systems Airworthiness Requirements (USAR) Version 3, 2005.

3. G. P. Guruswamy and C. Byun, "Fluid-Structural Interactions using Navier-Stokes Flow Equations Coupled with Shell Finite Element Structures.", NASA Ames Research Center, Moffett Field, California, 1993

4. G. Frulla, E. Cestino, "Design, manufacturing and testing of a HALE-UAV structural demonstrator", Composite Structures 83 pp.143–153, 2008

5. R. W. Sullivan, Y. Hwang, M. Rais-Rohani, T. Lacy, "Structural Analysis and Testing of an Ultralight Unmanned-Aerial-Vehicle Carbon-Composite Wing", Journal of aircraft, Vol. 46, No. 3, May–June 2009

6. Isaac, D.A. and Iverson, M.P., "Automated Fluid-Structure Interaction Analysis", ATK Thiokol Propulsion Brigham City, Utah

7. Kosmatka,J.B., and Panza, J., "Aeroelastic Stability of the GA-ASI Predator Aircraft," 1st Technical Conference and Workshop on Unmanned Aerospace Vehicles, AIAA, Portsmouth, Virginia, USA, 2002, AIAA 2002-3470.

8. Kosmatka,J.B., and Panza, J., "Aeroelastic Analysis of the Predator Aircraft With Wing Mounted FINDER Mini-UAVs," 2nd "Unmanned Unlimited" Systems, Technologies and Operations- Aerospace, Land, and Sea Conference and Workshop and Exhibit, AIAA, San Diego, CA, USA, 2003, AIAA 2003-6501.

9. Pitcher, N.A., "A Static Aeroelastic Analysis of a Flexible Wing Mini Unmanned Aerial Vehicle," M.Sc. Thesis, Air Force Institute of Technology,

Wright-Patterson AFB OH School of Engineering and Management, Department of Engineering Physics, OH, USA, 2008.

10. Di Palma, L., Paletta, N., Pecora,M., "Aeroelastic Design of a Joined-Wing UAV," SAE AeroTech Congress and Exhibition, Seattle, WA, USA, 2009.

11. Striz, A.G., and Venkayya, V.B., "Influence of Structural and Aerodynamic Modeling on Flutter Analysis," Journal of Aircraft, Vol. 31, No.5, 1994, pp. 1205-1211.

12. Weisshaar, T.A., "Aeroelasticity's Role in Innovative UAV Design and Optimization," Technical paper, School of Aeronautics and Astronautics, Purdue University, IN, USA.

13. Fluent Flow Modeling Software, http://www.fluent.com/

14. ESDU (Engineering Sciences Data Unit) 95010, "Computer program for estimation of spanwise loading of wings with camber and twist in subsonic attached flow", The Royal Aeronautical Society, 1997, www.esdu.com

15. Soysal, S., "Structural Design, Analysis and Composite Manufacturing Applications for a Tactical Unmanned Air Vehicle", 2008

16. Schaeffer, H.G.: MSC.Nastran Primer for Linear Static Analysis. MSC Software Corporation, Santa Ana, California (2001)

17. A.M. Kuethe and J.D. Schetzer, Foundations of Aerodynamics, Section 4.11 (2nd edition), John Wiley & Sons, Inc., New York (1959)

18. Evonik Röhm GmbH: Rohacell A.
http://www.rohacell.com/en/performanceplastics8344.html 25 Jan 2007 (2007)

19. Center for Composite Material Research web site, "http://www.ncat.edu/~ccmradm/ccmr/meen613/Chapter4_FailureTheories.pdf" (2011)

20. Gürdal, Z., Haftka, R.T., Hajela, P., Design and Optimization of Laminated Composite Materials, John Wiley and Sons Inc. 1999.

21. Turgut, T., "Manufacturing and Structural Analysis of a Lightweight Sandwich Composite UAV Wing", 2007

22. MSC. Nastran Version 68, Aeroelastic Analysis User's Guide, MSC.Software Corporation, 2004.

23. Harder, R.L. and Desmarais,R.N., "Interpolation Using Surface Splines," Journal of Aircraft, Vol. 9, No. 2, 1972, pp. 189-191.f

24. MSC. FlightLoads, MSC. Flightloads and Dynamics User's Guide, Version 2006, MSC.Software Corporation, 2006.

25. Appa, Kari., "Finite Surface Spline," Journal of Aircraft, Vol. 26, No. 5, 1989, pp. 495-496.m

26. Bathe, K.J., Finite Element Procedures in Engineering Analysis,, Prentice-Hall, Englewood Cliffs, NJ, USA, 1982, p111.

27. Striz, A.G., and Venkayya, V.B., "Influence of Structural and Aerodynamic Modeling on Flutter Analysis," Journal of Aircraft, Vol. 31, No.5, 1994, pp. 1205-1211.

28. Yates, Jr. E.C., AGARD standard aeroelastic configurations for dynamic response. Candidate configuration I.-Wing 445.6, NASA Technical Memorandum 100492, 1987.

29. Kolonay, R. M., Teknik Sunuş, "Computational Aeroelasticity," ODTÜ Kültür Kongre Merkezi, Ankara, Türkiye, 2001.

30. MSC. Software Corporation, MSC. Nastran Linear Static Analysis User's Guide, Version 2003, MSC.Software Corporation, 2003, p. 297.

31. Zona Technology Inc., ZAERO User's Manual, Version 8.2, Zona Technology Inc., 2008.

APPENDIX

Appendix A

Description of interpolation of CA data from Fluent to Nastran

Interpolation of the CA data from Fluent to Nastran is described in this section. It is known that mesh type used in the CA analysis and in the FE analysis are different from each other. Therefore, in order to transfer loads from Fluent to Nastran, an interpolation procedure should be implemented.

Primarily, CAD geometry of air vehicle is drawn by CATIA V5 and geometry is exported to a step file. This step file is imported to Gambit, which is the preprocessor program for Fluent. After transferring geometry to Gambit, solution domain is meshed for the CA analysis and CA analysis is performed by Fluent. Fine mesh density required by the computational aerodynamics analysis should be used in the analysis performed by Fluent.

After the CA analysis, pressure data file has to be created. "Interpolate" option, which is under the "File" menu in Fluent, is used to create the pressure data file. In order to create the pressure data file "Write Data" should be selected in "Options" menu and "Pressure" should be selected in "Fields" menu. Figure A1 shows the Fluent interface menu used to create pressure data file.
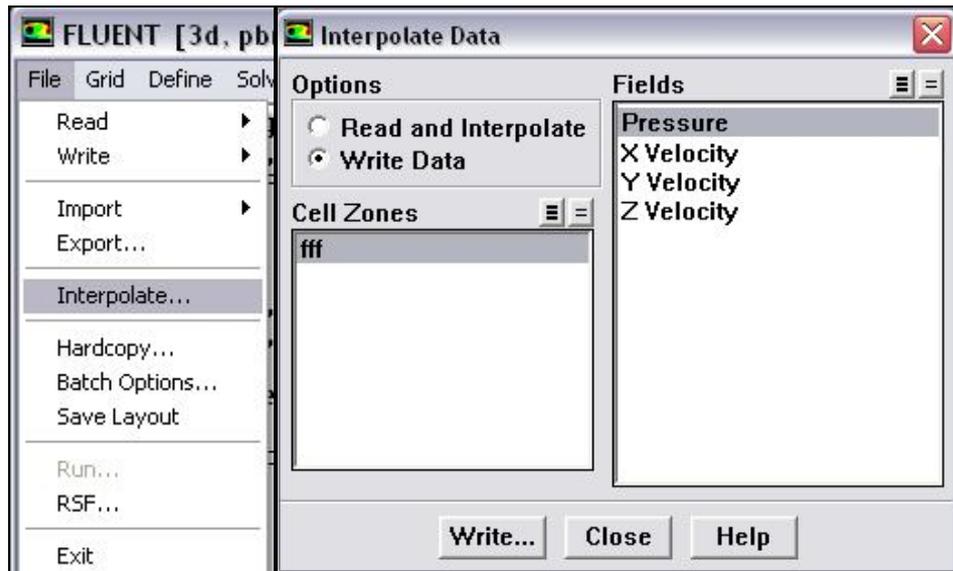
Figure A1: Creation of the Pressure Data File

After creation of the pressure data file, another domain mesh is created in Gambit preprocessor. In this mesh, finite element type quadrilateral elements (QUAD4) are used on all surfaces of the aircraft. Using this surface mesh, a volume mesh is created in Gambit and the new mesh domain is imported to Fluent. It should be noted that coordinates of the aircraft in both models should be the same to perform a successfull interpolation.

The new solution mesh is opened inside the Fluent program, and then "Interpolate" option is used again to transfer the pressure data created to the new domain mesh that is created. Figure describes this procedure. This time, "Read and Interpolate" should be selected instead of "Write Data". Thus, pressure data is transfered to the new domain, indicated by "fff" in Figures A1 and A2, by interpolation.
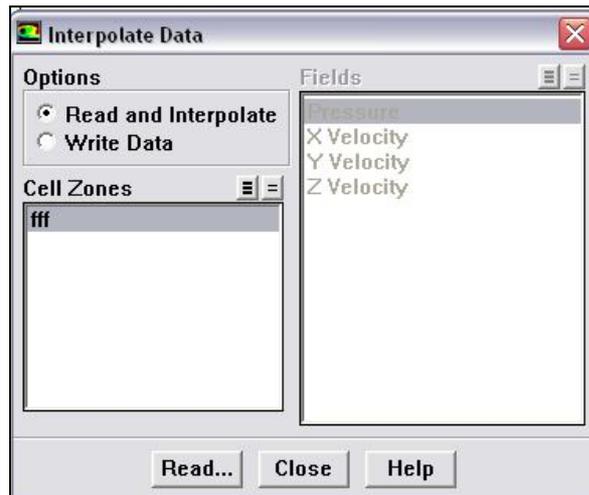
Figure A2: Interpolation of the pressure data to the new solution mesh

In the next step of the interpolation, "Export" option under the "File" menu is used to transfer the surface mesh, which is composed of QUAD4 elements, on the aircraft surfaces to Patran. By selecting "NASTRAN" in "File type" menu, "forces" in "structural loads" menu and all surfaces of the aircraft in "surfaces" menu, all nodes, aerodynamic forces on nodes and elements on aircraft surfaces are saved in the Nastran input file (*bdf) format . In order to create the Nastran input file, all the selections to be done are shown in Figure A3.
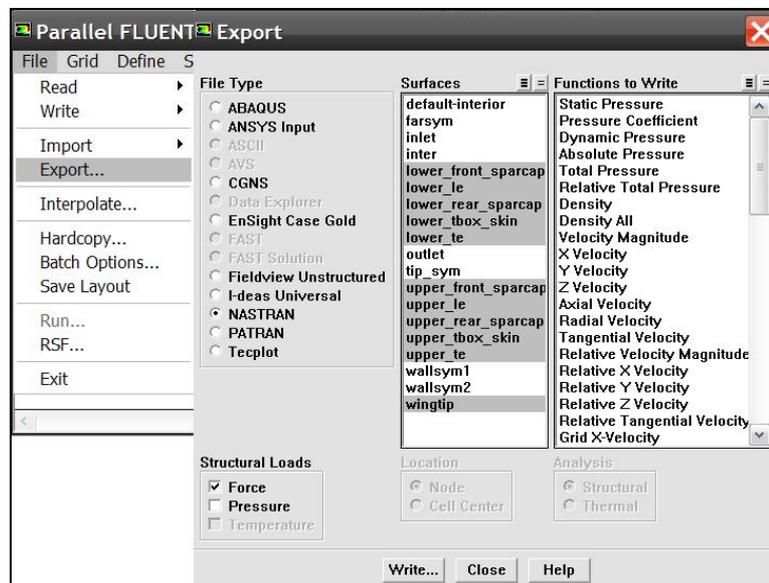
Figure A3: Menu selections inside Fluent for the creation of Nastran input files

İt should be noted that if the surfaces which have pressure load on them are selected individually, then separate Nastran input files (.bdf) may be generated for each surface.

Nastran input files created by "Export" option are transferred to Patran by "Import" option in Patran. Figure A4 shows menu selections to be made in order to import Nastran input files to Patran. "Model" is selected under the "object" menu and "MSC Nastran Input" is selected under the "Source" menu. "Nodes", "Elements" and "Load Sets" should be selected in "MSC Nastran Input Options" menu.
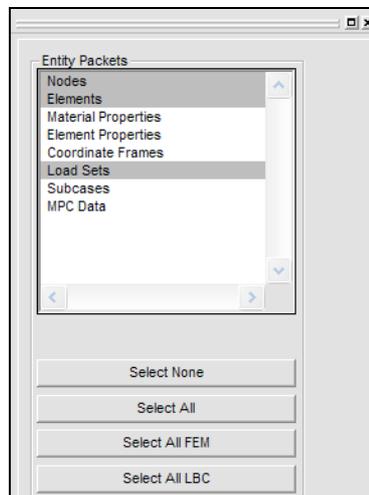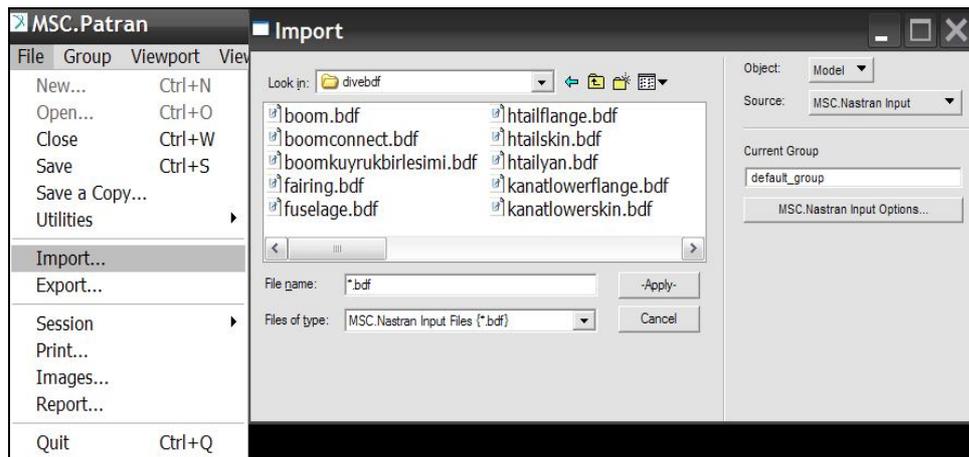
Figure A4: Menu selections to be made in the Patran environment in order to import Nastran input files to Patran

After transferring the mesh of external surfaces of the UAV with the loads acting on the nodes, mesh of the internal geometry of the airplane or the wing, whichever

substructure is going to be analyzed structurally, is created compatibly with the external mesh. Figure A5 shows the flowchart of the interpolation procedure.
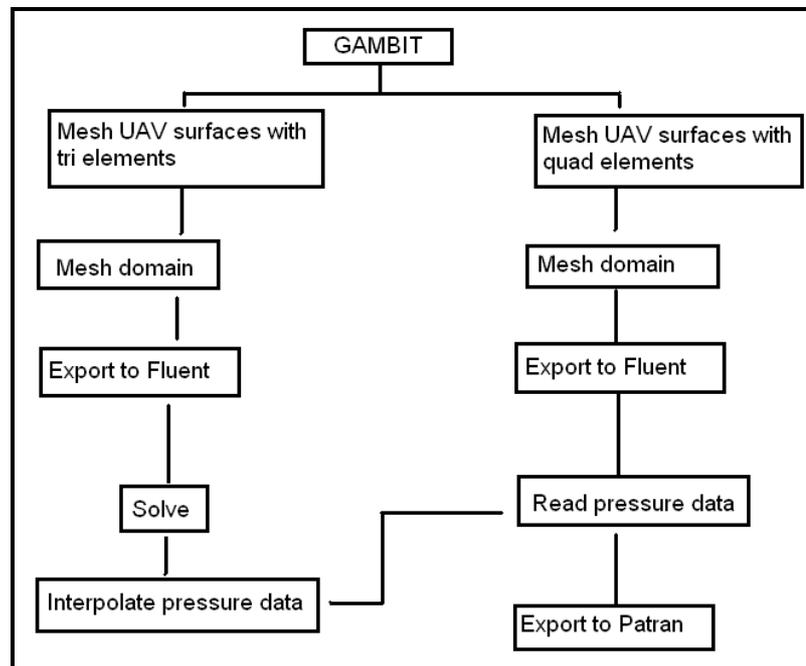
Figure A5: Flow chart of load transfer from Fluent to Nastran between two different solution meshes

Appendix B

Failure index and strength ratio summary of the UAV

Table B1. Failure Indices for the Wing Ribs - Dive Speed Condition

Rib 1 (Root) Layer #	Material	FI	SR	Rib 4 layer #	Material	FI	SR
1	Carbon/Epoxy	0.08	3.54	1	Carbon/Epoxy	~ 0	168.448
2	Hornbeam	MOS=%	15.274	2	Hornbeam	MOS=%	280.315
3	Carbon/Epoxy	0.07	3.77	3	Carbon/Epoxy	~ 0	161.787
4	Blue Foam			4	Blue Foam		
5	Carbon/Epoxy	0.037	5.208	5	Carbon/Epoxy	~ 0	119.682
6	Hornbeam	MOS=%	31.25	6	Hornbeam	MOS=%	355.66
7	Carbon/Epoxy	0.033	5.470	7	Carbon/Epoxy	~ 0	111.394
Rib 2 layer #	Material	FI	SR	Rib 5 layer #	Material	FI	SR
1	Carbon/Epoxy	0.045	4.688	1	Carbon/Epoxy	~ 0	259.192
2	Hornbeam	MOS=%	36.441	2	Hornbeam	MOS=%	1198.387
3	Carbon/Epoxy	0.045	4.708	3	Carbon/Epoxy	~ 0	284.790
4	Blue Foam			4	Blue Foam		
5	Carbon/Epoxy	0.044	4.755	5	Carbon/Epoxy	~ 0	371.009
6	Hornbeam	MOS=%	86.486	6	Hornbeam	MOS=%	1448.077
7	Carbon/Epoxy	0.044	4.761	7	Carbon/Epoxy	~ 0	395.257
Rib 3 layer #	Material	FI	SR	Rib 6 (Tip) layer #	Material	FI	SR
1	Carbon/Epoxy	0.037	5.179	1	Carbon/Epoxy	~ 0	579.122
2	Hornbeam	MOS=%	45.482	2	Hornbeam	MOS=%	10220.51
3	Carbon/Epoxy	0.037	5.172	3	Carbon/Epoxy	~ 0	701.045
4	Blue Foam			4	Blue Foam		
5	Carbon/Epoxy	0.038	5.099	5	Carbon/Epoxy	~ 0	1549.087
6	Hornbeam	MOS=%	95.547	6	Hornbeam	MOS=%	43025
7	Carbon/Epoxy	0.039	5.069	7	Carbon/Epoxy	~ 0	1673.855

Table B2. Failure Indices for the Wing Ribs - Stall condition

Rib 1 (Root) Layer #	Material	FI	SR	Rib 4 layer #	Material	FI	SR
1	Carbon/Epoxy	0.006	12.63	1	Carbon/Epoxy	~ 0	149.468
2	Hornbeam	MOS=%	19.259	2	Hornbeam	MOS=%	280.315
3	Carbon/Epoxy	0.005	13.737	3	Carbon/Epoxy	~ 0	147.905
4	Blue Foam			4	Blue Foam		
5	Carbon/Epoxy	0.003	19.969	5	Carbon/Epoxy	~ 0	141.766
6	Hornbeam	MOS=%	32.692	6	Hornbeam	MOS=%	355.66
7	Carbon/Epoxy	0.002	22.576	7	Carbon/Epoxy	~ 0	136.663
Rib 2 layer #	Material	FI	SR	Rib 5 layer #	Material	FI	SR
1	Carbon/Epoxy	~ 0	106.312	1	Carbon/Epoxy	~ 0	322.062
2	Hornbeam	MOS=%	67.128	2	Hornbeam	MOS=%	1198.387
3	Carbon/Epoxy	~ 0	104.298	3	Carbon/Epoxy	~ 0	336.007
4	Blue Foam			4	Blue Foam		
5	Carbon/Epoxy	~ 0	91.475	5	Carbon/Epoxy	~ 0	349.746
6	Hornbeam	MOS=%	124.651	6	Hornbeam	MOS=%	1448.077
7	Carbon/Epoxy	~ 0	87.359	7	Carbon/Epoxy	~ 0	353.194
Rib 3 layer #	Material	FI	SR	Rib 6 (Tip) layer #	Material	FI	SR
1	Carbon/Epoxy	0	85.424	1	Carbon/Epoxy	~ 0	376.203
2	Hornbeam	MOS=%	73.118	2	Hornbeam	MOS=%	10220.51
3	Carbon/Epoxy	~ 0	86.498	3	Carbon/Epoxy	~ 0	434.129
4	Blue Foam			4	Blue Foam		
5	Carbon/Epoxy	~ 0	79.991	5	Carbon/Epoxy	~ 0	968.279
6	Hornbeam	MOS=%	150.259	6	Hornbeam	MOS=%	43025
7	Carbon/Epoxy	~ 0	78.175	7	Carbon/Epoxy	~ 0	1291.652

Table B3. Failure Indices for the Spar Webs – Dive Speed condition

Front spar web –x[1]				Rear spar web -x			
Layer #	Material	FI	SR	Layer #	Material	FI	SR
1	Carbon/Epoxy	0.046	4.662	1	Carbon/Epoxy	0.024	6.409
2	Carbon/Epoxy	0.046	4.658	2	Carbon/Epoxy	0.025	6.348
3	Carbon/Epoxy	0.046	4.654	3	Carbon/Epoxy	0.025	6.286
4	Carbon/Epoxy	0.046	4.65	4	Carbon/Epoxy	0.026	6.223
5	Carbon/Epoxy	0.046	4.646	5	Carbon/Epoxy	0.026	6.159
Front spar web +x				Rear spar web +x			
Layer #	Material	FI	SR	Layer #	Material	FI	SR
1	Carbon/Epoxy	0.068	3.823	1	Carbon/Epoxy	0.019	7.3
2	Carbon/Epoxy	0.065	3.918	2	Carbon/Epoxy	0.019	7.344
3	Carbon/Epoxy	0.062	4.018	3	Carbon/Epoxy	0.018	7.364
4	Carbon/Epoxy	0.059	4.123	4	Carbon/Epoxy	0.03	5.793
5	Carbon/Epoxy	0.056	4.233	5	Carbon/Epoxy	0.049	4.58

Table B4. Failure Indices for the Spar Webs – Stall condition

Front spar web -x				Rear spar web -x			
Layer #	Material	FI	SR	Layer #	Material	FI	SR
1	Carbon/Epoxy	0.038	5.155	1	Carbon/Epoxy	0.039	5.057
2	Carbon/Epoxy	0.038	5.1	2	Carbon/Epoxy	0.039	5.056
3	Carbon/Epoxy	0.039	5.046	3	Carbon/Epoxy	0.039	5.055
4	Carbon/Epoxy	0.04	4.992	4	Carbon/Epoxy	0.039	5.052
5	Carbon/Epoxy	0.041	4.94	5	Carbon/Epoxy	0.039	5.049
Front spar web +x				Rear spar web +x			
Layer #	Material	FI	SR	Layer #	Material	FI	SR
1	Carbon/Epoxy	0.059	4.121	1	Carbon/Epoxy	0.023	6.559
2	Carbon/Epoxy	0.057	4.184	2	Carbon/Epoxy	0.024	6.515
3	Carbon/Epoxy	0.055	4.249	3	Carbon/Epoxy	0.024	6.472
4	Carbon/Epoxy	0.054	4.315	4	Carbon/Epoxy	0.024	6.43
5	Carbon/Epoxy	0.052	4.384	5	Carbon/Epoxy	0.025	6.387

[1] For the spar webs 1 –x refers to the web in the –x direction and +x refers to the web in the +x direction

Table B5. Failure Indices for the Upper Flanges of the Spars – Dive speed condition

Front spar flange				Rear spar flange			
Layer #	Material	FI	SR	Layer #	Material	FI	SR
1	Carbon/Epoxy	0.038	5.134	1	Carbon/Epoxy	0.02	7.01
2	Carbon/Epoxy	0.039	5.034	2	Carbon/Epoxy	0.021	6.861
3	Carbon/Epoxy	0.041	4.939	3	Carbon/Epoxy	0.022	6.72
4	Carbon/Epoxy	0.043	4.846	4	Carbon/Epoxy	0.023	6.585
5	Carbon/Epoxy	0.044	4.758	5	Carbon/Epoxy	0.024	6.454
6	E-glass/Epoxy	0.039	5.081	6	E-glass/Epoxy	0.05	4.491
7	E-glass/Epoxy	0.04	4.989	7	E-glass/Epoxy	0.052	4.4
8	Epoxy	MOS=% 14.8		8	Epoxy	MOS=%50	
9	E-glass/Epoxy	0.052	4.377	9	E-glass/Epoxy	0.069	3.809
10	E-glass/Epoxy	0.054	4.308	10	E-glass/Epoxy	0.071	3.743

Table B6. Failure Indices for the Upper Flanges of the Spars – Stall condition

Front spar flange				Rear spar flange			
Layer #	Material	FI	SR	Layer #	Material	FI	SR
1	Carbon/Epoxy	0.03	5.766	1	Carbon/Epoxy	0.027	6.05
2	Carbon/Epoxy	0.032	5.635	2	Carbon/Epoxy	0.029	5.921
3	Carbon/Epoxy	0.033	5.511	3	Carbon/Epoxy	0.03	5.73
4	Carbon/Epoxy	0.034	5.392	4	Carbon/Epoxy	0.033	5.493
5	Carbon/Epoxy	0.036	5.278	5	Carbon/Epoxy	0.036	5.274
6	E-glass/Epoxy	0.025	6.266	6	E-glass/Epoxy	0.043	4.849
7	E-glass/Epoxy	0.027	6.138	7	E-glass/Epoxy	0.044	4.755
8	Epoxy	MOS=% 26.739		8	Epoxy	MOS=%23.68	
9	E-glass/Epoxy	0.035	5.308	9	E-glass/Epoxy	0.07	3.79
10	E-glass/Epoxy	0.037	5.216	10	E-glass/Epoxy	0.073	3.689

Table B7. Failure Indices for the Upper Skin of the Wing – Dive speed condition

Upper skin Layer #	Material	FI	SR
1	E-glass/Epoxy	0.464	1.469
2	E-glass/Epoxy	0.464	1.467
3	Epoxy	MOS=% 35.3	
4	E-glass/Epoxy	0.47	1.459
5	E-glass/Epoxy	0.471	1.457

Table B8. Failure Indices for the Upper Skin of the Wing – Stall condition

Upper skin Layer #	Material	FI	SR
1	E-glass/Epoxy	0.512	1.398
2	E-glass/Epoxy	0.515	1.393
3	Epoxy	MOS=% 47.482	
4	E-glass/Epoxy	0.543	1.356
5	E-glass/Epoxy	0.547	1.352

Table B9. Failure Indices for the Lower Flanges of the Spars (Region 1) – Dive speed condition

Front spar flange Layer #	Material	FI	SR	Rear spar flange Layer #	Malzeme	FI	SR
1	Carbon/Epoxy	0.056	4.225	1	Carbon/Epoxy	0.143	2.646
2	Carbon/Epoxy	0.057	4.183	2	Carbon/Epoxy	0.142	2.653
3	E-glass/Epoxy	0.044	4.749	3	E-glass/Epoxy	0.225	2.109
4	E-glass/Epoxy	0.046	4.688	4	E-glass/Epoxy	0.229	2.088
5	Epoxy	MOS=% 76.3		5	Epoxy	MOS=% 162.8	
6	E-glass/Epoxy	0.059	4.128	6	E-glass/Epoxy	0.265	1.944
7	E-glass/Epoxy	0.06	4.095	7	E-glass/Epoxy	0.269	1.927

Table B10. Failure Indices for the Lower Flanges of the Spars (Region 1) – Stall condition

Front spar flange Layer #	Material	FI	SR	Rear spar flange Layer #	Material	FI	SR
1	Carbon/Epoxy	0.049	4.537	1	Carbon/Epoxy	0.029	5.825
2	Carbon/Epoxy	0.05	4.486	2	Carbon/Epoxy	0.032	5.624
3	E-glass/Epoxy	0.034	5.427	3	E-glass/Epoxy	0.048	4.58
4	E-glass/Epoxy	0.035	5.356	4	E-glass/Epoxy	0.049	4.505
5	Epoxy	MOS=% 42.361		5	Epoxy	MOS=% 61.1	
6	E-glass/Epoxy	0.043	4.849	6	E-glass/Epoxy	0.072	3.727
7	E-glass/Epoxy	0.0436	4.788	7	E-glass/Epoxy	0.075	3.641

Table B11. Failure Indices for the Lower Flanges of the Spars (Region 2) – Dive speed condition

Front spar flange Layer #	Material	FI	SR	Rear spar flange Layer #	Material	FI	SR
1	Carbon/Epoxy	0.101	3.146	1	Carbon/Epoxy	0.02	6.994
2	Carbon/Epoxy	0.099	3.174	2	Carbon/Epoxy	0.021	6.886
3	Carbon/Epoxy	0.098	3.202	3	Carbon/Epoxy	0.022	6.782
4	Carbon/Epoxy	0.096	3.231	4	Carbon/Epoxy	0.022	6.68
5	Carbon/Epoxy	0.094	3.259	5	Carbon/Epoxy	0.023	6.581
6	Carbon/Epoxy	0.092	3.288	6	Carbon/Epoxy	0.024	6.484
7	Carbon/Epoxy	0.091	3.317	7	Carbon/Epoxy	0.024	6.39
8	E-glass/Epoxy	0.59	1.302	8	E-glass/Epoxy	0.13	2.769
9	E-glass/Epoxy	0.576	1.317	9	E-glass/Epoxy	0.134	2.736
10	Epoxy	MOS=%	76.3	10	Epoxy	MOS=%	145.5
11	E-glass/Epoxy	0.478	1.446	11	E-glass/Epoxy	0.159	2.508
12	E-glass/Epoxy	0.466	1.465	12	E-glass/Epoxy	0.162	2.481

Table B12. Failure Indices for the Lower Flanges of the Spars (Region 2) – Stall condition

Front spar flange Layer #	Material	FI	SR	Rear spar flange Layer #	Material	FI	SR
1	Carbon/Epoxy	0.099	3.173	1	Carbon/Epoxy	0.025	6.323
2	Carbon/Epoxy	0.098	3.196	2	Carbon/Epoxy	0.026	6.172
3	Carbon/Epoxy	0.097	3.219	3	Carbon/Epoxy	0.028	6.026
4	Carbon/Epoxy	0.095	3.242	4	Carbon/Epoxy	0.029	5.885
5	Carbon/Epoxy	0.094	3.265	5	Carbon/Epoxy	0.03	5.748
6	Carbon/Epoxy	0.093	3.288	6	Carbon/Epoxy	0.032	5.616
7	Carbon/Epoxy	0.091	3.31	7	Carbon/Epoxy	0.033	5.488
8	E-glass/Epoxy	0.595	1.296	8	E-glass/Epoxy	0.155	2.542
9	E-glass/Epoxy	0.584	1.309	9	E-glass/Epoxy	0.158	2.515
10	Epoxy	MOS=%	42.361	10	Epoxy	MOS=%	61.1
11	E-glass/Epoxy	0.498	1.416	11	E-glass/Epoxy	0.184	2.33
12	E-glass/Epoxy	0.488	1.432	12	E-glass/Epoxy	0.188	2.308

Table B13. Failure Indices for the Lower Skin of the Wing – Dive speed condition

Lower skin Layer #	Material	FI	SR
1	E-glass/Epoxy	0.069	3.794
2	E-glass/Epoxy	0.069	3.795
3	Epoxy	MOS=% 336.2	
4	E-glass/Epoxy	0.071	3.761
5	E-glass/Epoxy	0.071	3.741

Table B14. Failure Indices for the Lower Skin of the Wing – Dive speed condition

Lower skin Layer #	Material	FI	SR
1	E-glass/Epoxy	0.081	3.507
2	E-glass/Epoxy	0.081	3.513
3	Epoxy	MOS=% 307.96	
4	E-glass/Epoxy	0.079	3.56
5	E-glass/Epoxy	0.079	3.566

Table B15. Failure Indices for the Upper Skin of the Horizontal Tail – Dive speed condition

Upper skin Layer #	Material	FI	SR
1	E-glass/Epoxy	0.01915	7.227
2	Epoxy	MOS= % 226.69	
3	E-glass/Epoxy	0.01878	7.298

Table B16. Failure Indices for the Upper Skin of the Horizontal Tail – Stall condition

Upper skin Layer #	Material	FI	SR
1	E-glass/Epoxy	0.00016	79.108
2	Epoxy	MOS=% 4041.414	
3	E-glass/Epoxy	0.00022	67.443

Table B17. Failure Indices for the Lower Skin of the Horizontal Tail – Dive speed condition

Lower skin Layer #	Material	FI	SR
1	E-glass/Epoxy	0.024	6.5
2	Epoxy	MOS=% 535.66	
3	E-glass/Epoxy	0.018	7.4

Table B18. Failure Indices for the Lower Skin of the Horizontal Tail – Stall condition

Lower skin Layer #	Material	FI	SR
1	E-glass/Epoxy	0.00032	56.0382
2	Epoxy	MOS=% 2660.943	
3	E-glass/Epoxy	0.00029	59.1464

Table B19. Failure Indices for the Spar Webs of the Horizontal Tail – Dive speed condition

Front spar web Layer #	Material	FI	SR	Rear spar web Layer #	Material	FI	SR
1	Carbon/Epoxy	0.01856	7.34	1	Carbon/Epoxy	0.01459	8.278
2	Carbon/Epoxy	0.01843	7.367	2	Carbon/Epoxy	0.01461	8.274

Table B20. Failure Indices for the Spar Webs of the Horizontal Tail – Stall condition

Front spar web Layer #	Material	FI	SR	Rear spar web Layer #	Material	FI	SR
1	Carbon/Epoxy	0.0021	21.815	1	Carbon/Epoxy	0.00109	30.23
2	Carbon/Epoxy	0.0021	21.952	2	Carbon/Epoxy	0.00113	29.762

Table B21. Failure Indices for the Upper Flange of the Front Spar of the Horizontal Tail – Dive speed condition

Upper flange of the front spar Layer #	Material	FI	SR
1	Carbon/Epoxy	0.00844	10.887
2	Carbon/Epoxy	0.00903	10.522
3	E-glass/Epoxy	0.00606	12.849
4	Epoxy	MOS=% 2597.368	
5	E-glass/Epoxy	0.00938	10.328

Table B22. Failure Indices for the Upper Flange of the Front Spar of the Horizontal Tail – Stall condition

Upper flange of the front spar Layer #	Material	FI	SR
1	Carbon/Epoxy	0.00004	165.631
2	Carbon/Epoxy	0.00004	158.336
3	E-glass/Epoxy	0.00008	114.917
4	Epoxy	MOS=% 24304.762	
5	E-glass/Epoxy	0.00016	79.243

Table B23. Failure Indices for the Lower Flanges of the Spars of the Horizontal Tail – Dive speed condition

Rear spar flange Layer #	Material	FI	SR	Front spar flange (flange 1) Layer #	Material	FI	SR
1	Carbon/Epoxy	0.00195	22.651	1	Carbon/Epoxy	0.00326	17.524
2	Carbon/Epoxy	0.00204	22.147	2	Carbon/Epoxy	0.00362	16.616
3	E-glass/Epoxy	0.00283	18.798	3	Carbon/Epoxy	0.00401	15.79
4	Epoxy	MOS=% 159.330		4	Carbon/Epoxy	0.006	14.42
5	E-glass/Epoxy	0.00309	17.99	5	E-glass/Epoxy	0.00361	16.637
				6	Epoxy	MOS=% 2462.500	
				7	E-glass/Epoxy	0.01412	8.416

Table B24. Failure Indices for the Lower Flanges of the Front Spar of the Horizontal Tail – Stall condition

Rear spar flange Layer #	Material	FI	SR	Front spar flange (flange 1) Layer #	Material	FI	SR
1	Carbon/Epoxy	0.00002	206.599	1	Carbon/Epoxy	0.00006	134.011
2	Carbon/Epoxy	0.00002	217.435	2	Carbon/Epoxy	0.00002	225.274
3	E-glass/Epoxy	0.00008	108.497	3	Carbon/Epoxy	0.00002	232.656
4	Epoxy	MOS=% 18494.1		4	Carbon/Epoxy	0.00002	220.575
5	E-glass/Epoxy	0.0001	101.202	5	E-glass/Epoxy	0.00004	160.202
				6	Epoxy	MOS=% 10521.7	
				7	E-glass/Epoxy	0.00077	36.113

Table B25. Failure Indices for the Lower Flange-2 of the Front Spar of the Horizontal Tail – Dive speed condition

Flange-2 of front spar Layer #	Material	FI	SR
1	Carbon/Epoxy	0.00365	16.56
2	Carbon/Epoxy	0.00405	15.704
3	E-glass/Epoxy	0.00838	10.924
4	Epoxy	MOS=% 465.517	
5	E-glass/Epoxy	0.02869	5.904

Table B26. Failure Indices for the Lower Flange-2 of the Front Spar of the Horizontal Tail – Stall condition

Flange-2 of front spar Layer #	Material	FI	SR
1	Carbon/Epoxy	0.00004	168.405
2	Carbon/Epoxy	0.00002	218.904
3	E-glass/Epoxy	0.00011	96.161
4	Epoxy	MOS=% 7156.637	
5	E-glass/Epoxy	0.0006	40.762

Table B27. Failure Indices for the skin of the Vertical Tail – Dive condition

Vertical tail skin Layer #	Material	FI	SR
1	E-glass/Epoxy	0.02184	6.766
2	Epoxy	MOS=% 606.897	
3	E-glass/Epoxy	0.02092	6.914

Table B28. Failure Indices for the spar webs of the Vertical Tail – Dive condition

Spar webs Layer #	Material	FI	SR
1	Carbon/Epoxy	0.0072	11.817
2	Carbon/Epoxy	0.0076	11.477

Table B29. Failure Indices for flange (flange 1) of the front spar of the Vertical Tail – Dive condition

Flange-1 of the spar of the vertical tail

Layer #	Material	FI	SR
1	Carbon/Epoxy	0.00551	13.472
2	Carbon/Epoxy	0.00301	18.239
3	E-glass/Epoxy	0.00502	14.113
4	Epoxy	MOS=% 1726.281	
5	E-glass/Epoxy	0.01931	7.197

Table B30. Failure Indices for flange (flange 2) of the front spar of the Vertical Tail – Dive condition

Flange-2 of the spar of the vertical tail

Layer #	Material	FI	SR
1	Carbon/Epoxy	0.00047	46.134
2	Carbon/Epoxy	0.00046	46.729
3	Carbon/Epoxy	0.00045	47.144
4	Carbon/Epoxy	0.00055	42.825
5	E-glass/Epoxy	0.00293	18.488
6	Epoxy	MOS=% 5224.675	
7	E-glass/Epoxy	0.00376	16.317

Appendix C

Determination of tensile properties of composite materials

Although mechanical properties of metallic materials can be found easily from literature, mechanical properties of composite materials can be sensitive to various factors like the manufacturing method, environmental conditions, fiber and resin selection etc. It is always recommended to perform a mechanical test for composite materials. This section describes a representative test procedure for E-glass/Epoxy and Carbon/Epoxy woven fabric lamina. Test specimens, prepared for the tensile testing, are manufactured by the vacuum bagging method.

E-glass/Epoxy and Carbon/Epoxy test specimens are prepared according to ASTM D 3039/D 3039M – 00 standard. Specimen length is 25cm and specimen width is 2.5cm. In order to provide desired thickness specified in the standard, E-glass/Epoxy specimen consists of 8 layers and Carbon/Epoxy consists of 7 layers. Total thickness of E-glass/Epoxy specimen is 1.8 mm and total thickness of Carbon/Epoxy specimen is 2.2 mm. Figure C1 shows the prepared specimens.

Figure C1: *Specimens prepared according to ASTM D 3039/D 3039M*

Specimen tabs are glued at edges of specimens in order to prevent grip damage. Tabs are made up of E-glass/Epoxy and they are 3 mm thick, 4 cm length. To prevent stress concentration caused by the tab edge, one edge of tabs are cut with

30 degrees of chamfer angle. Tabs are glued to specimens by Araldite 2011. Figure C2 shows the specimens after tabs are glued.
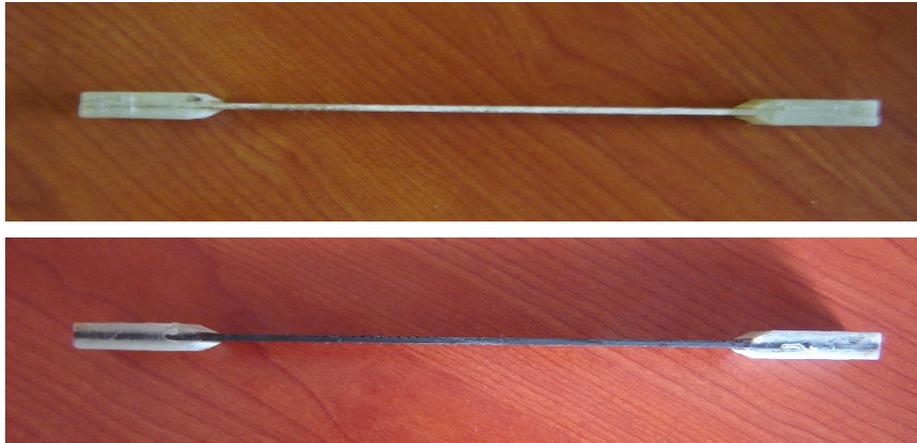
Figure C2: *Specimens after tabs are glued*

Tensile testings have been performed by 250 KN Zwick/Roell test machine. Grappling pressure has been set to 100 bars and test speed is 1 mm/sec. Force- % Elongation graphs are created in 8 cm gage length by extensometer. Photograph of test machine after test specimen is placed is shown Figure C3.
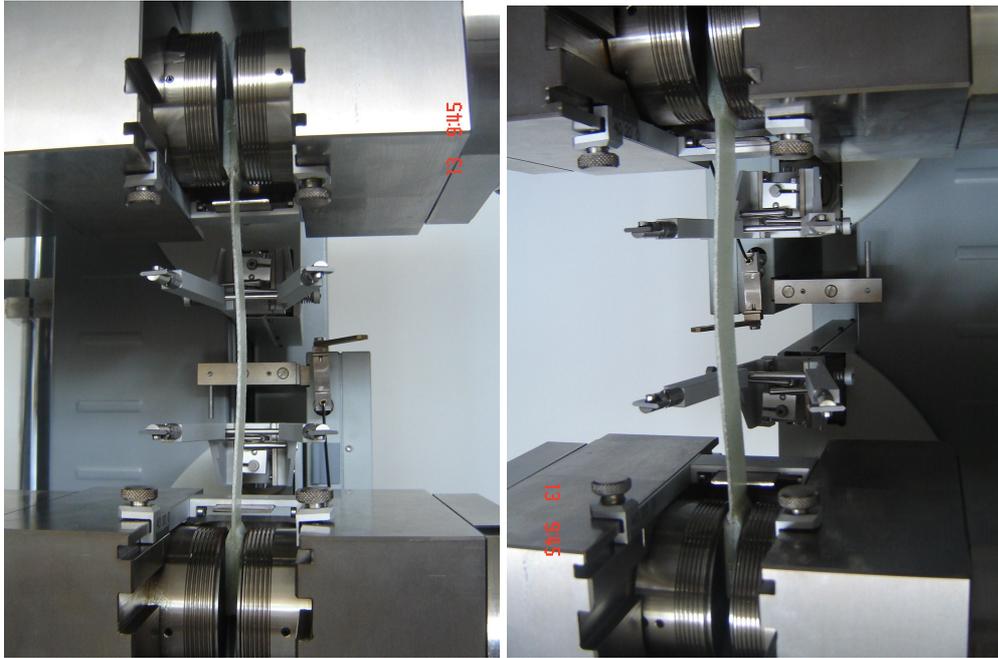
Figure C3: *250 kN Zwick/Roell tensile testing machine*

As it is seen in Figure C3, buckling occurs after grappling pressure is applied because of the compression at tabs of the specimen. 10 N initial load is applied in order to remove this buckling. Woven E-glass/Epoxy and Carbon/Epoxy specimens after tests are shown in Figure C3. Fracture has occurred in gage region for E-glass/Epoxy specimen; however, fracture is near tab of the specimen for Carbon/Epoxy specimen. Possible reason of this is that one of tab has slightly slipped during glue operation of Carbon/Epoxy specimen tabs.

Figure C3: *Specimens after the tensile tests*

Table C1 shows the test results. Each layer thickness for Carbon/Epoxy specimen is 0.314 mm and each layer thickness for E-glass/Epoxy specimen is 0.225 mm. Carbon/Epoxy specimen raptures under 34.09 kN load and maximum elongation is 1.15%. E-glass/Epoxy specimen breaks under 19.92 kN load and the maximum elongation is 2.25%. The failure stress is 758 MPa for Carbon/Epoxy and 433 MPa for E-glass/Epoxy.The elastic modulus of Carbon/Epoxy is 71 GPa and the elastic modulus of E-glass/Epoxy is 26 GPa.

Table C1: *Tensile test results*

Specimen #	Material	Number of layer	Total thickness (mm)	Layer thickness (mm)	Maximum Elongation (%)	F_{max} (kN)	E (GPa)	σ_{max} (MPa)
1	Carbon/Epoxy	7	2.2	0.314	1.15	34.09	71	758
2	E-glass/Epoxy	8	1.8	0.225	2.25	19.92	26	443

Tensile test report in Figure C5 summarizes test results for both specimens. Green line is Load- Elongation curve of Carbon/Epoxy specimen and red line is Load-Elongation curve of E-glass/Epoxy.

Figure C5: *Tensile test report*